Ultra-High-Resolution Spectroscopy of the ISM Towards Orion

Richard John Price

Thesis submitted for the Degree of Doctor of Philosophy
of the University of London

Department of Physics & Astronomy
UNIVERSITY COLLEGE LONDON

2002

To my parents

"If we knew what it was we were doing,
it would not be called research, would it?"

Albert Einstein.

Abstract

Firstly, we report ultra-high-resolution observations ($R \approx 880,000$) of Na I D_1, Ca II K, K I, CH and CH^+ for interstellar sightlines towards twelve bright stars in Orion, including four stars in the M42 region. Secondly, we report high-resolution observations ($R \approx 110,000$) of Na I D_1 & D_2 and Ca II H & K towards twelve stars with various locations in and around the λ Orionis association.

Model fits have been constructed for the absorption-line profiles, providing estimates for the column density, velocity dispersion, and central velocity for each constituent velocity component. These data enable the detection of many more absorption components than previously recognised, providing a more accurate perspective on the absorbing medium. This is especially so for the line-of-sight to the Orion Nebula, a region not previously studied at very-high resolution. A comparison between the absorption occurring in sightlines with small angular separations (namely the M42 and λ Orionis association) has been used, along with comparisons with other studies, to estimate the line-of-sight velocity structures. Na°/Ca^+ abundance ratios are derived for individual clouds, providing an indication of their physical state. Where absorption from both Na° and K° is observed for a particular cloud, a comparison of the velocity dispersions measured for each of these species provides rigorous limits on both the kinetic temperature and turbulent velocity prevailing in each cloud. Our results indicate the turbulent motions to be subsonic in each case.

The comparison of observations made at different epochs has revealed temporal variability in the interstellar absorption-line profiles of two stars, δ Ori and ζ Ori. In the case of δ Ori, our observations reveal the transient cloud to be cool ($T_{\rm k} \lesssim 280$ K), with a heliocentric velocity of $+21.3$ km s^{-1}. The component is detected in Na I D_1, where clear hyperfine splitting is seen, and Ca II K. Following a discussion of the possible origins of

this component it is concluded that an interstellar, rather than circumstellar, origin is most likely. This is one of very few detections of variable interstellar absorption reported in the literature, and we suggest an origin within filamentary material associated with the expanding H I shell surrounding the Orion-Eridanus superbubble. These detections highlight the presence of small-scale spatial structure in the interstellar medium down to scales on the order of a few astronomical units.

Furthermore, the comparison of observations made towards the two closely spaced stars δ Ori A and δ Ori C, highlights the presence of variations in absorption between the two sight-lines. Such differences are indicative of small-scale spatial structure in the interstellar medium in this direction over distances of less than $\lesssim 15,000$ AU (the projected separation of the two stars).

Contents

List of Figures

List of Tables

Chapter 1

Introduction

1.1 The Interstellar Medium

The first detection of absorption lines from cold diffuse matter in interstellar space was made by Hartmann (1904) in an historic study of the spectrum and orbit of δ Orionis, a star now studied extensively here. In this study Hartmann demonstrated the Ca II K line to appear "extraordinarily weak, but almost perfectly sharp" and also reported the "quite surprising result that the calcium line at λ3934 does not share in the periodic displacements of the lines caused by the orbital motion of the [spectroscopic binary] star". The stationary nature of the line led Hartmann to conclude that the gas responsible for the absorption was not present in the atmosphere of δ Ori, but was instead located within an isolated cloud of matter residing somewhere along the line-of-sight to this star. This was of course a discovery which would open up a new branch of astronomy, launching the study of the interstellar medium (ISM).

Following the identification of interstellar Ca II absorption by Hartmann, interstellar Na was detected by Heger (1919) through the observation of stationary absorption from the atoms D lines at λ5890 and λ5896 Å towards δ Ori and β Sco.

Subsequent observations of the H and K lines of Ca II by Beals (1936) revealed double and asymmetric profiles in the spectra of ϵ & ζ Ori, these were the first steps in the study of the very complex interstellar sightline towards Orion. Asymmetric absorption line profiles are the result of the superposition of multiple absorption lines, each corresponding to the same atomic transition, but occurring in interstellar clouds with different radial velocities.

These observations highlight that matter is not distributed homogeneously and were the first evidence for the presence of multiple discrete clouds within the ISM. The centres of each absorption line are displaced from their natural wavelength due to Doppler shifts caused by the individual motions of the clouds.

Early surveys were conducted in order to identify the distribution of these clouds through the ISM. Observations of Ca II towards 50 stars made by Adams (1943) showed 80% of his sample to possess complex interstellar absorption consisting of between two and five components, with marked variations in the complexity also observed to occur between different regions of the sky. Furthermore, the strength of absorption is not seen to be well correlated with distance in the local spiral arm (e.g. Hobbs, 1974).

Since these early days of interstellar research many more high-resolution/high signal-to-noise surveys of interstellar matter have been made, exploiting the advances which have been made in instrument technology. These include the studies made by Hobbs (1969*a*,*b*,*c*, 1978*a*); Marschall and Hobbs (1972); Hobbs and Welty (1991); Welty *et al.* (1994, 1996); Welty and Hobbs (2001).

In addition to atomic/ionic species, many molecules have also been identified in the ISM, many of which where first discovered in the direction of Orion (reviewed by Genzel and Stutzki, 1989). Some of these molecules have only been detected in the tenuous conditions of the ISM since they are readily destroyed by collisions in laboratory experiments. Molecules produce transitions in both emission and absorption at frequencies from the far ultraviolet right through to the radio.

Due to the low energies of the ISM, all atoms, ions and molecules may be considered to be in their ground state; consequently, all observable absorption lines are due to the excitation of electrons from their ground states. These lines are not however confined to the visible part of the spectrum, in fact most, including those from the dominant ion stages, occur in the ultraviolet and require the use of spaced-based telescopes. The earliest large scale observations in the ultraviolet were performed with the *Copernicus* satellite, launched in 1972. Following *Copernicus* (which utilised a resolving power of $R \approx 3 \times 10^4$), came the *International Ultraviolet Explorer* (IUE; $R \approx 10^4$) which was launched in 1977, and the *Hubble Space Telescope (HST)* with the Goddard High Resolution Spectrograph (GHRS; $R \approx 10^5$) launched in 1990. Ground state transitions which occur in the visible part of the spectrum (and can therefore be observed from the ground) are generally weak (with the exception of the Ca II, Na I and K I doublets) since these transitions arise from

trace ion stages.

Studies of the ISM are crucial in our understanding of a wide variety of astrophysical processes. It is the very matter present in denser regions of the ISM that will become incorporated in the next generation of stars. In turn, stellar mass loss (from stellar winds to supernovae explosions) is continually enriching the ISM with the products of stellar nucleosynthesis, a cyclical process without which the heavy elements essential for the formation of our planet (and life) would not be available.

1.1.1 The Gas

The ISM is considered to be composed of gas in three main phases, which exist in near pressure equilibrium (McKee and Ostriker, 1977). The densest of these phases is the cold neutral medium, next is the warm, partially ionised intercloud medium and finally a hot, fully ionised medium. Each of these phases is discussed individually below. The values quoted in this section have been obtained from Bowers and Deeming (1984*b*); Duley and Williams (1984); Dyson and Williams (1997) and Longair (1994).

The '*Cold Neutral Medium*' (CNM), constitutes the most significant fraction of the mass of the ISM ($\approx$ 80 %) although the much higher density of the gas in the CNM means it occupies the smallest fraction of the interstellar volume ($\approx$ 5 %). The hydrogen is neutral and often present in the molecular form. Observations show neutral hydrogen to be largely confined to clouds in the Galactic plane, with scale heights of around 250 pc. The CNM is itself composed of gas with a wide range of densities and temperatures which may be separated into three broad groups; diffuse clouds, dark clouds and giant molecular clouds.

The diffuse clouds, with which this Ph.D. is mainly concerned, are the most tenuous component of the CNM with typically densities of $n \approx 20$ cm^{-3} and temperatures $T_{\rm k} \approx 80\ K$. The ability of ultraviolet photons to penetrate diffuse clouds provides an important heating mechanism and, due to effective molecular dissociation, prevents significant formation of molecular species. Diffuse clouds have a large range of sizes, although those with lower column densities are, in general, more abundant in the ISM (Kulkarni and Heiles, 1987). Diffuse clouds are not thought to be spherical in shape, but considered to take the form of sheets and filaments, sculpted by the influence of stellar winds and supernovae explosions (discussed by Dickey and Lockman, 1990).

Dark clouds are rather denser, $n \approx 10^3$–10^6 cm^{-3}, and therefore extinguish starlight more strongly (hence their name). Since the bulk of these clouds are therefore shielded from the interstellar radiation field, their temperatures are typically lower, $T_k \approx 10$–20 K, with central regions possibly as low as 2.7 K, in equilibrium with the cosmic microwave background radiation. The exclusion of dissociating radiation permits much of the hydrogen to be present in the molecular form and also allows the formation of many other complex molecular species. Refractory elements such as iron are almost entirely absent (exhibiting $\lesssim$1% of their cosmic abundance), thought to be the result of their inclusion in dust grains.

Molecular clouds, which are detectable through their emission at millimetre and submillimetre wavelengths, have masses of up to 10^6 $M_\odot$ and sizes of up to 30 pc, while giant molecular clouds (GMCs) can be as large as 100 pc. Much of the hydrogen in these regions is present in the molecular form and is shielded from the interstellar radiation field by a combination of dust and the molecular hydrogen itself (known as self-shielding). The CO molecule has proved to be a useful tracer of molecular material (Figure 3.1 in § 3.1 illustrates the molecular clouds in the Orion and Monoceros region; taken from Maddalena *et al.*, 1986). GMCs have typical densities, n of only $\approx$ few $\times 10^2$ cm^{-3} and temperatures are low, $T_k \approx 10$ K. Much denser cores are also present which are likely to contain protostars. These cores have typical densities of $n \approx 10^6$ cm^{-3}, and higher temperatures leading to the emission of far infrared radiation (to which the molecular material is optically thin) from heated dust grains (dust grains are discussed further in § 1.1.2). GMCs form vast complexes such as that found in the constellation of Orion (the sightline with which this Ph.D. is concerned), making them the largest of all interstellar structures. A scale height of $\approx$ 100 pc, means that these structures are restricted to the plane of the Galaxy.

The warm intercloud medium is thought to be composed of two separate components, the '*Warm Neutral Medium*' (WNM), in which hydrogen is largely neutral (ionisation fraction is ≈ 0.1), and the '*Warm Ionised Medium*' (WIM), in which hydrogen is mainly ionised (ionisation fraction is ≈ 0.7). The gas exists at a temperature of $\approx$ 8000 K, and a density of $n \approx 0.1$ cm^{-3}.

The '*Hot Ionised Medium*' (HIM), which is also known as the '*coronal phase*', is the most tenuous component of the ISM with densities of only $n \approx 10^{-4}$ cm^{-3}. Temperatures are very high, typically 10^7 K, leaving hydrogen and helium fully ionised and heavier elements highly ionised. The HIM is a strong emitter in soft X-rays (0.1 to 1.0 keV) and may

also be detected through observations of ultraviolet absorption lines from highly ionised species such as O VI. The detection of O VI, which is formed in gas with temperatures around 10^6 K, was first made with the *Copernicus* spectrometer (Rogerson *et al.*, 1973; Jenkins and Meloy, 1974; York, 1974). Heating of the gas is thought to be the result of energy input from massive stars, novae and supernovae explosions. Rapidly moving matter produced by these phenomena create shock waves which heat the interstellar gas to its high temperature. The overlap of successive supernovae explosions means that a significant portion of the ISM is likely to be filled with this hot phase; however, the exact fraction of the volume it occupies is not known. Observations made by Jenkins (1978) suggest it to be $\lesssim 20\%$, while Cox and Smith (1974) and McKee and Ostriker (1977) have suggested much higher values, ≈ 70–80%.

These distinct phases exist in preference to a continuum of conditions as a result of thermal instabilities at intermediate temperatures. Field *et al.* (1969) were able to show that below a temperature of 10^4 K there exists two stable regimes. One is present at ≈ 8000 K, and the other at a much lower temperature of ≈ 80 K, thus accounting for the cold and warm phases discussed above. The third phase, that of the hot medium, is then produced from the overlap of supernova remnants. It is unclear whether it is the warm or hot phases which form the substrate of the ISM; however, if the volume filling factor of the hot phase is large, then the cold and warm phases may be considered to be distributed in the form of clouds (with the warm gas perhaps forming halos around the cold gas). The molecular clouds are not thought to account for a fourth phase since they are self-gravitating, and therefore not isobaric (e.g. Solomon *et al.*, 1987).

1.1.1.1 H II regions

Early-type stars are thought to form from the dense gas of molecular clouds and as a result are frequently found in the vicinity of their parent clouds, e.g. those observed in Orion. Once a massive star has formed in such a region its intense flux of ultraviolet radiation (specifically photons with wavelengths shortward of 912Å) ionises all the hydrogen in the vicinity of the star, creating an ionised envelope (helium is singly ionised and other elements are singly or doubly ionised). The size of the ionised zone rapidly grows until an equilibrium between recombination and ionisation is reached and a Strömgren sphere is formed. If the star is located just beneath the surface of the molecular cloud, the

expanding ionised zone may breach the confines of the cloud, allowing the ionised material (which is under a significantly greater pressure) to spew into the surrounding medium. This is known as the champagne phase (Tenorio-Tagle, 1979). Alternatively, if the star is positioned above the surface of the molecular cloud, an ionisation front is formed over its surface. The H II region then resembles a blister, e.g. M42 in Orion. H II regions are expected to have temperatures in the range 7000 K to 13000 K (e.g. Osterbrock, 1989, pg. 122); densities, n, are typically ≈ 10–10^2 cm^{-3} within the ionised part of the nebula (e.g. Osterbrock, 1989, pg. 5).

1.1.2 The Dust

In addition to a gaseous component, the ISM is known to possess a significant amount of material in the form of small, solid dust grains (approximately 1% by mass). Typical dimensions of these grains are 10^{-5}–10^{-6} cm. Dust can be detected through its attenuating influence on starlight, known as extinction. Dust preferentially scatters radiation at shorter wavelengths which results in the apparent reddening of starlight (and accounting for the presence of blue reflection nebulae). The grains also efficiently absorb incident radiation with wavelengths equal to, or smaller than, their own physical size.

As a result, it is possible to estimate the distance traversed by stellar radiation (and therefore the distance to the star) by comparing the observed colour of a star with that predicted by stellar models (e.g. those presented by Deutschman *et al.*, 1976). It is possible to estimate the distance, d, to a star using the relation,

$$m - M = 5 \log d - 5 + A_{\rm v}, \tag{1.1}$$

where m and M are the apparent and absolute magnitudes of the star respectively and $A_{\rm v}$ is the visual extinction, given by,

$$A_{\rm v} \approx 3.1\ E(B-V), \tag{1.2}$$

where

$$E(B-V) = (B-V)_{observed} - (B-V)_{intrinsic}. \tag{1.3}$$

Interstellar dust grains may also be inferred from the linear polarisation of reddened starlight, which also indicates that some of the dust must be non-spherical and have their axes aligned.

The heating of the grains, caused by the absorption of radiation, results in strong far-infrared emission with characteristic temperatures in the range 30–500 K (up to a limit, typically between 800 K and 1300 K, set by the evaporation temperature of the particular grain material). As such, dust is a very important coolant in regions of star formation, radiating away the gravitational energy of a collapsing cloud core which will result in the formation of a new star.

The dust grains are composed of refractory elements such as iron and silicon, leading to their apparent depletion with respect to cosmic values. The presence of material on grain surfaces (known as adsorbed material) also leads to lower abundances of certain gas phase species. Thus in regions where adsorbed material has been removed from the grain surfaces, an underlying depletion will still be present due to the inclusion of refractory elements in the dust grains themselves. Grain surfaces also play an important role in interstellar chemistry, providing crucial sites for the formation of many molecular species, especially H_2. The adsorbed atoms and molecules may migrate over the surface of the grain, react with other atoms and molecules, and then return to the gas phase. Following the formation of these molecules the dust acts as a shield against the interstellar radiation field.

1.2 Absorption Line Spectroscopy

Absorption line spectroscopy is a powerful tool in understanding many aspects of interstellar clouds. As radiation from a background star passes through an interstellar cloud, present somewhere along the line-of-sight to that star, photons are removed from the stellar continuum at specific locations relating to the electronic transitions of the absorbing atoms (plus rotational and vibrational transitions in the case of molecules). However, it is worth pointing out that the same atoms and molecules, if present in the photosphere of the background star, will also produce absorption lines at the same locations with strengths and widths characteristic of the target observed. It is therefore important to select background stars with appropriate spectral types and/or high rotational velocities such that blending of interstellar lines with their stellar counterparts does not mask the interstellar contribution to the absorption line profile. Although the Ca II and Na I lines do not reach full strength in stellar spectra until spectral types as late as G and K (e.g. Bowers and Deeming, 1984*a*), their strength builds from early B–type (e.g. Crawford, 1990). O– and early B–type stars therefore make the best background stars since their high photospheric temperatures do not permit the formation of these species. Later B–type stars may also be suitable if their projected rotational velocities ($v \sin i$; where v is the stars equatorial rotational velocity and i is the angle of inclination between the line-of-sight and the rotational axis of the star) are large enough to broaden the stellar line to the point where it may be clearly disentangled from the interstellar contribution and therefore treated as the local continuum.

1.2.1 Absorption Line Profiles

The removal of photons of a particular wavelength from the stellar continuum causes the intensity of the radiation to fall below the continuum at that wavelength, producing an absorption line. The residual intensity of the radiation, $I(\lambda)$, at any point across the line, λ, is described by the expression,

$$I(\lambda) = I_{\lambda}^{0}\, e^{-\tau_{\lambda}}, \tag{1.4}$$

where τ_{λ} is optical depth and I_{λ}^{0} is the intensity in the absence of absorption (the continuum intensity; generally normalised such that $I_{\lambda}^{0} = 1$).

The optical depth may be expressed in terms of the total column density of the absorbers, N, through the relation,

$$\tau_\lambda = N \ \frac{f\pi e^2 \lambda_0^2}{m_e c^2} \ \phi(\lambda), \tag{1.5}$$

where f is the oscillator strength of the transition, e is the electron charge, λ_0 is the rest wavelength, m_e is the mass of an electron, c is the speed of light and $\phi(\lambda)$ is the form of the absorption line profile which is the result of a combination of natural and Doppler line broadening (e.g. Cowie and Songaila, 1986).

Natural line broadening is a consequence of the uncertainty principle and the location of the electron in the energy level. The natural profile is Lorentzian in shape, described by the function $\phi_{\rm nat}(\lambda)$, such that,

$$\phi_{\rm nat}(\lambda) = \frac{1}{\pi} \frac{\Gamma}{(\lambda - \lambda')^2 + \Gamma^2} \tag{1.6}$$

where λ' is the wavelength of the centre of the line and λ is any point on the line. Γ is the damping constant (e.g. Spitzer, 1968, pg. 20), such that $\Gamma = (\lambda_0^2/4\pi c)/\gamma$; where γ, the radiation-damping constant, is the sum of the transition probabilities from the upper level to all lower levels (e.g. Cowie and Songaila, 1986). Natural broadening makes a negligible contribution to the line profile unless the line has a large column density (discussed further in § 1.2.2).

Doppler line broadening arises from a combination of the random motions of the absorbers in the cloud (thermal broadening) and the bulk motions of parcels of gas within the cloud (turbulent broadening). If the velocity distribution of the absorbers is considered to be Maxwellian, the Doppler profile, $\psi_i(v)$, is Gaussian in shape, given by the expression,

$$\psi_i(v) = \frac{1}{b_i\sqrt{\pi}} \ \exp \frac{-(v - v_i)^2}{b_i^2}, \tag{1.7}$$

where $v = c(\lambda - \lambda_0)/\lambda_0$, v_i is the central velocity of component i and b_i is its broadening parameter which is discussed further below (e.g. Cowie and Songaila, 1986). The contribution from the Doppler profile dominates in the optically thin case ($\tau << 1$), and absorption occurs (primarily) in the core of the line profile.

Examples of Lorentzian and Gaussian profiles are given by Dyson and Williams (1997, pg. 12). The resulting line profile, which is a convolution of the natural and Doppler broadening, is known as a Voigt profile, and is given by $\phi(\lambda)$, where,

$$\phi(\lambda) = \sum_i \left(\frac{N_i}{N}\right) \frac{1}{\pi} \int_{-\infty}^{\infty} \frac{\Gamma}{(\lambda - \lambda')^2 + \Gamma^2} \ \psi_i(v') \ dv', \tag{1.8}$$

where N_i is the column density of component i.

The broadening parameter, b (presented in Equation 1.7), describes the broadening exhibited by an absorption line as a result of both the thermal (related to the prevailing kinetic temperature) and non-thermal (or turbulent) motions of the absorbers. The kinetic temperature, $T_{\rm k}$, of a gas is defined such that,

$$\frac{1}{2}m\overline{v}^2 = \frac{3}{2}kT_{\rm k}. \tag{1.9}$$

where m is the mass of the atom/ion observed and k is Boltzmann's constant. Re-arranging for $\overline{v}$ we find,

$$\overline{v} = \sqrt{\frac{3kT_{\rm k}}{m}}. \tag{1.10}$$

However, $\overline{v}$ is the mean three-dimensional space velocity of the absorbers which is not measured in an absorption line. The broadening of an interstellar absorption line is solely due to the one dimensional motions of the absorbers, σ, which is their line-of-sight rms velocity. In the purely thermal case (i.e. no non-thermal motions), σ may be expressed such that

$$\sigma = \sqrt{\frac{kT_{\rm k}}{m}}. \tag{1.11}$$

Since $\sigma = b/\sqrt{2}$, b is then related to $T_{\rm k}$ via the expression,

$$b = \sqrt{\frac{2kT_{\rm k}}{m}}. \tag{1.12}$$

If non-thermal/turbulent motions are present, we have,

$$b = \sqrt{\frac{2kT_{\rm k}}{m} + 2v_{\rm t}^2}, \tag{1.13}$$

where $v_{\rm t}$ is the line-of-sight turbulent velocity. b and σ are related to the full width at half maximum of the line (FWHM) via the expression,

$$b = \sqrt{2}\sigma = \frac{\rm FWHM}{2\sqrt{\ln 2}}. \tag{1.14}$$

1.2.2 Equivalent Width

The equivalent width of the absorption line is defined as the width (usually expressed in mÅ) of a completely saturated rectangular strip of the continuum possessing the same spectrally integrated area as the absorption line itself. The equivalent width of a line, W_λ, is given by the expression,

$$W_\lambda = \int \frac{I_\lambda^0 - I_\lambda}{I_\lambda^0}\, d\lambda. \tag{1.15}$$

Similarly, the total equivalent width of a line profile composed of several blended lines may also be expressed in the same way. Equivalent widths provide an important method of comparing the strength of absorption lines, since they are independent of instrumental resolution.

The relation between the equivalent width of a line and the column density of absorbers is given by the "*curve of growth*" (COG), a plot of log (W_λ/λ) against log $(Nf\lambda)$. However, the increase of W_λ with N is not linear.

In the optically thin case ($\tau \lesssim 1$), photons are available for each absorber, independent of its location with respect to the line centre. As a result the shape of the line is dominated by the Doppler profile given by Equation 1.7. W_λ increases linearly with Nf and the line is said to be on the linear part of the COG (e.g. Cowie and Songaila, 1986). The column density of the absorbers may be estimated from W_λ using the expression,

$$N = 1.13 \times 10^{20} \frac{W_\lambda}{\lambda_0^2 f}, \tag{1.16}$$

where both λ and W_λ are given in Å (see Cowie and Songaila, 1986). As the line becomes optically thick ($\tau > 1$) it begins to saturate, that is the intensity reaches zero in the core of the line. Since there are no further photons available for absorption in the line centre, the rate of increase of W_λ is dramatically reduced. W_λ now increases with $(\ln Nf)^{1/2}$ and the line is said to be on the flat part of the COG (e.g. Cowie and Songaila, 1986). At this point column density estimates from the equivalent width are highly uncertain.

When the optical depth becomes very large ($\tau >> 1$), there are many absorbers displaced from the core of the line into the wings due to natural broadening. As a result the shape of the line profile begins to be dominated by the Lorentzian profile given by Equation 1.6 and the contribution to W_λ made by the wings begins to dominate over that made by the core of the line. W_λ begins to increase once more, proportionally to $(Nf)^{1/2}$; the line is on the square-root part of the COG (e.g. Cowie and Songaila, 1986). At this

point it again becomes possible to estimate the column density of the absorbers from W_λ, using the relation

$$N = 1.06 \times 10^{39} \frac{W_\lambda^2}{\lambda_0^4 \gamma f}, \tag{1.17}$$

where γ is the radiation damping constant (e.g. Cowie and Songaila, 1986).

1.2.3 Fine and Hyperfine Atomic Structure

Atomic fine structure is the result of a coupling between the spin magnetic moment of the electron and its orbital angular momentum. The interaction causes a splitting of the energy levels, producing multiplets of states with slightly different energies. The coupling is the result of the existence of a magnetic field internal to the atom. Both Ca II and Na I exhibit fine structure, the H & K lines in the case of Ca II, and the D_1 & D_2 lines in the case of Na I.

There also exists an interaction between the total angular momentum of the electron and the spin magnetic moment of the nucleus, producing hyperfine atomic structure. The spin–spin coupling of the hyperfine splitting (hfs) is an order of magnitude weaker than that of the fine structure spin–orbit interaction. Only atoms with odd numbers of protons and/or neutrons possess an overall nuclear spin, therefore, both Na and K exhibit hfs. In the case of the Na I D_1 & D_2 transitions the hfs amounts to a separation of 1.08 km s^{-1} (or 21 mÅ) and 1.01 km s^{-1} (or 20 mÅ) respectively (e.g. Welty *et al.*, 1994), and as a result may be clearly resolved at ultra-high-resolution. The effect is weaker for K I λ7699, amounting to a separation of 0.35 km s^{-1} (or 9 mÅ, e.g. Welty *et al.*, 1994).

Hyperfine splitting does cause a noticeable broadening of the line profile of both Na I and K I at high-resolution and therefore has been accounted for in the modelling of these transitions (see Table 2.8).

1.3 Spectrographs

Astronomical spectrographs are used to disperse the light of a star (or other object) into a spectrum so that the intensity of light may be measured as a function of wavelength. The basic optical layout of a spectrograph is described by Kitchin (1998, cf. his figure 4.1.5, pg. 308). Firstly, the light collected by the telescope is projected onto an entrance slit, located in the telescope's focal plane. The light passing through the slit is then rendered parallel by a collimating lens. The light is then passed to a dispersive element shown to be a prism by Kitchin (1998), however modern astronomical spectrographs generally use gratings rather than prisms to disperse the light. Finally, a camera is used to focus the light onto a detector.

Firstly, we will consider the slit. Assuming that the resolving power of the instrument (R, discussed below) is not limited by any of the other components, the width of the slit, S, will directly effect the resolving power achieved by the spectrograph. This is because the width of the slit projects to a given width at the detector, S', below which features cannot be resolved. S is related to S' via the expression,

$$S' = S \times \frac{f_{\rm cam}}{f_{\rm col}} \times M, \tag{1.18}$$

where $f_{\rm cam}$ and $f_{\rm col}$ are the focal lengths of the camera and collimator respectively and M is a magnification factor produced by the grating. Altering the slit width therefore adjusts the resolving power achieved by the instrument: the narrower the slit, the narrower the projected slit width and the higher the resolution achieved (although resolution is actually a convolution of the broadening caused by the slit, grating and other optical components).

The resolving power, R, is defined by the instrument's ability to distinguish closely spaced features. Resolution is typically measured in terms of wavelength ($\Delta\lambda$) or velocity (Δv), such that features with greater separations may be resolved. R is given by the expression,

$$R = \frac{\lambda}{\Delta\lambda} = \frac{c}{\Delta v}, \tag{1.19}$$

where λ is the wavelength observed and c is the speed of light. However, as resolution is increased, the energy contained within the spectrum is generally spread over a greater area (due to the increased dispersion). Thus, as the resolving power of an instrument is increased, the integration time required for a given signal-to-noise ratio on a given

target also increases. A balance therefore exists between resolution and the limiting target magnitude. In addition to this dilution of the stellar light, higher resolution spectrographs require narrower slits (so that the resolving power of the spectrograph is not limited by the projected slit width). Such narrow entrance slits reject a large fraction of the incident stellar light, leading to the use of image slicers (see § 2.1.1).

A collimating lens is located beyond the slit, rendering the light parallel. The beam is then passed to a grating, which consists of a large number of narrow, closely spaced, parallel reflectors. Typical astronomical gratings have between 100 and 1000 reflectors per millimetre and between 1000 and 50,000 reflectors in total. The grating disperses the light into a spectrum. The intensity profile, I, produced by a grating composed of reflectors of width b, each separated by a, is given by,

$$I = I_0 \times \left[\frac{\sin^2 \left[\frac{N\pi a}{\lambda} (\sin\alpha \pm \sin\beta) \right]}{N^2 \sin^2 \left[\frac{\pi a}{\lambda} (\sin\alpha \pm \sin\beta) \right]} \right] \times \left[\frac{\sin^2 \left[\frac{\pi b}{\lambda} (\sin\alpha \pm \sin\beta) \right]}{\left[\frac{\pi b}{\lambda} (\sin\alpha \pm \sin\beta) \right]^2} \right], \tag{1.20}$$

where I_0 is the intensity of the incident beam, α is the angle of incidence, β is the angle of diffraction and λ is the wavelength of the incident light (e.g. Meaburn, 1976, pg. 49).

Equation 1.20 is composed of two parts, the first term in brackets is due to the interference pattern produced by N reflectors. This term has maxima, given by the "*grating equation*" (as described by Meaburn, 1976, pg. 50), when,

$$\frac{m\lambda}{a} = \sin\alpha \pm \sin\beta, \tag{1.21}$$

where m is an integer. These maxima have a width, $\delta\lambda$, at a given wavelength, λ, given by,

$$\frac{\lambda}{\delta\lambda} = mN. \tag{1.22}$$

where m is the order of interference and N is the number of grooves on the grating. Since $\lambda/\delta\lambda$ is a measure of resolving power, Equation 1.22 describes the maximum resolution which may be obtained with a particular spectrograph. In particular, an instrument's maximum resolving power, $R_{\rm max}$, is dependent on the number of grooves on the grating and the order of interference in which the instrument is used such that,

$$R_{\rm max} = m \times N. \tag{1.23}$$

By rearranging Equation 1.21 for β, we find,

$$\beta = \sin^{-1}\left[\frac{m\lambda}{a} - \sin\alpha\right], \tag{1.24}$$

illustrating the diffracted light to be concentrated into separate segments known as orders. Each order is identified by its relevant value of m, and is separated from its neighbour by what is known as the "*free spectral range*", given by,

$$\Delta\lambda \approx \frac{\lambda}{m}. \tag{1.25}$$

However, the second term in brackets in Equation 1.20 is due to the diffraction pattern produced by one reflector and has a maximum value (of unity) when $m = 0$. This of course corresponds to a resolving power of zero (from Equation 1.23), and is therefore not of use.

To overcome this problem the grating may be blazed such that each reflector is inclined to the grating by an angle δ. This allows the spectrograph to operate in a useful order ($m > 0$). The condition for this is that,

$$\alpha - \delta = \delta - \beta. \tag{1.26}$$

Only the second term in brackets in Equation 1.20 is affected by the blazing of the grating.

To achieve even higher resolutions, echelle gratings with larger blaze angles may be used. Echelle gratings have a more coarse ruling, with as little as 10 grooves per millimetre, but the large blaze angle allows the spectrograph to operate in very high orders. The large dispersions attained by echelle gratings allows very high resolutions to be obtained.

However, because the echelle operates in such high orders, the free spectral range becomes small, to the point where orders overlap. To abate this problem, echelle spectrographs uses a cross-disperser; a second, low dispersion grating or prism positioned such that its dispersion is perpendicular to that of the echelle. The individual orders are then separated and stacked perpendicular to the dispersion direction. The resulting spectra may then be passed to a camera which focuses then records the light, typically using a "*Charge-Coupled Device*" or CCD.

The introduction of solid state devices such as CCDs into astronomical spectroscopy revolutionised the study of the ISM. The substantially higher quantum efficiency of CCD chips has allowed modern spectrographs to operate at much higher resolutions. Current CCDs are sensitive to radiation between $\approx$ 4000Å and 11000Å with a peak in quantum

efficiency of $\approx 90\%$ at 7500Å (although CCDs may be coated to increase efficiency at particular wavelengths). Furthermore, CCDs have a linear response which is highly desirable in spectroscopy. Probably the most important advantage of the CCD is that it outputs its data in a digital format, allowing the swift and accurate reduction of the raw data on a computer. This is in contrast to the plate measuring machines needed for photographic plates which were far less accurate.

1.4 Aims and Objectives

The aim of the current project is to investigate the ISM in the direction of Orion utilising absorption-line profile models for a range of stars in the constellation. The observations (including details of the instruments) and data reduction procedures are discussed in Chapter 2.

In Chapter 3 the individual absorption components present in each model are used to investigate the line-of-sight velocity structure of the Orion region, and the intervening ISM. Comparisons of absorption components found independently for Ca II, Na I and K I have been made in order to identify individual interstellar clouds producing recognisable absorption in one or more of these species. Where clouds are observed in both Na I and Ca II, Na°/Ca^{+} abundance ratios are derived, providing information on the physical conditions which prevail in the cloud. Where observations of closely spaced sightlines are available (i.e. the M42 region), comparisons between sightlines enable the identification of absorption systems, where absorption from individual interstellar clouds may be seen in more than one sightline. Chapter 4 presents a similar analysis for the λ Ori association using observations obtained with the Mount Stromlo echelle spectrograph.

In Chapter 5 a comparison of our data with earlier studies is made, revealing temporal variability in the interstellar absorption-line profiles of two stars, δ Ori and ζ Ori. Furthermore, the comparison of observation of the closely spaced stars δ Ori A & C reveal differences in the absorption occurring in these two sightlines. Both of these detections highlight the presence of small-scale structure in the ISM over scales down to only a few astronomical units.

Where both Na I and K I line components are observed for a particular cloud, rigorous limits on both the kinetic temperature and line-of-sight root-mean-square turbulent velocity may be derived. The results of this analysis are discussed in Chapter 6.

Final conclusions and recommendations for future work are presented in Chapter 7.

Chapter 2

Observations and Data Reduction

2.1 The Observations

The primary set of observations, which were available from the outset of this Ph.D., were obtained with the Ultra-High-Resolution Facility (hereinafter UHRF; discussed in detail in § 2.1.1) on the Anglo-Australian Telescope. These initial observations were acquired during three observing runs in 1994 (by M. J. Barlow and I. A. Crawford) and one in 1996 (by I. A. Crawford).

Following the start of this Ph.D. additional observations were made to supplement the primary data set. Firstly, the UHRF was again utilised to observe K I towards β Ori, while the discovery of small-scale interstellar structure in the line-of-sight to δ Ori (discussed in detail in Chapter 5), led to the acquisition of further observations of this target (and its binary companion) through both user and service observations with the UHRF and user observations with the Mount Stromlo echelle spectrograph (hereinafter MSES).

A selection of targets located in and around the λ Ori association were also observed as part of an additional study of the expanding neutral shell present around the association and the foreground interstellar material in this direction. These observations were performed using the Mount Stromlo 74-inch telescope in conjunction with the coudé echelle spectrograph and the 130-inch camera (discussed in detail in § 2.1.2).

In all, a total of 24 stars have been observed in the direction of Orion, including 4 in the M42 region and 13 in the λ Ori association. A comprehensive list of the observations made during each observing run is given in Tables 2.1 to 2.7 while Tables 3.2 and 4.1 list the relevant properties of the stars observed.

Table 2.1: List of observations made in 1994. A total of three observing runs were made during 1994, January (20–23), April (23–24) and December (16–18). Superscripts, following the listed exposure times (columns 3–7), have been used to identify when each observation was made. ^{a}, ^{b} and ^{c} represent January, April and December respectively. These observations were made by M. J. Barlow and I. A. Crawford. The UHRF was operated in its highest resolution mode and used in conjunction with a Thomson CCD chip (January) and a Tektronix CCD chip (April and December).

Target		Integration Time (s)				
		Ca II	Na I	K I	CH	CH^+
HD 34085	β Ori	2200 (3)^a	3600 (4)^a	—	—	—
HD 36486	δ Ori A	1200 (1)^a	3600 (3)^a	—	—	—
HD 36822	ϕ^1 Ori	2400 (2)^c	1800 (1)^c	—	—	1200 (1)^c
HD 36861	λ Ori	2800 (3)^c	—	—	—	1800 (2)^c
HD 37020	θ^1 Ori A	5400 (3)^c	—	—	—	—
HD 37022	θ^1 Ori C	5400 (4)^c	—	—	3600 (2)^c	2400 (2)^c
HD 37041	θ^2 Ori A	3600 (2)^c	2250 (1)^c	—	3600 (2)^c	1200 (1)^c
HD 37043	ι Ori	3600 (2)^c	3600 (3)^a	—	—	—
HD 37128	ϵ Ori	3000 (3)^a	2000 (2)^a	2400 (2)^a	—	—
HD 37468	σ Ori	3600 (2)^b	1200 (2)^b	—	—	—
HD 37742	ζ Ori	3000 (3)^a	3000 (3)^a	2400 (2)^a	—	—
HD 38771	κ Ori	—	2400 (2)^a	2400 (2)^a	—	—

Table 2.2: List of observations made in 1996 (December 2). These observations were made by I. A. Crawford. The UHRF was operated in its highest resolution mode and used in conjunction with a Tektronix CCD chip.

Target		Integration Time (s)				
		Ca II	Na I	K I	CH	CH^+
HD 37022	θ^1 Ori C	—	2400 (2)	—	—	—
HD 36861	λ Ori	—	1200 (1)	—	—	—

Table 2.3: List of observations made in 1999 (January 29). These observations were made by the author and I. A. Crawford. The UHRF was operated in its highest resolution mode and used in conjunction with the AAO MITLL2 CCD chip.

Target		Integration Time (s)				
		Ca II	Na I	K I	CH	CH^+
HD 34085	β Ori	—	—	200 (1)	—	—

Table 2.4: List of observations made in 1999 (July 31). These observations were made by I. A. Crawford. The UHRF was operated in its highest resolution mode and used in conjunction with a Tektronix CCD chip.

Target		Integration Time (s)				
		Ca II	Na I	K I	CH	CH^+
HD 36486	δ Ori A	—	1000 (1)	—	—	—

2.1.1 The UHRF

The UHRF is an echelle spectrograph used on the 3.9-metre Anglo-Australian Telescope (AAT) at the Siding Spring Observatory, located near Coonabarabran, New South Wales. The construction of the instrument was motivated by the requirement of ultra-high-resolution in the study of narrow absorption lines produced in cool interstellar gas. The UHRF was installed at the coudé focus of the AAT within the environment already occupied by the University College London Echelle Spectrograph (UCLES). UHRF and UCLES have been designed to share much of the slit-area facilities and control software.

Development of the UHRF was funded by an SERC grant and performed at the Optical Science Laboratory of the Department of Physics and Astronomy at University College London. The UHRF received its first astronomical light during commissioning tests in July 1992. The instrument was found to deliver its designed resolving power of $R \approx 10^6$ (at which the majority of the observations reported here were obtained), making it the highest resolution optical spectrograph ever constructed. The instrument has been designed with two further resolution modes, of (nominally) $R \approx 3 \times 10^5$ and $R \approx 6 \times 10^5$, the former of

Table 2.5: List of observations made in 2000 (February 10–21). These observations were made by the author and I. A. Crawford using the MSES. The instrument was operated with a slit width of 250μm (producing a resolving power of $R \approx 110,000$) and used in conjunction with a SITe CCD chip. Those observations listed above the double line lie in the direction of the λ Ori association (used in § 4) while those below the double line are not (used in § 5).

Target		Integration Time (s)				
		Ca II	Na I	K I	CH	CH^+
HD 34989		3600 (2)	3600 (2)	—	—	—
HD 35468	γ Ori	—	1200 (1)	—	—	—
HD 36653		—	3600 (2)	—	—	—
HD 36861	λ Ori	2200 (2)	3000 (4)	—	—	—
HD 36881		3820 (3)	2400 (2)	—	—	—
HD 36894		—	7200 (4)	—	—	—
HD 36895		5400 (3)	5400 (3)	—	—	—
HD 37171		—	3600 (2)	—	—	—
HD 37320		—	3600 (2)	—	—	—
HD 37490	ω Ori	5400 (3)	1800 (1)	—	—	—
HD 38622		—	3600 (2)	—	—	—
HD 38710		—	1800 (1)	—	—	—
HD 34085	β Ori	1200 (1)	—	—	—	—
HD 36485	δ Ori C	—	5400 (3)	—	—	—
HD 36486	δ Ori A	1800 (1)	2200 (2)	—	—	—

Table 2.6: List of observations made in 2000 (March 15). The observations were made by R. Stathakis through UHRF service observations. The UHRF was operated in its highest resolution mode and used in conjunction with a Tektronix CCD chip.

Target		Integration Time (s)				
		Ca II	Na I	K I	CH	CH^+
HD 36486	δ Ori A	—	1800 (1)	—	—	—

Table 2.7: List of observations made in 2000 (August 16–17). The observations were made by the author. The UHRF was operated in its lowest resolution mode and used in conjunction with a Tektronix CCD chip.

Target		Integration Time (s)				
		Ca II	Na I	K I	CH	CH^+
HD 36485	δ Ori C	5400 (3)	2400 (2)	—	—	—
HD 36486	δ Ori A	600 (1)	900 (1)	—	—	—

which has also been utilised in this work.

The very narrow slit widths required for ultra-high-resolution spectroscopy (≈ 35 μm) mean that most of the stellar light falling onto the slit is lost ($\approx 97\%$). To increase the low throughput, the spectrograph is operated with a confocal image slicer (Diego, 1993). The image slicer used with the UHRF is based on the "Bowen-Walraven" design, making use of multiple internal reflections (a schematic of a Bowen-Walraven image slicer is given in figure 4.2.8 of Kitchin, 1998, pg. 351). The image slicer was found to increase throughput by an order of magnitude, helping to abate the problem of lower limiting magnitudes generally associated with very-high dispersion.

A total of three separate CCD detectors were used in the UHRF observations. The particular detector used during each run is recorded in the captions of Tables 2.1 to 2.7. The AAO Thomson CCD has dimensions of 1024 by 1024 pixels, with each pixel being 19 μm in size. The AAO Tektronix CCD is of the same size (1024 by 1024), but with 24 μm pixels. The AAO MITLL2 CCD is much larger, with 4096 by 2048 pixels, each of which is 15 μm in size.

To reduce the readout noise, the CCD output was binned by factors of either four or eight in the spatial direction (perpendicular to the dispersion direction). While readout noise may be reduced further with higher factors of binning, a balance must be attained with the loss of data associated with cosmic ray hits. A cosmic ray incident upon a single pixel will not only destroy the information contained in that pixel, but each pixel grouped together in that particular bin.

A measurement of the resolving power attained with the UHRF may not be gained by the usual method of measuring the width of an arc line. Because the UHRF operates at

such a high resolving power, the profiles of the arc lines are resolved by the instrument. Instead, the velocity resolution of the UHRF may be measured from the observed width of a stabilised He-Ne laser line, which can be considered to be infinitely narrow. Measurements show, a velocity resolution of 0.34 ± 0.01 km s^{-1} FWHM, equivalent to $\Delta\lambda/\lambda = 880,000$, to have been obtained for each of the observations. However, this is an indirect method of measuring the resolving power since it is necessary to initially focus the instrument on the laser line and subsequently re-focus at the observing wavelength. Thus the measured resolution is *representative* of the observations.

Focusing of the UHRF is performed via the Hartmann method. Two separate observations of the Th-Ar arc spectrum are made with one of each of the two Hartmann shutters open. Through cross-correlation of the profiles obtained it is possible to iteratively focus the instrument to an optimum point by moving the collimator-echelle unit.

Other aspects of the instrument and observing procedures have been described in detail by Diego *et al.* (1995) and Barlow *et al.* (1995).

2.1.2 The Mount Stromlo Echelle Spectrograph

The Mount Stromlo 74-inch telescope is located at the Mount Stromlo Observatory, outside Canberra in the Australian Capital Territory. The coudé echelle spectrograph was used in conjunction with the 130-inch camera. Using the 130-inch camera, which is the longest focal length available, provides the highest possible resolving power.

A slit width of 250 μm was used, providing a velocity resolution, as measured from the width of an *unresolved* Th-Ar arc line, of 2.73 km s^{-1} FWHM, equivalent to $R \approx 110,000$.

The observations were obtained using a SITe CCD with dimensions of 4096 by 2048 pixels, each being 15 μm in size. The CCD output was binned by a factor of three in the spatial direction in order to reduce the readout noise.

The instrumental response function (IRF) of the instrument has been measured in detail by Crawford *et al.* (1987).

2.2 Data Reduction

All of the observations obtained in 1994 were reduced prior to the commencement of this Ph.D. by I. Crawford. All of the subsequent observations were reduced in a similar manner (detailed below) by the author. The spectra were extracted from the individual CCD images using the FIGARO data-reduction package (Shortridge *et al.*, 1999) at the UCL Starlink node.

2.2.1 Extraction

The CCD images were firstly orientated such that wavelength increased in the increasing x-direction. Cosmic rays were removed in two stages; those found in proximity to interstellar absorption lines were removed manually, while those remaining were removed automatically with FIGARO. Bias levels were measured from the overscan region and uniformly removed from the CCD images. The slope of the orders with respect to the edge of the CCD was corrected such that they became parallel. Finally, the locations of both the order and the inter-order regions were measured, and spectra were extracted for each.

2.2.2 Background Correction

Removal of the background level from the stellar spectra (largely due to a combination of scattered light and CCD dark current) was achieved by extracting spectra of both the order (stellar and background counts) and inter-order (background counts) regions. The inter-order spectra are smoothed to remove pixel-to-pixel variations; their strengths are scaled (by the ratio of the number of pixel-rows extracted in the order and the inter-order spectra) to account for the differing coverage of each region, and then subtracted from the spectrum obtained from the order region.

In the case of the MSES observations, an examination of the background levels revealed some unexpected variations between different exposures of the same target. However, an inspection of the raw images revealed that, whatever its cause, this background was constant across the chip in the spatial direction, and that the values measured between the orders are an appropriate correction for the background underlying the orders themselves. Moreover, we have three additional reasons to be confident that the backgrounds in the MSES data have been dealt with correctly: (1) Individual observations of a target yield essentially identical line profiles once the backgrounds were subtracted; (2) The line-profile

analysis (see § 2.3) shows the background removal to be accurate to within $\approx \pm 10\%$, as outside this range it proves impossible to model simultaneously the absorption in both D lines; (3) The MSES δ Ori A and λ Ori spectra are identical to the independent UHRF spectra, after allowing for the difference in resolution. For all these reasons we are confident that the data reduction process has correctly dealt with the backgrounds in the MSES data.

2.2.3 Flatfielding

Flatfielding is required to remove pixel-to-pixel variations in the response of the CCD and larger-scale variations across the chip. The CCD is uniformly exposed with a quartz lamp, allowing the identification of any variations in the sensitivity of the chip. Exposures are obtained for each wavelength regime; care must be taken to ensure that no part of the chip is saturated.

The resulting flatfield image may be utilised in one of two ways. Firstly, it may be extracted over the same pixel range as the stellar spectrum which is to be flatfielded. The stellar spectrum is then divided by the normalised flatfield spectrum, removing any flatfield features present. Secondly, the stellar image may be divided by the normalised flatfield image (the number of counts in each pixel of the flatfield image is divided by the average number of counts). The UHRF data have been flatfielded using the former method while the latter method has been utilised for the MSES data.

In the case of the UHRF observations, the CCD chips used have good cosmetic properties, providing a clean response; furthermore, the stellar spectra occupy a large number of pixel-rows, thus reducing the significance of any pixel-to-pixel variations.

2.2.4 Wavelength Calibration

Wavelength calibration has been performed using arc spectra obtained with a Th-Ar emission lamp at regular intervals during the observing sessions. Lines identified in the arc spectrum are assigned known values of wavelength which, following the use of low order polynomial fitting (typically first and second order), allows a wavelength scale to be assigned to the pixels in the arc spectrum. Wavelength scales are then copied to the stellar spectra from the nearest (in time) wavelength calibrated arc spectrum.

In the case of the UHRF K I λ7699 data, only two identifiable Th-Ar lines were found to occupy the spectral range of our observations, thus limiting our ability to accurately

calibrate wavelengths for these data. A comparison of corresponding Na I and K I absorption components indicates there to be a velocity shift of ≈ -0.3 km s^{-1} present in the K I spectra. Since the K I observations are modelled independently and only exhibit a small number of absorption lines (which may easily be associated with corresponding Na I lines), a velocity shift has not been applied to the K I data for the following analysis.

An indication of the accuracy of the wavelength calibration process for the Na I and Ca II regions may be obtained from the comparison of radial velocities of clouds producing well-determined absorption in both of these species (e.g. the detection of both Na I D_1 and Ca II K absorption, at velocities of 2.90 ± 0.01 & 2.88 ± 0.01 km s^{-1}, respectively, towards ϵ Ori in the UHRF data, see Figure 3.10). Furthermore, comparison of these data with previous studies has, in general, shown excellent agreement. However, in the case of six stars for which observations are presented here and in the Na I survey of Welty *et al.* (1994), a small systematic velocity offset of $\approx -0.30 \pm 0.1$ km s^{-1} is detected in the Welty *et al.* (1994) data. Hobbs and Welty (1991) and Welty *et al.* (1994) discuss the presence of a velocity offset of $+0.58 \pm 0.35$ km s^{-1} in the data presented by Hobbs (1969*a*). This suggests that the shift is likely to be present in the Welty et al. data and we do not believe it to be in any way related to the shift detected between our Na I and K I data.

2.2.5 Rectification

Continuum normalisation is generally achieved by division of low-order polynomial fits to the continuum. In the case of β Ori, the presence of strong stellar Ca II absorption has created some uncertainty with this procedure, resulting in the use of a manually drawn continuum.

A typical spectral range of $\approx$ 130 km s^{-1} was obtained for the UHRF data which in general, is centred on the interstellar absorption. In the case of the UHRF Ca II observations of θ^1 Ori A & C and θ^2 Ori A, a lack of well-determined red-wing continuum does lead to some uncertainty in the normalisation process; however, the requirement of only first and second order polynomial fits to the (blue) continuum alleviates this uncertainty to some extent. Due to their lower dispersion, the MSES data possess a much larger spectral range and have been normalised in the same manner.

2.2.6 Atmospheric Correction

Removal of telluric water lines from the Na I and K I spectra has been achieved by the division by an atmospheric template spectrum. In the case of the UHRF data, the atmospheric template is taken as that observed towards the bright, lightly-reddened star α Vir. We note that α Vir actually exhibits a single weak interstellar Na I absorption component at a velocity of -11.2 km s^{-1} (Welsh *et al.*, 1990) which, at the time of observation corresponded to a geocentric radial velocity of -40 km s^{-1}. This is some 40 km s^{-1} lower than the lowest velocity absorption detected towards Orion (in the geocentric frame). These atmospheric templates have been acquired with the UHRF during 1994 (Na I) and 1993 (K I). In the case of the MSES data, the spectrum of the unreddened star ϵ CMa (observed with the MSES) has been taken as an atmospheric template.

The strength of the absorption lines present in the atmospheric template have been scaled to account for the small variations in the strength of the atmospheric lines present in the different stellar spectra (a result of varying air mass and atmospheric conditions). The intensity of an absorption line increases as a function of increasing optical depth, thus the telluric spectrum cannot be scaled linearly to fit the stellar spectrum. The line intensity of an absorption line, I, is related to optical depth, τ, through Equation 1.4,

$$I(\lambda) = I_\lambda^0 \, e^{-\tau_\lambda} \ ,$$

where I_λ^0 is the continuum intensity. For $I_\lambda^0 = 1$ (i.e. a normalised spectrum),

$$\tau_\lambda = -\ln I(\lambda) \ . \tag{2.1}$$

The ratios between the optical depths of atmospheric lines present in a given stellar spectrum and their counterparts in the atmospheric template spectrum are therefore constant. Let

$$\phi = \frac{\tau_\lambda^*}{\tau_\lambda^t} \ , \tag{2.2}$$

where τ_λ^* and τ_λ^t refer to the optical depth of an atmospheric line in the stellar and atmospheric template spectra respectively. Therefore, from Equation 1.4,

$$\phi = \frac{\ln I_\lambda^*}{\ln I_\lambda^t} \ , \tag{2.3}$$

where $\ln I_\lambda^*$ and $\ln I_\lambda^t$ refer to the line intensity in the stellar and atmospheric template spectra respectively. Therefore, by converting the y-axes of the atmospheric template

spectrum and a given stellar spectrum to a logarithmic scale, it is possible to measure the relevant value of ϕ. The atmospheric template can be subsequently scaled to fit the telluric lines present in the particular stellar spectrum, i.e.,

$$\ln I_\lambda^{t'} = \phi \ln I_\lambda^t \ . \tag{2.4}$$

where $I_\lambda^{t'}$ is the scaled template spectrum. The stellar spectrum can then be divided by the scaled template, thus removing the telluric lines.

Atmospheric Na I absorption is also known to occur, with varying strengths (McNutt and Mack, 1963; Barlow *et al.*, 1995). Absorption from telluric Na I will be present at 0 km s^{-1} in the geocentric frame; however, McNutt and Mack (1963) noted that telluric Na I absorption was only detectable during the northern winter (similarly, Barlow *et al.*, 1995, find atmospheric Na I to only be present during the southern winter). This is consistent with the non-detection of telluric Na I in our data, obtained during the southern summer.

The spectra were then converted to the heliocentric velocity frame using corrections obtained from the RV routine (Wallace and Clayton, 1996) and the individual exposures were added. All velocities referred to here are heliocentric unless otherwise stated.

2.2.7 Zero-Level Errors

During the analysis of the UHRF data, a small discrepancy in the zero level was found in the cores of saturated Na I D_1 lines towards λ and ϕ^1 Ori. The lines were seen to reach 0.01 and 0.02 of the continuum respectively; the zero level of the two spectra were therefore readjusted. This provides a guide to the likely uncertainty in the zero level of the remaining (uncorrected) Na I spectra. Since fully saturated interstellar Ca II K lines have never been observed, it is not possible to assess the zero level error for the Ca II region in this manner; however, the excellent agreement seen between these observations and those presented in other studies (see § 5.2) suggests zero level errors in the Ca II region to be minor (i.e. of the order 1–2%).

A similar effect is also detected in the MSES data. Since the MSES data set contains a larger selection of saturated absorption profiles (from both the Na I D_1 and the stronger Na I D_2 transitions) it has been possible to assess the systematic nature of the error.

Examination shows each spectrum to possess a zero-level error of $\approx 2\%$ which has been corrected in all Na I MSES data (including non-saturated lines).

2.3 Line Profile Analysis

The absorption line profiles for all of the 1994 and 1996 UHRF data were initially modelled using the IS line fitting routines in the DIPSO spectral analysis program (Howarth *et al.*, 1998). Given the relevant atomic data the IS routine produces the absorption line profile resulting from the individual clouds included in the input model. Each of the clouds must be characterised by a central velocity, $v_{\odot}$, a broadening parameter, b, and a column density of absorbers, N.

The resulting *intrinsic* absorption line profile, which does not account for instrumental broadening, may be convolved with the instrumental response function (assumed to be Gaussian; FWHM 0.34 & 0.78 km s^{-1} for the UHRF in its highest and lowest resolution mode respectively; FWHM 2.78 km s^{-1} for the MSES) to produce the observed line profile.

The development of the VAPID (Voigt Absorption Profile Interstellar Dabbler) line fitting code (Howarth, Price, Crawford and Hawkins, 2002) has allowed these models to be optimised, such that the model component parameters produce an absorption line profile with the minimum root-mean-square (rms) residuals with the data. VAPID is discussed in detail below.

2.3.1 VAPID

The VAPID code has been developed by Prof. I. D. Howarth to optimise model parameters through least-squares fitting to observed spectra. VAPID requires an input model file containing values of $v_{\odot}$, b and N for each absorption component, and at least one data file (which also contains relevant atomic data and instrumental information). Each parameter in the model file may be fixed or free – when fixed, VAPID will predict the resulting absorption line profile, when free, it will evaluate the set of component parameters which produce the minimum rms residuals to the input data-set. VAPID generates Voigt profiles using the VOIGTL routine of Lynas-Gray (1993) and minimisation of the rms residuals is performed using a version of the Marquadt algorithm as implemented by Press *et al.* (1992).

VAPID permits the use of multiple data-sets, either of the same transition (e.g., three observations of the Ca II K transition towards a given star), or of different transitions originating from the same atomic state (e.g., the D_1 and D_2 lines of Na I). The individual data-sets may be characterised by different signal-to-noise ratios and resolutions. Only

one input model is required since the fitting parameters of any transitions involved will be identical. Simultaneously modelling the D lines of Na I, or the H and K lines of Ca II in this way, produces self-consistent absorption models.

The errors on each data-point in a data-set may be scaled by the square-root of the value of the data point (since the signal-to-noise ratio is often approximately proportional to the square-root of the number of counts). Furthermore, when modelling multiple data-sets, it is possible further to scale the error on each data-point in a particular data-set by (1/SNR) where SNR is the continuum signal-to-noise ratio achieved in that data-set.

A further feature of VAPID is that it allows a data-set to contain absorptions from more than one transition. In this instance, each component in the input model is associated with one of the transitions and the features are modelled simultaneously. This allows blended transitions to be modelled and has been utilised for the "synchronised" model presented in § 5.2.2.

The quality of the resulting fit to the data may be measured with chi-square, χ^2, given by the expression,

$$\chi^2 = \sum_i \left\{ \frac{1}{\sigma_i^2} [y_i - y(x_i)]^2 \right\}, \tag{2.5}$$

where σ_i is the uncertainty on the data-point, y_i is the observed y value and $y(x_i)$ is the computed value (e.g. Bevington, 1969, pg. 188).

Single-parameter, 1σ error estimates are obtained for the fitted parameters from the covariance matrix when optimising. These errors are scaled to correspond to a reduced chi-square, χ^2_ν, of unity over the absorption line profile (specifically, where the intensity in the modelled line profile is below 0.999). χ^2_ν is given by

$$\chi^2_\nu = \frac{\chi^2}{\nu}, \tag{2.6}$$

where ν is the number of degrees of freedom; $\nu = N - n$, where N is the number of data points and n is the number of fitting parameters (e.g. Bevington, 1969, pg. 188).

The goodness of the fit to the data may be assessed through a comparison between the quality of the fit in the line and in the continuum (using an *F-test*); a good fit will give similar values of χ^2_ν in both regions.

Although VAPID is not able to introduce additional absorption components automatically, the goodness of the fit in the line of a model with n free parameters, χ^2_n, may be

compared with that of another model with m free parameters (where $m = n + i$; typically $i = 3$ corresponding to the addition of one extra component) to ascertain whether a statistically significant improvement to the fit has been obtained with the addition of the extra component(s). In this case,

$$F[i,(N-m)] = \frac{\chi_n^2 - \chi_m^2}{\chi_m^2} \times \frac{N-m}{i} \tag{2.7}$$

A large value of this ratio indicates that a significant improvement to the fit has been obtained. For any given fit, VAPID specifies the values of χ^2 that are required if an additional absorption component is to provide an improvement in the fit which is statistically significant at the 5% and 1% levels.

During the primary fitting procedure, all component parameters were unconstrained, such that the optimum fit could be achieved. The number of components employed in each model was kept to a minimum, such that any additional components did not provide a significant statistical improvement to the fit (with the exception of the K I model of κ Ori, discussed in § 6.2.4).

In a small number of cases this has resulted in the inclusion of very broad components which statistically, cannot be replaced by multiple, narrower components (λ Ori Ca II, component 14; σ Ori Ca II, component 3c; ζ Ori Ca II, component 9; see Tables 3.6, 3.12 and 3.13 respectively). Nevertheless, we feel that the use of unconstrained model parameters is preferable since although the Ca II, Na I and K I models have been independently generated, the generally good agreement between the Ca II, Na I and K I absorption model components suggests that the majority of the individual clouds have been identified.

By reconstructing the absorption models presented in the high resolution/high signal-to-noise surveys conducted by Welty *et al.* (1994, Na I), Welty *et al.* (1996, Ca II) and Welty and Hobbs (2001, K I) it becomes possible to compare their exact component structures with those derived here with VAPID.

In the case of Ca II we find that, with the exception of θ^1 Ori C, towards which we identify significant additional structure, the higher S/N achieved by Welty *et al.* (1996) in their Ca II observations has in general allowed the use of a greater number of components. The small number of very broad Ca II components modelled by VAPID (noted above) are not seen in the Welty *et al.* (1996) models. In general, very good agreement is present between the Na I component structures modelled here and by Welty *et al.* (1994). The higher resolution employed by us typically enables additional sub-structure to be resolved

Table 2.8: Wavelengths (λ) and corresponding oscillator strengths (f) adopted for the line-profile analyses. Hyperfine splitting of the Na I D_1 & D_2 and K I λ7699 transitions has been accounted for in the modelling process. The information is taken from: (1) Morton (1991); (2) Welty *et al.* (1994); (3) Black and van Dishoeck (1988); (4) Lambert and Danks (1986).

Line	λ (Å)	f	(ref.)
Ca II H	3968.468	0.3145	(1)
Ca II K	3933.663	0.6346	(1)
Na I D_1	5895.9108	0.1193	(2)
	5895.9321	0.1988	(2)
Na I D_2	5889.9386	0.2367	(2)
	5889.9584	0.3944	(2)
K I	7698.969	0.1272	(2)
	7698.978	0.2121	(2)
CH $R_2(1)$	4300.313	0.0051	(3)
CH^+ R(0)	4232.548	0.0055	(4)

while the higher S/N that we have achieved allows us to identify additional weak components. In the case of the K I observations, there is good agreement between the column densities found here and those of Welty and Hobbs (2001). The higher S/N achieved by Welty and Hobbs (2001) in their K I observation of ϵ Ori makes possible the detection of a weak component at a velocity of 17.17 km s^{-1} (corresponding to our cloud 8 towards this star). The higher resolution employed here has, in the case of ζ Ori, resolved three additional components, while for κ Ori, further sub-structure is suggested in the spectrum and although not statistically significant, has been modelled on the grounds of our Na I observations (see § 6.2.4).

2.3.2 Atomic Data

The atomic data adopted for the various transitions have been taken from a variety of sources. Table 2.8 provides a summary of the adopted values of wavelength, λ, and corresponding oscillator strength, f. Hyperfine splitting of the Na I D_1 & D_2 and K I λ7699 transitions (see § 1.2.3), has been accounted for in the modelling process.

CHAPTER 3

The Orion Region[1]

Using ultra-high-resolution observations ($R \approx 9 \times 10^5$) of Na I, Ca II, K I, CH and CH^+, the interstellar sightlines towards twelve bright stars in Orion will be investigated. In particular, the observations of four stars in the M42 region are used to determine the line-of-sight velocity structure of the interstellar gas in this direction.

3.1 Introduction

At a distance of approximately 450 pc, the Orion giant molecular cloud complex is the closest region to the sun showing evidence for ongoing OB star formation. The molecular gas has been extensively mapped by Maddalena *et al.* (1986) using the $J = 1 \rightarrow 0$ rotational transition of CO at 115,271 MHz as a tracer. Figure 3.1, which highlights the molecular clouds in the Orion and Monoceros regions, has been taken from Maddalena *et al.* (1986). The Orion A & B clouds, which form the backdrop of the constellation, are named after their most prominent radio sources, Orion A (*Messier* 42) and Orion B (*NGC* 2024) respectively and are the two main clouds in the complex, each with gas masses of $\approx 10^5\ M_\odot$ (Maddalena *et al.*, 1986). The northern tip of the Orion B cloud is observed to be connected to the Galactic plane by the northern filament, while in the south, the Orion A cloud is seen to be connected to the Galactic plane by the southern filament and the crossbones. Approximately 8° to the east of the Orion A cloud and at a distance of $\approx$ 850 pc is the Mon R2 cloud. Although the Orion complex and Monoceros clouds appear

[1] The majority of the work presented in this chapter has been previously published in Price *et al.* (2001*a*)

joined on the sky by the southern filament and crossbones, incompatible radial velocities make it unclear whether they are actually connected.

The formation of the molecular cloud complex is uncertain, so too is whether the Orion and Monoceros complexes have a common origin. The explanation provided by Franco *et al.* (1988) describes a high-velocity cloud falling from the southern Galactic hemisphere and colliding with the Galactic disk. Fragmentation of the cloud, induced by tidal forces, then produced the Orion and Monoceros complexes. The collision initiated an oscillation of the complex about the Galactic plane (explaining its current location below the Galactic plane) and produced shocks, resulting in the onset of star formation.

The Orion OB1 association (also known as I Orion OB) is comprised of 56 stars with spectral types from O6 to B2 contained within four subgroups, Ia to Id (Blaauw, 1964). These subgroups are progressively younger from Ia which has an age of 8×10^6 years to Id with an age of $< 0.5 \times 10^6$ years (Warren and Hesser, 1978). The stellar winds, ionising radiation and supernova explosions produced by the first members of the Ia association are thought to have disrupted the parent molecular cloud, clearing molecular material from the vicinity. The subsequent ionisation/shock fronts which are formed are then thought to have triggered the formation of the next generation of stars at the new surface of the molecular cloud which in turn results in further disruption of the molecular complex. This form of sequential star formation results in the older stellar subgroups residing at the greatest distances from the parent molecular cloud.

The youngest subgroup, Id (of which the θ^1 OB association stars are the brightest members), is therefore present near (although above) the surface of Orion Molecular Cloud 1 (OMC1; a prominent molecular emission region in the southern part of the Orion GMC complex), producing the Great Nebula in Orion (M42; NGC 1976; Orion A). However, there is evidence for still younger stars likely to be present beneath the surface of the molecular clouds. Strong infrared emission from cloud cores within the Becklin-Neugebauer Kleinnmann-Low (BN-KL) nebula is considered likely to come from dust heated in the regions around the most recent massive star formation (e.g. Genzel and Stutzki, 1989). The BN-KL nebula is located behind the θ^1 OB association, near the front surface of OMC 1.

In the model of the Orion region proposed by Cowie *et al.* (1979), the Orion OB1 association is located on the western side of the molecular-cloud complex, centred around the point where the Orion A & B GMCs meet. Using observations of the high-density

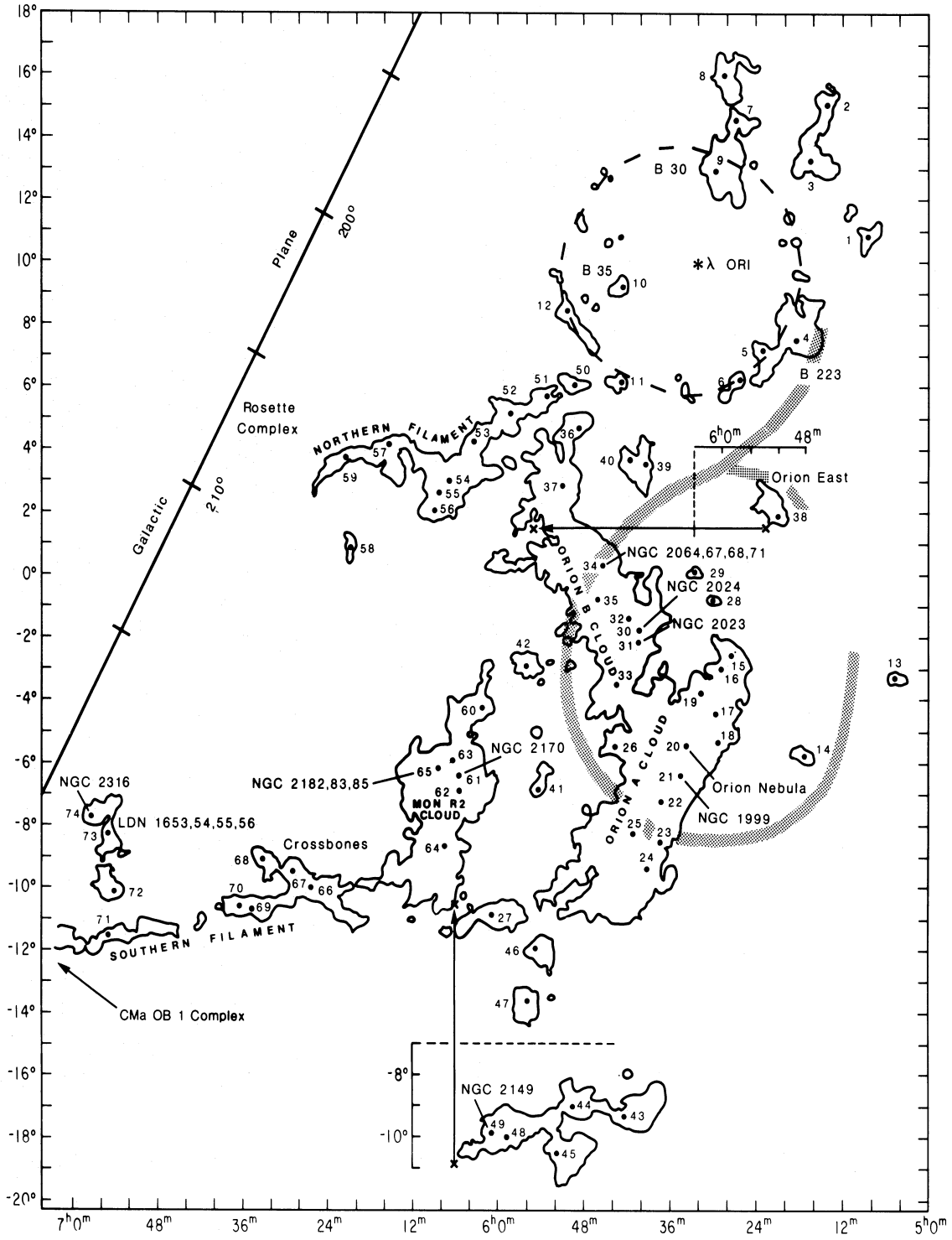

Figure 3.1: A 1.28 K km s^{-1} contour map of the $J = 1 \rightarrow 0$ rotational transition of CO at 115,271 MHz, illustrating the molecular clouds in the Orion and Monoceros regions (Equinox 1950; taken from Maddalena *et al.*, 1986). Numbered points refer to CO emission peaks listed in Maddalena *et al.* (1986). The shaded arc identifies UV emission from Barnard's loop (O'Dell *et al.*, 1967; Isobe, 1973), while the dashed line identifies the extent of the λ Ori ring (see Chapter 4).

tracer CS, Bally *et al.* (1990) find the molecular material on the western faces of the GMCs (closest to the OB association and therefore more strongly affected by the shocks they produce) to contain the densest gas. Consequently, it is these regions which show signs of the most active star formation.

Furthermore, using observations of CO, Bally *et al.* (1990) find the molecular gas located nearest to the centre of the association to exhibit the most positive velocities (typically $v_{\odot} = +27$ km s^{-1}) while that located at larger distances possesses smaller velocities (typically $v_{\odot} = +22$ km s^{-1}). These features are considered to be a result of shocks and ionising radiation from the association's stars (Bally *et al.*, 1990).

Many of the molecular clouds in the complex are observed to have comet-like structures, with dense heads and tails which point away from the centre of the OB association (Bally *et al.*, 1990). It is the influence of the association stars that is also considered to produce the many loops and shell structures visible in this direction. In the model for the region proposed by Cowie *et al.* (1979), Barnard's Loop (Pickering, 1890; Barnard, 1895), which has the form of an incomplete elliptical ring centred on the OB1 association (not enclosing the λ Orionis association) is interpreted as being an H II region at the inner edge of a dense shell of swept-up material. This is considered to be a part of the much larger Orion-Eridanus superbubble (Reynolds and Ogden, 1979; Brown *et al.*, 1995; Heiles, 1999). Exterior to Barnard's Loop, Cowie *et al.* (1979) suggest the presence of a fast-moving (100 km s^{-1}), low-density shell centred on the Orion OB1 association, denoted "Orion's Cloak" due to the way in which it appears to cover the Hunter's back.

The apparent brightness of the stars in Orion aids the spectroscopic study of the intervening interstellar matter. It has been with observations of these stars that many pioneering studies have been performed. From the observations of δ Ori, with which Hartmann (1904) first discovered the interstellar medium (ISM), to the observations of ϵ & ζ Ori which highlighted the existence of multiple discrete interstellar clouds, rather than a homogeneous substrate of gas (Beals, 1936). More recently, many molecular species have been identified for the first time in the Orion region (summarised by Genzel and Stutzki, 1989). Many of the previous high-resolution surveys of matter in the ISM (e.g. Hobbs, 1969*a*,*b*,*c*, 1978*a*; Marschall and Hobbs, 1972; Hobbs *et al.*, 1991; Welty *et al.*, 1994, 1996; Welty and Hobbs, 2001) have *included* observations of stars in the direction of Orion; however, none have concentrated on the ISM in this direction. The work of O'Dell *et al.* (1993), while focusing on the inner Orion Nebula, utilised lower-resolution ($R \approx 9 \times 10^4$)

Ca II K observations of the four Trapezium stars and is therefore unable to reveal the complex line-profiles now observed with the Ultra-High-Resolution Facility (hereinafter UHRF).

3.2 The Observations

Here we present ultra-high-resolution observations of Na I, Ca II, K I, CH and CH^+ towards twelve bright stars in Orion. The line-profile parameters resulting from the modelling of these data, heliocentric radial velocity, $v_\odot$, velocity dispersion, b, and column density, N, are listed in Tables 3.3 to 3.14, along with the 1σ, single-parameter errors. In the case of Na I and K I, $v_\odot$ corresponds to the weighted mean velocity of the two hyperfine split components (discussed in § 1.2.3). The corresponding best-fitting model profiles, after convolution with the instrumental response function, are shown in Figures 3.2 to 3.13, overplotted on the observed line profiles.

The generally good agreement which can be seen between the (independently generated) Ca II, Na I and K I absorption model components suggests that the majority of the individual clouds have been identified.

Where observations of more than one atom/ion are available for a given star, the comparison of absorption *components* present in each waveband enables the identification of individual interstellar *clouds*. These clouds are numbered according to radial velocity in Table 3.3 to 3.14. Furthermore, where observations of stars with small angular separations are available, specifically the M42 region, it is possible to identify absorption *systems*, where individual interstellar clouds produce absorption (characterised by components with similar parameters) in more than one sightline. The identification of the absorption *systems* present in the line-of-sight to the M42 region will be made in § 3.4.1 of this chapter. The absorption *systems* are also numbered according to velocity, but during the discussion of § 3.4.1 the *systems* will be referred to by an M (denoting M42) followed by a bold number, so as to reduce confusion with individual clouds. A similar analysis will be performed for the λ Ori association in Chapter 4.

Observations of CH λ4300 and/or $CH^+\lambda$4233 have been made towards a number of our targets; however, no absorption components have been positively identified in any of these spectra. Table 3.1 lists the signal-to-noise (S/N) ratio and upper limits to the equivalent widths (W_λ) and column density of any absorption present in each of these spectra. In

Table 3.1: Signal-to-noise ratios (S/N) achieved for observations of CH λ4300 and CH^+ λ4232, along with 2σ upper limits to the equivalent widths (W_λ) and column densities (N), assuming representative b-values of 1.7 and 2.4 km s^{-1} for the CH and CH^+ lines respectively (based on previous UHRF observations; e.g. Crawford, 1995).

Star	Molecule	S/N	W_λ (mÅ)	log N (cm^{-2})
θ^1 Ori C	CH	52	≤ 0.6	≤ 11.8
θ^1 Ori C	CH^+	41	≤ 0.9	≤ 12.0
θ^2 Ori A	CH	62	≤ 0.5	≤ 11.8
θ^2 Ori A	CH^+	41	≤ 0.9	≤ 12.0
λ Ori	CH^+	65	≤ 0.6	≤ 11.8
ϕ^1 Ori	CH^+	37	≤ 1.0	≤ 12.0

general, these values represent better limits than those determined in previous studies (e.g. Hobbs, 1973; Federman, 1982; Lambert and Danks, 1986).

Table 3.2: Stellar data for the targets observed with the UHRF. Unless otherwise stated, stellar positions (columns 3 & 4), and spectral types (column 6) have been obtained from the SIMBAD astronomical database. Where available, V magnitudes (column 5) and distances (column 8) have been obtained from the Hipparcos and Tycho catalogues (ESA, 1997). In the cases of θ^1 Ori A & C and θ^2 Ori A, distances are not available from the Hipparcos catalogue and have been taken from Goudis (1982). Column 7 displays values of E(B-V) derived using the tabulations of Deutschman *et al.* (1976), and data from the SIMBAD database. Stellar heliocentric radial velocities (column 9) have been obtained from Wilson (1953) and Evans (1967).

1	2	3	4	5	6	7	8	9
Star	HD	l	b	V	Sp. Type	E(B-V)	Dist.	$RV_\odot$
		(° ′)	(° ′)				(pc)	(km s^{-1})
β Ori	34085	209 14	-25 15	0.28	B8 Iab	-0.01	237^{+56}_{-38}	20.7±0.9
δ Ori	36486	203 52	-17 44	2.20	O9.5II	0.11	281^{+85}_{-53}	16.0±2.0
ϕ^1 Ori	36822	195 24	-12 17	4.38	B0 III	0.16	302^{+92}_{-57}	33.2±0.9
λ Ori	36861	195 03	-12 00	3.52	O8 IIIf	0.16	324^{+109}_{-66}	33.4±0.5
θ^1 Ori A	37020	209 01	-19 23	4.98	O7	0.35	≈ 450	33.4±2.0
θ^1 Ori C	37022	209 01	-19 23	5.13	O6	0.36	≈ 450	28.0±5.0
θ^2 Ori A	37041	209 03	-19 22	4.98	O9.5V	0.22	≈ 450	35.6±2.0
ι Ori	37043	209 31	-19 35	2.74	O9 III	0.10	407^{+185}_{-97}	21.5±0.9
ϵ Ori	37128	205 13	-17 14	1.69	B0 Iab	0.07	412^{+246}_{-113}	25.9±0.9
σ Ori	37468	206 49	-17 20	3.77	O9.5V	0.13	352^{+166}_{-85}	29.1±2.0
ζ Ori	37742	206 27	-16 35	1.70	O9.5Ib	0.07	251^{+62}_{-42}	18.1±0.9
κ Ori	38771	214 31	-18 30	2.04	B0 Iab	0.06	221^{+46}_{-32}	20.5±2.0

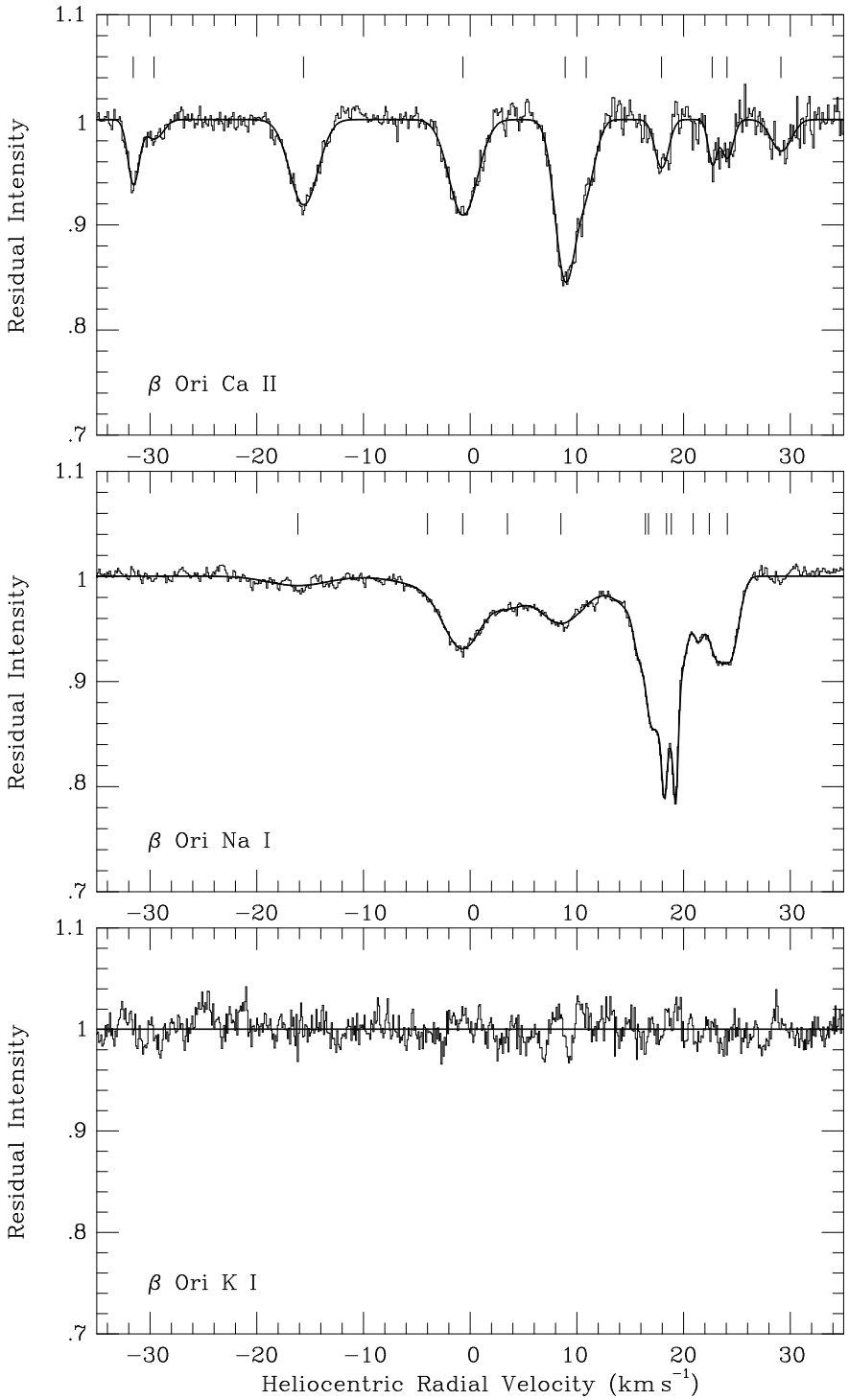

Figure 3.2: Theoretical line profiles (thick solid line) are shown plotted over the interstellar Ca II, Na I and K I spectra (thin solid line) observed towards β Ori. The vertical scale has been expanded to display more clearly weaker absorption in the Ca II, Na I and K I regions. Tick marks are used to indicate the velocities of the individual model components, as listed in Table 3.3. In the case of both Na I and K I absorption, tick marks represent the weighted-mean of the two hyperfine components.

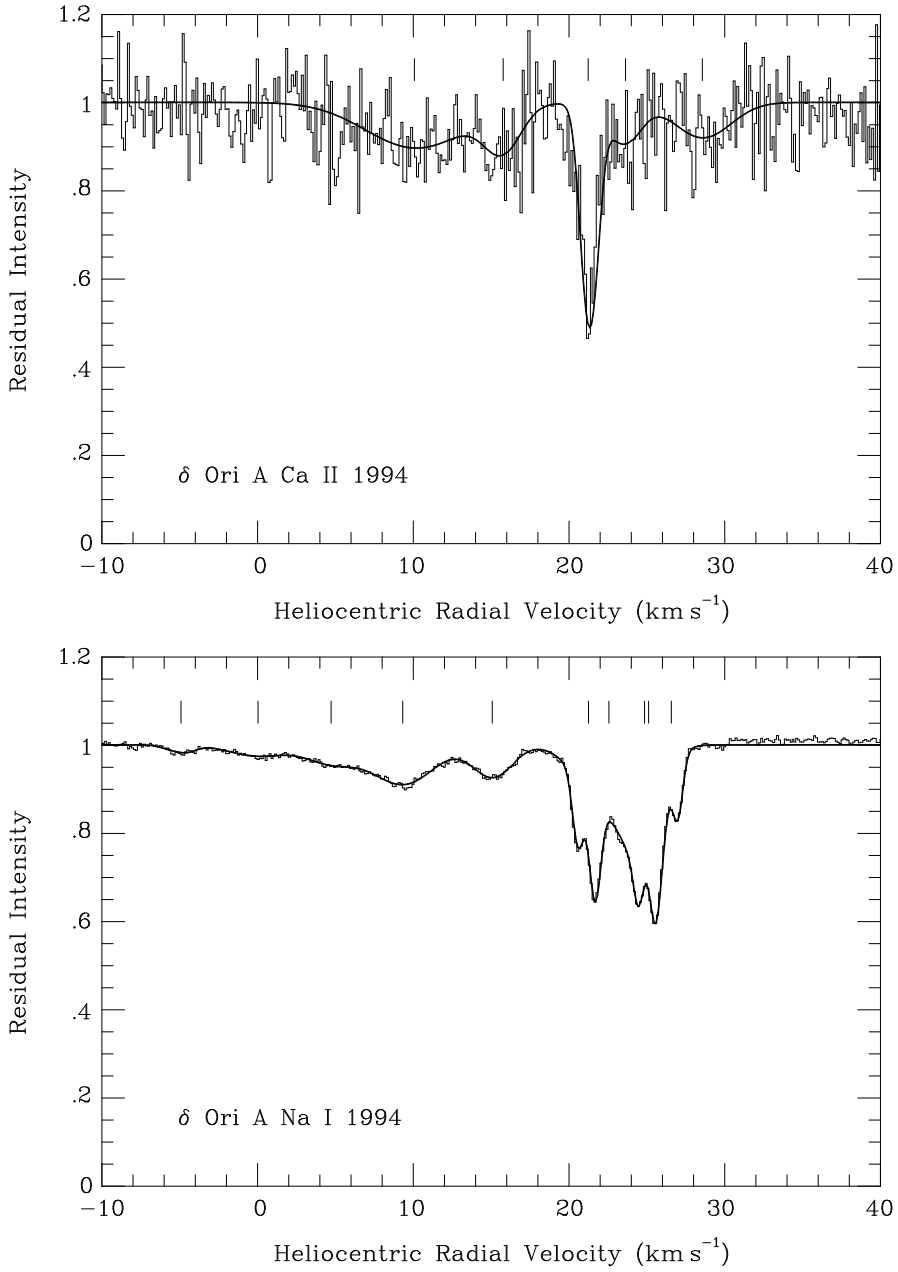

Figure 3.3: Theoretical line profiles are shown plotted over the interstellar Ca II and Na I spectra observed towards δ Ori. Tick marks are used to indicate the velocities of the individual model components, as listed in Table 3.4.

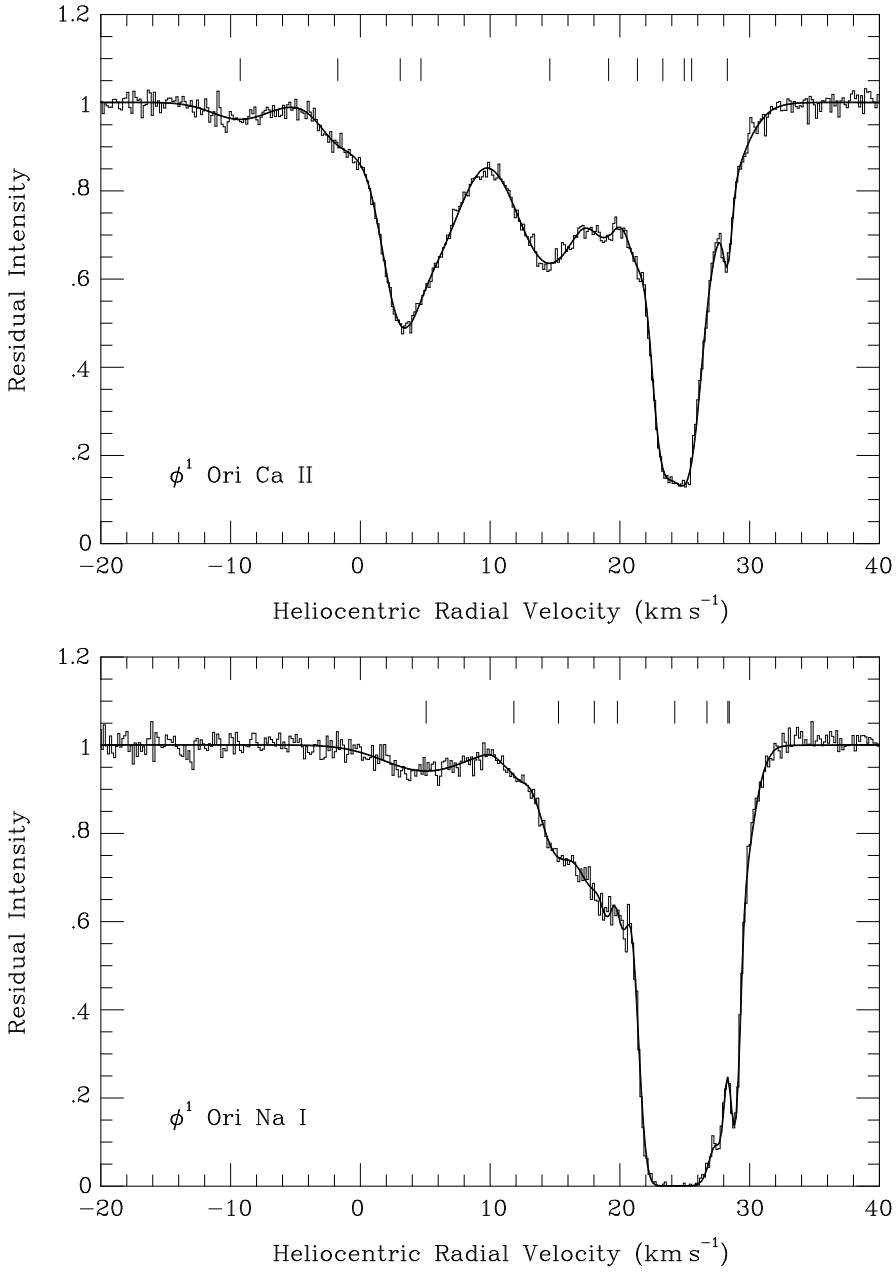

Figure 3.4: Theoretical line profiles are shown plotted over the interstellar Ca II and Na I spectra observed towards ϕ^1 Ori. Tick marks are used to indicate the velocities of the individual model components, as listed in Table 3.5.

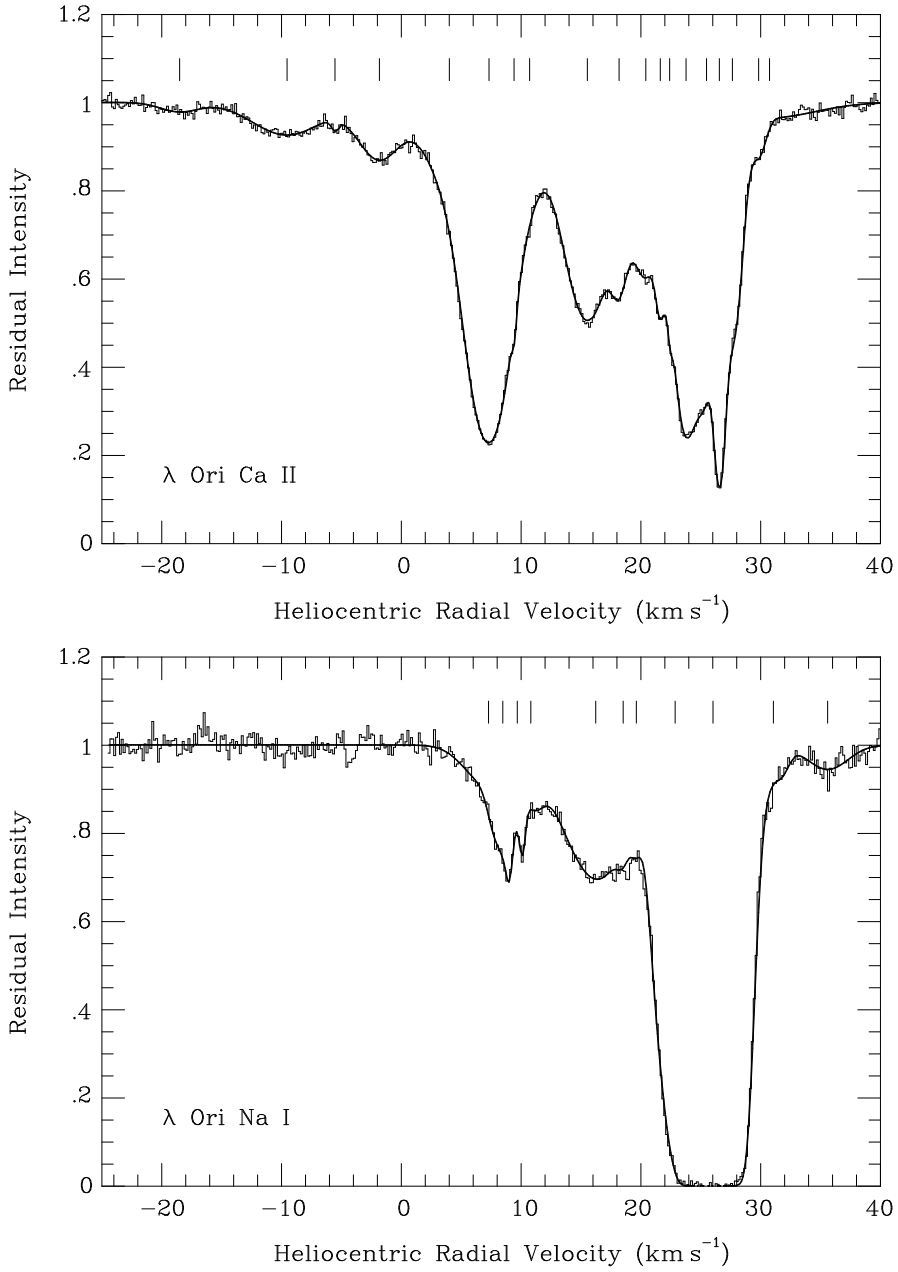

Figure 3.5: Theoretical line profiles are shown plotted over the interstellar Ca II and Na I spectra observed towards λ Ori. Tick marks are used to indicate the velocities of the individual model components, as listed in Table 3.6.

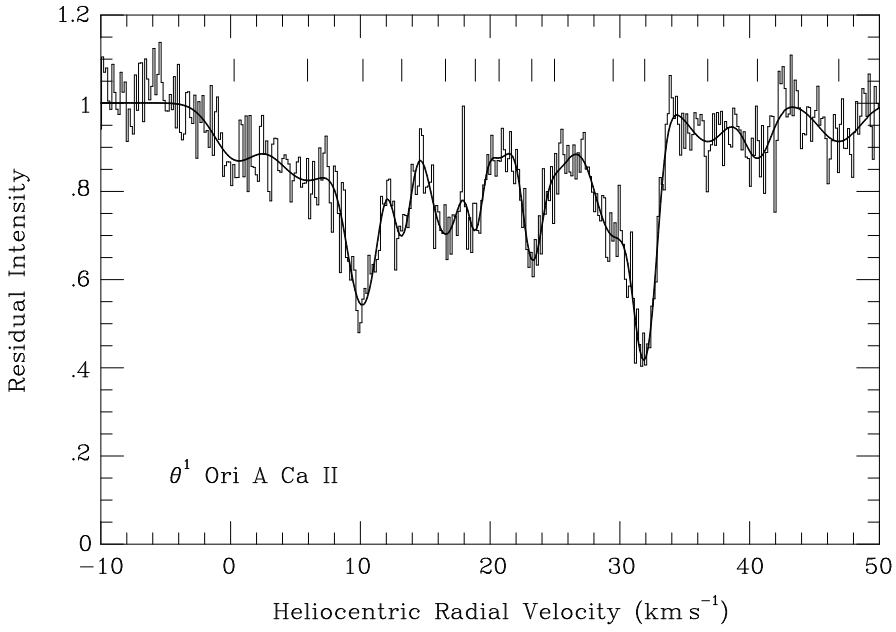

Figure 3.6: Theoretical line profiles are shown plotted over the interstellar Ca II spectrum observed towards θ^1 Ori A. Tick marks are used to indicate the velocities of the individual model components, as listed in Table 3.7.

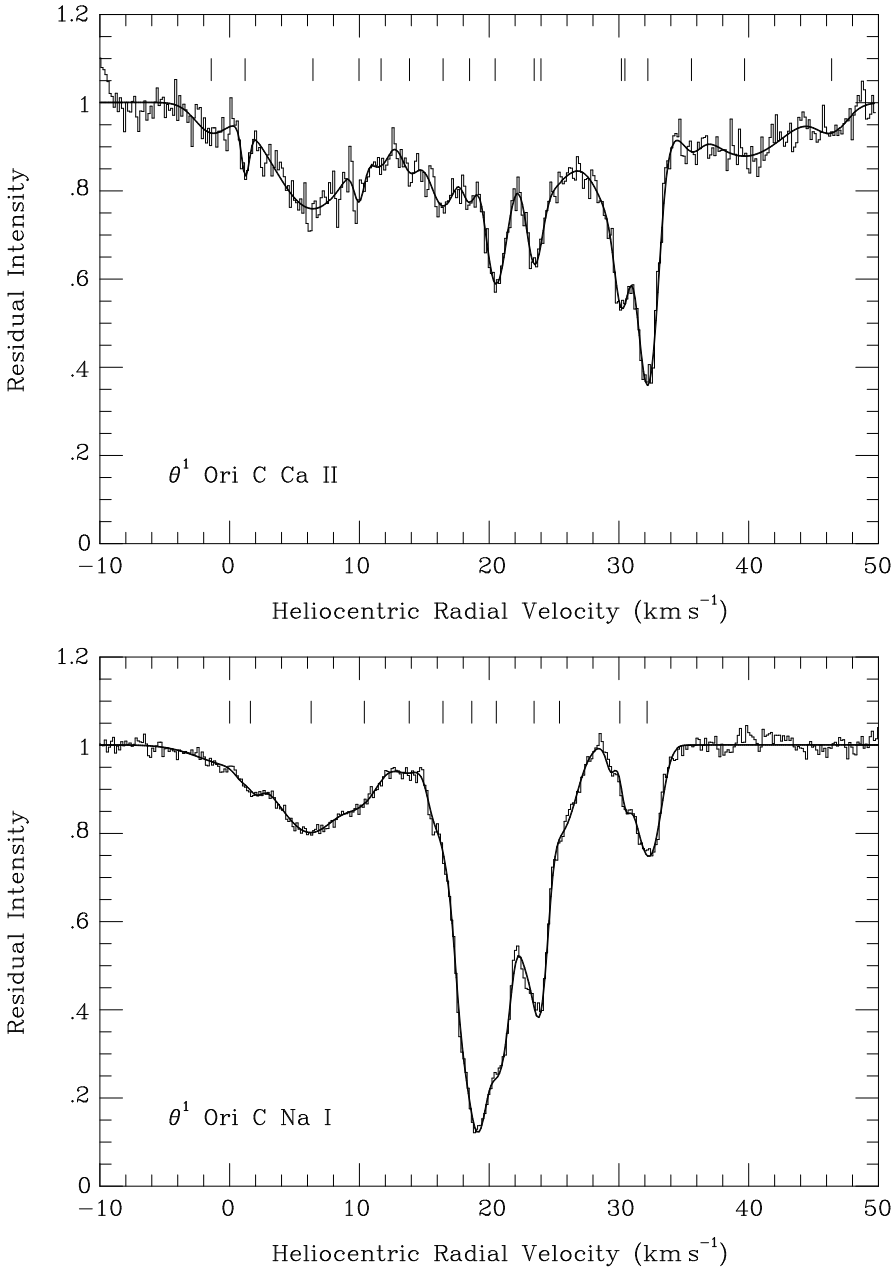

Figure 3.7: Theoretical line profiles are shown plotted over the interstellar Ca II and Na I spectra observed towards θ^1 Ori C. Tick marks are used to indicate the velocities of the individual model components, as listed in Table 3.8.

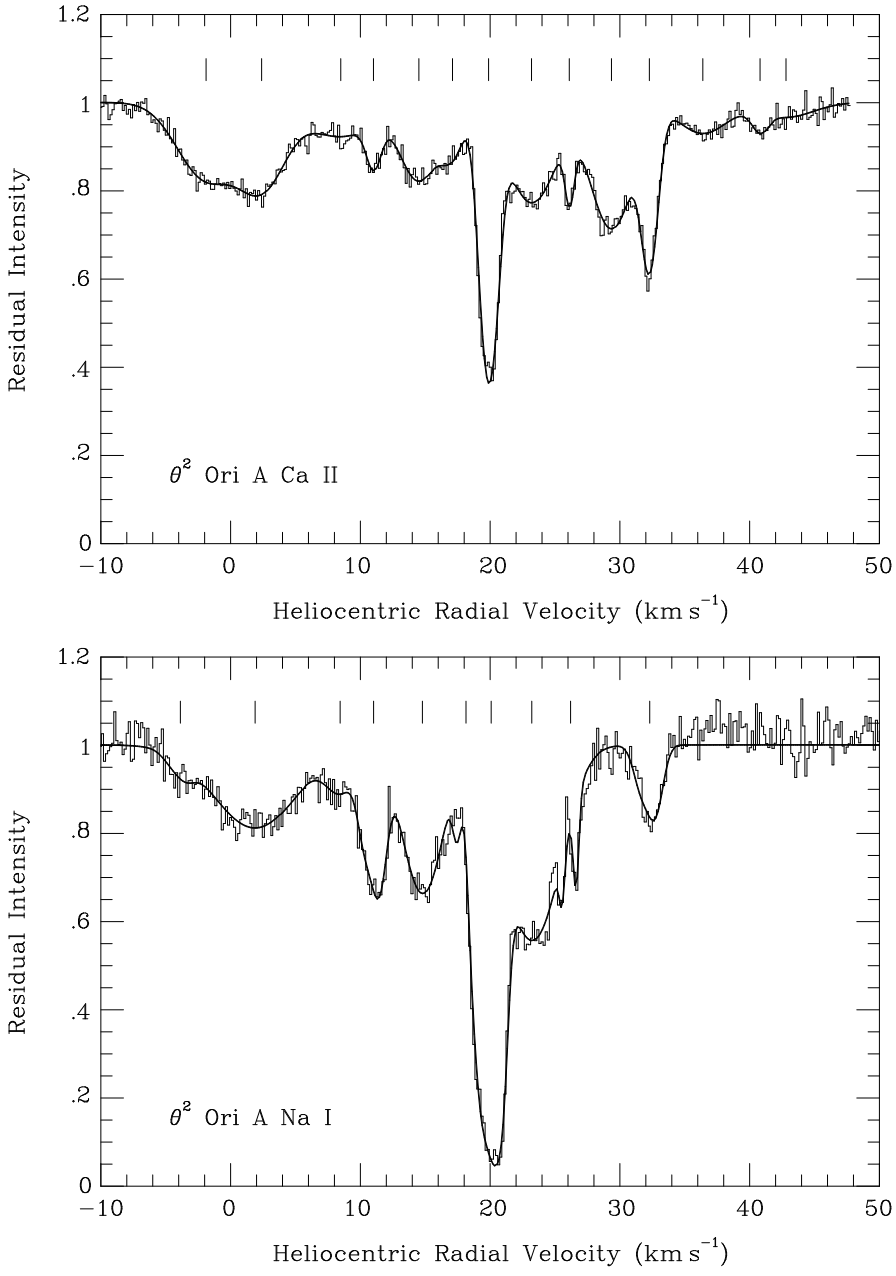

Figure 3.8: Theoretical line profiles are shown plotted over the interstellar Ca II and Na I spectra observed towards θ^2 Ori A. Tick marks are used to indicate the velocities of the individual model components, as listed in Table 3.9.

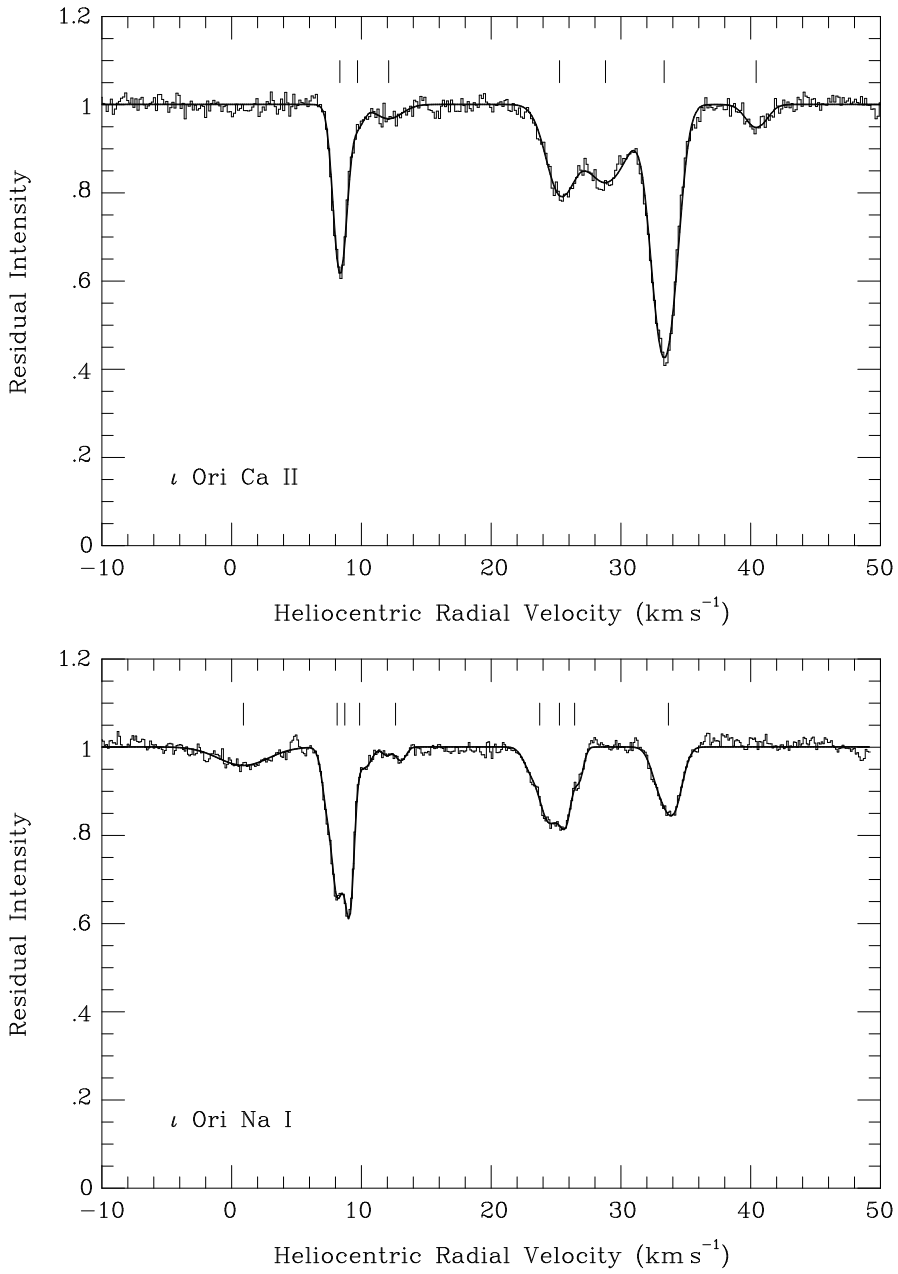

Figure 3.9: Theoretical line profiles are shown plotted over the interstellar Ca II and Na I spectra observed towards ι Ori. Tick marks are used to indicate the velocities of the individual model components, as listed in Table 3.10.

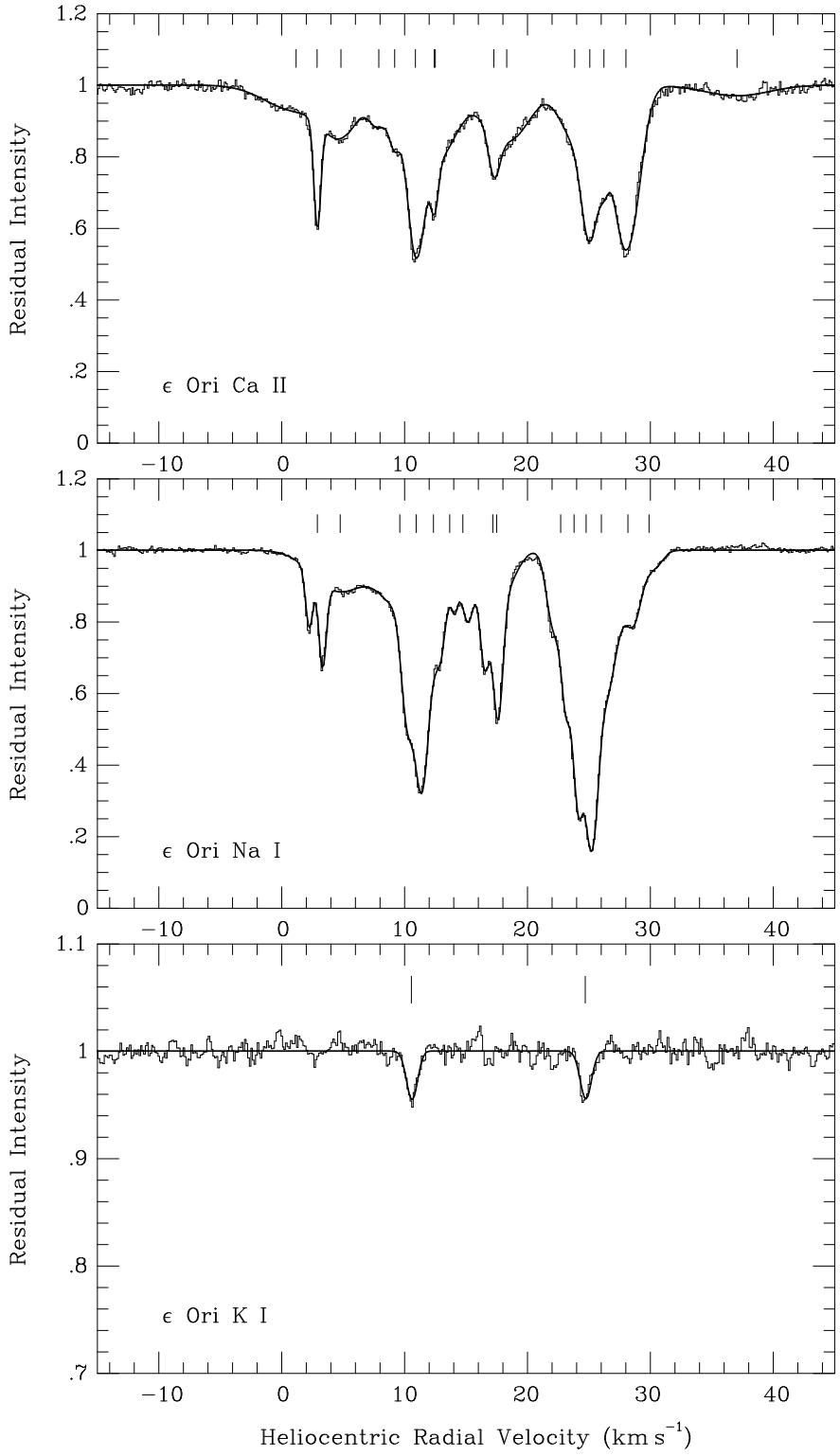

Figure 3.10: Theoretical line profiles are shown plotted over the interstellar Ca II, Na I and K I spectra observed towards ϵ Ori. The vertical scale has been expanded to display more clearly weaker absorption in the K I region. Tick marks are used to indicate the velocities of the individual model components, as listed in Table 3.11.

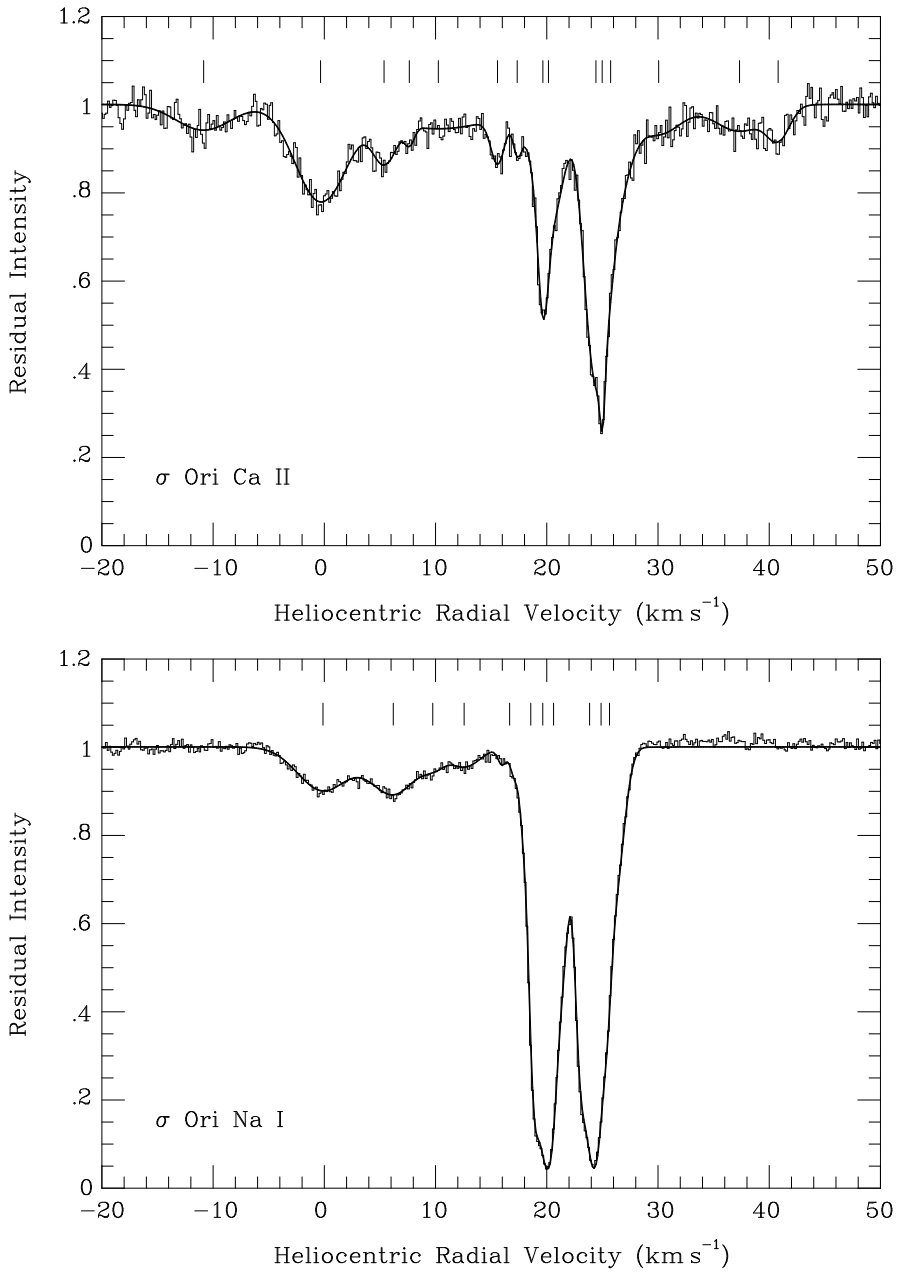

Figure 3.11: Theoretical line profiles are shown plotted over the interstellar Ca II and Na I spectra observed towards σ Ori. Tick marks are used to indicate the velocities of the individual model components, as listed in Table 3.12.

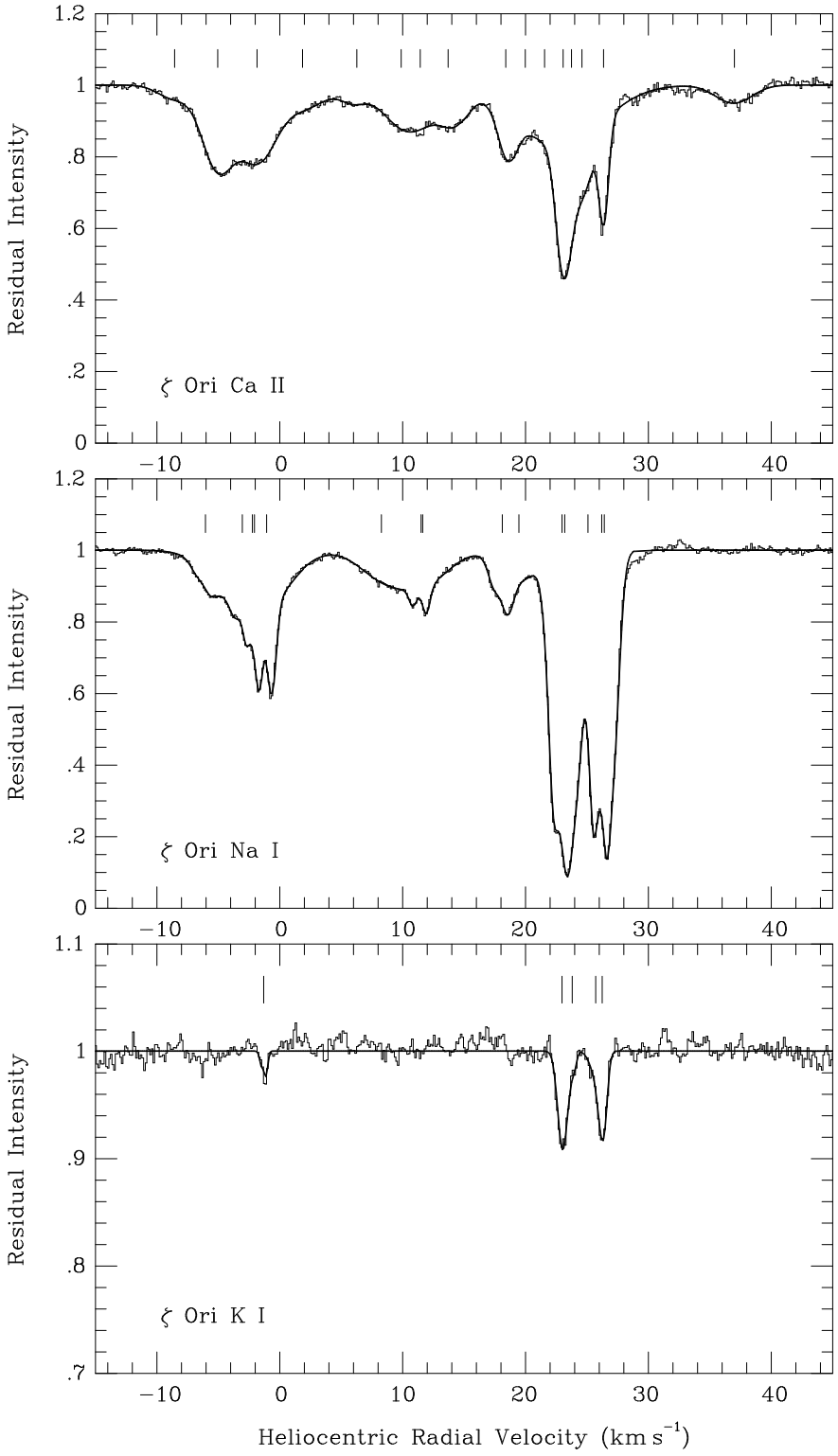

Figure 3.12: Theoretical line profiles are shown plotted over the interstellar Ca II, Na I and K I spectra observed towards ζ Ori. The vertical scale has been expanded to display more clearly weaker absorption in the K I region. Tick marks are used to indicate the velocities of the individual model components, as listed in Table 3.13.

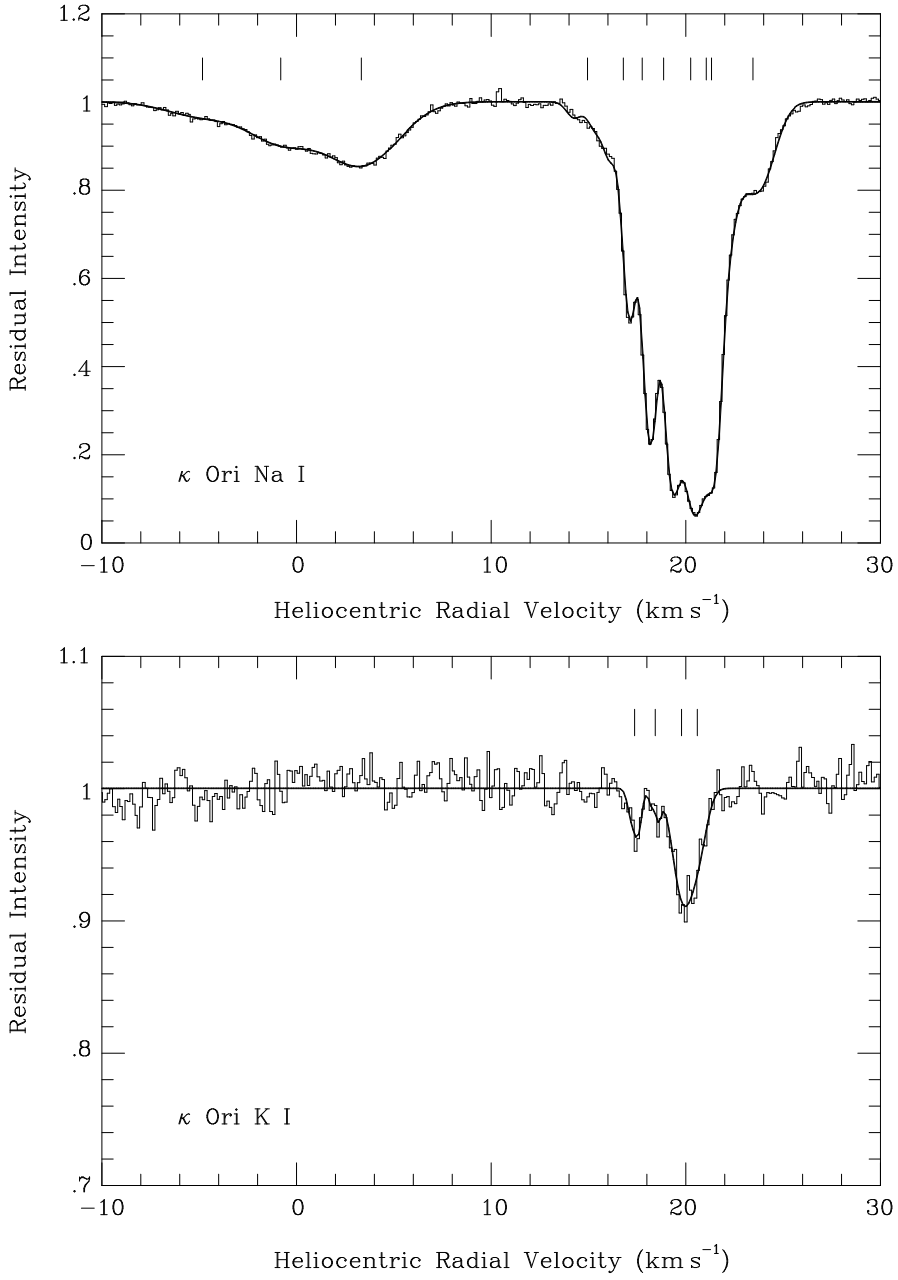

Figure 3.13: Theoretical line profiles are shown plotted over the interstellar Na I and K I spectra observed towards κ Ori. The vertical scale has been expanded to display more clearly weaker absorption in the K I region. Tick marks are used to indicate the velocities of the individual model components, as listed in Table 3.14.

Table 3.3: Component parameters derived from the absorption line modelling of β Ori. Values of $v_\odot$ (heliocentric radial velocity), b (velocity dispersion) and N (column density) are shown in columns 2–4 (for Ca II), 6–8 (for Na I) and 9–11 (for K I). Total equivalent widths (W_λ) and achieved S/N ratios are displayed above columns 2–4, 6–8 and 9–11 for Ca II, Na I and K I respectively. In the case of both Na I and K I absorption, central velocities are with respect to the weighted-mean of the two hyperfine split components. Where Ca II, and/or Na I, and/or K I components appear in the same row, and are hence identified by the same cloud number (column 1), absorption is considered to occur in the same individual interstellar cloud. Column 5 gives cloud Na°/Ca^+ abundance ratios. Where multiple entries are made with a single cloud number (towards a given star), absorption is considered to arise in multiple unresolvable clouds and an average Na I/Ca II ratio is obtained from the summed Na I and Ca II column densities. Variable systems (discussed in Chapter 5) are identified in column 1 with a superscript "†".

	Ca II				Na I			K I		
Star/ Cloud	$v_\odot$ (km s^{-1})	b (km s^{-1})	log N (cm^{-2})	$\frac{Na^\circ}{Ca^+}$	$v_\odot$ (km s^{-1})	b (km s^{-1})	log N (cm^{-2})	$v_\odot$ (km s^{-1})	b (km s^{-1})	log N (cm^{-2})
β **Ori**	S/N: 139; W_λ: 17.7 ± 0.3 mÅ				S/N: 192; W_λ: 37.2 ± 0.2 mÅ			S/N: 78; W_λ :	< 1 mÅ	
1†	-31.58 ± 0.06	0.71 ± 0.07	10.10 ± 0.05	< 0.04						
2	-29.63 ± 0.25	1.14 ± 0.39	9.76 ± 0.12	< 0.12						
3	-15.62 ± 0.04	1.81 ± 0.06	10.62 ± 0.01	0.30	-16.15 ± 0.29	3.83 ± 0.45	10.10 ± 0.04			
4				> 6.92	-4.00 ± 6.29	3.83 ± 3.74	10.08 ± 0.98			
5	-0.68 ± 0.04	1.84 ± 0.06	10.68 ± 0.01	1.23	-0.70 ± 0.14	2.37 ± 0.41	10.77 ± 0.21			
6				> 14.79	3.49 ± 0.29	1.99 ± 0.56	10.27 ± 0.17			
7a†	8.90 ± 0.10	1.31 ± 0.08	10.77 ± 0.04	0.66	8.50 ± 0.14	3.04 ± 0.38	10.71 ± 0.05			
7b	10.87 ± 0.24	1.18 ± 0.21	10.29 ± 0.13							
8				> 26.30	16.42 ± 0.04	0.58 ± 0.05	10.25 ± 0.07			
9				> 33.88	16.71 ± 2.46	3.33 ± 1.69	10.74 ± 0.46			
10	17.93 ± 0.06	0.87 ± 0.08	10.05 ± 0.03	7.08	18.40 ± 0.11	1.33 ± 0.23	10.90 ± 0.22			
11				> 44.67	18.85 ± 0.01	0.22 ± 0.02	10.27 ± 0.03			
12				> 16.98	20.90 ± 0.07	0.61 ± 0.16	10.07 ± 0.33			
13	22.68 ± 0.08	0.54 ± 0.11	9.82 ± 0.09	2.88	22.41 ± 0.11	0.82 ± 0.15	10.28 ± 0.14			
14	24.07 ± 0.11	0.74 ± 0.17	9.89 ± 0.08	5.01	24.10 ± 0.07	0.98 ± 0.08	10.59 ± 0.04			
15	29.12 ± 0.10	1.30 ± 0.15	10.03 ± 0.04	< 0.07						

Table 3.4: Component parameters derived from the absorption line modelling of δ Ori. See caption to Table 3.3 for further details.

	Ca II				Na I			K I		
Star/ Cloud	$v_\odot$ (km s^{-1})	b (km s^{-1})	log N (cm^{-2})	$\frac{\mathrm{Na}^\circ}{\mathrm{Ca}^+}$	$v_\odot$ (km s^{-1})	b (km s^{-1})	log N (cm^{-2})	$v_\odot$ (km s^{-1})	b (km s^{-1})	log N (cm^{-2})
δ **Ori**	S/N: 14; W_λ: 36.1 ± 2.0 mÅ				S/N: 185; W_λ: 60.8 ± 0.2 mÅ					
1				> 0.89	-4.92 ± 0.12	0.83 ± 0.23	9.86 ± 0.06			
2				> 1.70	0.03 ± 0.34	2.44 ± 0.46	10.37 ± 0.08			
3				> 2.57	4.72 ± 0.20	2.12 ± 0.43	10.52 ± 0.11			
4	10.07 ± 1.05	7.63 ± 1.31	11.31 ± 0.07	0.45	9.32 ± 0.12	2.63 ± 0.18	10.96 ± 0.03			
5	15.77 ± 0.31	1.26 ± 0.57	10.50 ± 0.22	1.51	15.07 ± 0.04	1.56 ± 0.07	10.68 ± 0.01			
6†	21.23 ± 0.05	0.74 ± 0.07	11.07 ± 0.04	0.74	21.25 ± 0.53	0.45 ± 0.33	10.94 ± 0.11			
7a	23.63 ± 0.25	1.13 ± 0.42	10.59 ± 0.13	7.08	22.56 ± 0.01	2.41 ± 0.01	11.12 ± 0.02			
7b					24.85 ± 0.07	1.38 ± 0.15	11.16 ± 0.10			
8				> 10.23	25.11 ± 0.01	0.36 ± 0.02	10.74 ± 0.04			
9				> 6.31	26.57 ± 0.01	0.38 ± 0.03	10.54 ± 0.04			
10	28.56 ± 0.48	2.59 ± 0.74	10.79 ± 0.10	< 0.02						

Table 3.5: Component parameters derived from the absorption line modelling of ϕ^1 Ori. See caption to Table 3.3 for further details.

	Ca II				Na I			K I		
Star/ Cloud	$v_\odot$ (km s^{-1})	b (km s^{-1})	log N (cm^{-2})	$\frac{\mathrm{Na}^\circ}{\mathrm{Ca}^+}$	$v_\odot$ (km s^{-1})	b (km s^{-1})	log N (cm^{-2})	$v_\odot$ (km s^{-1})	b (km s^{-1})	log N (cm^{-2})
ϕ^1 **Ori**	S/N: 68; W_λ: 155.8 ± 0.5 mÅ				S/N: 52; W_λ: 215.6 ± 0.9 mÅ					
1	-9.26 ± 0.29	3.01 ± 0.44	10.50 ± 0.05	< 0.13						
2	-1.74 ± 0.53	2.04 ± 0.50	10.60 ± 0.21	< 0.09						
3a	3.07 ± 0.08	1.61 ± 0.19	11.11 ± 0.13	0.16	5.07 ± 0.45	4.40 ± 0.72	10.99 ± 0.06			
3b	4.67 ± 0.32	3.84 ± 0.22	11.69 ± 0.05							
4a	14.60 ± 0.09	3.63 ± 0.15	11.65 ± 0.02	0.50	11.83 ± 0.50	0.82 ± 0.66	10.34 ± 0.32			
4b					15.27 ± 0.54	1.81 ± 0.76	11.30 ± 0.19			
5	19.13 ± 0.24	1.65 ± 0.29	11.04 ± 0.14	1.62	18.03 ± 0.26	1.21 ± 0.56	11.25 ± 0.24			
6	21.35 ± 0.23	1.07 ± 0.33	10.91 ± 0.39	1.91	19.81 ± 0.07	0.64 ± 0.08	11.19 ± 0.10			
7a	23.31 ± 0.09	0.98 ± 0.11	11.52 ± 0.12	7.19	24.23 ± 0.09	1.61 ± 0.05	12.91 ± 0.05			
7b	24.96 ± 0.12	1.20 ± 0.12	11.67 ± 0.11		26.71 ± 0.24	0.88 ± 0.50	11.70 ± 0.59			
7c	25.53 ± 1.21	3.36 ± 0.64	11.66 ± 0.22		28.32 ± 1.64	1.64 ± 0.87	11.60 ± 0.62			
8	28.28 ± 0.03	0.40 ± 0.06	10.39 ± 0.06	14.79	28.43 ± 0.02	0.41 ± 0.05	11.56 ± 0.11			

Table 3.6: Component parameters derived from the absorption line modelling of λ Ori. See caption to Table 3.3 for further details.

Star/ Cloud	Ca II $v_\odot$ (km s^{-1})	Ca II b (km s^{-1})	Ca II log N (cm^{-2})	$\frac{\text{Na}^\circ}{\text{Ca}^+}$	Na I $v_\odot$ (km s^{-1})	Na I b (km s^{-1})	Na I log N (cm^{-2})	K I $v_\odot$ (km s^{-1})	K I b (km s^{-1})	K I log N (cm^{-2})
λ Ori	S/N: 98; W_λ: 194.0 ± 0.4 mÅ				S/N: 51; W_λ: 240.2 ± 0.9 mÅ					
1	-18.51 ± 0.31	2.24 ± 0.45	10.11 ± 0.07	< 0.29						
2	-9.54 ± 0.15	4.01 ± 0.26	10.92 ± 0.02	< 0.06						
3	-5.54 ± 0.12	0.38 ± 0.21	9.45 ± 0.20	< 0.55						
4	-1.83 ± 0.17	2.48 ± 0.22	10.96 ± 0.05	< 0.04						
5	4.01 ± 1.24	2.74 ± 0.97	11.15 ± 0.32	< 0.03						
6a	7.32 ± 0.09	2.24 ± 0.13	11.94 ± 0.06	0.20	7.28 ± 3.20	2.51 ± 2.02	10.95 ± 0.70			
6b					8.47 ± 0.14	0.79 ± 0.33	10.93 ± 0.40			
7	9.41 ± 0.04	0.15 ± 0.09	9.83 ± 0.10	4.37	9.68 ± 0.06	0.29 ± 0.16	10.47 ± 0.29			
8	10.71 ± 0.31	1.72 ± 0.39	10.83 ± 0.20	0.71	10.81 ± 0.68	1.08 ± 1.00	10.68 ± 0.62			
9	15.53 ± 0.04	2.71 ± 0.11	11.70 ± 0.02	0.96	16.23 ± 0.31	3.67 ± 0.61	11.68 ± 0.07			
10	18.18 ± 0.09	0.89 ± 0.12	10.79 ± 0.18	0.35	18.52 ± 0.20	0.43 ± 0.28	10.34 ± 0.42			
11	20.41 ± 0.17	1.61 ± 0.47	11.31 ± 0.13	0.15	19.62 ± 0.27	0.56 ± 0.37	10.48 ± 0.38			
12a	21.62 ± 0.04	0.51 ± 0.11	10.63 ± 0.22	13.49	22.86 ± 0.60	1.46 ± 0.42	12.08 ± 0.27			
12b	22.40 ± 0.04	0.24 ± 0.09	10.16 ± 0.20		26.02 ± 0.12	1.76 ± 0.08	13.18 ± 0.05			
12c	23.77 ± 0.13	1.34 ± 0.20	11.70 ± 0.09							
12d	25.48 ± 0.08	0.91 ± 0.23	11.29 ± 0.23							
12e	26.55 ± 0.02	0.54 ± 0.03	11.39 ± 0.07							
12f	27.64 ± 0.07	1.03 ± 0.09	11.32 ± 0.05							
13	29.83 ± 0.09	0.76 ± 0.15	10.28 ± 0.13	1.95	31.06 ± 0.31	1.01 ± 0.58	10.57 ± 0.16			
14	30.74 ± 2.41	5.28 ± 1.90	10.70 ± 0.25	0.93	35.59 ± 0.38	2.25 ± 0.64	10.67 ± 0.09			

Table 3.7: Component parameters derived from the absorption line modelling of θ^1 Ori A. See caption to Table 3.3 for further details.

	Ca II				Na I			K I		
Star/ Cloud	$v_\odot$ (km s^{-1})	b (km s^{-1})	log N (cm^{-2})	$\frac{\mathrm{Na^\circ}}{\mathrm{Ca^+}}$	$v_\odot$ (km s^{-1})	b (km s^{-1})	log N (cm^{-2})	$v_\odot$ (km s^{-1})	b (km s^{-1})	log N (cm^{-2})
θ^1 Ori A	S/N: 17; W_λ: 119.2 ± 1.9 mÅ									
1	0.27 ± 0.73	2.18 ± 0.75	10.85 ± 0.29							
2	5.93 ± 0.68	3.64 ± 2.22	11.27 ± 0.24							
3	10.20 ± 0.10	1.57 ± 0.23	11.38 ± 0.12							
4	13.19 ± 0.11	0.98 ± 0.18	10.95 ± 0.08							
5	16.56 ± 0.17	1.68 ± 0.34	11.20 ± 0.07							
6	18.86 ± 0.21	0.75 ± 0.35	10.73 ± 0.47							
7	20.69 ± 0.89	1.49 ± 2.46	10.72 ± 0.66							
8	23.21 ± 0.22	0.97 ± 0.52	10.99 ± 0.72							
9	24.96 ± 2.57	1.88 ± 4.00	10.90 ± 1.13							
10	29.48 ± 0.45	2.03 ± 1.26	11.29 ± 0.28							
11	31.91 ± 0.10	1.09 ± 0.15	11.37 ± 0.15							
12	36.77 ± 0.46	1.95 ± 0.75	10.68 ± 0.14							
13	40.60 ± 0.28	1.39 ± 0.41	10.70 ± 0.12							
14	46.87 ± 0.37	2.16 ± 0.53	10.73 ± 0.09							

Table 3.8: Component parameters derived from the absorption line modelling of θ^1 Ori C. See caption to Table 3.3 for further details.

	Ca II				Na I			K I		
Star/ Cloud	$v_\odot$ (km s^{-1})	b (km s^{-1})	log N (cm^{-2})	$\frac{\mathrm{Na}^\circ}{\mathrm{Ca}^+}$	$v_\odot$ (km s^{-1})	b (km s^{-1})	log N (cm^{-2})	$v_\odot$ (km s^{-1})	b (km s^{-1})	log N (cm^{-2})
θ^1 **Ori C**	S/N: 32; W_λ: 120.7 $\pm$ 1.2 mÅ				S/N: 71; W_λ: 172.2 $\pm$ 0.8 mÅ					
1	-1.42 ± 0.26	1.73 ± 0.39	10.48 ± 0.09	1.78	0.00 ± 2.65	3.46 ± 1.83	10.73 ± 0.44			
2	1.19 ± 0.07	0.36 ± 0.12	10.14 ± 0.11	1.12	1.60 ± 0.20	0.69 ± 0.34	10.19 ± 0.25			
3	6.42 ± 0.14	4.07 ± 0.27	11.48 ± 0.02	0.91	6.28 ± 0.31	3.41 ± 0.93	11.44 ± 0.13			
4a	9.97 ± 0.13	0.53 ± 0.20	10.24 ± 0.24	1.15	10.38 ± 0.28	1.62 ± 0.79	10.75 ± 0.36			
4b	11.67 ± 0.33	1.14 ± 0.82	10.50 ± 0.30							
5	13.86 ± 0.28	1.02 ± 0.58	10.57 ± 0.39	0.98	13.84 ± 0.33	1.43 ± 0.93	10.56 ± 0.22			
6	16.45 ± 0.17	1.68 ± 0.68	11.08 ± 0.16	0.89	16.44 ± 0.08	0.76 ± 0.08	11.03 ± 0.03			
7	18.49 ± 0.14	0.71 ± 0.28	10.50 ± 0.33	21.38	18.66 ± 0.03	0.77 ± 0.02	11.83 ± 0.02			
8	20.46 ± 0.06	1.10 ± 0.18	11.13 ± 0.13	5.13	20.55 ± 0.04	1.18 ± 0.06	11.84 ± 0.02			
9	23.47 ± 0.09	0.77 ± 0.17	10.70 ± 0.17	7.24	23.46 ± 0.02	0.77 ± 0.03	11.56 ± 0.02			
10	23.99 ± 0.71	3.36 ± 1.62	11.31 ± 0.19	0.63	25.42 ± 0.17	1.43 ± 0.18	11.11 ± 0.05			
11	30.19 ± 0.07	0.68 ± 0.19	10.72 ± 0.29	0.56	30.07 ± 0.05	0.47 ± 0.06	10.47 ± 0.05			
12	30.46 ± 0.71	2.70 ± 0.75	11.40 ± 0.09	< 0.01						
13	32.23 ± 0.05	0.89 ± 0.09	11.29 ± 0.10	0.69	32.17 ± 0.03	1.00 ± 0.06	11.13 ± 0.01			
14	35.59 ± 0.33	1.01 ± 0.60	10.16 ± 0.37	< 0.13						
15	39.68 ± 0.39	4.44 ± 0.89	11.19 ± 0.07	< 0.02						
16	46.39 ± 0.30	1.64 ± 0.48	10.42 ± 0.16	< 0.09						

Table 3.9: Component parameters derived from the absorption line modelling of θ^2 Ori A. See caption to Table 3.3 for further details.

	Ca II				Na I			K I		
Star/	$v_\odot$	b	log N		$v_\odot$	b	log N	$v_\odot$	b	log N
Cloud	(km s^{-1})	(km s^{-1})	(cm^{-2})	$\frac{\text{Na}^\circ}{\text{Ca}^+}$	(km s^{-1})	(km s^{-1})	(cm^{-2})	(km s^{-1})	(km s^{-1})	(cm^{-2})
θ^2 Ori A	S/N: 59; W_λ: 101.4 $\pm$ 0.7 mÅ				S/N: 33; W_λ: 184.0 $\pm$ 1.6 mÅ					
1a	-1.89 ± 0.46	3.01 ± 0.35	11.18 ± 0.09	1.20	-3.87 ± 0.40	0.96 ± 0.87	10.30 ± 0.29			
1b	2.39 ± 0.27	2.48 ± 0.47	11.13 ± 0.15		1.89 ± 0.20	4.31 ± 0.46	11.51 ± 0.03			
2	8.49 ± 0.68	3.67 ± 2.50	10.90 ± 0.28	0.62	8.44 ± 0.33	1.18 ± 0.63	10.69 ± 0.17			
3	11.01 ± 0.08	0.76 ± 0.19	10.37 ± 0.19	7.08	11.02 ± 0.08	0.78 ± 0.11	11.22 ± 0.04			
4	14.51 ± 0.25	1.96 ± 0.47	11.00 ± 0.15	3.02	14.78 ± 0.07	1.89 ± 0.15	11.48 ± 0.02			
5	17.10 ± 0.23	1.21 ± 0.32	10.55 ± 0.22	2.14	18.14 ± 0.06	0.44 ± 0.06	10.88 ± 0.07			
6	19.88 ± 0.01	0.90 ± 0.02	11.38 ± 0.01	4.79	20.08 ± 0.02	0.74 ± 0.03	12.06 ± 0.01			
7	23.19 ± 0.08	2.52 ± 0.21	11.24 ± 0.03	3.39	23.21 ± 0.11	2.68 ± 0.19	11.77 ± 0.03			
8	26.10 ± 0.04	0.44 ± 0.07	10.34 ± 0.07	2.09	26.20 ± 0.03	0.22 ± 0.07	10.66 ± 0.09			
9	29.35 ± 0.06	2.19 ± 0.12	11.30 ± 0.02	< 0.03						
10	32.27 ± 0.02	0.84 ± 0.04	11.00 ± 0.03	0.78	32.30 ± 0.08	0.79 ± 0.15	10.89 ± 0.04			
11	36.39 ± 0.34	2.62 ± 0.55	10.71 ± 0.09	< 0.12						
12	40.80 ± 0.17	0.86 ± 0.42	10.05 ± 0.37	< 0.32						
13	42.80 ± 1.57	2.94 ± 1.59	10.43 ± 0.29	< 0.25						

Table 3.10: Component parameters derived from the absorption line modelling of ι Ori. See caption to Table 3.3 for further details.

	Ca II				Na I			K I		
Star/ Cloud	$v_\odot$ (km s^{-1})	b (km s^{-1})	log N (cm^{-2})	$\frac{\mathrm{Na}^\circ}{\mathrm{Ca}^+}$	$v_\odot$ (km s^{-1})	b (km s^{-1})	log N (cm^{-2})	$v_\odot$ (km s^{-1})	b (km s^{-1})	log N (cm^{-2})
ι Ori	S/N: 87; W_λ: 45.5 ± 0.4 mÅ				S/N: 110; W_λ: 46.0 ± 0.4 mÅ					
1				> 18.20	0.91 ± 0.13	2.58 ± 0.19	10.62 ± 0.03			
2a	8.34 ± 0.02	0.67 ± 0.03	10.96 ± 0.02	1.95	8.13 ± 0.16	0.56 ± 0.08	10.97 ± 0.16			
2b					8.72 ± 0.05	0.38 ± 0.07	10.93 ± 0.18			
3	9.70 ± 0.20	0.64 ± 0.33	9.93 ± 0.22	2.14	9.86 ± 0.12	0.67 ± 0.19	10.26 ± 0.08			
4	12.10 ± 0.26	1.47 ± 0.42	10.12 ± 0.10	0.72	12.63 ± 0.09	0.49 ± 0.10	9.98 ± 0.06			
5				> 30.90	23.74 ± 0.15	0.77 ± 0.12	10.59 ± 0.11			
6	25.27 ± 0.07	1.47 ± 0.08	10.92 ± 0.04	0.93	25.26 ± 0.07	0.86 ± 0.17	10.89 ± 0.08			
7				> 14.45	26.43 ± 0.06	0.37 ± 0.13	10.10 ± 0.21			
8	28.81 ± 0.11	2.41 ± 0.20	11.10 ± 0.03	< 0.01						
9	33.33 ± 0.01	1.21 ± 0.02	11.45 ± 0.01	0.26	33.66 ± 0.02	0.87 ± 0.04	10.87 ± 0.01			
10	40.42 ± 0.11	1.12 ± 0.16	10.22 ± 0.05	< 0.07						

Table 3.11: Component parameters derived from the absorption line modelling of ϵ Ori. See caption to Table 3.3 for further details.

	Ca II				Na I			K I		
Star/ Cloud	$v_\odot$ (km s^{-1})	b (km s^{-1})	log N (cm^{-2})	$\frac{\text{Na}^\circ}{\text{Ca}^+}$	$v_\odot$ (km s^{-1})	b (km s^{-1})	log N (cm^{-2})	$v_\odot$ (km s^{-1})	b (km s^{-1})	log N (cm^{-2})
ϵ **Ori**	S/N: 114; W_λ: 85.4 ± 0.3 mÅ				S/N: 192; W_λ: 156.6 ± 0.1 mÅ			S/N: 127; W_λ: 2.7 ± 0.3 mÅ		
1	1.17 ± 0.82	3.47 ± 0.62	10.84 ± 0.13	< 0.02						
2	2.88 ± 0.01	0.31 ± 0.02	10.61 ± 0.02	1.78	2.90 ± 0.01	0.35 ± 0.01	10.86 ± 0.02			
3	4.82 ± 0.13	2.02 ± 0.37	10.87 ± 0.14	1.78	4.76 ± 0.29	2.89 ± 0.22	11.12 ± 0.04			
4a	7.90 ± 0.21	1.06 ± 0.30	10.49 ± 0.19	2.29	9.61 ± 0.47	2.03 ± 0.61	11.10 ± 0.18			
4b	9.19 ± 0.08	0.60 ± 0.14	10.37 ± 0.27							
5	10.88 ± 0.02	0.86 ± 0.13	11.09 ± 0.21	2.63	10.94 ± 0.01	0.63 ± 0.02	11.51 ± 0.03	10.55 ± 0.04	0.54 ± 0.07	9.87 ± 0.04
6	12.41 ± 0.02	0.36 ± 0.07	10.33 ± 0.13	6.76	12.35 ± 0.02	0.75 ± 0.04	11.16 ± 0.05			
7a	12.50 ± 0.97	2.24 ± 0.92	11.15 ± 0.28	0.54	13.67 ± 0.04	0.17 ± 0.10	9.86 ± 0.11			
7b					14.74 ± 0.02	0.59 ± 0.03	10.84 ± 0.02			
8	17.26 ± 0.03	0.59 ± 0.06	10.41 ± 0.07	5.62	17.18 ± 0.01	0.47 ± 0.01	11.16 ± 0.02			
9	18.31 ± 0.19	2.50 ± 0.24	11.06 ± 0.05	0.81	17.49 ± 0.07	1.50 ± 0.09	10.97 ± 0.04			
10a	23.84 ± 0.71	1.65 ± 0.48	10.85 ± 0.26	3.09	22.70 ± 0.02	0.70 ± 0.03	11.17 ± 0.01			
10b					23.79 ± 0.02	0.35 ± 0.03	10.86 ± 0.06			
11	25.07 ± 0.04	0.87 ± 0.12	11.06 ± 0.16	4.57	24.77 ± 0.01	0.58 ± 0.02	11.72 ± 0.02	24.70 ± 0.04	0.56 ± 0.07	9.87 ± 0.04
12	26.22 ± 0.08	0.53 ± 0.10	10.40 ± 0.15	9.55	26.01 ± 0.05	0.93 ± 0.07	11.38 ± 0.04			
13	28.01 ± 0.02	1.36 ± 0.03	11.36 ± 0.01	0.41	28.17 ± 0.05	0.81 ± 0.06	10.97 ± 0.04			
14				> 23.44	29.89 ± 0.20	0.91 ± 0.24	10.39 ± 0.10			
15	37.05 ± 0.26	3.69 ± 0.37	10.48 ± 0.04	< 0.04						

Table 3.12: Component parameters derived from the absorption line modelling of σ Ori. See caption to Table 3.3 for further details.

	Ca II				Na I			K I		
Star/ Cloud	$v_\odot$ (km s^{-1})	b (km s^{-1})	log N (cm^{-2})	$\frac{\mathrm{Na^\circ}}{\mathrm{Ca^+}}$	$v_\odot$ (km s^{-1})	b (km s^{-1})	log N (cm^{-2})	$v_\odot$ (km s^{-1})	b (km s^{-1})	log N (cm^{-2})
σ Ori	S/N: 43; W_λ: 91.0 ± 1.0 mÅ				S/N: 114; W_λ: 154.7 ± 0.5 mÅ					
1†	-10.85 ± 0.27	3.45 ± 0.40	10.75 ± 0.04	< 0.04						
2	-0.34 ± 0.21	3.09 ± 0.29	11.30 ± 0.10	0.58	-0.14 ± 0.18	3.02 ± 0.22	11.06 ± 0.03			
3a	5.37 ± 0.13	1.44 ± 0.36	10.60 ± 0.22	1.00	6.27 ± 0.13	2.90 ± 0.34	11.08 ± 0.04			
3b	7.64 ± 0.20	0.54 ± 0.34	9.80 ± 0.29		9.71 ± 0.27	0.57 ± 0.33	9.85 ± 0.30			
3c	10.25 ± 2.35	7.54 ± 7.26	11.06 ± 0.40		12.43 ± 0.27	2.01 ± 0.45	10.55 ± 0.07			
4	15.57 ± 0.09	0.82 ± 0.19	10.40 ± 0.15	< 0.04						
5	17.34 ± 0.10	0.50 ± 0.18	10.08 ± 0.18	1.55	16.65 ± 0.08	0.46 ± 0.07	10.27 ± 0.06			
6a				6.92	18.52 ± 0.05	0.41 ± 0.06	10.83 ± 0.11			
6b	19.65 ± 0.03	0.55 ± 0.07	10.76 ± 0.10		19.66 ± 0.02	0.66 ± 0.03	12.00 ± 0.03			
6c	20.15 ± 0.17	1.67 ± 0.24	11.16 ± 0.07		20.80 ± 0.11	0.79 ± 0.11	11.52 ± 0.08			
7a	24.42 ± 0.08	1.27 ± 0.24	11.47 ± 0.40	3.02	23.87 ± 0.02	0.63 ± 0.02	11.79 ± 0.03			
7b	24.98 ± 0.03	0.22 ± 0.06	10.53 ± 0.07		24.50 ± 0.06	1.56 ± 0.03	11.91 ± 0.02			
7c	25.74 ± 2.43	1.97 ± 1.54	11.16 ± 0.87							
8	30.06 ± 1.01	2.75 ± 1.55	10.71 ± 0.28	< 0.04						
9	37.33 ± 0.78	3.12 ± 1.58	10.72 ± 0.21	< 0.04						
10	40.80 ± 0.21	1.37 ± 0.46	10.42 ± 0.30	< 0.05						

Table 3.13: Component parameters derived from the absorption line modelling of ζ Ori. See caption to Table 3.3 for further details.

	Ca II				Na I			K I		
Star/ Cloud	$v_\odot$ (km s^{-1})	b (km s^{-1})	log N (cm^{-2})	$\frac{\text{Na}^\circ}{\text{Ca}^+}$	$v_\odot$ (km s^{-1})	b (km s^{-1})	log N (cm^{-2})	$v_\odot$ (km s^{-1})	b (km s^{-1})	log N (cm^{-2})
ζ **Ori**	S/N: 111; W_λ: 79.7 ± 0.3 mÅ				S/N: 156; W_λ: 150.7 ± 0.3 mÅ			S/N: 116; W_λ: 5.0 ± 0.2 mÅ		
1	-8.56 ± 0.39	1.84 ± 0.37	10.29 ± 0.12	< 0.06						
2a	-5.05 ± 0.14	1.75 ± 0.17	11.09 ± 0.08	1.40	-6.05 ± 0.07	0.69 ± 0.11	10.32 ± 0.07			
2b	-1.85 ± 0.16	2.07 ± 0.46	11.12 ± 0.15		-3.05 ± 0.06	0.44 ± 0.11	10.13 ± 0.14			
2c	1.85 ± 0.88	2.33 ± 1.51	10.62 ± 0.37		-2.23 ± 0.06	3.43 ± 0.10	11.43 ± 0.01			
2d					-2.06 ± 0.03	0.26 ± 0.07	10.22 ± 0.06			
2e†					-1.07 ± 0.01	0.44 ± 0.02	10.98 ± 0.02	-1.31 ± 0.06	0.04 ± 0.42	9.31 ± 0.13
3a	6.27 ± 0.37	1.92 ± 0.93	10.43 ± 0.29	0.76	8.27 ± 1.17	2.51 ± 0.58	10.82 ± 0.38			
3b	9.88 ± 0.18	1.84 ± 0.48	10.78 ± 0.16							
4	11.43 ± 0.06	0.38 ± 0.14	9.70 ± 0.19	4.27	11.50 ± 0.02	0.38 ± 0.04	10.33 ± 0.06			
5	13.70 ± 0.22	2.36 ± 0.52	10.89 ± 0.13	1.29	11.63 ± 1.05	2.76 ± 0.65	11.00 ± 0.26			
6†	18.39 ± 0.22	0.95 ± 0.16	10.68 ± 0.26	0.96	18.11 ± 0.03	0.62 ± 0.05	10.66 ± 0.05			
7a	19.98 ± 0.51	1.17 ± 0.80	10.52 ± 0.34	1.48	19.46 ± 0.19	1.98 ± 0.20	10.83 ± 0.04			
7b	21.55 ± 0.08	0.52 ± 0.17	10.10 ± 0.32							
8a	23.06 ± 0.05	0.84 ± 0.05	11.17 ± 0.08	6.03	22.97 ± 0.01	0.32 ± 0.02	11.19 ± 0.06	22.97 ± 0.04	0.44 ± 0.06	10.13 ± 0.04
8b					23.19 ± 0.01	0.82 ± 0.02	11.87 ± 0.01	23.80 ± 0.16	0.16 ± 0.39	9.20 ± 0.30
9	23.74 ± 1.61	5.69 ± 0.88	11.10 ± 0.18	< 0.02						
10	24.59 ± 0.20	1.21 ± 0.30	10.96 ± 0.13	1.51	25.08 ± 0.03	0.51 ± 0.04	11.14 ± 0.06			
11a	26.35 ± 0.01	0.52 ± 0.02	10.77 ± 0.04	11.48	26.20 ± 0.01	0.24 ± 0.03	11.09 ± 0.05	25.71 ± 2.01	0.58 ± 0.94	9.60 ± 1.86
11b					26.41 ± 0.03	0.76 ± 0.02	11.74 ± 0.02	26.24 ± 0.13	0.31 ± 0.32	9.94 ± 0.84
12	37.00 ± 0.09	1.96 ± 0.12	10.45 ± 0.02	< 0.04						

Table 3.14: Component parameters derived from the absorption line modelling of κ Ori. See caption to Table 3.3 for further details.

	Ca II				Na I			K I		
Star/	$v_\odot$	b	log N		$v_\odot$	b	log N	$v_\odot$	b	log N
Cloud	(km s^{-1})	(km s^{-1})	(cm^{-2})	$\frac{\mathrm{Na}^\circ}{\mathrm{Ca}^+}$	(km s^{-1})	(km s^{-1})	(cm^{-2})	(km s^{-1})	(km s^{-1})	(cm^{-2})
κ Ori					S/N: 145; W_λ: 121.1 $\pm$ 0.3 mÅ			S/N: 85; W_λ: 5.1 $\pm$ 0.2 mÅ		
1					-4.83 ± 0.73	2.44 ± 0.57	10.49 ± 0.17			
2					-0.81 ± 0.18	2.21 ± 0.43	10.89 ± 0.12			
3					3.33 ± 0.15	2.46 ± 0.13	11.15 ± 0.03			
4†					14.95 ± 0.04	0.50 ± 0.04	10.27 ± 0.02			
5					16.79 ± 0.03	0.44 ± 0.03	10.77 ± 0.04			
6					17.76 ± 0.01	0.45 ± 0.02	11.34 ± 0.02	17.37 ± 0.05	0.17 ± 0.14	9.57 ± 0.07
7					18.86 ± 0.01	0.43 ± 0.02	11.50 ± 0.02	18.43 ± 0.12	0.03 ± 1.08	9.28 ± 0.89
8					20.25 ± 0.10	0.70 ± 0.04	11.87 ± 0.12	19.78 ± 0.64	0.62 ± 0.37	10.17 ± 0.62
9					21.05 ± 0.02	0.37 ± 0.05	11.38 ± 0.20	20.59 ± 0.92	0.54 ± 0.71	9.85 ± 1.27
10					21.32 ± 0.70	0.78 ± 0.46	11.34 ± 0.58			
11					23.45 ± 0.06	1.04 ± 0.06	11.04 ± 0.02			

3.3 Na°/Ca^{+} Abundance Ratios

It has long been recognised that interstellar absorption components display a very wide range of Na°/Ca^{+} ratios. This is primarily due to variations in the gas-phase abundance of Ca, governed by a balance between preferential Ca adsorption onto grain surfaces in quiescent dense environments, and removal from grain surfaces by shocks and sputtering in energetic environments (e.g. Jura, 1976; Barlow and Silk, 1977; Barlow, 1978; Phillips *et al.*, 1984). Although interpretation is complicated by the fact that Ca^{+} and Na° do not necessarily dominate in the same regions of an interstellar cloud (e.g. Barlow *et al.*, 1995), in those cases where an origin in the same cloud can plausibly be assumed the Na°/Ca^{+} ratio can yield information on the prevailing physical conditions (Crawford, 1992).

Na°/Ca^{+} ratios have been calculated for each of the clouds identified in these data (column 5, Tables 3.3 to 3.14). Where a single Na I component corresponds well to a single Ca II component, a Na°/Ca^{+} ratio is derived for the cloud. Where one or more Na I components correspond to one or more Ca II components a mean Na°/Ca^{+} ratio is given for the system as a whole. Error limits on the ratio are found by calculating the range of Na°/Ca^{+} ratios allowed within the error bounds of the Na° and Ca^{+} column densities. In the situation where a Na I or Ca II component has no corresponding Ca II or Na I component, lower and upper limits to the Na°/Ca^{+} ratio are given by calculating upper limits to associated absorption which may be present but undetected. Following Welsh *et al.* (1990) the 2σ upper limit to the equivalent-width, W_{λ}, of an undetected line is found assuming

$$W_{\lambda} \lesssim \frac{2\Delta\lambda\sqrt{N_{cont}}}{\mathrm{S/N}}, \tag{3.1}$$

where $\Delta\lambda$ is the width of one data pixel in Å, N_{cont} is the assumed width, in the continuum, of the undetected absorption-line in pixels, and S/N is the continuum signal-to-noise ratio of the observation. Here, the FWHM of a Ca II line has been taken to be 1.3 times larger than that of a corresponding Na I line (found through the comparison of all Ca II, Na I pairs in Tables 3.3 to 3.14) and the line-width in the continuum is taken to be 2.5 times larger than the FWHM. The column density of the line is then found assuming

$$N \lesssim 1.13 \times 10^{20} \frac{W_{\lambda}}{f\lambda^2}, \tag{3.2}$$

where f is the oscillator strength of the transition (see Table 2.8) and W_{λ} & λ are both

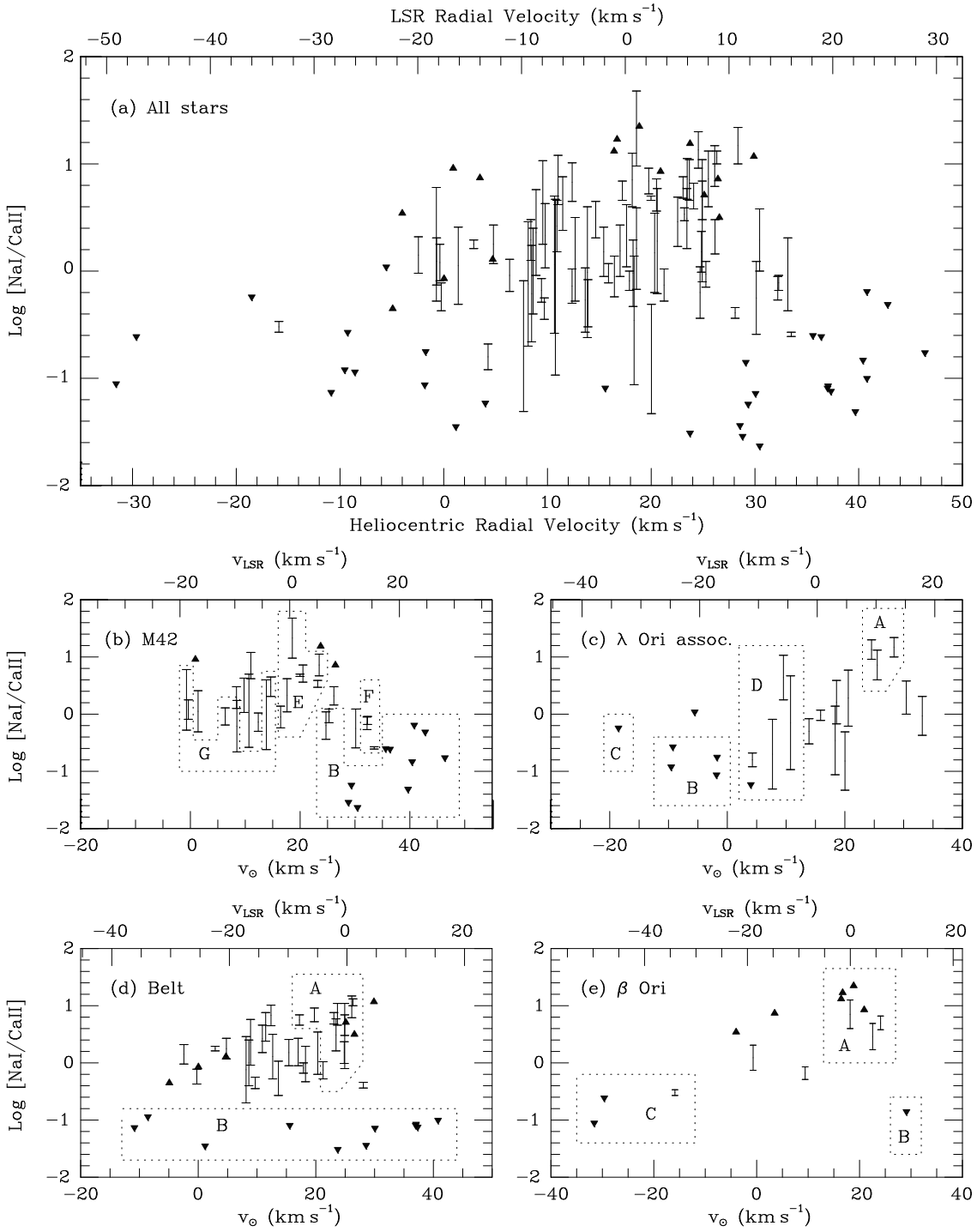

Figure 3.14: Na° to Ca^{+} column density ratios plotted as a function of radial velocity (upward and downward pointing triangles represent lower and upper limits, respectively). Fig 3.14(a) shows all clouds identified towards the Orion stars, Fig 3.14(b)–(e) display clouds identified in selected sightlines, and illustrate the broad groupings discussed in § 3.3. The groupings are complete in the most part; however, there are a small number of instances where it has not been possible to include points in their correct group.

given in Å (Cowie and Songaila, 1986). If an "undetected" line is present in a blended region, the upper limit derived for N may be slightly underestimated.

Figure 3.14(a) displays all calculated Na°/Ca^{+} ratios as a function of radial velocity (taken as a mean of the constituent components). Figures 3.14(b)–3.14(e) show similar individual plots for the M42 region, the λ Ori association, the Belt stars and β Ori, respectively. Velocities with respect to the Local Standard of Rest (LSR) and Sun are marked at the top and bottom of each figure, respectively.

When considering Fig 3.14(a) in terms of LSR radial velocities, a clear illustration of the fall-off of the Na°/Ca^{+} ratio with absolute radial velocity can be seen (Routly and Spitzer, 1952). However, while Routly and Spitzer (1952) surmised that clouds with small Na°/Ca^{+} ratios are preferentially found at larger absolute velocities, further investigation of Fig 3.14(a) shows such clouds to be distributed throughout the velocity range. The situation is therefore more likely to be that clouds with small Na°/Ca^{+} ratios possess a larger distribution of velocities. Furthermore, additional clouds characterised by low Na°/Ca^{+} ratios are likely to be present at low absolute velocities but simply masked by the much stronger absorption from the colder/denser clouds that generally occupy these velocities. A similar effect was noted by Crawford *et al.* (1989) in their study of the ISM towards the Sco OB1 association.

Anticipating discussions made in the following sections, many of the points in Figures 3.14(b)–3.14(e) have been collected together into broad groups of clouds possessing similar characteristics. These groups are labelled with letters, representing:

A) cold diffuse/partially molecular clouds
B) warm intercloud gas
C) possible mass-loss material
D) λ Ori shell material
E) M42 neutral lid
F) M42 foreground clouds
G) H II region(s) foreground to M42

An inspection of the average radial velocities of cold diffuse/partially molecular clouds with larger Na°/Ca^{+} ratios (group A), highlights a small systematic change in radial velocity. In the south, κ Ori exhibits its strongest Na I absorption around +20 km s^{-1}, in the Belt region this becomes +22 to +25 km s^{-1}, while it is at +25 km s^{-1} for the λ Ori

association. We feel that this may be understood in terms of the absorption arising within the neutral shell of material surrounding the Orion-Eridanus superbubble (e.g. Heiles, 1999) and is discussed below.

3.3.1 The Orion-Eridanus Shell

The observations of H I presented by Brown *et al.* (1995) reveal the presence of a large expanding shell of neutral material centred at the Galactic coordinates $(l, b) \approx (195°, -35°)$. The structure in known as the Orion-Eridanus shell, and it thought to have been produced by the ongoing stellar winds and successive supernovae explosions of stars in the Orion OB1 association (Reynolds and Ogden, 1979; Brown *et al.*, 1995; Heiles, 1999).

From figure 8 of Brown *et al.* (1995), we see that the line-of-sight to the southern Orion stars may indeed preferentially intersect lower velocity gas. This is consistent with our "group A" absorption largely arising in the neutral gas marking the boundary of the Orion-Eridanus shell. The projected line-of-sight velocity, v_p, of gas present in an expanding shell is given,

$$v_p = \pm \frac{V_0}{r_{\rm s}} \sqrt{R^2(\cos^2\theta - 1) + r_{\rm s}^2}, \tag{3.3}$$

where, V_0 is the shell's expansion velocity in km s^{-1}, $r_{\rm s}$ and R are the radius of the shell and distance to its centre in pc (e.g. Cleary, 1977). $\cos\theta$ is given by the expression,

$$\cos\theta = \sin b \sin b_0 + \cos b \cos b_0 \cos(l - l_0), \tag{3.4}$$

where l & b and l_0 & b_0 are the Galactic coordinates of the line-of-sight and the centre of the shell respectively.

A spherical shell located at a distance of 450 pc, centred at $(l, b) = (195°, -35°)$, with a radius of $\approx 22°$, a systemic velocity of +15 km s^{-1} and expanding at a rate of 40 km s^{-1}, does indeed show a reduction in the line-of-sight expansion velocity between the north and south of the constellation. Material in the near side of the aforementioned shell is expected to have velocities of +19.8 km s^{-1} in the line-of-sight to κ Ori (observed to have strong absorption around +20 km s^{-1}) and +26.6 km s^{-1} in the line-of-sight to λ Ori (observed to have strong absorption around +25 km s^{-1}). A change in velocity is also expected across the Belt stars, however, the shell velocities from Equation 3.3 are somewhat larger than those observed. Material in the line-of-sight to ζ Ori would be expected to have a velocity of +34.0 km s^{-1} (observed to have strong absorption around +23 to +26 km s^{-1}), while

for ϵ Ori this velocity is expected to be +36.9 km s^{-1} (observed to have strong absorption around +25 to +28 km s^{-1}). The absence of strong absorption towards stars in the M42 region and δ & β Ori are likely to be due to inhomogeneities in the shell.

In the model of the Orion region presented by Cowie *et al.* (1979), Barnard's loop is considered to be a H II region marking the inner edge of a dense, inhomogeneous shell of neutral material. The strong interstellar absorption components seen between +20 and +30 km s^{-1} in observations of Orion stars (e.g. Hobbs, 1969*a*, and now here) is then considered to be a result of this shell material. However, observations of stars both interior and exterior (on the sky) to Barnard's loop show similar absorption spectra. For example, our observations of λ and ϕ^1 Ori (exterior to Barnard's Loop) show good agreement with those of 23 Ori (interior to Barnard's Loop) presented by Welty *et al.* (1999). Furthermore, material present in an expanding shell outlined by Barnard's loop would be expected to possess radial velocities with a greater dependence on the line-of-sight probed (due to its smaller size), which is not seen. This is consistent with the model of the region presented by Reynolds and Ogden (1979, their fig 6) in which Barnard's Loop is one of the many loops and filaments associated with the H I shell marking the boundary of the much larger Orion-Eridanus superbubble.

3.4 Discussion

3.4.1 The M42 Region

M42 appears as a blister on the surface of OMC-1 and is generally assumed to be at a distance of 450 pc (e.g. Goudis, 1982). This makes it the closest bright H II region, and therefore the best spatially resolved object in its class. At the heart of M42 lies the Trapezium, four early-type stars designated θ^1 Ori A–D. In proximity to the Trapezium, Trumpler (1931) and Baade and Minkowski (1937) also noticed many fainter stars, which have been named the Trapezium cluster. It is the UV radiation produced by the Trapezium (primarily θ^1 Ori C) that creates the nebula's principal ionisation front, eroding into OMC-1, and in turn giving rise to the optical emission. Ionised material expands away from the ionisation front, with progressively higher ionisation stages being detected at higher velocities relative to the front (O'Dell *et al.*, 1993). Originally postulated by Zuckerman (1973), the idea of a 'neutral lid' lying across the face of M42, was advanced by O'Dell and Wen (1992, cf. their figure 7) using the 21-cm absorption-line observations by van der

Werf and Goss (1989). This lid itself possesses secondary ionisation fronts on both its near and far sides (O'Dell *et al.*, 1993, cf. their figure 3). On its far side, ionisation again comes primarily from θ^1 Ori C, however, emission from this region is observed to be much weaker than that from the principal ionisation front, placing the front 7 times further from θ^1 Ori C than the principle ionisation front formed against OMC-1 (Wen, 1993). On its near side, the ionisation source is ι Ori, $31'$ distant (corresponding to a linear distance of ≈ 4 pc at the distance of M42; see Table 3.2), located in the foreground to the neutral lid (O'Dell *et al.*, 1993).

Previous studies of the M42 region, such as the comprehensive investigation by O'Dell *et al.* (1993), have been able to generate three-dimensional models of the emission and absorption regions (cf. figure 3 of O'Dell *et al.*, 1993) but have relied on observations made at significantly lower resolutions. The resolution employed by O'Dell *et al.* (1993, 3.3 km s^{-1} FWHM) in their Ca II K observations of the Trapezium stars is unable to reveal the complex structure present in the UHRF data, and perhaps leads to an incomplete view of the absorbing medium in this direction. To supplement their data set, O'Dell *et al.* (1993) digitised Na I D_2 spectra of θ^1 Ori C and θ^2 Ori A from Hobbs (1978*a*) and included them in their analysis.

Here we discuss our ultra-high-resolution observations of Ca II K towards θ^1 Ori A, and both Ca II K and Na I D_1 towards θ^1 Ori C, θ^2 Ori A and ι Ori. The increased resolution employed by this study has shown many of the components analysed by O'Dell *et al.* (1993) in fact to be blends of multiple components. In a number of cases, components seen in the UHRF data are themselves thought to be blends of still narrower lines (discussed later).

In the case of the M42 region, a particular effort has been made to identify individual velocity systems. By comparing the absorption models constructed from line fitting, it has been possible to segregate the absorption into such systems, where absorption occurring in each system is thought to arise in an individual interstellar cloud sampled by more than one sightline. The absorption components comprising each system are shown in Figure 3.15 with identifiers of the form M$\boldsymbol{x}$, where 'M' denotes 'M42' (in order to reduce confusion with individual clouds), and $\boldsymbol{x}$ is a number which increases with the system's mean central velocity. Throughout the following discussion of M42, the reader is referred to Figure 3.16 which illustrates the line-of-sight velocity structure for the main absorbing systems in the direction of M42.

For the purpose of discussion, the material giving rise to absorption in this direction

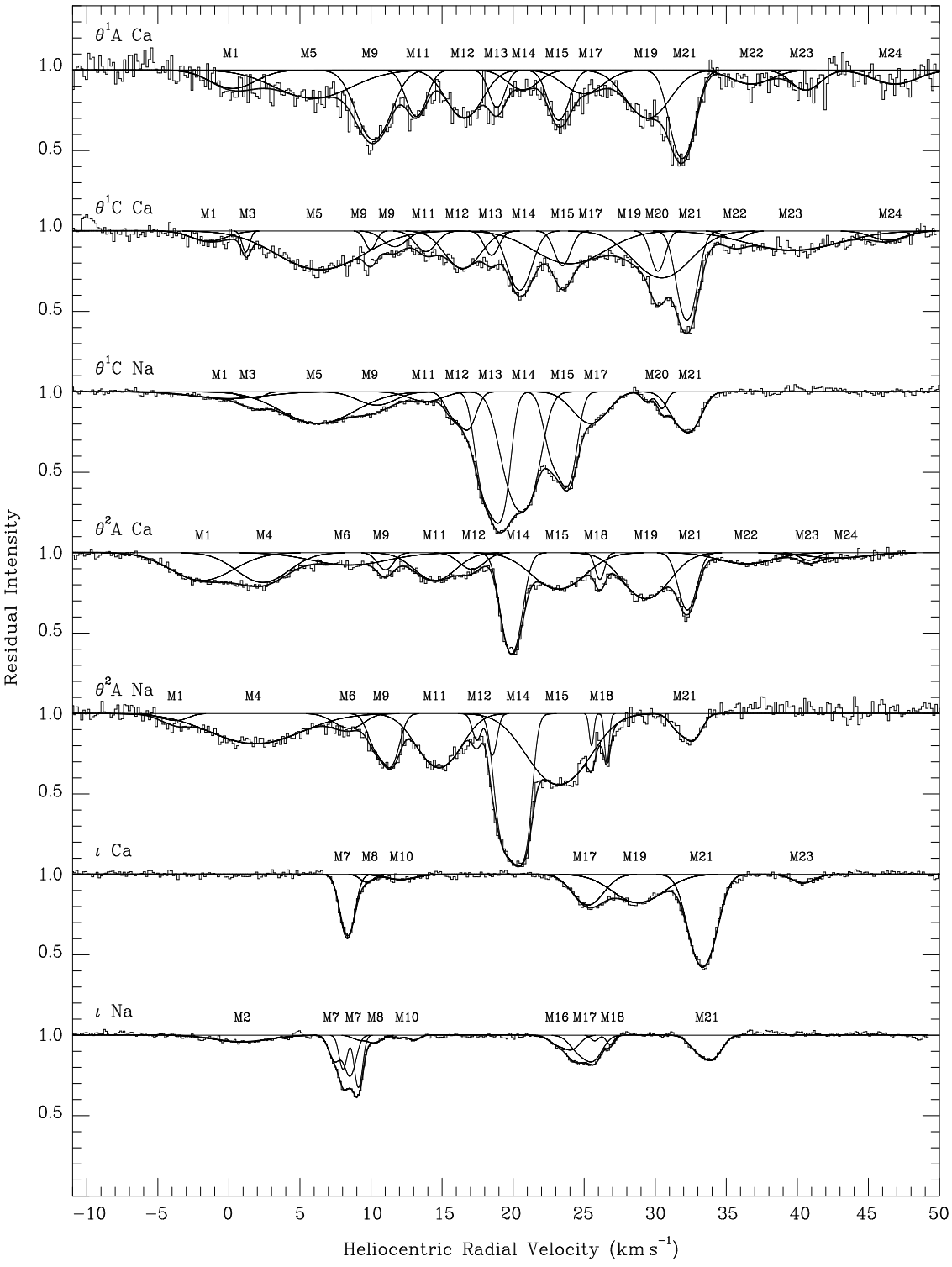

Figure 3.15: Absorption systems identified in the line-of-sight to the M42 region. Systems are numbered according to radial velocity and discussed in § 3.4.1. The components which constitute systems **M1 M9** & **M11** show a large amount of variation between sightlines, making their identification somewhat uncertain. Where an identifier is given more than once for a given spectrum, each component is associated with the particular absorption system.

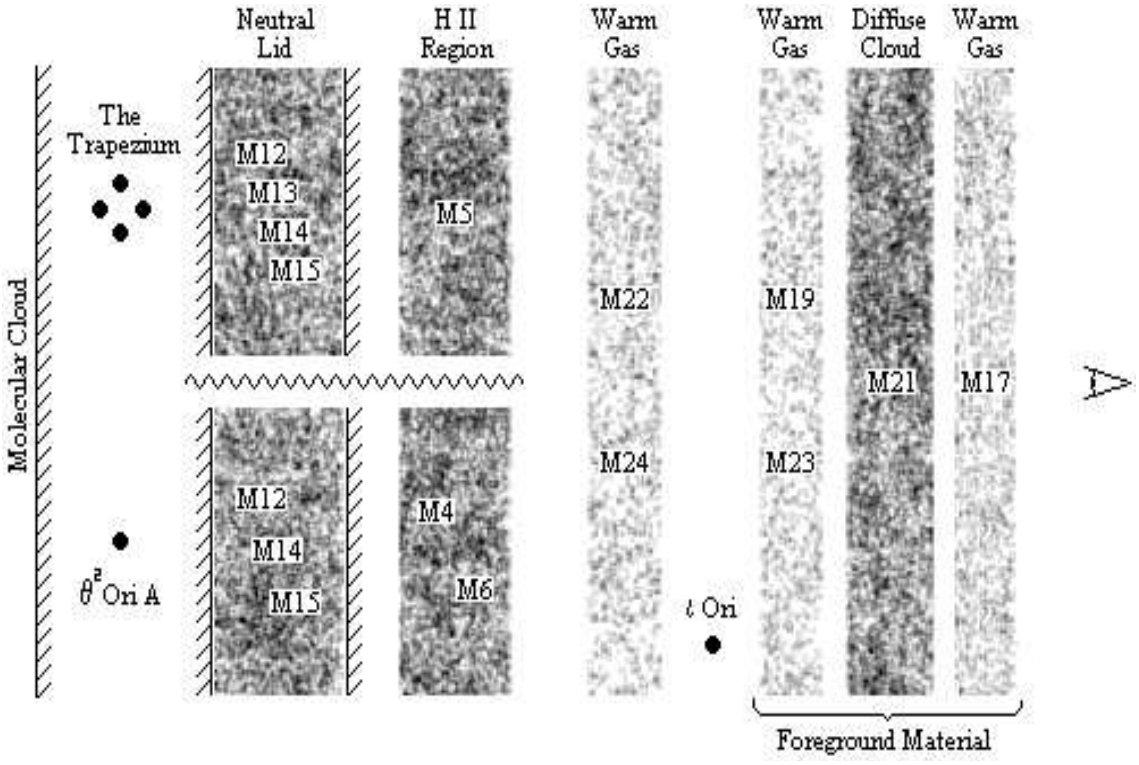

Figure 3.16: Line-of-sight velocity structure of the main absorption systems present in the direction of M42. Cloud boundaries marked with diagonal hatching are ionisation fronts. The sinusoidal line represents a transition in the line-of-sight absorption occurring towards the Trapezium stars and θ^2 Ori (e.g. see figure 1 of Peimbert, 1982). For simplicity, systems M**22** & M**24** and systems M**19** & M**23** are shown to be present in the same region, however they are not necessarily associated. System M**17** is located within 75 pc of the Sun while all other systems are beyond 75 pc. ι Ori is located $\approx$ 40 pc foreground to the Trapezium stars. Angular separations of θ^1 Ori A and θ^1 Ori C, θ^2 Ori A & ι Ori project to linear distances (at M42) of 0.03 pc, 0.3 pc and 4 pc respectively.

will be segregated into three main sections: § 3.4.1.1 will be devoted to the 'Neutral lid' (represented by group E in Figure 3.14); The 'Foreground H II region and secondary ionisation fronts' will be discussed in § 3.4.1.2 (represented by group G in Figure 3.14); and § 3.4.1.3 will discuss the 'Foreground Material' (represented by group F in Figure 3.14). The remaining components are subsequently discussed in § 3.4.1.4.

3.4.1.1 Neutral lid

The existence of the neutral lid was originally postulated by Zuckerman (1973) and later developed by O'Dell and Wen (1992) using observations made by van der Werf and Goss (1989) who identified three H I 21-cm absorption components at +16, +21 & +24 km s^{-1}

(which they label C, B & A respectively). These components are expanding away from OMC-1, which itself has a radial velocity of +27 km s^{-1} (Goudis, 1982). Component A corresponds to the H I in the envelope of OMC-1, component C is present in a layer between the ionisation front and the shock front which precedes it and component B is probably located between A and C (van der Werf and Goss, 1989). O'Dell *et al.* (1993) identify three absorption systems (none of which are detected towards all four of the Trapezium stars) at velocities of +15, +20 & +23 km s^{-1}, where ordering along the line-of-sight corresponds to that adopted by van der Werf and Goss (1989).

The observations obtained here clearly demonstrate the presence of several components towards each star, with discernible absorption in both Na I and Ca II occurring at velocities corresponding to the aforementioned H I 21–cm components. Here we detect four systems (numbered M**12**, M**13**, M**14** and M**15**), with velocities of $\approx$ +17, +19, +20 and +23 km s^{-1} respectively (see Figure 3.15). The ordering we adopt along the line of sight reflects that deduced by van der Werf and Goss (1989). None of these absorption systems are observed towards ι Ori, which displays an altogether less complicated spectrum, consistent with ι Ori being foreground to the neutral lid. We infer that H I components A & B correspond to our systems M**13**, M**14** & M**15**. The average Na°/Ca^{+} ratios measured for these systems being 21.4, 5.0 and 5.3 respectively (see § 3.3 and Tables 3.8 to 3.10), consistent with the partial depletion of Ca onto dust grains. System M**12** on the other hand, which we associate with H I component C (which van der Werf and Goss, 1989, locate between the ionisation and shock fronts), possesses a much lower Na°/Ca^{+} ratio of $\approx$ 1.5. Although a shock velocity of $\approx$ 5 km s^{-1} is insufficient to remove adsorbed Ca from grain surfaces (e.g. Barlow, 1978), the low Na°/Ca^{+} ratio suggests there to be little depletion.

The neutral lid absorption detected towards the two Trapezium stars, θ^1 Ori A & C, appears well correlated between both stars in Ca II and between Na I and Ca II towards θ^1 Ori C. Comparison of this absorption with that seen towards the 2.5′ distant (projecting to a linear distance of 0.3 pc) θ^2 Ori A, while revealing some similarity, also reveals clear differences. This is consistent with the view of the region depicted by Peimbert (1982, cf. their figure 1), where both θ^2 Ori A and the Trapezium stars possess a shroud of neutral material, but are however segregated. Thus, the neutral lid components observed in each direction would not be expected to be identical. System M**12** is observed towards each of the stars although it appears slightly narrower and weaker towards θ^2 Ori A. The

cloud observed at $\approx +20$ km s^{-1} towards θ^2 Ori A (in both Na I and Ca II), is located between the velocities of systems M**13** & M**14** observed towards the Trapezium stars. We associated it with system M**14**, which possesses a similar Na°/Ca$^+$ ratio. This leaves system M**13**, with its large Na°/Ca$^+$ ratio, only present towards the Trapezium.

The Na I and Ca II components detected towards θ^2 Ori A at a velocity of 23.2 km s^{-1} possess both a velocity and Na°/Ca$^+$ ratio compatible with their association with system M**15** as observed towards θ^1 Ori A & C; however, their broad nature is inconsistent with cool H I gas (van der Werf & Goss estimate the H I spin temperature of this gas to be only ≈ 25 K, with a factor of 2 uncertainty) and we therefore suggest them to be the result of a blend of closely spaced, unresolved components, each arising within the neutral lid.

3.4.1.2 Foreground H II region and secondary ionisation fronts

As discussed earlier, the neutral lid is itself thought to possess secondary ionisation fronts on both its near and far sides. On its far side, emission from [O III] and [S III] is detected at $\approx +12$ km s^{-1}, while on its near side emission from [O II] and [O III] has been detected at a velocity of $\approx +3$ km s^{-1} (O'Dell *et al.*, 1993). While O'Dell *et al.* (1993) were unable to detect Ca II absorption arising in the far side secondary ionisation front in their own spectra, they do associate a Na I component observed towards θ^2 Ori A (from the spectra of Hobbs, 1978*a*) with this region. With regards to the near side secondary ionisation front, O'Dell *et al.* (1993) detect Ca II absorption towards θ^1 Ori A & B and θ^2 Ori A, with Na I absorption towards θ^2 Ori A also inferred.

In our observations, many components are identified below a velocity of $+15$ km s^{-1} (see Figure 3.15). In general, good agreement is seen between Na I and Ca II on a given sightline; however, less correlation is found between the Trapezium stars and θ^2 Ori A. These differences, coupled with the absence of similar components towards ι Ori, suggest the absorption to be arising in proximity to M42. The differences in cloud distributions between the Trapezium stars and θ^2 Ori A in this velocity range (echoed by the neutral lid absorption discussed in § 3.4.1.1), again suggests θ^2 Ori A to be disconnected from the Trapezium stars. At the core of M42 is the Orion Bar, a region of enhanced Hα emission running from the northeast to the southwest, passing between the Trapezium stars and θ^2 Ori A with a separation of only $30''$ from θ^2 Ori A. The Bar is considered to be an ionisation front viewed edge-on (Balick *et al.*, 1974), again suggesting the presence

of a transition in the line-of-sight absorption occurring between the Trapezium stars and θ^2 Ori A. The Bar may be seen in the frontispiece (located at the front of this thesis) where it appears as a defined ridge in the nebulosity, running diagonally across the bottom left of the image (for details regarding the frontispiece please refer to the Acknowledgements). A clearer impression of the Bar may be gained from [O I] λ6300Å imagery presented by Goudis (1982, pg. 92, figure 2.1.9, after Münch and Taylor (1974)).

Many of the components with velocities less than $\approx +15$ km s^{-1} are seen to be very broad, a signature of relatively high temperature and/or highly turbulent gas. However, the b-values measured for many of these components imply temperatures in excess of 7000 K (about where collisional ionisation of Na° is expected to become important; Pottasch, 1972) suggesting possible unresolved substructure to be present. As pointed out by O'Dell *et al.* (1993), the second and third ionisation energies of Ca are 11.9 & 50.9 eV respectively, making Ca^{++} the dominant ionisation stage in the H II region. However, the high electron density in denser parts of the H II region (from H ionisation) will enhance the recombination rate of Ca^{++} to Ca^{+}, perhaps compensating for the higher photoionisation rate. Similarly Na has first and second ionisation energies of 5.1 & 47.3 eV so that Na^{+} will be the dominant ion stage of Na in H II regions as well as in neutral clouds. O'Dell *et al.* (1993) therefore suggest that either narrower lines, formed in a much cooler photodissociation region, or broader lines arising within an ionised zone, may be observed. This being the case, many of the components seen in this velocity range could be due to secondary ionisation fronts or the foreground H II region itself. The low Na°/Ca^{+} ratios suggest the gas to be disturbed, with Ca returned to the gas phase, while a poor correlation between sightlines is a signature of small-scale structure; neither of which would be unexpected for such a highly dynamic region of the ISM.

Absorption from He I at 3889Å arises from the metastable 2^3S state and is likely to come from the ionised zone. He I absorption components observed towards each of the Trapezium stars, at a radial velocity of $\approx +3$ km s^{-1}(Oudmaijer *et al.*, 1997; O'Dell *et al.*, 1993), correspond reasonably well to the broad system M**5** towards θ Ori A & C (Figure 3.15). Additional observation of θ^2 Ori A by O'Dell *et al.* (1993) suggests the He I absorption towards this star to be composed of two narrowly spaced components at ≈ -3 & $+5$ km s^{-1}. This is echoed in our systems M**4** & M**6**. Although we detect a velocity shift of ≈ 3 km s^{-1} between our observations and those of He I, the very broad nature of the He I line shows this to be small. We therefore associate systems M**4**, M**5** & M**6**

with foreground ionised gas, which according to the model of O'Dell *et al.* (1993) would be located on the near side of the neutral lid.

The components which constitute system M**1** and system M**11** show a large amount of variation between sightlines, making their association rather uncertain, and possibly indicating the absorption to arise in the M42 region. They have somewhat larger Na°/Ca^{+} ratios than observed for warm interstellar clouds. These systems possess velocities similar to the near and far ionisation fronts identified by O'Dell *et al.* (1993, $+3$ & $+12$ km s^{-1} respectively), such that system M**1** may come from the near secondary ionisation front, while system M**11** may be associated with the far secondary ionisation front.

3.4.1.3 Foreground material

Spectra of ι Ori show the line-of-sight to this star to intersect far fewer absorbing clouds than those toward the θ^1 & θ^2 Ori stars. This is consistent with a location for ι Ori foreground to M42 (and the neutral lid), compatible with the view of O'Dell *et al.* (1993). It also suggests that the majority of the absorption detected towards the θ^1 & θ^2 Ori stars occurs in the vicinity of M42. Indeed, extended sightlines free from interstellar material are not uncommon.

Observations of ι Ori can be used to identify intervening absorbing material, such as the Na I and Ca II absorption of system M**7**, at a velocity of $\approx +8.4$ km s^{-1}. There is evidence that the Na I component is actually double, and it has been modelled as such; however, the Ca II counterpart can be (and has been) accurately modelled with a single component. O'Dell *et al.* (1993) associate this system (as seen in ≈ 8 km s^{-1} FWHM-resolution observations made by Adams, 1944) with absorption centred at $+6.8$ km s^{-1} on the neighbouring sightlines to the more distant θ^1 Ori stars. In this study we find the absorption collected together by O'Dell *et al.* (1993) in their $+6.8$ km s^{-1} system to be composed of components with an array of line widths and column densities, over a range of velocities. We can make a tentative connection between the foreground system M**7** and system M**9**. The overall Na°/Ca^{+} ratio of system M**9** is 3.1 (1.2 towards θ^1 Ori C; 7.1 towards θ^2 Ori A), larger than generally measured for the systems below a velocity of $\approx +15$ km s^{-1} (largely attributed to absorption arising within a foreground H II region; see § 3.4.1.2), suggesting that the absorption may not be associated with the M42 region.

Systems M**8** & M**10** are only detected towards ι Ori. The very weak nature of both systems means that they would be difficult to detect in the more complex spectra of the

other stars.

Two other weak Na I components are detected in the spectrum of ι Ori, those of systems M**16** & M**18**. In the case of system M**16**, corresponding components are rendered undetectable in the spectra of other M42 stars due to the much stronger neutral lid absorption at these velocities. In the case of system M**18**, an association can be made with narrow Na I and Ca II components seen towards θ^2 Ori A but undetected towards the remaining stars.

System M**17** is not detected towards θ^2 Ori A, but is observed towards each of the other stars in both Na I and Ca II. Its absence from the spectrum of θ^2Ori A may be due to a significant amount of blending with the neighbouring (in velocity space) neutral lid components (discussed in § 3.4.1.1). System M**17** is characterised by fairly broad components with a low Na°/Ca^+ ratio. This suggests that the absorption arises in warm gas, thereby maintaining a significant amount of gas-phase Ca. Observations of γ Ori, which is located 12° away on the sky and at a Hipparcos distance of only 75 pc (ESA, 1997), have been made in Na I (Welsh *et al.*, 1990), revealing one component at a velocity of +25.8 km s^{-1}, but revealing four components between +15 and +30 km s^{-1} in Ca II (Vallerga *et al.*, 1993). Comparison of these components with those seen in our UHRF data suggests that system M**17** arises in the same cloud seen towards this foreground star, thus locating the system within 75 pc of the Sun.

System M**19** shows up as Ca II absorption seen towards each of the targets, although we note that the parameters characterising the component towards θ^1 Ori C, appear to give larger values of $v_\odot$, b and N compared to corresponding components in the other sightlines/ions. The broad nature of this system, coupled with its very low Na°/Ca^+ ratio mean that the absorption is likely to arise in foreground warm intercloud medium.

System M**21** can be confidently classed as a foreground diffuse cloud. Its constituent components exhibit excellent agreement between all the sightlines. The system is composed of relatively narrow components and possesses a fairly small mean Na°/Ca^+ ratio (≈ 0.6). The absence of similar absorption in the spectrum of the foreground star γ Ori, signifies that the cloud is likely to be located beyond a distance of 75 pc. We note that it has a relatively high radial velocity and feel that it is the main constituent of the +31 km s^{-1} system identified by O'Dell *et al.* (1993).

Above a velocity of $\approx$ +35 km s^{-1}, only Ca II absorption is detected, consistent with the findings of Routly and Spitzer (1952), whereby smaller Na°/Ca^+ ratios are found at

larger absolute LSR velocities. Systems M**22** & M**24** are observed towards θ^1 Ori A & C and θ^2 Ori A, and are thus likely to be located between ι Ori and the Trapezium stars, while system M**23** is also observed towards ι Ori and is thus located in the foreground. Due to their generally broad nature, and the lack of associated Na I absorption, each of these systems is likely to arise in the warm intercloud medium. These three systems comprise the +39 km s^{-1} system identified by O'Dell *et al.* (1993), which they inferred to have associated Na I absorption in the case of θ^1 Ori C. However, as will be discussed in § 5.2.5, we believe that this putative Na I component is likely to be telluric absorption in the original spectra of Hobbs (1978*a*).

3.4.1.4 Remaining Components

System M**2**, observed towards ι Ori, is unusual in that it consists of a very broad Na I component with no associated Ca II detectable here. The observation reported by Welty *et al.* (1994) echo the detection of Na I while those of Welty *et al.* (1996) show associated weak Ca II absorption to also be present at this velocity. Although rather weaker, this system bears some resemblance to system M**4**, observed towards θ^2 Ori A (discussed in § 3.4.1.2) and highlights the possibility that some of the absorption at this velocity may occur in the foreground, rather than being wholly associated with M42. Under the assumption of zero turbulence, this component is found to have a kinetic temperature of $\approx 10^4$ K, perhaps indicating the presence of highly blended substructure.

System M**3**, only observed towards θ^1 Ori C, is composed of narrow components in both Na I and Ca II, indicative of cold absorbing gas. Under the assumption of no internal cloud turbulence, a rigorous upper limit of 312 K can be placed on the kinetic temperature of the Ca^+ absorbers. This may indicate that the absorption arises in a compact knot of material small enough not to intersect neighbouring sightlines

System M**20** is blended between systems M**19** & M**21** and has only been confidently identified towards θ^1 Ori C where narrow components are observed in both Na I and Ca II. Possible asymmetry in system M**21** absorption towards θ^1 Ori A suggests there may also be a counterpart present towards this star as well. No corresponding absorption is seen towards θ^2 Ori A, thus locating system M**20** over the face of the Trapezium.

3.4.2 The λ Ori Association

UHRF observations and model fits for λ and ϕ^1 Ori, both of which are located in the λ Ori association, are presented in this chapter (Figures 3.4 & 3.5 and Tables 3.5 & 3.6). A comparison of the Ca II and Na I absorption occurring in the two sightlines has been used to identify individual clouds present in this direction.

A more detailed analysis of the ISM in the direction of the λ Ori association will be presented in Chapter 4, utilising additional lower-resolution ($R = 110,000$) observations of a number of targets with locations in and around the λ Ori association.

3.4.3 The Belt Region

Orion's Belt is composed of the three bright supergiant stars (from west to east) δ, ϵ and ζ Ori. Also discussed in this section is the O9.5 V star σ Ori, located $50'$ to the south of ζ Ori (projecting to a linear separation of 3 pc at a distance of 300 pc) and responsible for sculpting the Horsehead nebula. The Horsehead is found to have a radial velocity of $+28$ km s^{-1} (Milman *et al.*, 1975), and is located $35'$ to the east of σ Ori. The destructive UV radiation from the σ Ori system produces the ionisation of the H II region IC 434, against which the Horsehead appears in silhouette (see fig 5.1.1 of Goudis, 1982, for a map of the region). ζ Ori is located on the western edge of the Orion B cloud and, although very close on the sky to the nebula NGC 2024 (Orion B), it is thought to be in the foreground (at a distance of ≈ 250 pc; Table 3.2), and not to play a significant part in its ionisation (Goudis, 1982). The interstellar absorption towards both δ and ζ Ori has been found to exhibit temporal variability, as discussed in § 5.2.

With the exception of δ Ori, each of these stars exhibits strong Na I absorption, with generally large Na°/Ca$^+$ ratios, around a velocity of $+25$ km s^{-1}. In each case the absorption is found to be complex, and split into two separate systems. Although the Na I absorption towards ϵ Ori is blended into a single multi-component feature, the weaker Ca II lines clearly show the presence of two features. Corresponding absorption in K I (ϵ & ζ Ori), and in molecular hydrogen at these velocities (Spitzer and Morton, 1976; Jenkins and Peimbert, 1997; Jenkins *et al.*, 2000), coupled with the large Na°/Ca$^+$ ratios, leads to the conclusion that this absorption is due to foreground cool, diffuse clouds containing a small amount of molecular material. The broad similarities between these sightlines are consistent with the presence of an inhomogeneous layer of material overlying the area as

a whole, the radial velocity of which is in agreement with that of the Orion-Eridanus shell (Brown *et al.*, 1995).

Additional strong, narrow Na I absorption is also observed towards ϵ & ζ Ori at lower velocities. Similar components are not generally seen towards the other Orion stars and are possibly only associated with the Belt region. The strongest of these is cloud 5 towards ϵ Ori at a velocity of $\approx +11$ km s^{-1}. However the H I observations by Brown *et al.* (1995) do not rule out the presence of Orion-Eridanus shell material at these velocities in these sightlines.

H I observations made by Chromey *et al.* (1989) show the presence of an expanding shell in the Belt region, centred around σ Ori. The near and far sides of the σ Ori shell possess radial velocities of $\approx +22$ and $+37$ km s^{-1} respectively although the exact locations of the stars with respect to the shell are not known. Chromey *et al.* (1989) propose the shell material to be partially molecular, suggesting that some of the strong absorption that we observe around $+25$ km s^{-1} possibly arises in the near side of this shell. The velocity of the shell's far side coincides with the absorption seen around $+37$ km s^{-1} towards each of the Belt stars (discussed below). However, the low Na$^{\circ}$/Ca^{+} ratios measured for this absorption are not consistent with partially molecular gas and suggests that the stars lie in the foreground to the shell. In this case, the broad Ca II absorption observed at a velocity of $\approx +37$ km s^{-1} towards each of these four stars can be considered to arise from warm intercloud material. Although not detected towards δ Ori in our low S/N Ca II observation, absorption can be seen at this velocity in the lower resolution but higher S/N observation of Welty *et al.* (1996). This system may be associated with the similar absorption observed towards the M42 region (system M**23**, § 3.4.1.3).

The lowest-velocity broad Ca II absorption seen towards the Belt stars is also thought to originate from the warm intercloud medium. However, in the case of the sightline towards ζ Ori, Jenkins and Peimbert (1997) have inferred the presence of a standing bow shock using observations of H_2. Shifts in both the central velocity, and broadening detected for absorption from successive rotational levels of the H_2 molecule, are interpreted as being the result of H_2 forming in two separate regions behind the standing bow shock (Jenkins and Peimbert, 1997). Absorption from the lower rotational levels is considered to arise in cold, compressed gas (where H_2 is formed via grain surface reactions), while that from higher rotational levels is thought to come from much warmer gas closer to the shock front (where H_2 is produced through gas phase reactions).

The H_2 absorption arising from the lower rotational levels ($J = 0$ and 1) corresponds well with our observation of cold (variable) Na I and K I absorption, cloud 2e†. The temperature-turbulence analysis performed on this cloud in § 6.1 using Na I and K I components has shown the upper-limit of T_k to be 293 K, very similar to the upper limit which can be calculated from the corrected (cf. footnote b, table 6 of Jenkins and Peimbert, 1997) broadening of H_2 ($J = 0$) which yields $T_k < 289$ K. If the Na I and H_2 absorption is indeed occurring from the same region, a temperature-turbulence analysis for the two lines (as described in § 6.1) shows $1 < T_k < 289$ K while $0.02 < v_t < 0.32$ km s^{-1}. Similarly, H_2 absorption from the higher rotational levels ($J = 2$ to 5), which Jenkins & Peimbert attribute to gas with $T_k = 6500$ K, corresponds well with the broader Na I and Ca II components of our cloud 2c.

3.4.4 β Orionis

With V = 0.28, the B8 Ia star β Orionis (Rigel) is the brightest star in the constellation. β Ori is located at the western foot of Orion, just beyond the confines of Barnard's loop. The presence of strong photospheric Ca II absorption has created some uncertainty as to the location of the continuum level (noted in § 2.2.5), and therefore the true interstellar absorption contribution.

Numerous studies have revealed β Ori to be undergoing mass loss ($\dot{M} \approx 1.1 \times 10^{-6}$ $M_\odot$yr^{-1}; e.g. Barlow and Cohen, 1977), while Hα observations made by Israelian *et al.* (1997) have detected both the outflow and infall of material, at a range of velocities, interpreted by those authors as moving through closed magnetic loops around β Ori. The Ca II spectrum observed towards β Ori (Figure 3.2) is rather unusual in that it exhibits strong absorption out to a velocity of -35 km s^{-1}. With a stellar radial velocity of $+20.7$ km s^{-1} (Wilson, 1953), these components have outflow velocities of up to 55 km s^{-1} with respect to β Ori, and are likely to be a result of the ongoing mass loss. The very low Na°/Ca$^+$ ratios measured for the Ca II components below a velocity of -10 km s^{-1}, support a circumstellar origin. Furthermore, the line widths characterising the optimised Ca II model components imply gas with temperatures (under the assumption of zero turbulence) of 1200 K $< T_k <$ 8200 K.

Although the absorption components at ≈ 0 & $+10$ km s^{-1} may arise in either the warm ISM or the circumstellar environment of β Ori, the unusually strong, discrete appearance of the components, coupled with possible variability (discussed in § 5.2.4), argues for a

circumstellar origin.

The Na I spectrum of β Ori also appears to be somewhat unusual, reaching only ≈ 0.8 of the continuum intensity (although it should be noted that β Ori also possesses the weakest Ca II K absorption of the stars observed), while sightlines towards ζ and κ Ori (located at similar distances) exhibit much stronger absorption. Between velocities of +15 & +25 km s^{-1}, each Na I component is found to possess larger Na°/Ca^{+} ratios (≈ 10), consistent with an origin within diffuse interstellar clouds, where Ca is depleted onto grain surfaces. For example the cold ($T_{\rm k} < 67$ K) Na I component at +18.85 km s^{-1}, although close to a broader neighbouring component ($v_{\odot} = +18.40$ km s^{-1}) displays clear hyperfine splitting (hfs) with little or no associated Ca II absorption. Although broader, and possibly the result of a blend of narrower lines, Na I component 9 also possesses little or no associated Ca II absorption.

Detected in Ca II, cloud 15 possesses little or no associated Na I absorption and is located at a velocity of +29.12 km s^{-1} (i.e. travelling towards β Ori). This cloud is therefore likely to have an interstellar origin, within the warm intercloud medium, rather than the circumstellar environment.

3.4.5 κ Orionis

κ Ori is located at the southern tip of the Orion A cloud, which is part of the southern molecular cloud complex and outside the confines of Barnard's loop. Observations of both Na I and K I have been obtained for this star. Parameters derived from absorption-line modelling of the available data have been used in § 6.2.4 to derive limits on $T_{\rm k}$ and $v_{\rm t}$ for four clouds. Ca II observations of κ Ori were obtained by Welty *et al.* (1996) at a resolution of 1.20 km s^{-1} FWHM, and comparisons with our Na I & K I observations indicate the absorption towards this star to be contained within three broad velocity bands.

Below a velocity of +10 km s^{-1}, Welty *et al.* (1996) detect six broad Ca II components, three of which are present at velocities corresponding to Na I components detected here. The radial velocities of these components render the clouds blue-shifted with respect to κ Ori by between 12 and 30 km s^{-1}. These components may arise from shell material around κ Ori. The measured Na°/Ca^{+} ratios are seen to be lower for absorption at larger negative velocities. An H_2 component observed at +1.7 km s^{-1} by Spitzer and Morton (1976), indicates some of the absorption in this blended region to arise in relatively dense gas.

The very strong Na I absorption present between +15 and +25 km s^{-1} is associated with little Ca II absorption, generating much larger Na°/Ca^{+} ratios. Observations of H I by Hobbs (1971) show very strong 21–cm emission around +20 km s^{-1}, while the observations of Spitzer and Morton (1976) indicate some absorption from molecular hydrogen to be present at this velocity and possibly +24 km s^{-1}. This suggests these components to be the result of diffuse clouds with some associated molecular material.

While we have not detected Na I absorption above a velocity of +25 km s^{-1}, Welty *et al.* (1996) identify four broad Ca II components at these more positive radial velocities, characteristic of warm, intercloud gas.

3.5 Conclusions

The data presented here represent the highest resolution interstellar line observations obtained for many of the targets. Our observations of stars located within the Orion Nebula (a region not previously studied at such high resolution) have revealed two or three times as many absorption components as previously identified by Hobbs (1978*a*); O'Dell *et al.* (1993); Welty *et al.* (1996). Our ultra-high-resolution data have thus enabled a much more accurate perspective to be obtained of the absorbing medium in this direction, and highlight the necessity for ultra-high-resolution/high signal-to-noise observations when studying the diffuse ISM.

The UHRF data have enabled the identification of many individual interstellar clouds, for which Na°/Ca^{+} ratios have been obtained (§ 3.3). An examination of these Na°/Ca^{+} ratios provides an indication of the physical conditions prevailing within each cloud, and shows the presence of distinct groups, which are utilised in the analysis of the ISM in this direction.

Overall, we detect a small velocity gradient in the location of strong Na I absorption over the region (discussed in § 3.3). This is consistent with this absorption arising in the neutral gas marking the boundary of the Orion-Eridanus superbubble which shows a similar trend in H I observations made by Brown *et al.* (1995, cf. their figure 8.).

Observations of closely spaced targets in the M42 region (§ 3.4.1) have been used to discern the likely line-of-sight velocity structure. Differences in the absorption line profiles of θ^1 Ori A and θ^2 Ori A suggest that although both stars are located in M42, they are segregated; specifically, the neutral lid material, which shrouds the region, undergoes a

transition between the sightlines. This conclusion agrees with that of Peimbert (1982, cf. their figure 1).

Chapter 4

The λ Ori Association[1]

Using UHRF observations of λ Ori and ϕ^1 Ori (already presented in Chapter 3), along with further high resolution ($R \approx 110,000$) observations made with the 74-inch Mount Stromlo Telescope, the interstellar sightline toward the λ Ori association will be investigated.

4.1 Introduction

The O8 III star λ Orionis is located at the centre of the spherically symmetric H II region S264 (Sharpless, 1959), making it a good example of a classical Strömgren sphere. S264 is in a state of expansion (Mathews, 1965; Lasker, 1966) and is interior to expanding rings of molecular gas (Lang *et al.*, 2000; Maddalena and Morris, 1987) and dust (Zhang *et al.*, 1989). Also located within the boundaries of S264 is the B0 IV star ϕ^1 Orionis whose angular separation of $27'$ projects to a linear distance of ≈ 2.5 pc at the distance of the association (Table 3.2). Their similar location is reflected in their similar interstellar spectra.

The molecular gas, observed in CO, is some 10° in diameter (Maddalena and Morris, 1987), or ≈ 57 pc if we adopt a distance to λ Ori of 324 pc (Table 3.2). Kinematical models of this ring constructed by Maddalena and Morris (1987) suggest it to have a central radial velocity of +21.2 km s^{-1}, to be tilted by 36.4° to the line-of-sight, and to be expanding at a rate of 14.3 km s^{-1}; however, the more sensitive observations made by Lang *et al.* (2000) show that the inclination, and therefore the expansion velocity are uncertain. The

[1] Part of the work presented in this chapter has been previously published in Price *et al.* (2001*a*)

rings present size and velocity suggest its expansion started 2.4×10^6 years ago, consistent with an estimated age for λ Ori of 2–4 Myr (Murdin and Penston, 1977).

The radial velocity and proper motion of λ Ori have been measured to be ≈ 33.5 km s^{-1} and ≈ 2.13 mas yr^{-1} respectively (Wilson, 1963; Boss, 1937); however, Maddalena and Morris (1987) note that this is inconsistent with λ Ori being at the centre of the association throughout its evolution. Maddalena and Morris (1987) suggest a number of solutions to this problem, including the recent acceleration of the star through either a close encounter with another star or the expulsion of a stellar companion.

The dust ring seen by IRAS appears well defined, less elliptical and centred on λ Ori (Zhang *et al.*, 1989). As argued by Zhang *et al.* (1989), on the grounds of energy input, the ring-like appearance is quite probably the result of a projection effect of a shell (radius ≈ 30 pc, thickness ≈ 1 pc) since the outer edges of a shell, viewed tangentially, will possess column densities more readily observable than those seen radially. If the gas and dust were in the form of rings (not intersected by the line-of-sight) no detectable absorption would be produced in the spectra of the central stars, contrary to the observed strong absorption seen in Ca II and Na I towards λ & ϕ^1 Ori, discussed below. The powerful stellar wind generated by λ Ori once it reached the main sequence is believed to have produced a shell of swept-up material. According to Bergoffen and Van Buren (1988), during the early stages of the expansion, the shock velocity should have been sufficient to remove material from grain surfaces; gas present in the shell should therefore exhibit lower Na°/Ca^+ ratios.

4.2 The Observations

Ultra-high-resolution observations of both λ and ϕ^1 Ori have already been presented in Chapter 3, along with their best-fitting model parameters and absorption line profile models (Tables 3.5 & 3.6 and Figures 3.4 & 3.5). To supplement these data, further high-resolution ($R = 110,000$) observations of a number of targets with locations in and around the λ Ori association have been made with the Mount Stromlo echelle spectrograph (hereinafter MSES; the instrument and observing procedures are discussed in Chapter 2). The locations of these stars in relation to the molecular and infrared emission is displayed in Figure 4.1.

These new data consist of Na I D_1 & D_2 observations of twelve stars (including the re-observation of λ Ori) with further observations of Ca II H & K made to a selection of

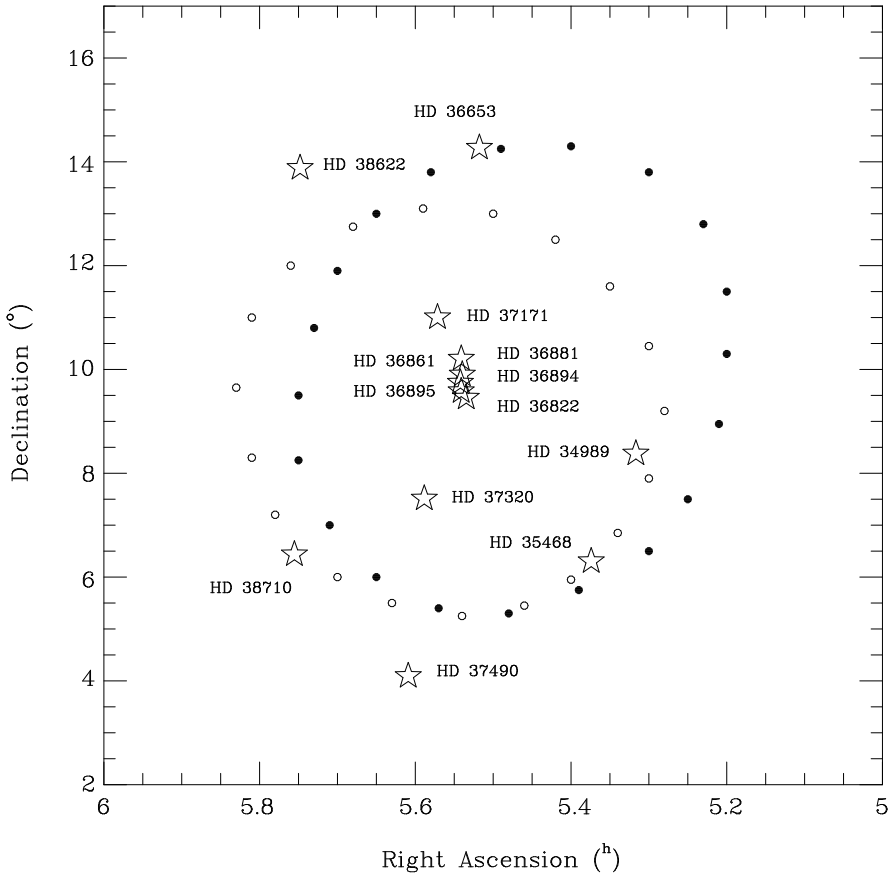

Figure 4.1: Positions of the targets observed in the λ Ori association (J1950.0). The solid circles indicate the location of the dust ring as modelled by Zhang *et al.* (1989). The open circles indicate the location of the CO ring as modelled by Maddalena and Morris (1987).

these targets. These data have been modelled in the usual manner, however the presence of possible stellar absorption towards a number of targets has required additional consideration (discussed in § 4.2.1 below). The resulting line-profile parameters, heliocentric radial velocity, $v_{\odot}$, velocity dispersion, b, and column density, N, are listed in Tables 4.2 to 4.13, along with the 1σ, single-parameter errors. In the case of Na I, $v_{\odot}$ corresponds to the weighted mean velocity of the two hyperfine split components. Where observations of both Na I and Ca II are available, values of Na°/Ca^{+} abundance ratios are obtained; however, due to a significant amount of blending, these values are somewhat uncertain. The corresponding best-fitting model profiles, after convolution with the instrumental response function, are shown in Figures 4.2 to 4.15, overplotted on the observed line profiles.

4.2.1 Stellar Line Removal

Many of the targets observed here are B-type stars which are known to exhibit stellar absorption with varying strengths (e.g. Crawford, 1990); however, in many cases, large projected rotational velocities ($v \sin i$; listed in column 10 of Table 4.1) broaden the stellar line sufficiently to act as the local continuum (i.e. the width of the stellar line at the continuum is significantly larger than the range over which interstellar absorption is present). For the remaining stars with small or unknown rotational velocities, an analysis of the possible presence of stellar absorption is made.

Both HD 34989 and HD 36881 exhibit strong blending of the Ca II *H* absorption with stellar Hϵ at 3970 Å, creating a discrepancy between the strength of the absorption present from the Ca II *H* & *K* transition. Both HD 34989 & HD 36881 have lower values of $v \sin i$ than HD 36861 & HD 37490 and the discrepancy is likely to be due to an uncertainty in the location of the continuum around the Ca II *H* line. The Ca II *H* absorption observed towards HD 34989 & HD 36881 has not been included in the analysis.

In the case of HD 36881, the star is known to have a radial velocity of $\approx +35$ km s^{-1} and a projected rotational velocity of only 15 km s^{-1}, placing likely stellar absorption in/near the red-wing of that from the interstellar material. Strong broad absorption from both Na I and, in particular Ca II may be seen near the measured radial velocity. The stellar lines have been modelled at the same time as the interstellar absorption so that the best fitting combination of stellar and interstellar absorption is found. Figure 4.7 shows the resulting model fits, where the stellar absorption profiles have been indicated with dashed lines. Models have been obtained which are able to simultaneously fit the interstellar absorption from both Na I *D* transitions, but are unable to accurately fit the stellar components.

For HD 36894, no information is available for either the star's radial or rotational velocity, the likely stellar Na I contamination is therefore not known. A star of its spectral type (B9 V) is expected to have a mean equatorial rotational velocity of ≈ 195 km s^{-1} (Allen, 1973, pg. 210). Since the inclination of the stars rotational axis with respect to the line-of-sight is not known, its value of $v \sin i$ cannot be determined. However, if a $v \sin i$ in excess of 35 km s^{-1} (a width in the continuum of > 70 km s^{-1}) may be considered to be broad enough to act as the local continuum, we may say that stellar Na I contamination

is only important for,

$$195 \sin i < 35 \tag{4.1}$$

therefore,

$$\sin i < \frac{35}{195}, \tag{4.2}$$

$$i < 10^{\circ}. \tag{4.3}$$

For a randomly orientated star, Guthrie (1986) gives the probability, P, of having $i < x$ as,

$$P = 1 - \cos x. \tag{4.4}$$

Thus, with $x = 10^{\circ}$, there is only a 1.6% chance that the axis of rotation of the star will be within 10° of the line-of-sight. The interstellar Na I profile of HD 36894 is therefore not likely to suffer from stellar Na I contamination.

For HD 36895, no information is available regarding the star's rotational velocity; however, the mean equatorial rotational velocity of a B2 V star is expected to be $\approx$ 210 km s^{-1} (Allen, 1973) and, on the grounds of the analysis performed for HD 36894 above, we again find there to only be a 1.4% chance of contamination from the stellar Na I absorption. Moreover, a spectral type of B2 IV–V means the equivalent width of the stellar Na I line will be very small (less than 5 mÅ, e.g. Crawford, 1990).

HD 37171 has a very large radial velocity (-111 km s^{-1}; Table 4.1) which displaces the stellar Na I absorption away from the interstellar counterparts; however, a very late spectral type of K5 III means that absorption lines from many other species are consequently displaced into the region of the Na I D lines. The interstellar Na I D_1 absorption, while not blended with any stellar absorption, is closely bracketed by Fe I absorption (at 5898.217 & 5899.060 Å). In the case of Na I D_2, strong blending is suffered with stellar Fe I (at 5892.460, 5892.691 & 5892.799 Å) and Ni I (at 5892.745 & 5892.868 Å) and as a result the Na I D_2 absorption has not been included in the analysis.

Although HD 37320 possesses a low projected rotation velocity, $v \sin i = 35$ km s^{-1}, the continuum width of its stellar Na I line will be significantly broader than the velocity range occupied by the interstellar absorption, ≈ 20 km s^{-1}. Moreover, a spectral type of B8 III suggests the equivalent width of the stellar Na I line to be small (less than 30 mÅ, e.g. Crawford, 1990).

Our Na I observations of γ Ori shows the D_2 region to exhibit two absorption components at velocities of +15.98 & +25.84 km s^{-1}, while only the latter component is observed in the D_1 region. Interestingly, the same phenomenon may be seen in the data presented by Welsh *et al.* (1990); however, in agreement with Welsh *et al.* (1990), we conclude that the Na I D_2 feature is most likely the result of a known telluric water line at this location which has not been fully corrected. A stellar origin for this line, due to C II at 5889.78 Å (just 9 km s^{-1} shortward of the D_2 line) is not expected since γ Ori has a $v \sin i$ of 60 km s^{-1}.

Table 4.1: Stellar data for the targets observed in and around the λ Ori association. Stellar positions (columns 3 & 4), and spectral types (column 6) have been obtained from the SIMBAD astronomical database. Where available, V magnitudes (column 5) and Hipparcos distances (column 9) have been obtained from the Hipparcos and Tycho catalogues (ESA, 1997). Derivations of E(B-V) (column 7) and photometric distances (column 8) have been made using the tabulations of Deutschman *et al.* (1976), and data from the SIMBAD database. Stellar rotational velocities (column 10) have been taken from the SIMBAD database and the Bright Star Catalogue (Hoffleit and Jaschek, 1982). Stellar heliocentric radial velocities (column 11) have been obtained from Wilson (1953) and Evans (1967). Radial velocities for material in the near and far side of the λ Ori shell have been obtained using Equation 3.3 (column 12).

1	2	3	4	5	6	7	8	9	10	11	12	
HD	Star	l	b	V	Sp. Type	E(B-V)	Phot. Dist.	Hipp. Dist.	$v \sin i$	$\mathrm{rv}_{\odot}$	v_{shell}	
		(° ′)	(° ′)				(pc)	(pc)	(km s^{-1})	(km s^{-1})	(km s^{-1})	
HD 34989		194 37	-15 37	5.78	B1 V	0.17	589	225^{+52}_{-36}	57	+26.0±5.0	10.7	31.8
HD 35468	γ Ori	196 55	-15 57	1.64	B2 III	0.03	107	74^{+6}_{-5}	60	+18.2±0.9	11.1	31.3
HD 36653		191 05	-9 59	5.59	B3 V	0.10	247	157^{+30}_{-22}	224	+19.1±2.0	—	—
HD 36822	ϕ^1 Ori	195 24	-12 17	4.38	B0 III	0.14	613	302^{+92}_{-57}	39	+33.5±0.9	7.0	35.4
HD 36861	λ Ori	195 03	-12 00	3.52	O8 IIIf	0.16	438	324^{+109}_{-66}	75	+33.4±0.5	7.2	35.2
HD 36881		194 47	-11 49	5.63	B9 III	0.23	116	448^{+260}_{-121}	15	+35.0±20.0	7.4	35.0
HD 36894		195 13	-12 03	7.62	B9 V	−0.08	298	—	—	—	7.1	35.3
HD 36895		195 20	-12 08	6.73	B2 IV–V	0.12	676	426^{+232}_{-111}	—	+28.0±5.0	7.1	35.3
HD 37171		194 20	-11 01	6.00	K5 III	0.09	150	251^{+66}_{-43}	—	−111.4±2.0	8.4	34.0
HD 37320		197 32	-12 35	5.86	B8 III	0.06	217	171^{+34}_{-24}	35	+18.5±2.0	7.6	34.9
HD 37490	ω Ori	200 43	-14 02	4.57	B3 III	0.12	281	498^{+437}_{-159}	191	+21.8±0.9	17.5	24.9
HD 38622		193 10	-7 20	5.27	B2 IV–V	0.10	357	245^{+65}_{-43}	60	+29.2±0.9	—	—
HD 38710		199 45	-10 59	5.30	A5 V	0.08	39	147^{+37}_{-25}	73	+43.0±5.0	12.5	29.9

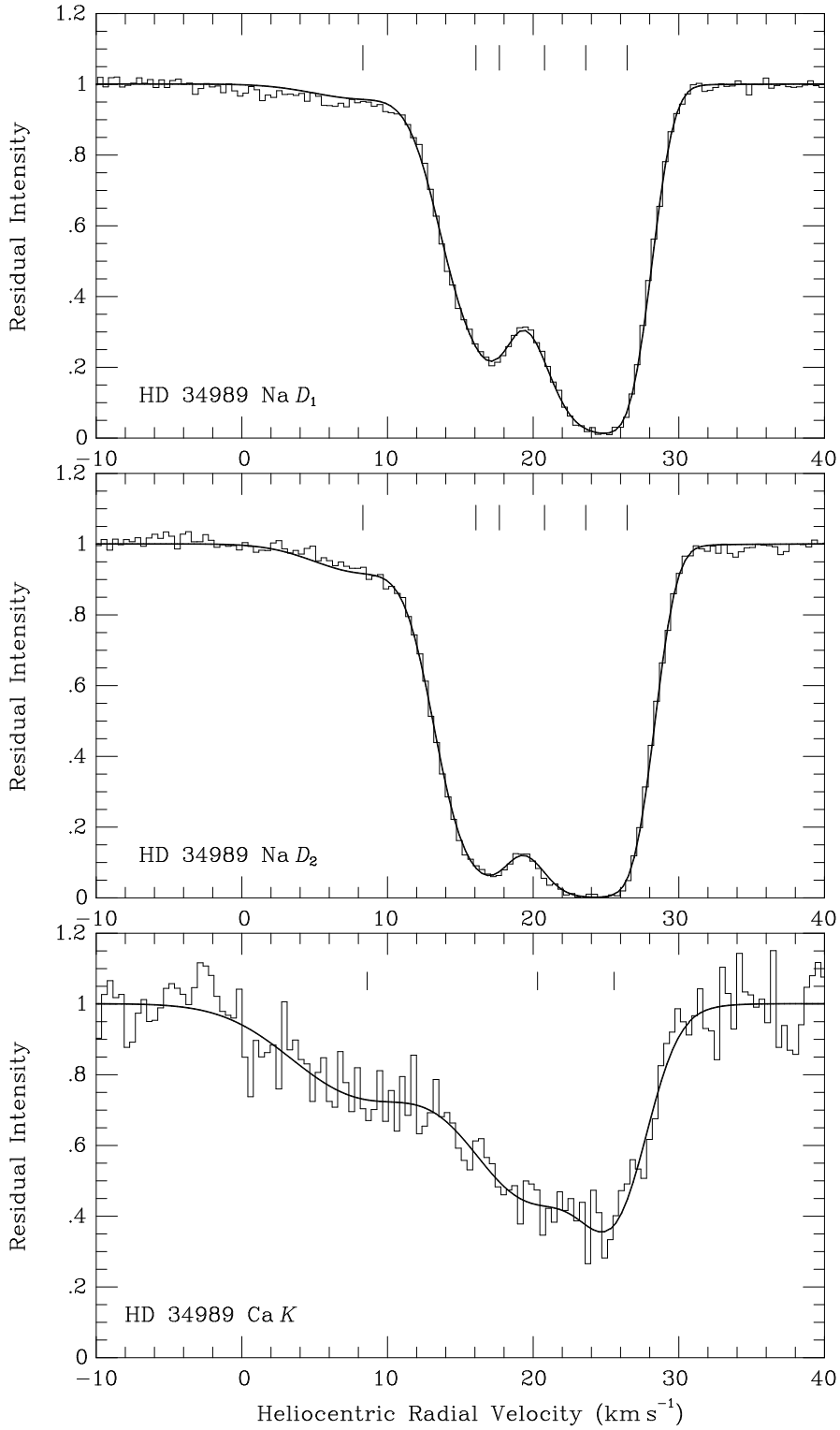

Figure 4.2: Theoretical line profiles (thick solid line) are shown plotted over the interstellar Na I D_1 & D_2 and Ca II K spectra (thin solid line) observed towards HD 34989. Tick marks are used to indicate the velocities of the individual model components, as listed in Table 4.2. In the case of Na I absorption components, tick marks represent the weighted-mean of the two hyperfine components.

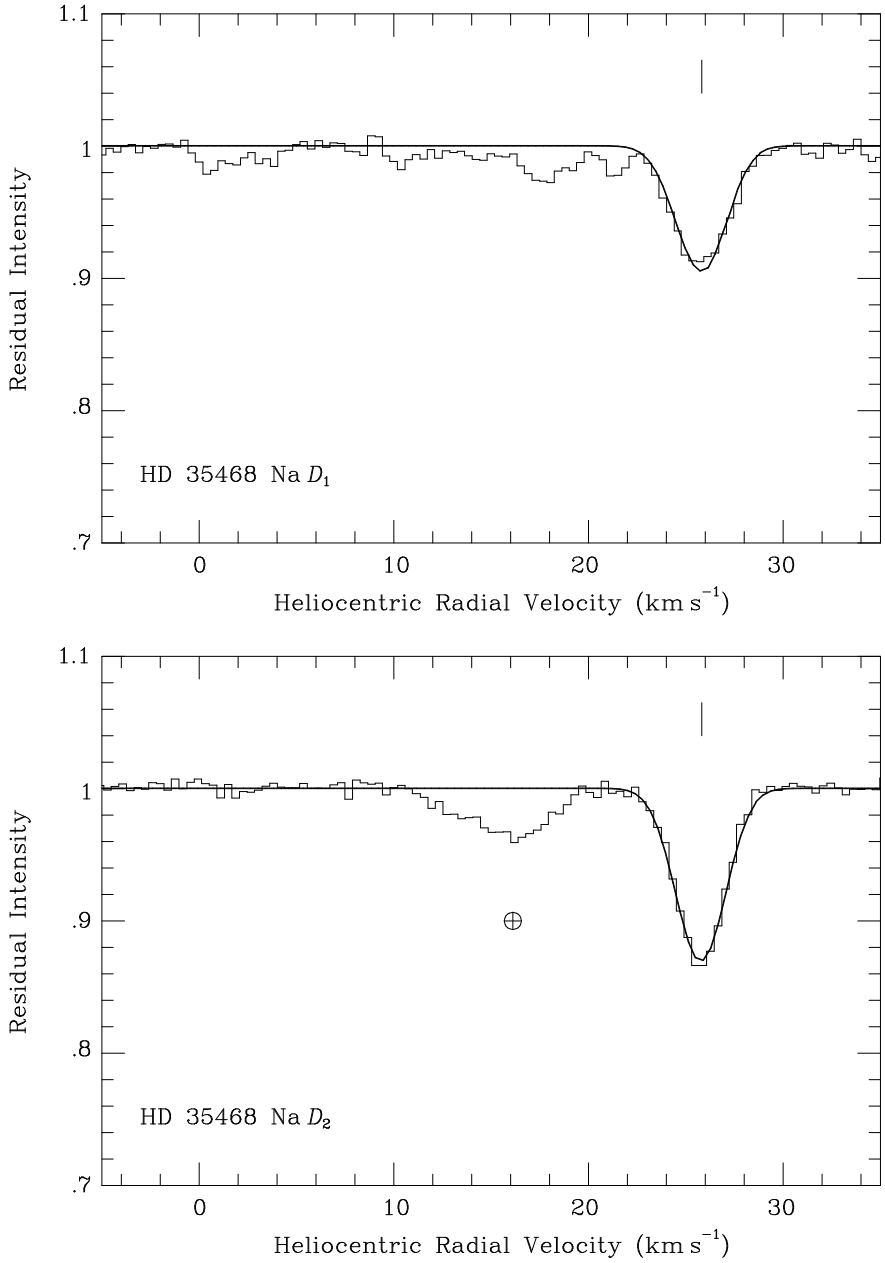

Figure 4.3: Theoretical line profiles are shown plotted over the interstellar Na I D_1 & D_2 spectra observed towards HD 35468. The vertical scale has been expanded to display weaker absorption more clearly. The feature indicated with the symbol '$\oplus$' is the location of residual telluric contamination which has not been fully removed. See caption for Figure 4.2 for further details.

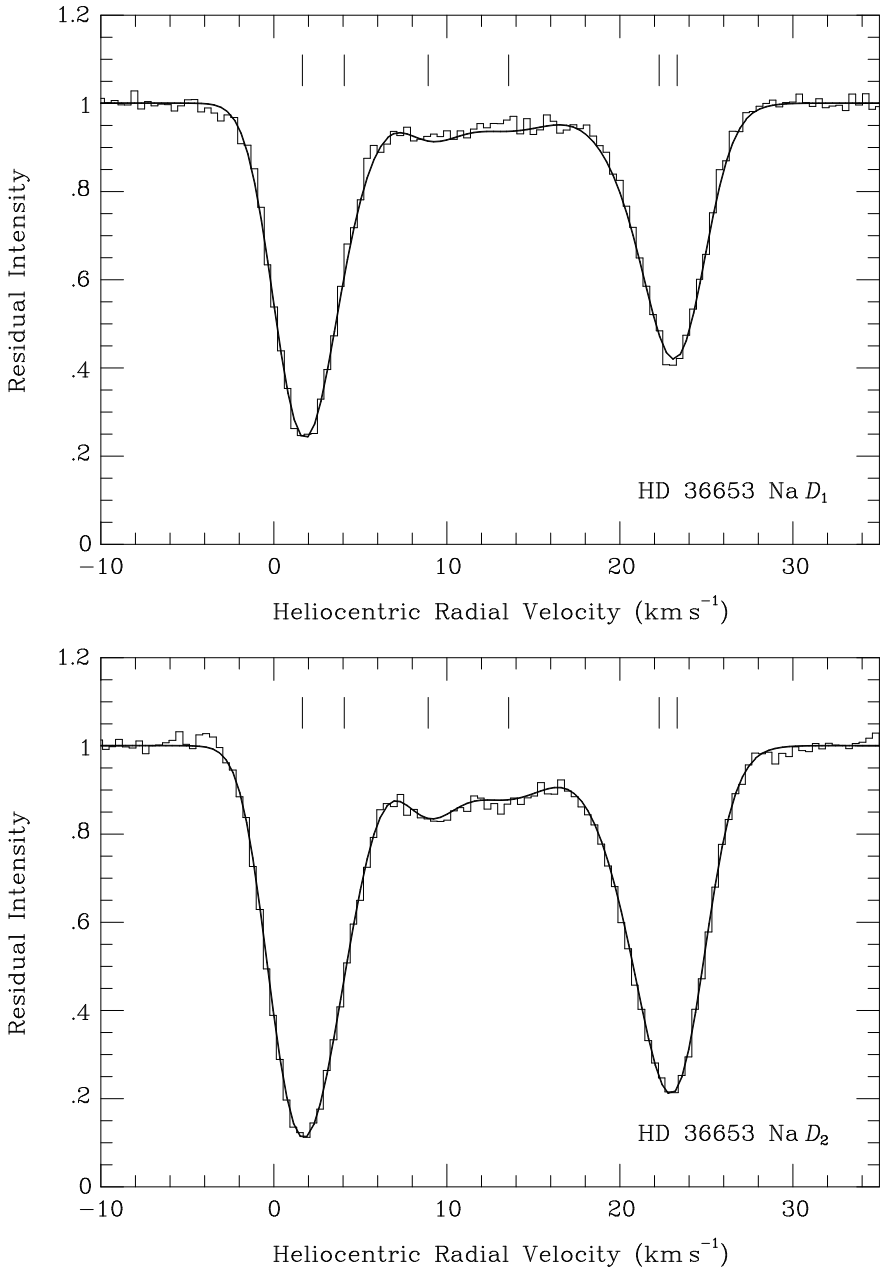

Figure 4.4: Theoretical line profiles are shown plotted over the interstellar Na I D_1 & D_2 spectra observed towards HD 36653. See caption for Figure 4.2 for further details.

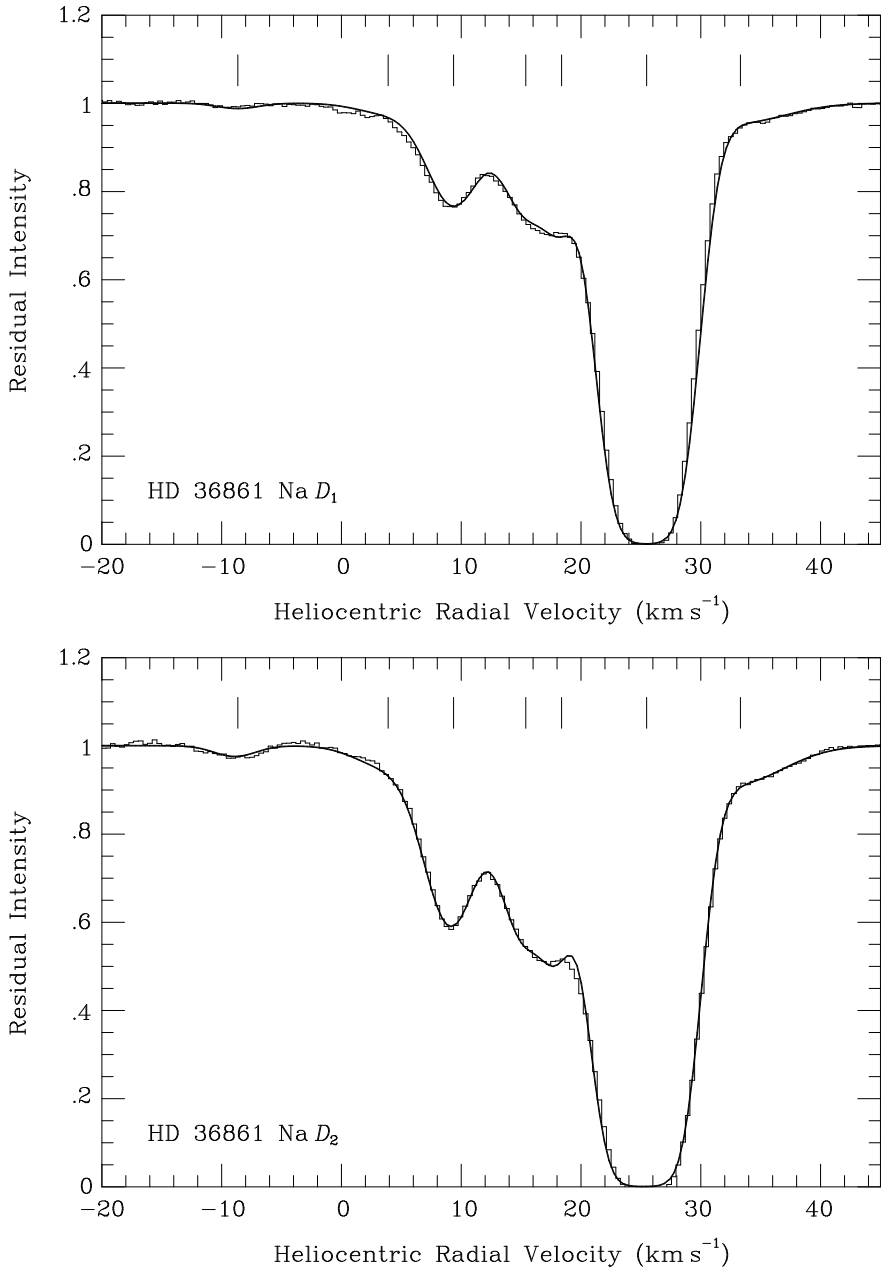

Figure 4.5: Theoretical line profiles are shown plotted over the interstellar Na I D_1 & D_2 spectra observed towards HD 36861. See caption for Figure 4.2 for further details.

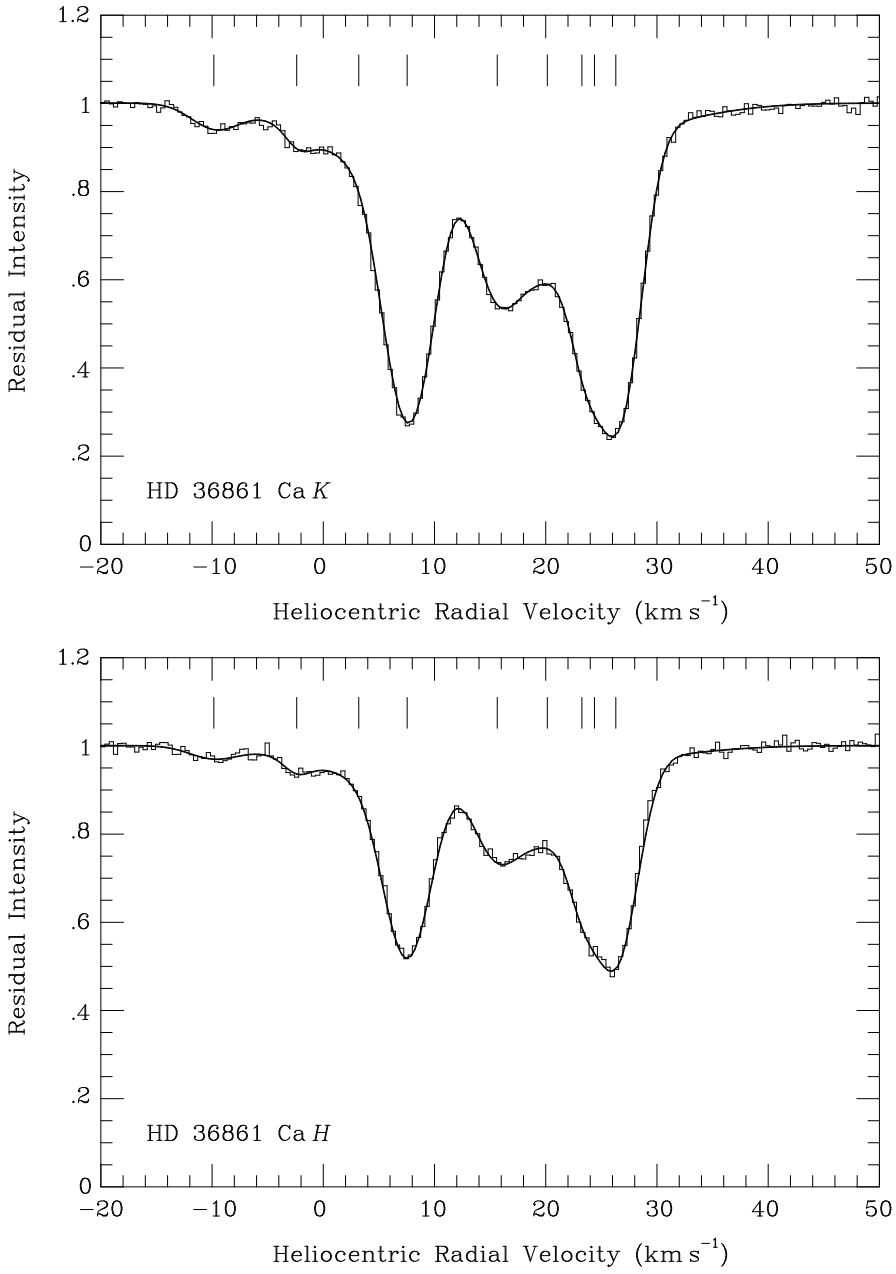

Figure 4.6: Theoretical line profiles are shown plotted over the interstellar Ca II *H* & *K* spectra observed towards HD 36861. See caption for Figure 4.2 for further details.

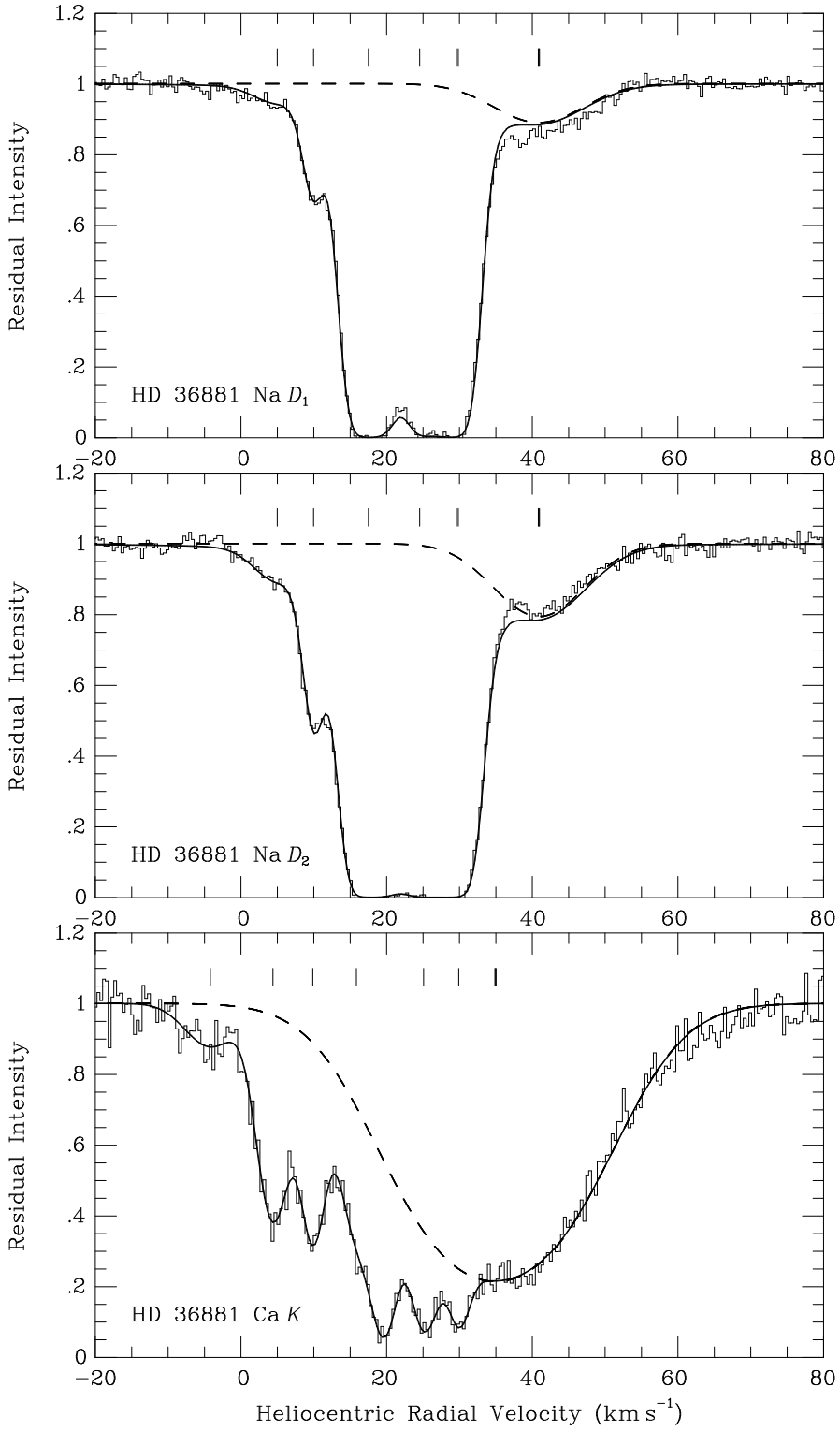

Figure 4.7: Theoretical line profiles are shown plotted over Na I D_1 & D_2 and Ca II K spectra observed towards HD 36881. Stellar absorption components are illustrated with dotted lines; their central velocities are marked with bold tickmarks. See caption for Figure 4.2 for further details.

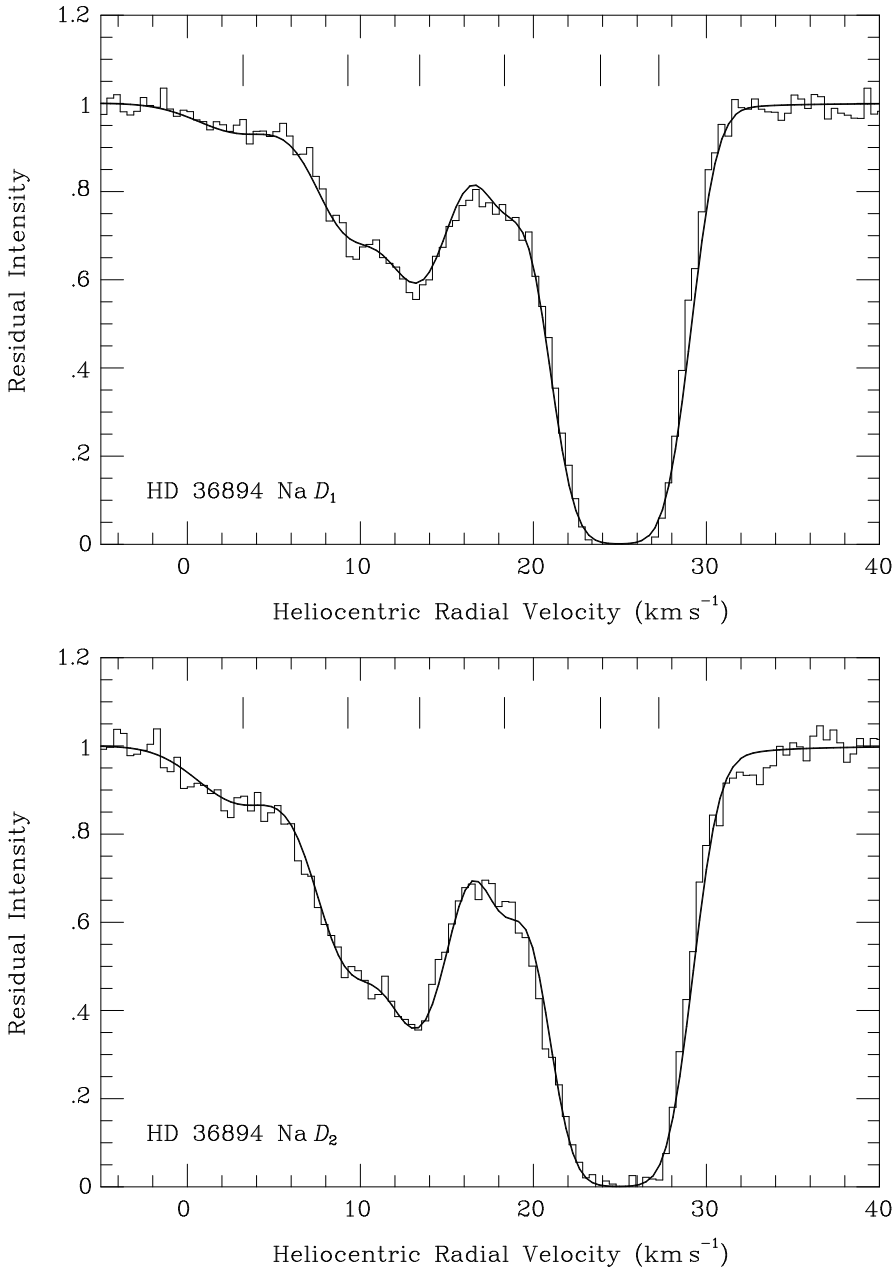

Figure 4.8: Theoretical line profiles are shown plotted over the interstellar Na I D_1 & D_2 spectra observed towards HD 36894. See caption for Figure 4.2 for further details.

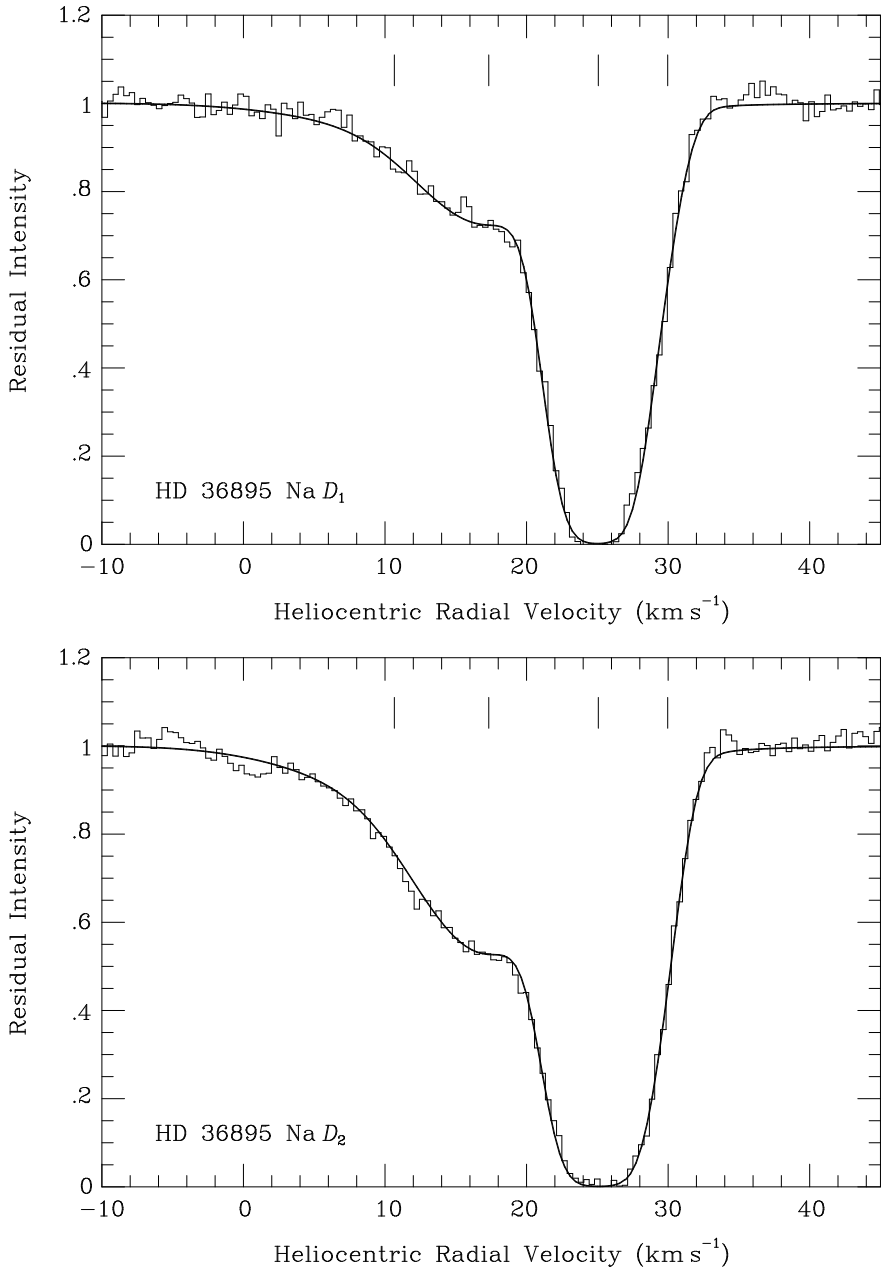

Figure 4.9: Theoretical line profiles are shown plotted over the interstellar Na I D_1 & D_2 spectra observed towards HD 36895. See caption for Figure 4.2 for further details.

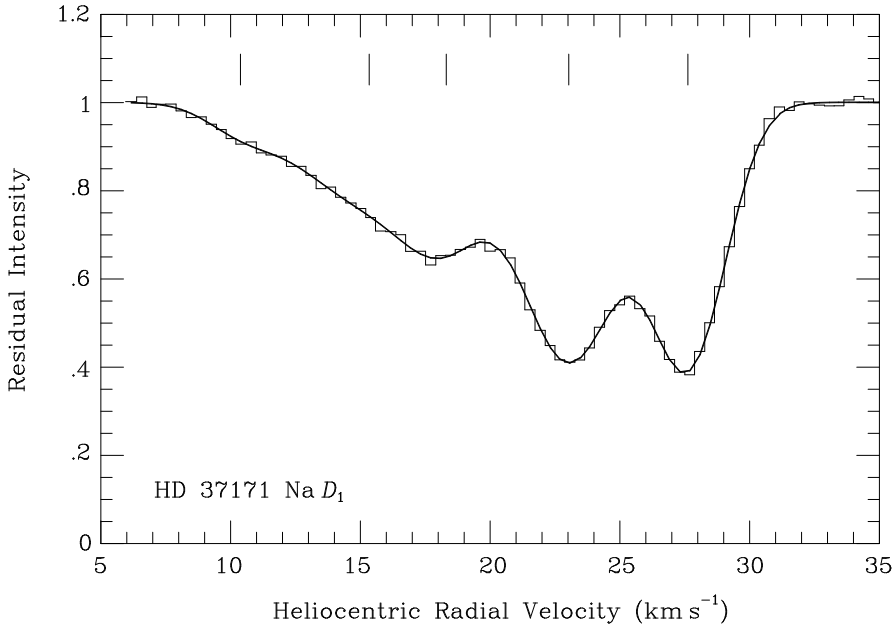

Figure 4.10: Theoretical line profile shown plotted over the interstellar Na I D_1 spectrum observed towards HD 37171. See caption for Figure 4.2 for further details.

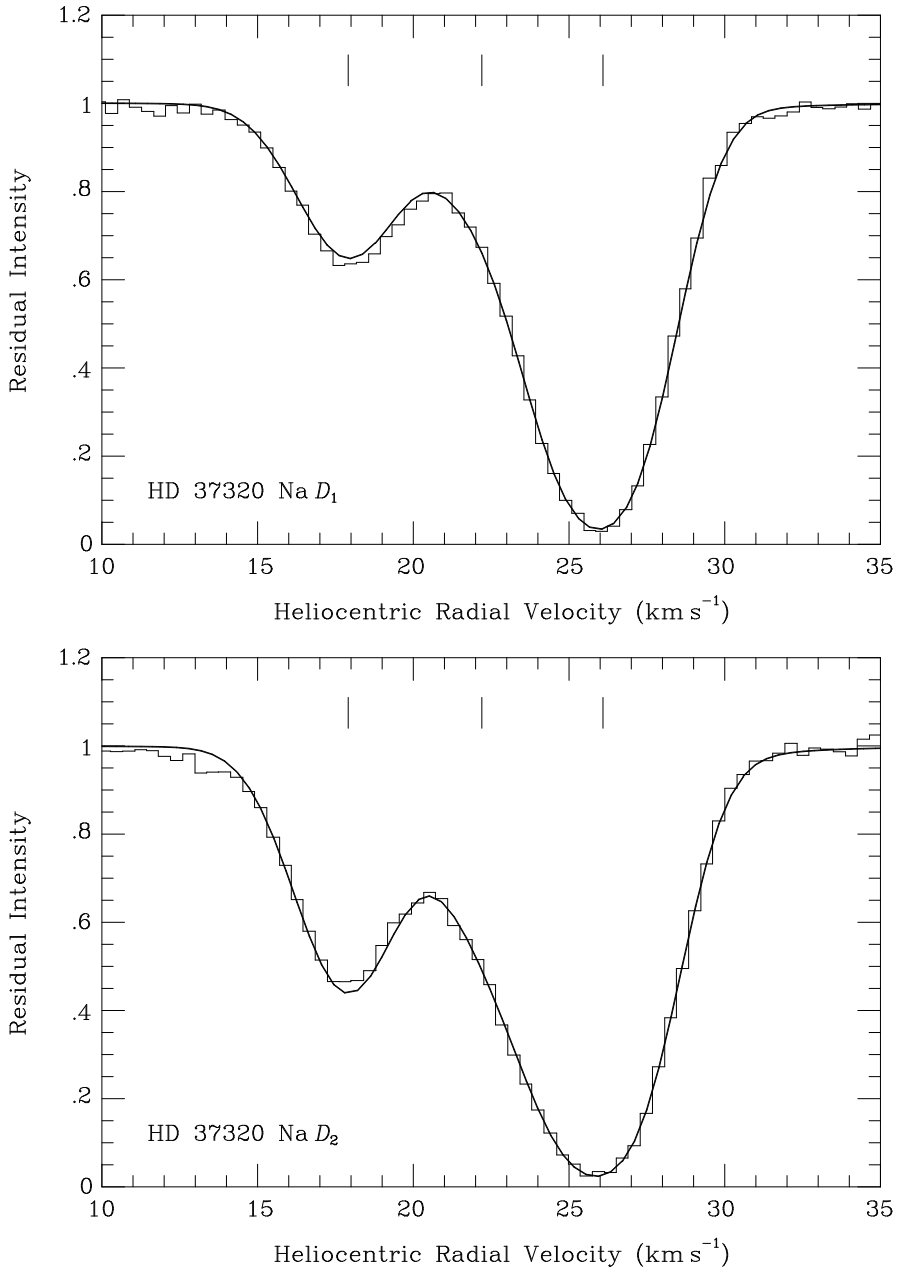

Figure 4.11: Theoretical line profiles are shown plotted over the interstellar Na I D_1 & D_2 spectra observed towards HD 37320. See caption for Figure 4.2 for further details.

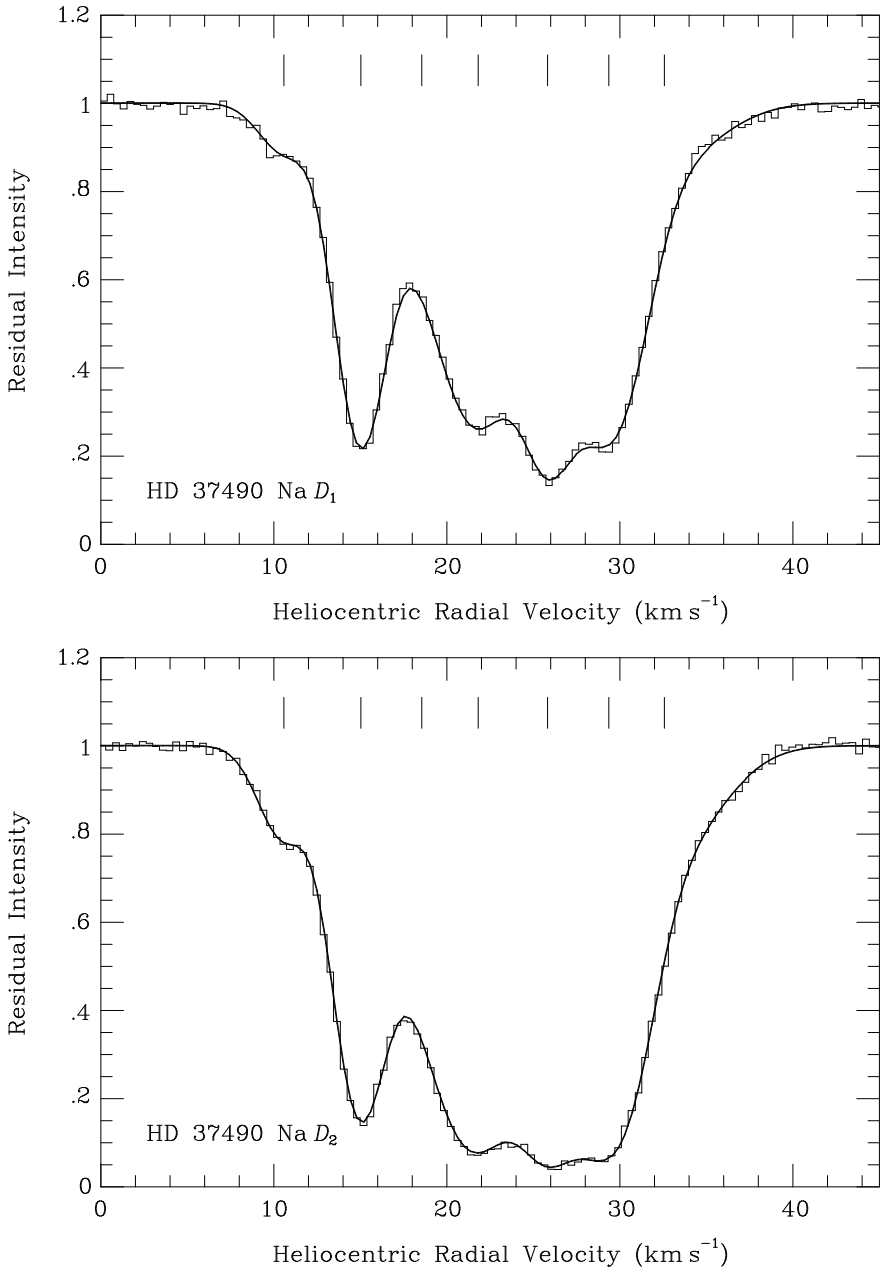

Figure 4.12: Theoretical line profiles are shown plotted over the interstellar Na I D_1 & D_2 spectra observed towards HD 37490. See caption for Figure 4.2 for further details.

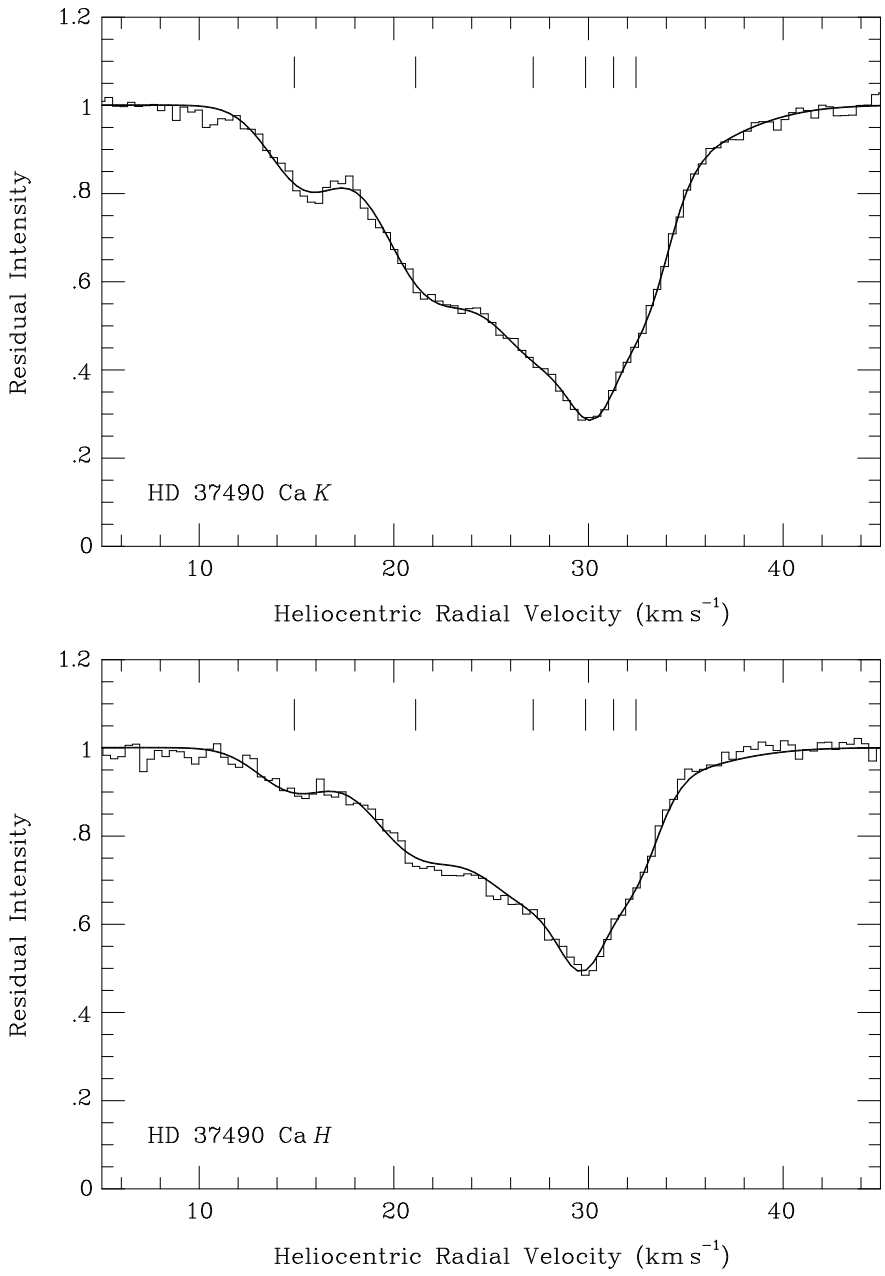

Figure 4.13: Theoretical line profiles are shown plotted over the interstellar Ca II *H* & *K* spectra observed towards HD 37490. See caption for Figure 4.2 for further details.

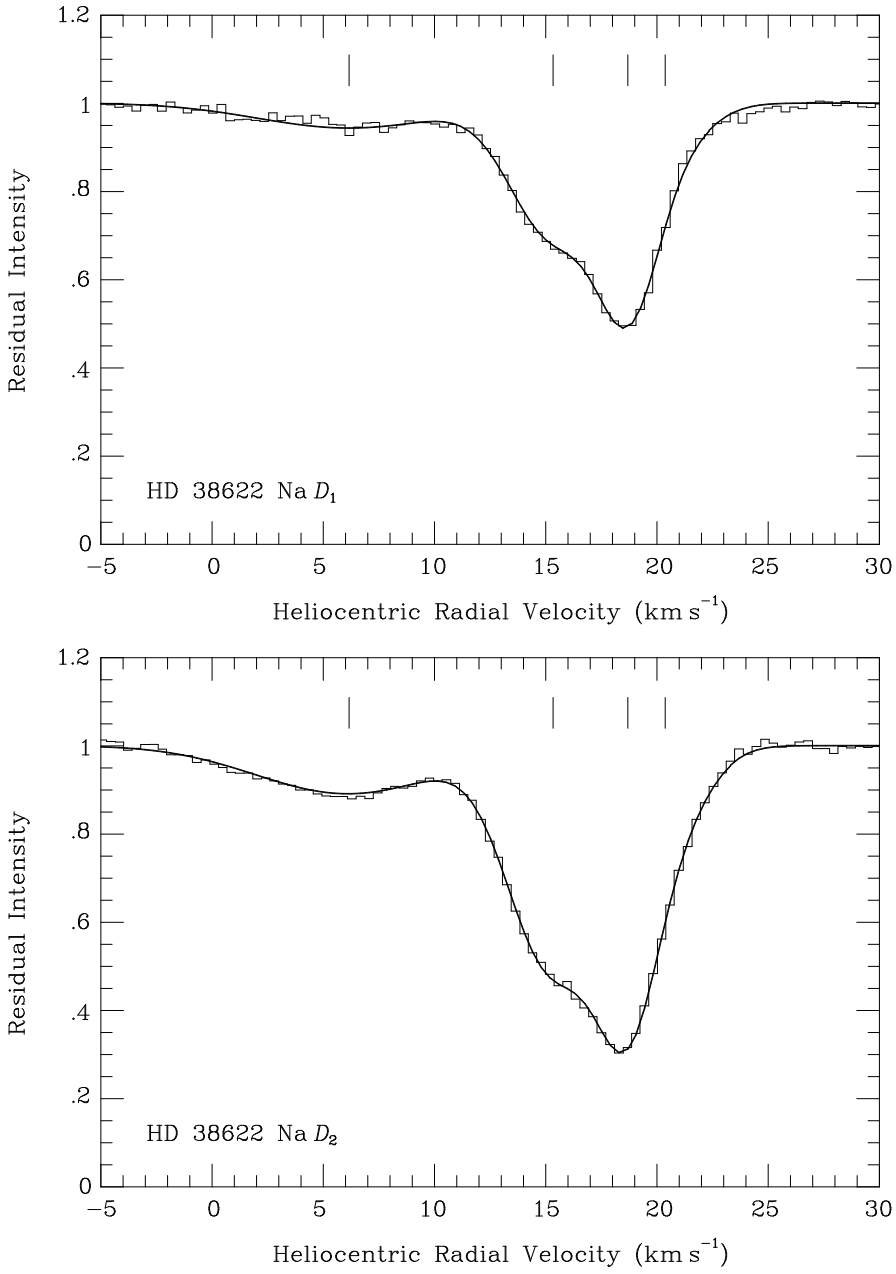

Figure 4.14: Theoretical line profiles are shown plotted over the interstellar Na I D_1 & D_2 spectra observed towards HD 38622. See caption for Figure 4.2 for further details.

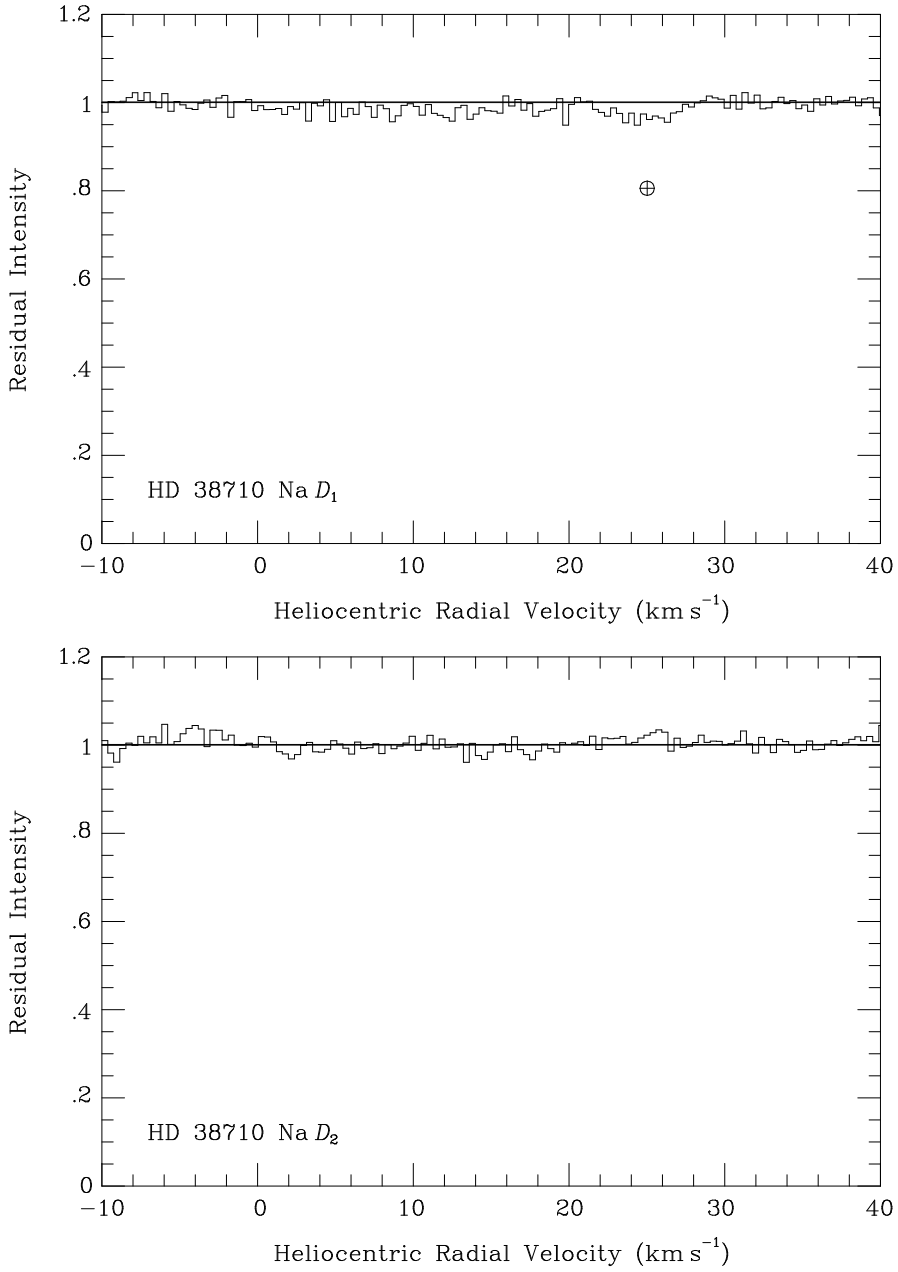

Figure 4.15: Theoretical line profiles are shown plotted over the interstellar Na I D_1 & D_2 spectra observed towards HD 38710. The feature indicated with the symbol '⊕' is the location of residual telluric contamination which has not been fully removed. See caption for Figure 4.2 for further details.

Table 4.2: Component parameters derived from the absorption line modelling of HD 34989. Achieved S/N ratios and total equivalent widths (W_λ) are displayed above columns 2–4 and 6–8 for Ca II and Na I respectively. Values of $v_\odot$ (heliocentric radial velocity), b (velocity dispersion) and N (column density) are shown in columns 2–4 (for Ca II) and 6–8 (for Na I). In the case of Na I absorption, central velocities are with respect to the weighted-mean of the two hyperfine split components. Where Ca II and Na I components appear in the same row, and are hence identified by the same cloud number (column 1), absorption is considered to occur in the same individual interstellar cloud. Column 5 gives cloud Na°/Ca^+ abundance ratios. Where multiple entries are made with a single cloud number (towards a given star), absorption is considered to arise in multiple unresolvable clouds and an average Na I/Ca II ratio is obtained from the summed Na I and Ca II column densities. Due to a large amount of blending of components, values of Na°/Ca^+ are somewhat uncertain.

	Ca II				Na I		
Star/ Cloud	$v_\odot$ (km s^{-1})	b (km s^{-1})	$\log N$ (cm^{-2})	$\frac{Na^\circ}{Ca^+}$	$v_\odot$ (km s^{-1})	b (km s^{-1})	$\log N$ (cm^{-2})
HD 34989	S/N: 14, W_λ: 143 ± 4 (K)				S/N: 97, W_λ: 259 ± 1 (D_1)		
					S/N: 79, W_λ: 299 ± 1 (D_2)		
1	8.60 ± 1.44	6.62 ± 1.48	11.74 ± 0.12	0.13	8.31 ± 1.26	4.36 ± 1.48	10.85 ± 0.14
2a	20.30 ± 1.03	5.51 ± 1.28	12.09 ± 0.13	4.32	16.07 ± 0.62	2.44 ± 0.43	12.10 ± 0.14
2b					17.68 ± 0.31	0.31 ± 0.18	11.68 ± 0.21
2c					20.78 ± 1.80	1.38 ± 1.62	11.80 ± 1.02
2d					23.61 ± 0.82	1.70 ± 2.15	12.47 ± 0.52
3	25.55 ± 0.29	2.31 ± 0.80	11.70 ± 0.24	10.96	26.45 ± 0.46	0.74 ± 0.30	12.74 ± 0.41

Table 4.3: Component parameters derived from the absorption line modelling of HD 35468. Achieved S/N ratios and equivalent widths (W_λ) are displayed in columns 2 & 3 respectively. Values of $v_\odot$ (heliocentric radial velocity), b (velocity dispersion) and N (column density) are shown in columns 5–7. Central velocities of the Na I components are with respect to the weighted-mean of the two hyperfine split components.

Line	S/N	W_λ (mÅ)	Comp	$v_\odot$ (km s^{-1})	b (km s^{-1})	log N (cm^{-2})
Na I D_1	159	8.5 ± 0.3	1	25.82 ± 0.05	0.08 ± 0.01	11.03 ± 0.04
Na I D_2	227	12 ± 1				

Table 4.4: Component parameters derived from the absorption line modelling of HD 36653. For further details refer to Table 4.3.

Line	S/N	W_λ (mÅ)	Comp	$v_\odot$ (km s^{-1})	b (km s^{-1})	log N (cm^{-2})
Na I D_1	75	136 ± 1	1	1.65 ± 0.15	1.08 ± 0.11	12.11 ± 0.06
Na I D_2	74	203 ± 1	2	4.07 ± 1.07	1.18 ± 1.23	11.18 ± 0.42
			3	8.92 ± 0.30	1.37 ± 1.09	10.77 ± 0.30
			4	13.57 ± 0.94	3.58 ± 2.17	10.97 ± 0.23
			5	22.27 ± 0.37	2.65 ± 0.39	11.55 ± 0.13
			6	23.31 ± 0.10	1.01 ± 0.26	11.69 ± 0.10

Table 4.5: Component parameters derived from the absorption line modelling of HD 36861. For further details refer to Table 4.2.

Cloud	Ca II				Na I		
	$v_\odot$ (km s^{-1})	b (km s^{-1})	$\log N$ (cm^{-2})	$\frac{\mathrm{Na^\circ}}{\mathrm{Ca^+}}$	$v_\odot$ (km s^{-1})	b (km s^{-1})	$\log N$ (cm^{-2})
	S/N: 119, W_λ: 196 ± 1 (K)				S/N: 263, W_λ: 248 ± 1 (D_1)		
	S/N: 119, W_λ: 117 ± 1 (H)				S/N: 227, W_λ: 319 ± 1 (D_2)		
1	-9.84 ± 0.29	2.59 ± 0.46	10.67 ± 0.09	0.23	-8.65 ± 1.14	1.68 ± 2.37	10.04 ± 0.25
2	-2.39 ± 0.23	0.03 ± 0.08	10.80 ± 1.39	< 0.01			
3	3.19 ± 3.12	7.19 ± 2.73	11.40 ± 0.24	0.12	3.90 ± 4.27	3.08 ± 4.02	10.47 ± 0.69
4	7.54 ± 0.04	2.39 ± 0.11	11.98 ± 0.04	0.30	9.36 ± 0.24	2.41 ± 0.66	11.45 ± 0.10
5	15.64 ± 0.67	2.73 ± 0.81	11.67 ± 0.25	0.56	15.39 ± 0.43	1.92 ± 0.91	11.42 ± 0.14
6	20.14 ± 0.68	2.37 ± 2.18	11.43 ± 0.45	0.63	18.38 ± 0.28	0.45 ± 0.47	11.23 ± 0.14
7a	23.25 ± 0.21	1.13 ± 0.52	11.50 ± 0.25	23.88	25.48 ± 0.02	2.13 ± 0.09	13.46 ± 0.10
7b	26.30 ± 0.16	1.96 ± 0.16	11.95 ± 0.05				
8	24.38 ± 11.97	10.37 ± 5.75	11.28 ± 0.74	0.44	33.31 ± 1.85	5.10 ± 2.09	10.92 ± 0.18

Table 4.6: Component parameters derived from the absorption line modelling of HD 36881. Cloud 7* represents the modelled stellar Ca II and Na I absorption components. Values of W_λ represent interstellar absorption only. For further details refer to Table 4.2.

Cloud	Ca II				Na I		
	$v_\odot$ (km s^{-1})	b (km s^{-1})	$\log N$ (cm^{-2})	$\frac{\mathrm{Na}^\circ}{\mathrm{Ca}^+}$	$v_\odot$ (km s^{-1})	b (km s^{-1})	$\log N$ (cm^{-2})
	S/N: 26, W_λ: 249 ± 3 (K)				S/N:74, W_λ: 432 ± 2 (D_1)		
					S/N:57, W_λ: 467 ± 2 (D_2)		
1	-4.20 ± 0.80	4.51 ± 1.24	11.22 ± 0.09	< 0.04			
2	4.39 ± 0.15	2.41 ± 0.29	11.87 ± 0.04	0.1	4.98 ± 1.76	4.08 ± 2.36	10.87 ± 0.30
3	9.86 ± 0.17	1.58 ± 0.40	11.82 ± 0.05	0.41	9.97 ± 0.13	1.06 ± 0.30	11.43 ± 0.06
4a	15.85 ± 1.33	2.47 ± 1.70	11.79 ± 0.31	136.70	17.50 ± 0.11	1.51 ± 0.25	14.53 ± 0.60
4b	19.64 ± 0.31	1.37 ± 0.57	12.27 ± 0.13				
5	25.08 ± 0.12	1.56 ± 0.37	12.07 ± 0.06	5.37	24.54 ± 0.89	1.63 ± 1.30	12.80 ± 0.42
6a	29.90 ± 0.15	0.75 ± 0.85	12.11 ± 1.33	76.17	29.66 ± 71.25	4.17 ± 28.87	11.60 ± 12.31
6b					29.77 ± 0.44	1.24 ± 0.78	13.99 ± 1.84
7*	34.95 ± 0.66	15.66 ± 0.53	12.81 ± 0.02	—	40.91 ± 2.47	8.40 ± 2.14	11.54 ± 0.19

Table 4.7: Component parameters derived from the absorption line modelling of HD 36894. For further details refer to Table 4.3.

Line	S/N	W_λ (mÅ)	Comp	$v_\odot$ (km s^{-1})	b (km s^{-1})	log N (cm^{-2})
Na I D_1	50	246 ± 2	1	3.22 ± 1.18	3.08 ± 1.55	10.95 ± 0.18
Na I D_2	41	307 ± 2	2	9.28 ± 0.60	1.85 ± 0.96	11.48 ± 0.19
			3	13.43 ± 0.43	1.76 ± 0.60	11.66 ± 0.11
			4	18.33 ± 0.26	0.28 ± 0.13	11.27 ± 0.13
			5	23.88 ± 1.12	1.20 ± 0.42	13.66 ± 2.06
			6	27.25 ± 1.32	0.69 ± 0.82	13.24 ± 1.98

Table 4.8: Component parameters derived from the absorption line modelling of HD 36895.For further details refer to Table 4.3.

Line	S/N	W_λ (mÅ)	Comp	$v_\odot$ (km s^{-1})	b (km s^{-1})	log N (cm^{-2})
Na I D_1	62	224 ± 1	1	10.66 ± 29.49	9.28 ± 13.43	11.19 ± 2.12
Na I D_2	53	288 ± 2	2	17.33 ± 0.55	6.14 ± 2.07	11.81 ± 0.52
			3	25.07 ± 0.04	1.56 ± 0.17	13.92 ± 0.31
			4	29.97 ± 0.22	0.20 ± 0.11	11.29 ± 0.15

Table 4.9: Component parameters derived from the absorption line modelling of HD 37171. For further details refer to Table 4.3.

Line	S/N	W_λ (mÅ)	Comp	$v_\odot$ (km s^{-1})	b (km s^{-1})	$\log N$ (cm^{-2})
Na I D_1	90	144 ± 1	1	10.38 ± 2.55	0.11 ± 15.01	10.56 ± 10.10
			2	15.34 ± 2.54	3.29 ± 2.55	11.53 ± 0.45
			3	18.31 ± 0.17	1.27 ± 1.09	11.35 ± 0.58
			4	23.03 ± 0.05	1.56 ± 0.11	11.90 ± 0.02
			5	27.62 ± 0.03	0.74 ± 0.07	11.91 ± 0.01

Table 4.10: Component parameters derived from the absorption line modelling of HD 37320. For further details refer to Table 4.3.

Line	S/N	W_λ (mÅ)	Comp	$v_\odot$ (km s^{-1})	b (km s^{-1})	$\log N$ (cm^{-2})
Na I D_1	98	141 ± 1	1	17.91 ± 0.04	1.30 ± 0.08	11.55 ± 0.01
Na I D_2	80	172 ± 1	2	22.20 ± 0.11	0.72 ± 0.31	11.20 ± 0.04
			3	26.09 ± 0.02	0.89 ± 0.04	13.60 ± 0.12

Table 4.11: Component parameters derived from the absorption line modelling of HD 37490. For further details refer to Table 4.2.

Cloud	Ca II				Na I		
	$v_\odot$ (km s^{-1})	b (km s^{-1})	$\log N$ (cm^{-2})	$\frac{\mathrm{Na}^\circ}{\mathrm{Ca}^+}$	$v_\odot$ (km s^{-1})	b (km s^{-1})	$\log N$ (cm^{-2})
	S/N: 97, W_λ: 127 ± 1 (K)				S/N: 93, W_λ: 284 ± 1 (D_1)		
	S/N: 64, W_λ: 79 ± 1 (H)				S/N: 96, W_λ: 361 ± 1 (D_2)		
1				> 17.38	10.58 ± 0.07	0.84 ± 0.21	10.94 ± 0.02
2	14.89 ± 0.20	1.99 ± 0.23	11.15 ± 0.05	13.49	15.03 ± 0.05	0.70 ± 0.07	12.28 ± 0.03
3				> 14.24	18.55 ± 3.92	1.91 ± 3.81	11.37 ± 1.58
4	21.12 ± 0.55	2.86 ± 0.53	11.65 ± 0.14	2.88	21.81 ± 0.94	2.12 ± 0.92	12.11 ± 0.28
5a	27.16 ± 0.57	3.48 ± 1.77	11.89 ± 0.47	1.84	25.82 ± 0.06	0.70 ± 0.09	12.14 ± 0.02
5b	29.85 ± 0.09	0.57 ± 0.17	11.66 ± 0.09		29.36 ± 0.06	1.89 ± 0.16	12.13 ± 0.05
5c	32.44 ± 0.13	0.35 ± 0.13	11.40 ± 0.10				
6	31.29 ± 9.14	5.70 ± 4.05	11.43 ± 1.09	0.79	32.57 ± 1.81	3.85 ± 1.10	11.33 ± 0.27

Table 4.12: Component parameters derived from the absorption line modelling of HD 38622. For further details refer to Table 4.3.

Line	S/N	W_λ (mÅ)	Comp	$v_\odot$ (km s^{-1})	b (km s^{-1})	$\log N$ (cm^{-2})
Na I D_1	128	72 ± 1	1	6.16 ± 0.17	5.46 ± 0.26	11.08 ± 0.02
Na I D_2	109	116 ± 1	2	15.33 ± 0.07	1.85 ± 0.10	11.53 ± 0.02
			3	18.69 ± 0.06	0.41 ± 0.07	11.69 ± 0.04
			4	20.37 ± 1.05	1.57 ± 0.86	10.99 ± 0.30

Table 4.13: Component parameters derived from the absorption line modelling of HD 38710. For further details refer to Table 4.3.

Line	S/N	W_λ (mÅ)	Comp	$v_\odot$ (km s^{-1})	b (km s^{-1})	$\log N$ (cm^{-2})
Na I D_1	67	< 3	–	—	—	—
Na I D_2	60	< 1				

4.3 Discussion

The much higher resolving power obtained with the Ultra-High-Resolution Facility (hereinafter UHRF) allows the resolution of more of the intricate component structure than may be seen in the MSES data (illustrated by a comparison of UHRF and MSES observations of λ Ori, Figures 3.5 and 4.5 & 4.6). The comparison of UHRF observations of Ca II and Na I absorption occurring in the sightlines to λ and ϕ^1 Ori, has allowed many separate absorption systems to be identified (listed in Table 4.14). System identifiers are of the form $\lambda\boldsymbol{x}$, where 'λ' denotes 'λ Ori association' (in order to reduce confusion with individual clouds), and $\boldsymbol{x}$ is a number which increases with the system's mean central velocity. Clouds identified in the MSES observations may also be correlated with the systems observed in the UHRF data, however their lower-resolution result in some blending between systems.

The components present at negative velocities possess very small Na°/Ca^+ ratios. System $\lambda\mathbf{1}$, which is only observed towards λ Ori, possesses a velocity more negative than any other cloud (apart from absorption associated with mass-loss from β Ori, see § 3.4.4). System $\lambda\mathbf{1}$ may be associated with, and accelerated by, λ Ori. Good agreement is seen between λ and ϕ^1 Ori for systems $\lambda\mathbf{2}$ and $\lambda\mathbf{4}$. Their broad nature and low Na°/Ca^+ ratios are consistent with the gas either being shocked material associated with the λ Ori shell and accelerated by association stars, or being in the warm intercloud medium, known to exhibit larger velocity ranges than diffuse clouds (Cowie and York, 1978). The detection of similar components in the Ca II spectra of the Belt stars suggests the latter case to be more likely. The weak absorption of system $\lambda\mathbf{3}$ seen towards λ Ori, is not detectable in the spectrum of ϕ^1 Ori.

The Na I absorption seen by Hobbs (1969*a*) at +16.8 and +25.8 km s^{-1} towards λ Ori is considered by Maddalena and Morris (1987) to reside at velocities consistent with the near and far sides of the shell, placing λ Ori behind the shell, rather than within it. However, if we assume that the expansion of the shell follows that of the ring, it is possible to use Equation 3.3 to derived expected radial velocities for material in the near and far side of the shell. Central radial and expansion velocities have been derived for the ring by Maddalena and Morris (1987, +21.2 and +14.3 km s^{-1} respectively), and from figure 2 of Lang *et al.* (2000), the centre of the ring is seen to be near $(l, b) = 196, -12.5$. Assuming the ring to be located at the same distance as λ Ori (Table 4.1) and have a radius of 5°

(Maddalena and Morris, 1987), we are able derive values for the expected shell velocities towards each star (listed in column 12 of Table 4.1). Material present in the near and far sides of the shell (if its expansion does indeed follow that of the ring) should therefore be found at +7 and +35 km s^{-1} (for the line-of-sight to λ Ori), rather than at the velocities of the Na I absorption observed by Hobbs (1969*a*), as suggested by Maddalena and Morris (1987). A lack of absorption at a velocity of +36 km s^{-1} (corresponding to the velocity of the far side of the shell) suggests that λ and ϕ^1 Ori indeed reside within the shell, as would be expected.

The very strong Ca II absorption observed between +4 & +11 km s^{-1} (system λ**5**), towards both λ and ϕ^1 Ori (and possibly HD 34989), corresponds well to the velocity implied for the near side of a shell around the association by the kinematic model of Maddalena and Morris (1987). Moreover, the small Na°/Ca$^+$ ratios are consistent with the expected removal of Ca from grain surfaces (Bergoffen and Van Buren, 1988). We therefore consider this absorption to arise within the near side of the expanding shell around the association. 23 Ori which is located at a similar distance but exterior to the λ Ori shell on the sky, has a similar Ca II spectrum, but does not exhibit strong absorption at a radial velocity of $\approx$ +7 km s^{-1} (Welty *et al.*, 1999), strengthening our conclusion for its origin being from a neutral shell around the λ Ori association. These detections do however represent a limited number of sightlines and therefore cannot be used to infer the presence of a complete shell. Indeed Zhang and Green (1991) have noted that the H I observations presented by Wade (1957, 1958), which also suggest the presence of a shell, are far too limited to infer the large-scale structure of the region.

The Na I absorption observed towards λ Ori, HD 36894 and HD 36881 at a velocity of $\approx$ +9 km s^{-1} (λ**5**) has been associated with Ca II absorption arising within the near side of the shell. Since a counterpart has not been detected towards the nearby HD 37171, this may indicate HD 37171 to be located foreground to the shell. However, this conclusion is rather uncertain since Na I absorption components corresponding to the shell material have not been detected towards ϕ^1 Ori or HD 36895, which are expected to lie behind the near side of the shell.

We suggest that the very narrow components of system λ**6** (characteristic of very cold gas; $T_{\rm k} < 117$ K in the case of Na I) corresponds well to molecular hydrogen absorption observed by Spitzer and Morton (1976), and arises within a particularly dense interstellar cloud. Although highly blended with neighbouring components, these components form

an integral part of an absorption model which statistically provides the best fit to the data. Furthermore, the excellent agreement seen between the independently modelled Na I and Ca II data, strongly suggests the detection to be genuine.

The Na I absorption present between +12 and +20 km s^{-1} (composed of systems **λ7**, **λ8** and **λ9**) appears very similar in many of the sightlines. System **λ7** is clearly detected towards HD 38622 which places the absorbing cloud within 250 pc. Very strong absorption is also observed at this velocity towards HD 34989 (at a distance of 225 pc) which may or may not be associated. Systems **λ8** & **λ9** are located foreground to system **λ7**, since they are also detected towards HD 37320 which has a distance of 170 pc. Significant additional absorption at similar velocities to systems **λ7**, **λ8** & **λ9** is present in the spectra of the more distant HD 37490 & HD 36881. There must therefore be additional absorbing clouds at this velocity located at around 400–450 pc.

The location of λ Ori's saturated Na I absorption around +25.7 km s^{-1} (**λ10**) corresponds well with its counterpart in the spectrum of ϕ^1 Ori. These saturated regions can be accurately fitted with single components (which will have no unique solution for b and N) but are undoubtedly the result of unresolved blends. This is supported by the following considerations: I) the identification of six Ca II components in this velocity region of the λ Ori spectrum; II) the unsaturated red wing towards ϕ^1 Ori, which requires a minimum of two components for an accurate fit; and III) the requirement of an additional component in the blue wing for λ Ori. IV) unsaturated Na I absorption at this velocity in the spectra of nearby, but less distant stars. However, since it is not possible to identify individual interstellar clouds, this region is treated as a single absorption system, **λ10**. The total column densities of Na° and Ca^+ indicate Na°/Ca^+ ratios of 13.49 and 7.19 for λ and ϕ^1 Ori respectively (see § 3.3), consistent with cool diffuse/partially molecular clouds (since Ca depletion is expected to be density dependent; e.g., Barlow, 1978). This is supported by the observation of an H_2 absorption component at a velocity of +25.4 km s^{-1} towards λ Ori (Spitzer and Morton, 1976). Separation of individual clouds within this region may, in principle, be achieved with observations of the much weaker lines of Na I at 3032 Å or K I at 7699 Å.

Observations of Na I towards HD 38710, which has a projected location on the south eastern limb of the λ Ori shell, shows there to be no detectable gas in this direction out to a distance of 150 pc (Table 4.1). Observations of Na I towards HD 35468 (γ Ori), located in the direction of the south western limb of the shell at a distance of ≈ 75 pc

Table 4.14: Velocity systems identified towards the λ Ori association. The top row lists the system identifiers, as referred to in the text. A short description is given for some of the systems, with $\overline{v}_{\odot}$ being the mean velocity of the constituent components. Cloud numbers given for targets above the double line refer to the UHRF models (see Tables 3.5 & 3.6); those below the double line refer to components in the MSES models (see Tables 4.2 to 4.12). Each target is followed by its distance in brackets (pc), estimated from its absorption profile. * Ca II absorption associated with blended Na I components is likely to be composed of contributions from each constituent cloud.

System		**λ1**	**λ2**	**λ3**	**λ4**	**λ5**	**λ6**	**λ7**	**λ8**	**λ9**	**λ10**	**λ11**	**λ12**
Description		Material accelerated by λ Ori	Warm intercloud material similar to Belt stars	Cool gas	Warm intercloud material similar to Belt stars	λ Ori shell material	Cold diffuse partially molecular gas	Located between 170 & 225 pc	Located between 160 & 170 pc		Foreground diffuse/partially molecular gas mostly located beyond 75 pc		
Velocity, $\overline{v}_{\odot}$:		-19	-9	-6	-2	$+7$	$+10$	$+15$	$+18$	$+20$	$+25$	$+30$	$+33$
UHRF:	HD 36861 [325]	1	2	3	4	5,6,8	7	9	10	11	12	13	14
	HD 36822 [300]		1		2	3		4	5	6	7,8		
MSES:	HD 35468 [75]										1		
	HD 36653 [160]										5,6		
	HD 37320 [170]								— 1 —		2,3		
	HD 34989 [225]					1		2a*	— 2b* —		2c/d*,3		
	HD 38622 [250]							2	— 3 —				
	HD 37171 [250]							1,2	— 3 —		4,5		
	HD 36895 [300]							———	2 ———		3,4		
	HD 36861 [325]					3,4		5	— 6 —		7	— 8 —	
	HD 36894 [350]					1,2		3	— 4 —		5,6		
	HD 37490 [400]							2	— 3 —		4,5	— 6 —	
	HD 36881 [450]				1	2,3		———	4 ———		5,6		

(Table 4.1), show weak absorption around $\approx +26$ km s^{-1}, a velocity corresponding to saturated absorption observed towards many of the association stars. Observations of Na I and Ca II towards HD 35468 (Welsh *et al.*, 1990; Vallerga *et al.*, 1993, respectively) confirm our detection. Similarly for HD 37320 and HD 37171, both located towards the centre of the association at a distances of ≈ 170 & 250 pc respectively, exhibit strong but not saturated absorption around +25 km s^{-1}. This suggests that while a small proportion of the absorption in the saturated region may occur within 75 pc of the Sun, the majority originates beyond this distance. This bolsters the idea that the saturated region is the result of many unresolved blends.

λ Ori, ϕ^1 Ori, HD 36894, HD 36895 and HD 36881 all lie towards the centre of the λ Ori association and as a result possess very similar line profiles. The differences which are present are likely due to their differing distances (more distant stars probing a larger number of clouds), rather than the detection of small-scale interstellar structure (see Chapter 5 for further details of small-scale structure). The saturated Na I absorption around 25 km s^{-1} (λ**10**) is essentially identical towards each star, while the +5 to +20 km s^{-1} region shows additional components at $\approx +9$ km s^{-1} towards both λ Ori and HD 36894; and at +13 km s^{-1} towards HD 36894. Extending this comparison to HD 36881, we see substantially more absorption at +18 & +30 km s^{-1}. This suggests λ Ori, ϕ^1 Ori, HD 36894 and HD 36895 to each be located at similar distances; the small differences in component structure suggesting ϕ^1 Ori and HD 36895 to be the closest, HD 36894 the furthest and λ Ori to probably lie somewhere between. HD 36881 would then be located significantly further, possibly behind the rear side of the λ Ori shell. The distance to HD 36895 would therefore be close to the lower limit found by Hipparcos (ESA, 1997), and HD 36894 (for which an Hipparcos distance is not known) would be located at ≈ 350 pc (similar to our derived photometric distance).

An examination of the Ca II K spectrum of HD 36881 highlights very strong absorption, particularly at more positive velocities; however, as discussed in § 4.2.1, a significant proportion is likely to come from a blended stellar line. With the removal of the modelled stellar Ca II K line, strong interstellar Ca II K is present to a velocity of $\approx +30$ km s^{-1}, somewhat lower than would be expected for the far side of the shell (35 km s^{-1}; Table 4.1). Furthermore, the saturated Na I absorption at this velocity (if occurring within the same gas as the Ca II K absorption) characterises this gas with a much larger Na$^{\circ}$/Ca^{+} abundance ratio than the near side of the shell observed towards λ Ori. However, HD 36881 may

still be present beyond the far side of the shell since uncertainty in the location/strength of the stellar line makes it difficult to detect possible absorption from the far side of the shell. Two Ca II components are present in the spectrum of HD 36881 at velocities near that expected for material in the near side of the shell (+4.39 & +9.86 km s^{-1} Table 4.6). Both of these components bear significant similarity (values of $v_{\odot}$, b, N and Na°/Ca^{+}) to the shell material observed towards λ Ori in both the UHRF and MSES data and have therefore been associated with λ**5**.

HD 37490 exhibits strong, but not saturated Na I absorption over a relatively wide velocity range. The line-of-sight to HD 37490 intersects a large number of interstellar clouds, suggesting it to indeed be located at a large distance; however, a comparison with the interstellar spectrum of HD 36881 suggests it to be in its foreground (unless the significant Na I absorption detected towards HD 36881 to be specifically related to the λ Ori association). Ca II absorption from shell material is expected to occur around +21 km s^{-1} for HD 37490 since it is located towards the periphery of the shell. Ca II absorption is detected at this velocity but cannot be confidently attributed to the shell material since it does not appear particularly strong and is therefore blended with neighbouring (in velocity space) absorption. Furthermore, Na I absorption present at the same velocity (if occurring within the same cloud), suggests the cloud to have a much larger Na°/Ca^{+} ratio than is expected for the shell material.

The unusual interstellar spectrum of HD 36653 exhibits strong absorption around +1 km s^{-1}. HD 36653 lies at a distance of only 157 pc, thus this absorption cannot be ascribed to a cloud present behind the λ Ori association. Although strong absorption is not seen at this velocity in the other sightlines observed here, η Ori (located to the south of Orion's belt), does exhibit saturated Na I absorption at velocities as low as +5 km s^{-1} (Hobbs, 1969*a*; Welty *et al.*, 1994); however, the absorption observed towards these two stars is not expected to be associated.

4.4 Conclusions

We have obtained ultra-high-resolution ($R \approx 9 \times 10^5$) observations of λ & ϕ^1 Ori and high-resolution ($R \approx 1 \times 10^5$) observations of 12 targets located in and around the association. These data represent the highest resolution interstellar line observations obtained for many of these targets.

Line profile modelling of the UHRF data has enabled the identification of many individual interstellar clouds, while the MSES data has allowed the further analysis of the interstellar matter in this direction. A comparison of the individual clouds observed in each sight-line has been used to identify velocity systems, given in Table 4.14. This has provided an indication as to the likely line-of-sight velocity structure of the absorbing medium.

Our observations have revealed the presence of shell material in the line-of-sight to both λ & ϕ^1 Ori (and possibly HD 34989). The velocities at which the absorption components are found agree with those expected from the kinematical ring model developed by Maddalena and Morris (1987) and show the observed ring to actually be a shell; however, the small number of sightlines probed does not rule out the possibility that the shell is incomplete.

Furthermore, the comparison of absorption occurring in closely spaced sightlines has also allowed the relative distances to stars to be gauged. The distance to HD 36895 is expected to be $\approx$ 300 pc, close to the lower limit measured by Hipparcos (ESA, 1997). HD 36894 is expected to be located at a distance of $\approx$ 350 pc, similar to our derived photometric distance.

Chapter 5

Small-Scale Structure in the Interstellar Medium[1]

The comparison of our observations with those reported in previous studies has revealed the presence of temporal variability in the interstellar absorption line profiles of two stars, δ and ζ Ori. Additional observations of δ Ori reveal further variability in this sightline. Furthermore, the comparison of observations of the closely spaced stars δ Ori A & C reveal differences in the absorption occurring in these two sightlines. Both of these detections highlight the presence of small-scale structure in the interstellar medium over scales down to only a few astronomical units.

5.1 Introduction

In recent years there has been an intriguing development in the study of the interstellar medium (ISM). It had been previously thought that the ISM did not possess significant structure below scales of approximately one parsec. However, it has now become clear that the ISM, especially the so called "cold neutral medium" (discussed in § 1.1.1), exhibits significant structure on scales as low as tens of astronomical units (reviewed by Heiles, 1997).

The primary method by which small-scale interstellar structure has been detected is through the observation of extended or closely spaced targets. The detection of differences

[1] The majority of the work presented in this chapter has been previously published in Price *et al.* (2000), Price *et al.* (2001*a*) and Price *et al.* (2001*b*)

in the absorption occurring in these closely spaced sightlines reflects differences in the line-of-sight structure of the intervening absorbing gas, therefore highlighting the presence of small-scale structure in the ISM.

Small-scale interstellar structure may also be detected through the observation of temporal variability in an interstellar absorption line profile. Such a detection is interpreted as a change in the column of gas, most likely due to the motion of a cloud across the line-of-sight. This directly implies the absorbers to be located in a spatially small parcel of gas, since even if the cloud has a relatively large velocity, its tangential size must be small.

In this chapter we report the detection of small-scale interstellar structure through both of these methods. Detection through temporal variability will be discussed in § 5.2 while detection through binary observations will be discussed in § 5.3.

5.2 Search For Temporal Variability

5.2.1 Introduction

The earliest reported detection of variability in an optical interstellar absorption profile appears to be that observed towards HD 72127, located behind the Vela supernova remnant; where rapidly moving small-scale structure might be expected (Hobbs *et al.*, 1982, 1991). Further detections of temporal variability have also been made towards HD 72089 and HD 72997 by Danks and Sembach (1995) and towards 7 out of 13 stars observed by Cha and Sembach (2000), which also lie behind the Vela supernova remnant. The very low $N(\mathrm{Na}^{\circ})/N(\mathrm{Ca}^{+})$ ratio towards HD 72127 (0.11; Hobbs *et al.*, 1982) is certainly consistent with grain destruction resulting from supernova induced shocks, although Danks and Sembach (1995) found larger values towards their stars, which they attributed to less than total grain destruction. Blades *et al.* (1997) also report transient interstellar absorption towards HD 28497 which lies behind an expanding shell of neutral hydrogen surrounding the Orion-Eridanus (Ori-Eri) superbubble (the Ori-Eri superbubble is discussed in more detail in § 3.3.1).

Reports of temporal variations in interstellar neutral hydrogen absorption have also been made by Frail *et al.* (1994), who utilise multi–epoch observations of 21–cm absorption towards high-proper-motion pulsars. The recent surge in activity in this area seems to have led to the re-discovery of the work presented by Dieter *et al.* (1976) and a host of other VLBI observations of extended extragalactic sources (discussed further in § 5.3), which point to the existence of small-scale interstellar structure.

The detection of temporal variability of optical absorption lines appear to be rare, with only a handful of detections made thus far. However, more recently, the rate at which these detections have been reported in the literature has increased. Reports of temporal variability in interstellar absorption lines have been made by Lauroesch *et al.* (2000), Crawford *et al.* (2000), Danks *et al.* (2000) and Welty and Fitzpatrick (2001). This is likely to be a result of the increasing quality (higher resolution/higher signal-to-noise) of newly acquired data and an increasing catalogue of existing data with which new observations may be compared.

With the exception of the variability detected towards κ Vel by Crawford *et al.* (2000), much of the temporal variability detected thus far is generally associated with dynamic gas in structures such as the Vela supernova remnant, Carina Nebula, or the Ori-Eri shell.

It is interesting to note that a compilation of Galactic shells made by Gahm (1994, cf. his figures 1 & 3) shows essentially all sightlines to intersect shell material at some point, suggesting that temporal variability may be rather common.

Previous observations of interstellar absorption toward the stars observed here have been made at a variety of resolutions, and include the studies by Hobbs (1969*a*); Marschall and Hobbs (1972); O'Dell *et al.* (1993); Welty *et al.* (1994, 1996); Welty and Hobbs (2001). The resolving power achieved by the Ultra-High-Resolution Facility (hereinafter UHRF) exceeds that of these earlier observations, although the Na I survey of Welty *et al.* (1994) did employ a comparable resolving power ($R = 6 \times 10^5$), while the Welty *et al.* (1996) Ca II survey (conducted mainly with a resolving power of $R = 2.5 \times 10^5$) included two UHRF observations of stars also observed here. Hobbs (1969*a*) estimated the resolving power of the PEPSIOS Fabry-Perot interferometer to be approximately 6×10^5, although a comparison between PEPSIOS and UHRF observations (Barlow *et al.*, 1995) suggested that the resolving power of the former was probably in the range $R \approx (1\text{–}2) \times 10^5$, and certainly not exceeding $R = 3 \times 10^5$ on data sampling grounds. For the purposes of comparison, we here assume a value of $R = 2 \times 10^5$ for the PEPSIOS data.

Comparisons have primarily been made with the studies by Welty *et al.* (1994, 1996); Welty and Hobbs (2001) and O'Dell *et al.* (1993), for which absorption models have been published. By reconstructing the relevant absorption models presented by the aforementioned authors it becomes easy to compare their observations with ours. Additional comparisons have also been made with the observations by Hobbs (1969*a*) and Marschall and Hobbs (1972); however, the presence of telluric absorption in the Na I spectra presented by the former, limits our ability to identify confidently temporal variability.

The small discrepancy in velocity scales found between our data and those of Welty *et al.* (1994, noted in § 2.2.4) has been allowed for through the application of small velocity shifts to the Welty *et al.* (1994) data, in order to achieve maximum agreement between data-sets.

During these comparisons the velocity resolution of our observations was degraded (through convolution with a Gaussian profile) to an *effective* level, equal to that utilised in the observations with which the comparison was being made. In order to calculate the width of the Gaussian profile appropriate to degrade the resolution of one observation to a level of another, the FWHM resolving power of both instruments need to be known.

For example, if we wish to compare an observation of a line with an intrinsic width, $I_{\rm int}$, made using an instrument with a velocity resolution, $FWHM_{\rm i}$, with an observation of the same line made using another instrument with a velocity resolution, $FWHM_{\rm j}$ (where $FWHM_{\rm i} < FWHM_{\rm j}$), then the width of the appropriate Gaussian profile, $FWHM_{\rm x}$, is given by,

$$FWHM_{\rm x}{}^2 = FWHM_{\rm j}{}^2 - FWHM_{\rm i}{}^2. \tag{5.1}$$

Thus, the width of the observed line ($I_{\rm obs}$) will be equal in both the data from the lower-resolution instrument, and the degraded data from the higher-resolution instrument, specifically,

$$I_{\rm obs} = \sqrt{I_{\rm int}^2 + FWHM_{\rm j}{}^2} = \sqrt{I_{\rm int}^2 + FWHM_{\rm i}{}^2 + FWHM_{\rm x}{}^2}. \tag{5.2}$$

In this way, we hope that any detected variations cannot be ascribed to the different resolving powers employed. Several examples of possible variability have been found. These are discussed individually in § 5.2.2 to 5.2.8 below.

5.2.2 δ Orionis

The O 9.5 II star δ Ori A (HD 36486) is the most westerly of the three stars defining Orion's Belt. It gained historical significance when Hartmann (1904) discovered the presence of stationary absorption lines in its spectrum, a detection which launched the study of the ISM.

As detailed in Table 2.1, a total of three 1200 s integrations of Na I D_1 and a single 1200 s integration of Ca II K were obtained with the UHRF in 1994. These observations may be compared with observations presented in earlier studies, which include those of Hobbs (1969*a*, 1984); Marschall and Hobbs (1972); Frisch *et al.* (1990); Welty *et al.* (1994, 1996).

Figure 5.1 shows a comparison of the earlier high-resolution spectra. In the case of Na I, Figure 5.1(a) highlights a clear and consistent increase in the strength of the +21 km s^{-1} component between 1966 and 1994. In the case of Ca II, Figure 5.1(b) highlights good agreement between the UHRF and Welty *et al.* (1996) data (which were both obtained in 1994), but the spectrum of Marschall and Hobbs (1972) (obtained in 1970), shows only

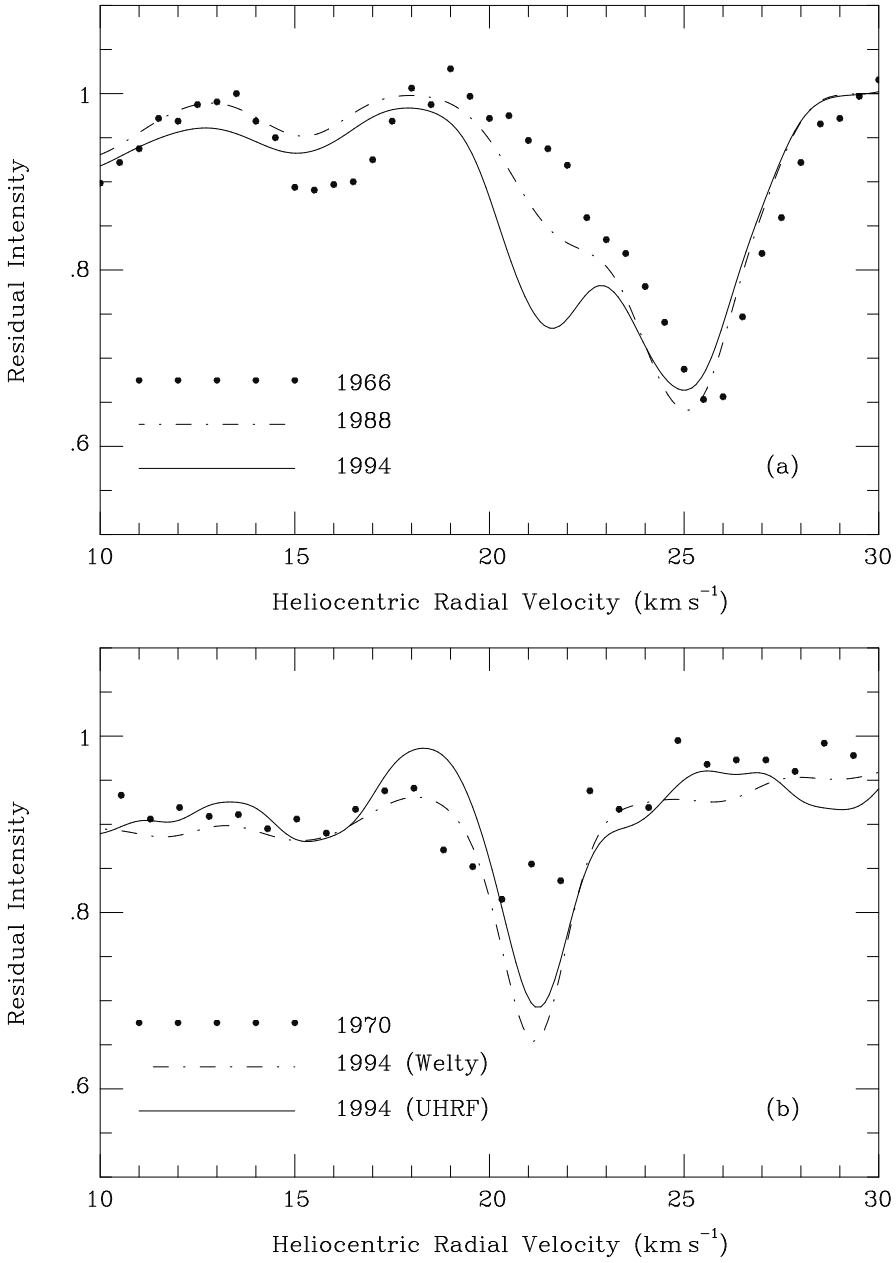

Figure 5.1: Comparison of (a) Na I and (b) Ca II observations towards δ Ori A on the dates indicated (c.f. Table 5.1). All the spectra have been reduced to a common, effective, resolving power of $R = 2 \times 10^5$.

weak absorption at this velocity. Thus, in agreement with the Na I results, a consistent increase in the Ca II absorption strength is found to have occurred between 1970 and 1994. Each of the spectra in Figure 5.1 have been plotted with an effective resolving power of $R = 2 \times 10^5$, making it clear that resolution effects are not responsible for the line profile variability. Table 5.1 summarises the previous high-resolution ($R > 10^5$) observations, and includes the estimated residual line intensity at a velocity of +21 km s^{-1}, in both the original spectra and at the common resolving power of 2×10^5.

A number of simple checks were performed in order to exclude the possibility that the apparent variation is an artefact. Each of the three individual 1994 Na I spectra were examined, and found to exhibit the same enhancement in line strength. Moreover, examination of the individual CCD images, and of the flatfield frames, revealed no anomalous features at this location in the spectra. As discussed in § 2.2.6, the removal of telluric water lines from the Na I spectra was achieved by the division by an atmospheric template spectrum, taken to be that observed towards the bright, lightly-reddened star α Vir. α Vir actually exhibits a single weak interstellar Na I absorption component at a heliocentric radial velocity of -11.2 km s^{-1}(Welsh *et al.*, 1990). At the time of observation, the α Vir cloud was located at a geocentric radial velocity of ≈ -40 km s^{-1} (a result of a combination of the Earth's orbital and rotational motion), whereas the geocentric radial velocity of δ Ori's variable component was $\approx +39$ km s^{-1}. The Na I absorption towards α Vir is therefore well clear of the region of interest here and can have played no part in the detection of the temporally variable component. Furthermore, we note that no atmospheric absorption was found to coincide with the location of the transient component reported here. Telluric sodium, which is known to occur with varying strengths (McNutt and Mack, 1963), is not observed here, consistent with its detection only during the winter. Moreover, absorption from telluric sodium, would if present, be at a geocentric radial velocity of 0 km s^{-1} and therefore not affect the variable component observed here. Additionally, the detection of the transient cloud in both Na I and Ca II at the same velocity (where the Na I exhibits clear hyperfine splitting with the expected 3:5 ratio) strongly implies the detection to be genuine.

Following the identification of this time-variable absorption component toward δ Ori A, two further UHRF spectra of the Na I D_1 region were obtained to investigate the phenomenon in more detail. The first of these was obtained through UHRF user observations by I. A. Crawford in 1999 July 31, the second was obtained through UHRF service obser-

Table 5.1: A comparison of previous high-resolution ($R > 10^5$) observations of interstellar lines towards δ Ori A. Columns 5 and 6 indicate the residual line intensity of the absorption found at +21 km s^{-1}, as measured from the original observations ($R_{\rm orig}$), and at the common, effective, resolving power of $R = 2 \times 10^5$ (R_{2e5}) shown in Figure 5.1. Column 7 gives the heliocentric radial velocity of the transient component. Column 8 gives the equivalent width of the transient component (* estimated from published spectrum; † estimated from published absorption parameters. In the case of Welty *et al.* (1994) the upper limit is due to the fact that the component they identify at this velocity is actually a blend of the variable component and the two, presumably stable, adjacent components identified in our higher resolution data). Column 9 gives the total equivalent width of the line profile (‡ values given in Hobbs (1974)).

1	2	3	4	5	6	7	8	9
Region	Reference	Observation Date	Resolution	Residual Line Intensities $R_{\rm orig}$	R_{2e5}	$v_\odot$[transient] km s^{-1}	W_λ[transient] (mÅ)	W_λ[total] (mÅ)
Na I D_1	Hobbs, 1969	1966	2×10^5	0.95	0.95	n/a	$\lesssim 5.0^*$	$49^\ddagger$
	Welty et al., 1994	1988	6×10^5	0.82	0.85	+21.81	$< 9.3^\dagger$	42.6
	This study	1994	9×10^5	0.64	0.74	$+21.3 \pm 0.1$	11.0 ± 1.0	60.8 ± 0.2
Ca II K	Marschall & Hobbs, 1972	1970	2×10^5	0.85	0.85	$+20.8 \pm 0.4$	$4.0 \pm 1.0^*$	$21^\ddagger$
	Welty et al., 1996	1994	2.5×10^5	0.62	0.66	+21.19	$6.8^\dagger$	45
	This study	1994	9×10^5	0.50	0.65	$+21.3 \pm 0.1$	9.4 ± 1.5	36.1 ± 2.0

vations in 2000 March 15. These new data highlight a consistent reduction in the strength of the absorption component at $\approx +21$ km s^{-1} from 1994 to 1999 and from 1999 to 2000. In the latter case, the changes highlight variations in the line-of-sight structure of the transient cloud over a period of only 7.5 months. Independent modelling of these new data does not allow the true changes in the variable component to be measured since they are, to some extent, masked by *phantom* changes in the neighbouring components (for which there is no evidence for variability). In fact, the lower signal-to-noise ratio achieved in the 1999 data only permits the use of 9 absorbing components. In order to remove this effect, absorption models may be produced with all parameters, apart from those of the transient component, constrained in one of two ways.

Fixed Method

The parameters of the non-variable components in the 1999 and 2000 data may be fixed to those found through the modelling of the higher signal-to-noise 1994 Na I D_1 spectrum; which, apart from changes associated with the transient component at a velocity of $+21.3$ km s^{-1}, appears identical. The parameters of the variable component are unconstrained and as a result take up values which produce the minimum available rms residuals in each data-set.

Synchronised Method

Following the further development of the VAPID routine by Prof. I. D. Howarth, it became possible to model each of the Na I data-sets simultaneously, with the parameters of the non-variable absorption components synchronised. This is achieved by allowing the parameters of the non-variable components to vary between each iteration performed by VAPID, so as to achieve the minimum rms residual, while at the same time forcing these parameters to be equal in each of the three data-sets. This method allows information on the non-variable components to be gleaned from each of the available data-sets. The parameters of the single variable absorption component at $\approx +21$ km s^{-1} are unconstrained so that the optimum fit may be found in this region, in each data-set. To ensure that the varying signal-to-noise ratios of each of the three data-sets are allowed for in this modelling procedure, the errors on each data-point in each data-set have been weighted by (1/SNR) where SNR is the signal-to-noise ratio achieved in that data.

Simultaneous modelling of the data in this manner yields more accurate information

about the changes experienced by the variable component. Table 5.2 lists the results of the constrained modelling of the δ Ori Na I data, via both of the aforementioned methods.

A comparison of the models obtained through each of the techniques (unconstrained; fixed; synchronised) highlights a strong consistency between the procedures. Firstly, with regard to the variable component, the parameters derived from each of the three modelling methods are mutually consistent for each of the observation dates. Secondly, with regard to the non-variable components, each of the parameters in the fixed model are well within the mutual errors of their counterparts in the synchronised model. Comparing the results of the unconstrained model to the 1994 data with those of the fixed and synchronised models shows the parameters to also be largely the same. In the case of the unconstrained model of the 1994 data, the parameters are, by definition, identical to those of the fixed model, and therefore also consistent with the synchronised model.

Figure 5.2a shows the UHRF spectra observed towards δ Ori A in 1994, 1999 and 2000. The data-sets are overplotted with the best fitting synchronised model profiles and off-set by an arbitrary amount for clarity. Figure 5.2b shows each of the synchronised model overplotted, illustrating the variations in the line profile graphically.

5.2.2.1 Location of the Transient Component

δ Ori is a well-known multiple star system: δ Ori A (HD 36486, V = 2.2), discussed further below; δ Ori B ($V = 14.0$), with a separation of 33 arcsec; and δ Ori C (HD 36485, $V = 6.85$), with a separation of 52 arcsec. Both B and C are sufficiently distant from A not to contribute to the observed flux from δ Ori A. However, δ Ori A is itself a multiple system: the primary is an eclipsing spectroscopic binary, with an orbital period of 5.73 days and a velocity amplitude of 97.9 km s^{-1} (Harvey *et al.*, 1987). The two stars are classified as O9.5 II and B1 III/IV (Galkina, 1976; Koch and Hrivnak, 1981), with somewhat uncertain V magnitudes of 2.90 and 4.4 respectively; both stars are significantly evolved from the main sequence. In addition, a third star, δ Ori D, was detected by Heintz (1980) and McAlister and Hendry (1982). The Hipparcos survey (ESA, 1997) found δ Ori D to be 1.35 magnitudes fainter, and 0.27 arcsec away from, δ Ori A. The small separations of these three stars leads to the observations being a composite of flux from all three.

Given the complex environment and the evolved nature of the component stars, a circumstellar origin for the variable absorption component reported here may at first sight appear the most likely. Indeed, δ Ori A is known to be losing a significant amount of

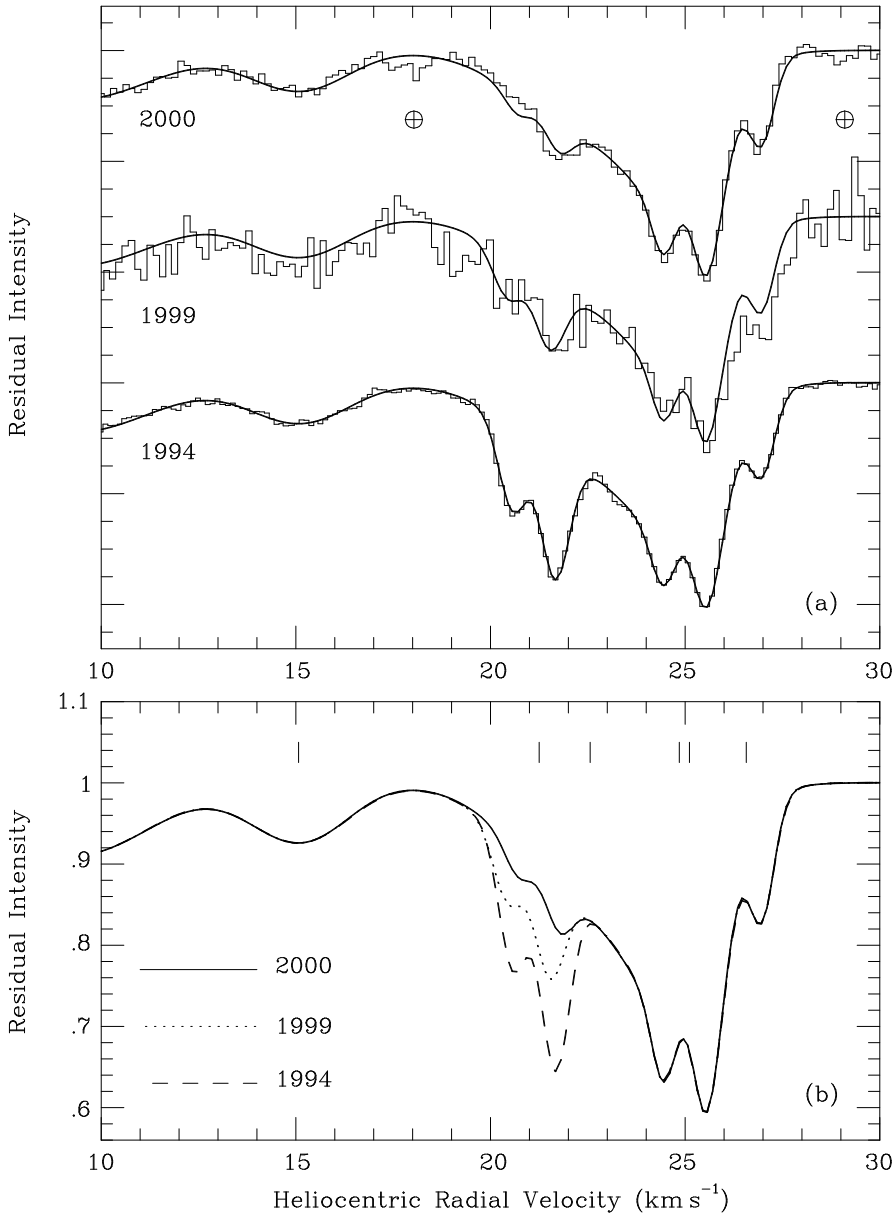

Figure 5.2: A comparison of the UHRF Na I D_1 spectra observed toward δ Ori A. Figure 5.2(a) displays spectra observed towards δ Ori A in 1994, 1999 and 2000, each is overplotted with its corresponding synchronised absorption model. Each spectrum is off-set by an arbitrary amount for clarity. The two features in the 2000 spectrum indicated with the symbol '$\oplus$' are the locations of residual telluric contamination which has not been fully removed. Figure 5.2(b) shows the 1994 (dashed line), 1999 (dotted line) and 2000 (solid line) synchronised absorption models overplotted, thus highlighting the variability in the +21.3 km s^{-1} component. The tickmarks indicate the velocities of the individual model components listed in Table 5.2.

Table 5.2: Constrained absorption models derived for δ Ori A in 1994, 1999 and 2000. Columns 3 & 4 display the signal-to-noise ratio and total equivalent width for each observation. Columns 6-8 display values of $v_\odot$, b and N for the fixed absorption model while columns 9-11 display the results of the synchronised absorption model. In both models, the non-variable component parameters are identical for each observation date and are listed separately from the variable component parameters. The variable components are identified with a †, cf. Table 3.4.

1	2	3	4	5	6	7	8	9	10	11
		S/N	W_λ	Comp	$v_\odot$ (km s^{-1})	b (km s^{-1})	log N (cm^{-2})	$v_\odot$ (km s^{-1})	b (km s^{-1})	log N (cm^{-2})
					Fixed Method			Synchronised Method		
Variable component:	1994	185	60.8 ± 0.2	$6^\dagger$	21.25 ± 0.01	0.45 ± 0.01	10.94 ± 0.02	21.26 ± 0.01	0.45 ± 0.01	10.94 ± 0.01
	1999	31	60 ± 3	$6^\dagger$	21.26 ± 0.07	0.44 ± 0.09	10.60 ± 0.05	21.13 ± 0.07	0.47 ± 0.09	10.64 ± 0.05
	2000	82	54 ± 1	$6^\dagger$	21.39 ± 0.05	0.39 ± 0.06	10.24 ± 0.04	21.38 ± 0.06	0.42 ± 0.07	10.23 ± 0.07
Non-variable components:				1	-4.92 ± 0.12	0.83 ± 0.23	9.86 ± 0.06	-4.95 ± 0.13	0.85 ± 0.23	9.85 ± 0.07
				2	0.03 ± 0.34	2.44 ± 0.46	10.37 ± 0.08	0.23 ± 0.32	2.72 ± 0.47	10.42 ± 0.07
				3	4.72 ± 0.20	2.12 ± 0.43	10.52 ± 0.11	4.84 ± 0.17	1.95 ± 0.34	10.49 ± 0.10
				4	9.32 ± 0.12	2.63 ± 0.18	10.96 ± 0.03	9.31 ± 0.10	2.67 ± 0.16	10.97 ± 0.02
				5	15.07 ± 0.04	1.56 ± 0.07	10.68 ± 0.01	15.07 ± 0.04	1.54 ± 0.06	10.67 ± 0.01
				7	22.56 ± 0.53	2.41 ± 0.33	11.12 ± 0.11	22.84 ± 0.22	2.51 ± 0.13	11.19 ± 0.04
				8	24.85 ± 0.07	1.38 ± 0.15	11.16 ± 0.10	24.88 ± 0.04	1.22 ± 0.09	11.10 ± 0.05
				9	25.11 ± 0.01	0.36 ± 0.02	10.74 ± 0.04	25.12 ± 0.01	0.34 ± 0.02	10.70 ± 0.04
				10	26.57 ± 0.01	0.38 ± 0.03	10.54 ± 0.04	26.58 ± 0.01	0.38 ± 0.02	10.57 ± 0.03

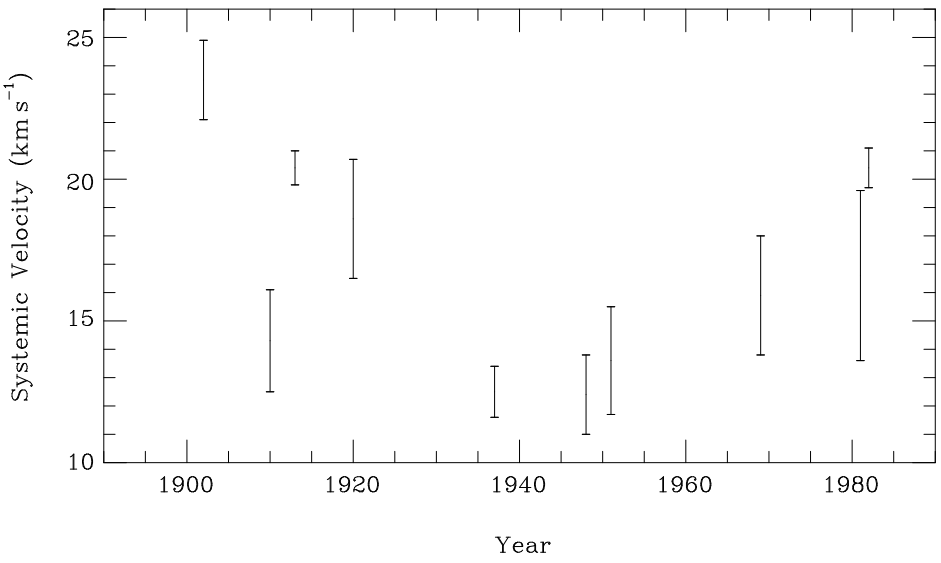

Figure 5.3: Systemic velocity measurements made of δ Ori A, taken from Table II of Harvey *et al.* (1987).

mass through a stellar wind ($\dot{M} \approx 10^{-6}\ M_{\odot}$ yr^{-1} Howarth and Prinja, 1989). Moreover, there have been various claims for the presence of circumstellar shells and envelopes, with expansion velocities ranging from 50 km s^{-1} (Singh, 1982) to 550 km s^{-1} (Galkina, 1976). However, the low radial velocity of the transient component is not consistent with an origin in such high-velocity shells. Moreover, a circumstellar origin in the vicinity of one or other of the spectroscopic binary stars is effectively excluded by the fact that this component has maintained a constant heliocentric velocity ($+21.3 \pm 0.5$ km s^{-1}; Tables 5.1 & 5.2) for at least 29 years, rather than sharing in the extreme (± 97.9 km s^{-1}) orbital velocity of the binary.

Absorption in a common envelope around *both* stars would not show this effect, but might be expected to be centred on the systemic velocity of the system. It is true that the velocity of this component, +21 km s^{-1}, is actually quite close to recent measurements of the systemic velocity (e.g. Harvey *et al.*, 1987). However, there is good evidence that the systemic velocity is in fact changing with time, whereas that of the variable absorption component is not. The various earlier measurements of the systemic velocity of δ Ori A ($V_{\circ}$) are plotted in Figure 5.3 (taken from Table II of Harvey *et al.*, 1987). They appear to indicate a velocity variation with a minimum value during the 1940's, and a period of the order of a century (consistent with a value suggested by Koch and Hrivnak, 1981), and possibly resulting from orbital interaction with δ Ori D. However, these velocity

variations are not echoed by the velocity of our transient component, and this apparent stability suggests it arises either in a common envelope around both δ Ori A and δ Ori D, or within the foreground ISM.

If the variable absorption does indeed arise in the foreground ISM, then the fact that its strength has varied significantly over only three decades indicates either a high tangential velocity, or a small spatial extent, for the absorbing cloud. By assuming a plausible upper limit of 50 km s^{-1} on the transverse velocity, and a transit time of 30 years (i.e. for the cloud to pass into and out of the line-of-sight), a length scale of < 300 AU can be imposed on the cloud. In this respect, it is notable that such small-scale structures have recently been detected in the ISM, on the basis of both pulsar dispersion measures (Frail *et al.*, 1994) and optical absorption lines towards the components of closely-spaced multiple star systems (Watson and Meyer, 1996). Indeed, both these studies concluded that such small-scale structure in the ISM may be ubiquitous. Thus the small spatial scale implied by the variability of this component towards δ Ori A cannot in itself be used to exclude an interstellar origin.

Furthermore, the comparison of the observations obtained in 1999 and 2000, illustrate the transient component to have undergone a significant change in column density over a period of only 7.5 months. For the period 1994-1999, a reduction in N[Na°] of 4.7×10^{10} cm^{-2} is observed, constituting a 54% change; for the period 1999-2000, a reduction in N[Na°] of 2.2×10^{10} cm^{-2} is observed, constituting a 55% change. If we again assume an upper limit of 50 km s^{-1} for the cloud velocity, the 1999-2000 variability represents detectable structure over scales < 6.6 AU.

Of course if the cloud is assumed to be stationary, its implied linear size is reduced substantially. In this situation, the changes in the line profile are due only to the displacement of the line-of-sight, a result of the proper motion of δ Ori. With a distance of 281 pc (Table 3.2) and a proper motion of 1.76×10^{-3} arcsec yr^{-1} (ESA, 1997), a linear distance of 0.5 AU is traversed by the line-of-sight (at the distance of δ Ori) each year. Thus a 30 year transit period would correspond to a cloud size of < 15 AU; the variability observed between 1999 and 2000 would then correspond to detectable structure over < 0.3 AU.

5.2.2.2 Physical Conditions of the Transient Component

Additional information concerning the physical conditions in the material giving rise to the variable component, and thus constraints on its proximity to the δ Ori system, can be provided by the line widths and the Na° to Ca^+ abundance ratio.

Line widths

The velocity dispersion parameter, b (which is discussed in more detail in § 1.2.1), is a measure of the width of a line. By assuming the case of purely thermal broadening ($v_t = 0$ km s^{-1}) it is possible to obtain a rigorous upper-limit to the transient cloud's kinetic temperature from the observed b-value. The very low line broadening measured for Na I, ($0.39 < b < 0.47$ km s^{-1}; Table 5.2) is characteristic of low gas temperatures. In the case of the 1994 observations, where the broadening in the line is more accurately determined (the greater strength of the component results in less blending with neighbouring absorption leaving the broadening–sensitive hyperfine structure more clearly defined), $b = 0.45$ km s^{-1}, corresponding to a limit of $[T_k]_{Na^0} \leq 280$ K. This is typical of interstellar cloud values, and shows no evidence for significant heating from nearby hot stars. The slightly broader line for the heavier Ca^+ ion yields $[T_k]_{Ca^+} \leq 1326$ K, although we note that the higher S/N data of Welty *et al.* (1996), yields $[T_k]_{Ca^+}$ to be $\leq$ 872 K.

Despite the fact that both the Na I and Ca II absorption have been observed to increased in strength over the same period (1966-1994), and must therefore be physically associated in some way, the fact that the absorption component due to the heavier Ca^+ ion is broader than that produced by Na°, means that the two species cannot be well-mixed spatially, as no combination of thermal and turbulent processes can reproduce the observed line widths. This effect is commonly observed in interstellar clouds, and is attributed to Ca^+ occupying a warmer and/or more turbulent (presumably outer) region of the cloud than Na°.

By assuming T_k= 0 K in Equation 1.13, we may similarly obtain rigorous upper limits to the turbulent velocity. This analysis yields $[v_t]_{Na^0} \leq 0.32$ km s^{-1}, and $[v_t]_{Ca^+} \leq 0.52$ km s^{-1} (our data) or $[v_t]_{Ca^+} \leq 0.42$ km s^{-1} (Welty *et al.*, 1996). Moreover, we find that the full, three-dimensional, turbulent velocity, $\equiv \sqrt{3}v_t$, is definitely subsonic, unless the kinetic temperature is very low (< 40 K for Na°). These low, sub-sonic, turbulent velocities are more in keeping with the diffuse ISM, than with the energetic circumstellar

environment of hot stars.

The Na°/Ca$^+$ ratio

We obtain a Na° to Ca$^+$ ratio of 0.74 ± 0.09 for the transient component in 1994 (using the value of N[Na I] obtained via the synchronised method); using the Ca$^+$ column density of Welty *et al.* (1996), where the component is probably better defined, gives a similar ratio of 0.91. As discussed by Crawford (1992, and references therein) these values are typical of values found in diffuse (non-molecular) interstellar clouds characterised by $n_{\rm H} \sim 10$ cm^{-3} and $T_{\rm k} \sim 100$ K, in which Ca atoms are significantly, although not entirely, depleted onto grain surfaces (specifically, $\delta_{\rm Ca} \approx -2$, where $\delta_{\rm Ca}$ is the logarithmic Ca depletion factor, relative to a gas of solar composition). This significant Ca depletion further suggests an interstellar location of the absorbing gas, as the energetic circumstellar environment of δ Ori might be expected to lead to partial or total grain destruction, resulting in $N({\rm Na}^\circ)/N({\rm Ca}^+) \lesssim 0.1$ (Crawford, 1992).

On the other hand, the fact that the observed $N({\rm Na}^\circ)/N({\rm Ca}^+)$ ratio is much smaller than the large values ($\gtrsim$10) typically found in dense ($n_{\rm H} \sim 10^3$ cm^{-3}) molecular clouds, where essentially all of the gas-phase Ca has become adsorbed on grain surfaces (Crawford, 1992, and references therein), is also of interest. As noted by Watson and Meyer (1996), the small spatial extent implied by time-variable interstellar lines implies an implausibly high cloud density unless the geometry is highly non-spherical. In the present case, taking the empirical relationship between $N({\rm Na}^\circ)$ and $N({\rm H})$ obtained by Ferlet *et al.* (1985),

$$\log N({\rm Na}^\circ) = 1.04[\log N({\rm H} + {\rm H}_2)] - 9.09, \tag{5.3}$$

and a path length of 300 AU (the upper limit to the *transverse* extent of the cloud found above), we obtain $n_{\rm H} \gtrsim 4 \times 10^3$ cm^{-3}. Similarly, if we assume there to be no cloud motion and the variability is solely due to the proper motion of δ Ori, a spatial density of $n_{\rm H} \gtrsim 8 \times 10^4$ cm^{-3} is required. Unless the material is far from equilibrium for some reason, such a high density is inconsistent with a $N({\rm Na}^\circ)/N({\rm Ca}^+)$ ratio of order unity, as observed.

Similarly high spatial densities are implied for the small-scale structure detected by Frail *et al.* (1994). Variations in H I absorption towards high-proper-motion pulsars is seen to occur over periods of ≈ 1 year. By assuming these changes to occur as a result of the pulsars' proper-motion, Frail *et al.* (1994) identify structure down to size scales of 5 AU.

Assuming these clouds to be spherical in some cases implies spatial densities in excess of 10^6 cm^{-3}. However, Gwinn (2001) has suggested that the variations in H I absorption observed towards pulsars may arise as a result of velocity gradients in the absorbing gas across the scattering disk. Such velocity gradients may also account for the variations in H I absorption detected over extended sources (e.g. Dieter *et al.*, 1976, see § 5.3).

Temporal variability in Na I has also been observed towards HD 32040 by Lauroesch *et al.* (2000). Although this detection again suggests very large spatial densities, an analysis of C I fine-structure equilibrium reveals spatial gas densities of the order 20–200 cm^{-3}. Furthermore, a similar analysis of the fine-structure excitation of C I associated with small-scale structure in the direction of μ Crucis performed by Lauroesch *et al.* (1998) implies cloud densities of $n_{\rm H} < 250$ cm^{-3}. These densities are much lower than previous estimates from H I 21-cm and Na I studies and again imply the material to be present in clouds with highly non-spherical geometry.

Indeed, in his extensive study of small-scale structure in the ISM, Heiles (1997) has argued persuasively that the material responsible must exist in the form of non-spherical clouds, which are postulated to be in the form of cold ($T_{\rm k} \approx 15$ K) and dense ($n_{\rm H} \approx 10^3$ cm^{-3}) curved sheets or filaments. These structures are distributed through the cold neutral medium with random orientations, separated by warmer, less dense material. When such sheets/filaments are aligned along the line-of-sight it becomes possible to achieve large variations in column density over small transverse scales without requiring implausibly high spatial densities. In addition to the geometric solution put forward by Heiles (1997), a number of other theories have been developed to explain the existence of small-scale interstellar structure. Elmegreen (1997) has proposed a fractal structure for the interstellar gas, generated as a result of turbulent processes. His model allows for small clouds, clustered around much larger complexes. Deshpande (2000) has commented that the observations are consistent with a single power law description of the H I distribution; structure on all scales will contribute to the differences observed in neighbouring sightlines and as a result a population of small, high-density clouds is not required.

Blades *et al.* (1997) suggested that the variable absorption detected towards HD 28497 may plausibly be located within shell material present around the Orion-Eridanus superbubble. This component was found to be very narrow, $b = 0.31 \pm 0.03$ km s^{-1}, and possess a $N({\rm Na}^{\circ})/N({\rm Ca}^{+})$ ratio of > 4.5, thus resembling the temporal variability now detected

towards δ Ori. It is noteworthy that δ Ori is also located behind the expanding shell of H I which marks the boundary of the Orion-Eridanus superbubble (c.f. the maps presented in figure 8 of Brown *et al.*, 1995). It is true that, at the precise velocity range occupied by the transient component, the maps of Brown et al. appear to show a gap in the ring, but this may just reflect a lower (and non-detectable) H I column density, rather than a total absence of gas at this velocity. As for the HD 28497 case, we therefore suggest that edge-on filamentary sheets at the boundary of the Orion-Eridanus shell are the most likely cause of the absorption line variability observed towards δ Ori.

If the variable absorption is indeed arising from gas within the shell around the Orion-Eridanus superbubble, then the upper limit on the cloud's tangential velocity may be set to the expansion velocity of the shell; found to be 40 km s^{-1} by Brown *et al.* (1995). This further reduces the likely extent of the cloud to ≈ 250 AU, while the absorption variations detected between 1999 and 2000 highlight the cloud to possess internal structure over scales of less than 5.3 AU.

Additional observations of δ Ori A and δ Ori C, obtained as part of a study of absorption differences between these two closely spaced sightlines (discussed in more detail in § 5.3), may also be included in the temporal variability analysis. These new data consist of a combination of Na I D_1 & D_2 and Ca II H & K observations of both δ Ori A & C obtained with the Mount Stromlo echelle spectrograph (hereinafter MSES; operated at $R = 110,000$), and the UHRF (operated at its lowest resolution mode, $R = 380,000$).

A visual comparison of the new MSES and UHRF Na I data, obtained in 2000 February and August respectively, with the existing UHRF Na I observation obtained in 2000 March (using a common *effective* resolving power), shows no evidence for further variability in the line profiles over either of these short periods (for either δ Ori A or C). Simultaneous modelling of these data with the $R \approx 10^6$ UHRF data, via either the fixed or synchronised method (as described above), is impractical since the now very weak component 6† is not well determined in these lower resolution data.

A comparison of the available Ca II observations of δ Ori A shows there to have been no significant change in the line profile between 1994 and 2000. This is for a period where the column density of Na° was seen to decrease by a factor of 4.5. Figure 5.4 shows a comparison of the Ca II spectra obtained by us with the UHRF and Welty *et al.* (1996) (both of which were obtained in 1994) and our subsequent MSES and UHRF observations

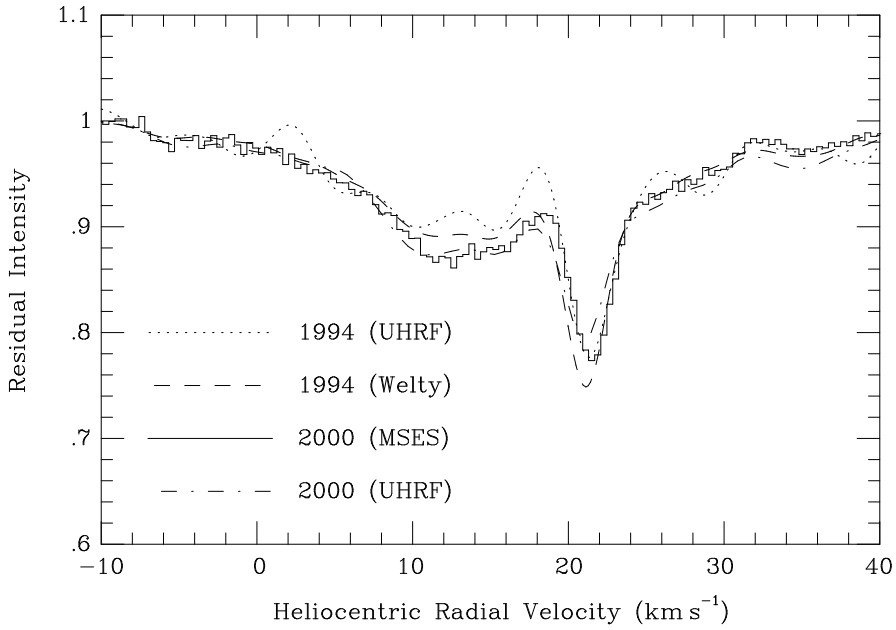

Figure 5.4: A comparison of Ca II observations towards δ Ori A made using the UHRF ($R \approx 10^6$) and Welty *et al.* (1996) (both of which were obtained in 1994) and subsequent MSES and UHRF ($R \approx 4 \times 10^5$) observations obtained in 2000.

obtained in 2000. This has, of course, resulted in a decrease in the Na°/Ca$^+$ ratio by the same factor, from 0.74 ± 0.09 in 1994 to 0.14 ± 0.04 in 2000 (using values of N[Na I] obtained via the synchronised method). The first thing to note is that even the higher of these values is still a fairly low ratio by cold neutral medium standards, where values > 1 (sometimes $>> 1$) are generally found owing to the preferential depletion of Ca onto grain surfaces (e.g. Crawford, 1992, and references therein). As discussed above, this relatively low ratio suggests an origin in either a low-density medium ($n_{\rm H} \sim 10$ cm^{-3}), or a denser environment within which adsorbed Ca atoms have been partially removed from the grain surfaces. The latter possibility strengthens the suggestion that this component possibly arises in shocked material associated with the Orion-Eridanus shell.

However, the fact that the observed change in Na°/Ca$^+$ is solely due to a reduction in Na°, rather than an increase in Ca$^+$, means that it cannot be interpreted simply as the line-of-sight sampling a region of less extreme Ca depletion. Following Heiles (1997), it seems more likely that we are here observing the gradual reduction of the Na$^+$ to Na° recombination rate as the line-of-sight gradually moves away from a high-density filament within which the recombination rate was enhanced. While at first sight such a situation might be expected also to result in a decrease in Ca II (owing to reduced recombination of

Ca^{++} to Ca^{+}), in practice Ca is probably sufficiently depleted that this effect is masked by Ca II arising in warmer, more diffuse regions of the cloud (e.g. Crinklaw *et al.*, 1994). It must be noted, however, that over the earlier period 1970 to 1994, when the Na° column density in this component increased substantially, there *is* evidence for a corresponding increase in the strength of Ca II (see Figure 5.1). Thus the Ca^{+} column density cannot be completely insensitive to changing physical conditions over small spatial scales.

We are able to show that a reduction in $n_{\rm H}$ will indeed lead to a lower recombination rate by considering the ionisation balance of Na. In equilibrium,

$$\frac{N[\mathrm{Na}^{\circ}]}{N[\mathrm{Na}^{+}]} = \frac{\alpha(\mathrm{Na}^{\circ})n_{\rm e}}{\Gamma(\mathrm{Na}^{\circ})}, \tag{5.4}$$

where $n_{\rm e}$ is the electron density and $\alpha(\mathrm{Na}^{\circ})$ and $\Gamma(\mathrm{Na}^{\circ})$ are the recombination and photoionisation rates of Na° respectively. From van Dishoeck (1988) and Shull and Van Steenberg (1982), the photoionisation and recombination rates may be expressed as,

$$\alpha = A_{rad}\left(\frac{T}{10^4}\right)^{-\chi_{rad}}, \tag{5.5}$$

and

$$\Gamma = k^0_{pi}\ exp[-\gamma_2 A_{\rm v}], \tag{5.6}$$

where A_{rad} & χ_{rad} and k^0_{pi} & γ_2 are fitting coefficients. T and $A_{\rm v}$ are the temperature and visual extinction respectively. Substituting Equations 5.5 & 5.6 into Equation 5.4 and assuming that the electron density is equal to the undepleted carbon abundance, $N[\mathrm{C}] = 3 \times 10^{-4} N[\mathrm{H}]$ (e.g. Allen, 1973), we find,

$$\frac{N[\mathrm{Na}^{\circ}]}{N[\mathrm{Na}^{+}]} = \frac{A_{rad}(T/10^4)^{-\chi_{rad}} 3 \times 10^{-4} n_{\rm H}}{k^0_{pi}\ exp[-\gamma_2 A_{\rm v}]}. \tag{5.7}$$

We can now see that a reduction in $n_{\rm H}$ will indeed lead to a lower recombination rate to Na°. We may take this analysis one stage further by including the ionisation balance of Ca, and as a result investigate the dependence of the $\mathrm{Na}^{\circ}/\mathrm{Ca}^{+}$ ratio on density.

Firstly, if we assume all Na to be in the neutral and singly ionised form and all Ca to be either singly or doubly ionised, we may write,

$$N[\mathrm{Ca}] = N[\mathrm{Ca}^{+}] + N[\mathrm{Ca}^{++}], \tag{5.8}$$

$$N[\mathrm{Na}] = N[\mathrm{Na}^{\circ}] + N[\mathrm{Na}^{+}]. \tag{5.9}$$

If Na I and Ca II were to exist co-spatially (this is not strictly true since the heavier Ca atom is observed to be subjected to greater broadening; however, Na I and Ca II will exist co-spatially to some extent and therefore influence the measured Na°/Ca^{+} ratio), and follow the analysis made by Crawford (1992), we may then write,

$$\frac{N[\mathrm{Ca}]}{N[\mathrm{Na}]} = \frac{N[\mathrm{Ca}^{+}] + N[\mathrm{Ca}^{++}]}{N[\mathrm{Na}^{\circ}] + N[\mathrm{Na}^{+}]}, \tag{5.10}$$

$$1 = \frac{N[\mathrm{Na}]}{N[\mathrm{Ca}]} \frac{N[\mathrm{Ca}^{+}] + N[\mathrm{Ca}^{++}]}{N[\mathrm{Na}^{\circ}] + N[\mathrm{Na}^{+}]}. \tag{5.11}$$

Multiplying through by $N[\mathrm{Na}^{\circ}]/N[\mathrm{Ca}^{+}]$ we find,

$$\frac{N[\mathrm{Na}^{\circ}]}{N[\mathrm{Ca}^{+}]} = \frac{N[\mathrm{Na}]}{N[\mathrm{Ca}]} \frac{(N[\mathrm{Ca}^{+}]/N[\mathrm{Ca}^{+}]) + (N[\mathrm{Ca}^{++}]/N[\mathrm{Ca}^{+}])}{(N[\mathrm{Na}^{\circ}]/N[\mathrm{Na}^{\circ}]) + (N[\mathrm{Na}^{+}]/N[\mathrm{Na}^{\circ}])}, \tag{5.12}$$

$$\frac{N[\mathrm{Na}^{\circ}]}{N[\mathrm{Ca}^{+}]} = \frac{N[\mathrm{Na}]}{N[\mathrm{Ca}]} \frac{1 + (N[\mathrm{Ca}^{++}]/N[\mathrm{Ca}^{+}])}{1 + (N[\mathrm{Na}^{+}]/N[\mathrm{Na}^{\circ}])}. \tag{5.13}$$

From Equation 5.4, and by conducting a similar analysis for Ca, we may write,

$$\frac{N[\mathrm{Na}^{\circ}]}{N[\mathrm{Ca}^{+}]} = \frac{N[\mathrm{Na}]}{N[\mathrm{Ca}]} \frac{1 + (\Gamma(\mathrm{Ca}^{+})/\alpha(\mathrm{Ca}^{+})n_{\mathrm{e}})}{1 + (\Gamma(\mathrm{Na}^{\circ})/\alpha(\mathrm{Na}^{\circ})n_{\mathrm{e}})}, \tag{5.14}$$

$$\frac{N[\mathrm{Na}^{\circ}]}{N[\mathrm{Ca}^{+}]} = \frac{N[\mathrm{Na}]}{N[\mathrm{Ca}]} \frac{n_e + (\Gamma(\mathrm{Ca}^{+})/\alpha(\mathrm{Ca}^{+}))}{n_e + (\Gamma(\mathrm{Na}^{\circ})/\alpha(\mathrm{Na}^{\circ}))}. \tag{5.15}$$

Values appropriate for k_{pi}^{0} and γ_2 are taken from van Dishoeck (1988); values for A_{rad} & χ_{rad} are taken from Shull and Van Steenberg (1982, for Ca) and Aldrovandi and Pequignot (1974, for Na). By assuming no visual extinction and the electron density to again be equal to the undepleted carbon abundance, Equation 5.15 becomes,

$$\frac{N[\mathrm{Na}^{\circ}]}{N[\mathrm{Ca}^{+}]} = \frac{N[\mathrm{Na}]}{N[\mathrm{Ca}]} \frac{3 \times 10^{-4} n_{\mathrm{H}} + (2.3 \times 10^{-12}/6.78 \times 10^{-13}(\mathrm{T}/10^{4})^{-0.8})}{3 \times 10^{-4} n_{\mathrm{H}} + (1.5 \times 10^{-11}/2.49 \times 10^{-13}(\mathrm{T}/10^{4})^{-0.67})}. \tag{5.16}$$

We find that by adopting a temperature of 100 K in both 1994 and 2000 (since there is no evidence for changes in the line width), a fall in density from 1500 to 50 cm^{-3} will indeed cause the Na°/Ca^{+} ratio to fall by the observed factor (≈ 4.2). If a temperature of 15 K is adopted (in line with the prediction of Heiles (1997) for "Tiny Scale Atomic Structure") a smaller drop in density is required, 500 to 50 cm^{-3}. Neither of these results require a change in the relative gas phase abundance of Na and Ca, and therefore do not suggest there to have been a change in the depletion of either Ca or Na.

Thus, although a majority of the Ca II is not likely to exist co-spatially with Na I (and will as a result mask the changes in the Na°/Ca^{+} ratio discussed here), a reduction in

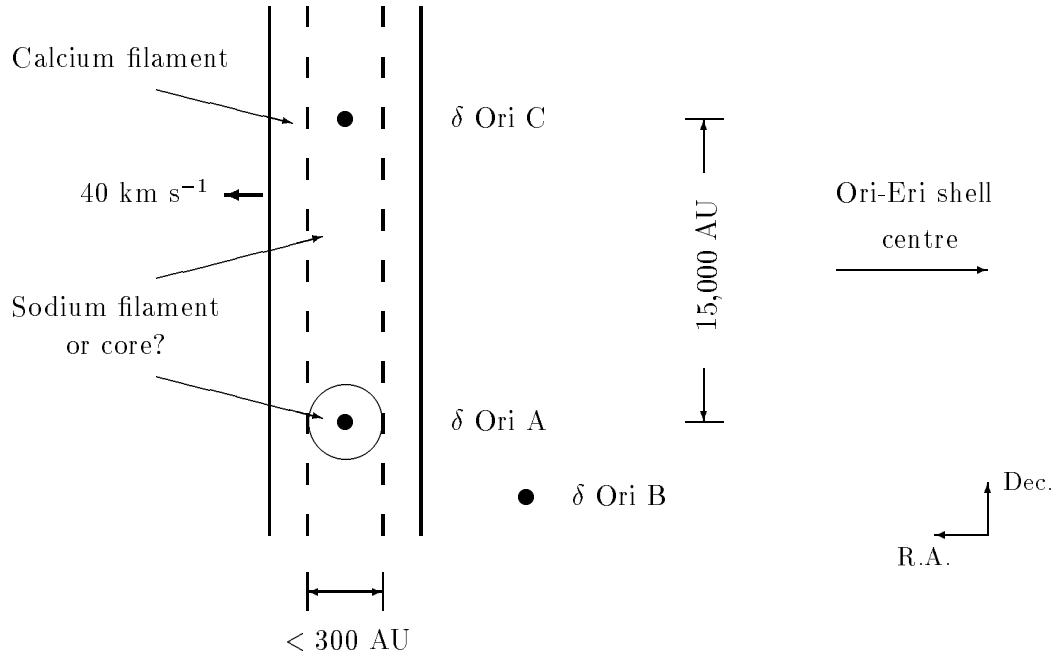

Figure 5.5: Relative positions of the stars in the δ Ori system and the cloud giving rise to the temporal variability. The cloud is known to produce detectable Ca II absorption in the line-of-sight to both δ Ori A & C (outlined with the solid vertical lines); however, the Na I absorption may either arise in a compact core present only in the sightline to δ Ori A (outlined with the circle) or be filamentary in nature, detectable in both sightlines (outlined with the dotted vertical lines). The tangential velocity of the cloud is shown to be equal to the expansion velocity of the Orion-Eridanus shell (40 km s^{-1}).

the density *will* tend to reduce the Na°/Ca^{+} ratio. A similar affect has been observed for κ Vel by Crawford *et al.* (2000) who detected an increase in the K I/Na I abundance ratio, consistent with their interpretation that the line-of-sight is entering a region of enhanced recombination (however, unlike Na I and Ca II, Na I and K I are expected to exist co-spatially).

We may also compare Ca II *K* observations of δ Ori A & C obtained with the UHRF in 2000 (see Figure 5.21 in § 5.3.2.2). This shows the transient component detected towards δ Ori A, to possess a Ca II *K* counterpart in the spectrum of δ Ori C. This suggests one of two possibilities; either, the transient cloud consists of a small Na I "core" (size < 300 AU; only intersected by the sightline to δ Ori A) within a much larger "halo" of Ca II (size $> 15,000$ AU); or, the cloud has the form of a filament (size: < 300 by $> 15,000$ AU) whose axis is roughly parallel with the line joining δ Ori A & C. In the latter case a Na I counterpart may be present in the sightline to δ Ori C. Interestingly, plotting the relative

positions of the stars in the δ Ori system (see Figure 5.5), shows the line joining δ Ori A & C to be tangential to the Ori-Eri shell, consistent with the latter possibility.

5.2.3 ζ Orionis

The Ca II observations of ζ Ori presented here and by Welty *et al.* (1996) were both obtained with the UHRF, in January and February 1994 respectively. Excellent agreement is seen between the two sets of observations, demonstrating consistent data reductions (and zero-level determinations). Figure 5.6(a) shows the comparison of these data.

Conversely, a comparison of the Na I spectrum of ζ Ori presented in this study with the absorption model published by Welty *et al.* (1994, generated from an observation made some six years earlier at a resolution of $R \approx 6 \times 10^5$) reveals the presence of apparent variations at a velocity of -1 km s^{-1}. Further minor variations are also present between the velocities of $+5$ & $+15$ km s^{-1}, but can however be easily ascribed to small differences in continuum normalisation. A comparison of these Na I data is shown in Figure 5.6(b).

Although Welty *et al.* (1994) were able to model the -10 to $+4$ km s^{-1} region of the ζ Ori Na I spectrum using only two components, there is evidence for highly blended substructure, which has been resolved (at least partially) by our UHRF observations. A re-evaluation of our Na I absorption model shows that by reducing the column density of component 2e† (located at -1.07 km s^{-1}; where † signifies a variable component, cf. Table 3.13) from $\log N = 10.98 \pm 0.02$ to $\log N = 10.45 \pm 0.05$ (with all other parameters held constant) it becomes possible to achieve good agreement with the absorption observed by Welty *et al.* (1994). This represents a factor of 3.4 ± 0.6 increase in the Na° column density of this absorbing cloud between 1988 and 1994, a period of ≈ 6 years.

A further comparison can also be made with the earlier, lower resolution observation presented by Hobbs (1969*a*). Figure 5.6(c) shows a comparison between our data and a spectrum digitised from the plot presented by Hobbs (1969*a*). If the spectrum digitised from Hobbs (1969*a*) is assumed to be an accurate representation of the Na I absorption at that time, it becomes possible to estimate a column density of $\log N = 11.25 \pm 0.04$ for component 2e† in 1966. However, the possible presence of telluric absorption in the Hobbs (1969*a*) data makes the changes over this period uncertain.

The comparison of our Na I D_1 data with that of Hobbs (1969*a*) reveals further possible variability at a radial velocity of $+19$ km s^{-1}; however, its authenticity is much less certain. Conducting a similar analysis for component 6†, located at $+18.11$ km s^{-1}. We find

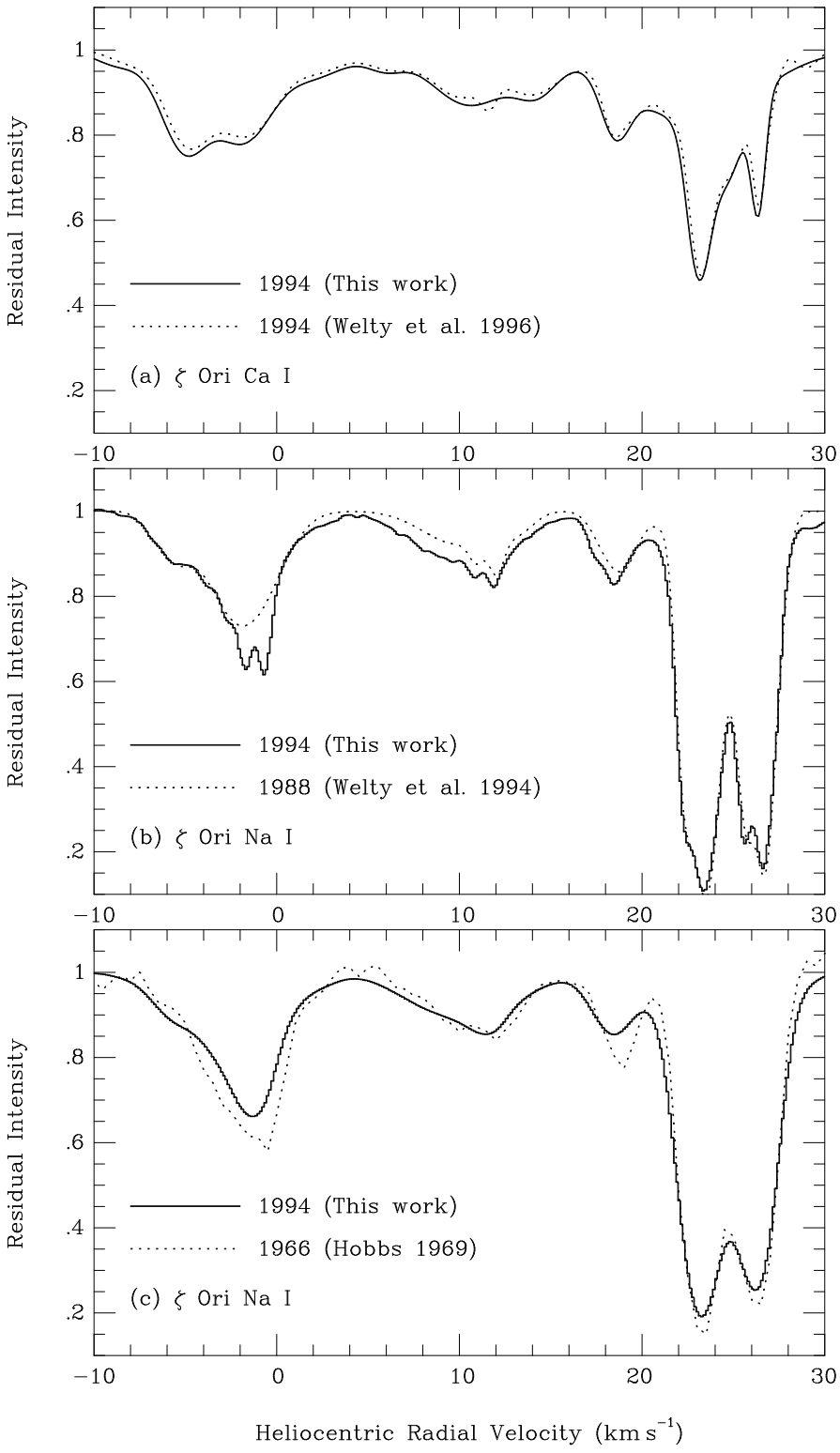

Figure 5.6: A comparison of (a) the Ca II K absorption models generated by us and Welty *et al.* (1996); (b) the UHRF and Welty *et al.* (1994) Na I D_1 spectra; (c) the UHRF and Hobbs (1969*a*) Na I D_1 spectra observed toward ζ Ori.

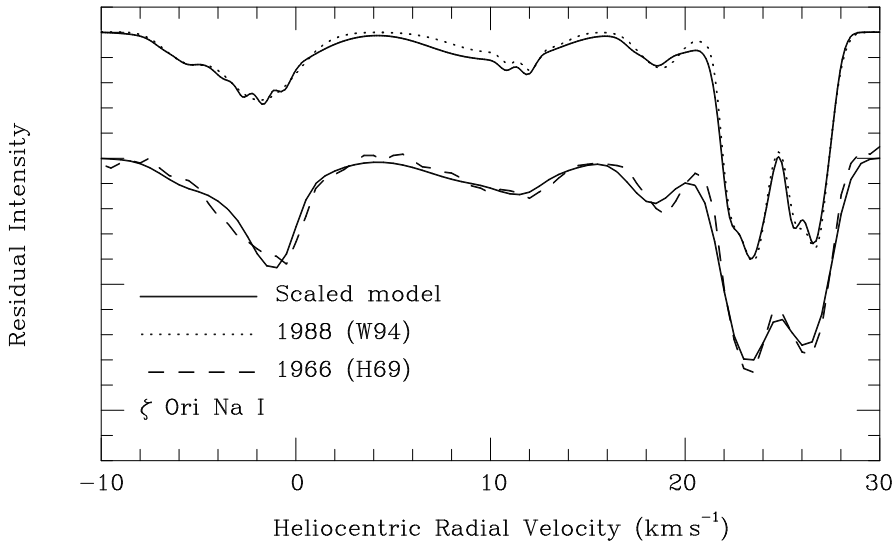

Figure 5.7: A comparison of our scaled absorption models with (a) the absorption model presented by Welty *et al.* (1994) and (b) the digitised spectrum of Hobbs (1969*a*).

that, by decreasing the column density of this component from $\log N = 10.66 \pm 0.05$ to $\log N = 10.42 \pm 0.05$ (all other parameters held constant) it becomes possible to achieve good agreement with the absorption observed by Welty *et al.* (1994). Also, by increasing the column density of component $6^{\dagger}$ to $\log N = 10.82 \pm 0.09$, optimum agreement is achieved with the observation of Hobbs (1969*a*). Figure 5.7 illustrates the comparison of our scaled absorption model with (a) the absorption model presented by Welty *et al.* (1994) and (b) the digitised spectrum of Hobbs (1969*a*).

Our measurements therefore suggest a factor of 6.3 ± 1.4 reduction in the Na° column density of component $2e^{\dagger}$ at a velocity of -1.07 km s^{-1} between 1966 and the late 1980s, subsequently followed by a factor of 3.4 ± 0.6 increase in the Na° column density by 1994. In the case of component $6^{\dagger}$ at $+18.11$ km s^{-1}, a factor of 2.5 ± 0.9 reduction in its column density was observed between 1966 and the late 1980s, followed by a factor of 1.7 ± 0.4 increase by 1994. However, it must be noted that only the change in component $2e^{\dagger}$ between the late 1980s and 1994 is considered to be completely reliable.

Temporal variations over such a small time period imply that the absorption occurs in a spatially small parcel of gas (at least in the transverse direction). Jenkins and Peimbert (1997); Jenkins *et al.* (2000) have suggested that molecular hydrogen observed towards ζ Ori at a velocity corresponding to that of component $2e^{\dagger}$ may be produced in the compressed region behind a bow shock present in this direction (discussed further in

§ 3.4.3).

Although the presence of a shock may account for the observed temporal variability, a small tangential displacement of the cloud, or the line-of-sight, due to the proper motion of ζ Ori, causing a shift in the line-of-sight probed, provides an equally plausible explanation (as invoked for δ Ori in § 5.2.2). In the case of ζ Ori (which has a proper motion of 4.73 mas yr^{-1}; ESA, 1997), the increase in column density of component 2e† between 1988 and 1994 highlights the presence of structure in the ISM down to scales of ≈ 7 AU. Indeed, Lauroesch *et al.* (2000) have also observed temporal variability in Na I towards HD 32039/40 over scales of $\approx$ 15–21 AU (inferred from the proper motion of the system). However the analysis of Lauroesch *et al.* (2000) assumes the cloud to be stationary. By assuming a plausible upper limit of 50 km s^{-1} for the tangential velocity of our cloud, the linear distance traced across the cloud may be as high as ≈ 70 AU, highlighting the importance of possible cloud motion.

The narrow line width measured for component 2e† (b[Na I] = 0.44) seems typical of temporally variable components observed elsewhere; e.g. the temporally variable component observed towards δ Ori (b[Na I] = 0.45); also see the discussion made in § 5.3.1. This adds to evidence suggesting that small-scale interstellar structure is preferentially found in cooler diffuse gas.

5.2.4 β Orionis

A comparison of our Ca II K spectrum with that presented by Marschall and Hobbs (1972) may be made in order to search for temporal variability; however, the intrinsically weak nature of these lines, and the presence of a strong stellar line both create some uncertainty with this procedure. This comparison is shown in Figure 5.8(a).

The strength of the absorption present around 0 km s^{-1} appears similar in both studies, but that near +9 km s^{-1} (our cloud 7a†; where † signifies a variable component, cf. Table 3.3) appears somewhat weaker in the Marschall & Hobbs data. Since β Ori is experiencing ongoing mass loss (discussed in § 3.4.4), these variable components are likely to have a circumstellar origin. Further absorption, below a velocity of -10 km s^{-1}, is also thought to arise within β Ori's circumstellar environment (§ 3.4.4), but an insufficient blueward range in the Marschall and Hobbs (1972) spectrum does not permit a comparison for these components. Modelling the Ca II K data of Marschall and Hobbs (1972, while fixing the parameters of component 7b, with which component 7a† is heavily blended, to

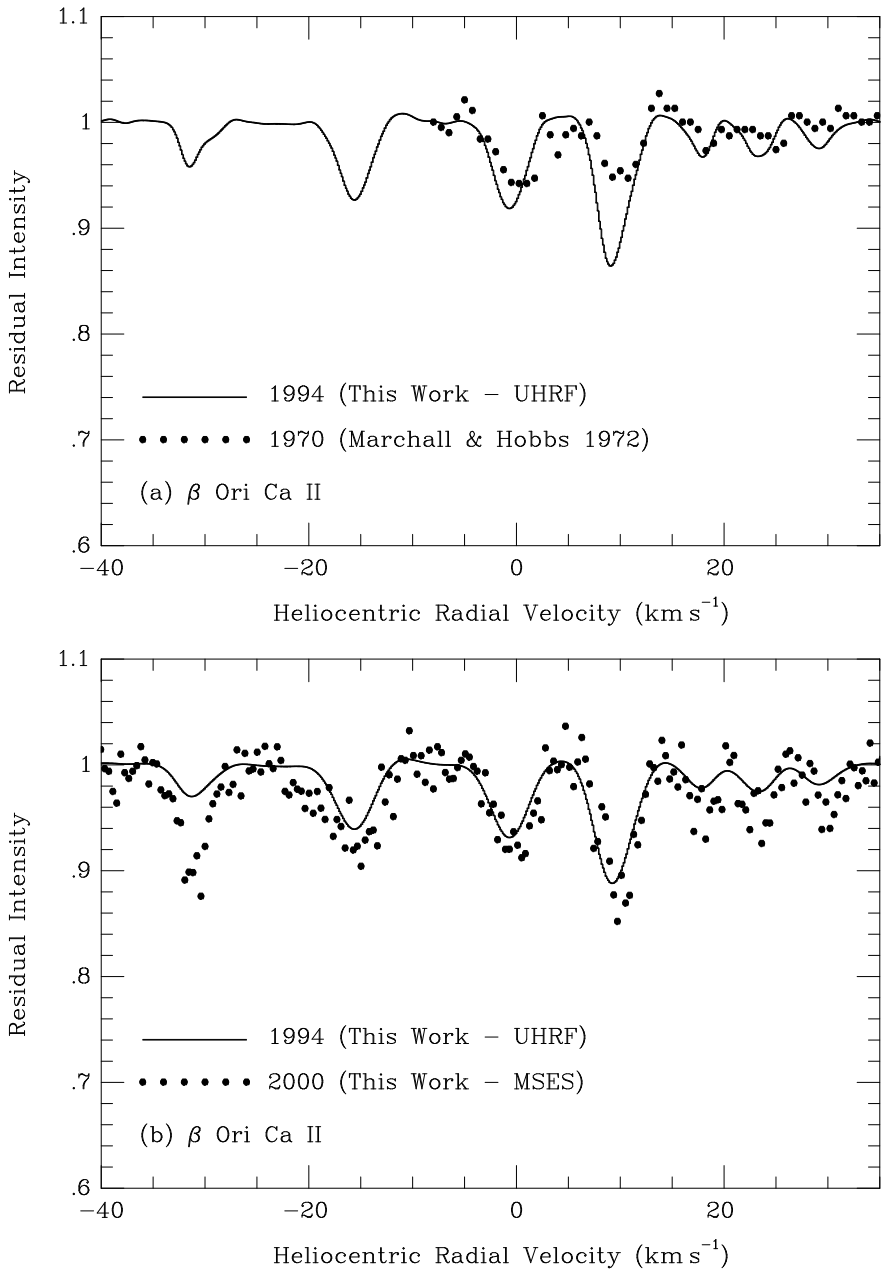

Figure 5.8: A comparison of Ca II K spectra observed towards β Ori with the UHRF and (a) Marschall and Hobbs (1972); and (b) the MSES.

the values obtained from the 1994 UHRF data, cf. Table 3.3) shows component 7a† to possess a column density of $N = 10.08 \pm 0.13$.

Additional Ca II H & K observations of β Ori obtained with the MSES in 2000 may also be used to identify possible variability. Figure 5.8(b) shows a comparison of the Ca II K data obtained with the UHRF with that of the MSES. The full spectral range of the MSES data allows the comparison of each absorption component, and as a result, shows a considerable increase in the strength of the -32 km s^{-1} component (our cloud 1†). Simultaneously modelling the H & K transitions in the MSES data show components 1† & 7a† (while fixing the parameters of components 2 & 7b, with which components 1† & 7a† are heavily blended, to the values obtained from the 1994 UHRF data, cf. Table 3.3) to possess column densities of $N = 10.74 \pm 0.03$ and $N = 10.78 \pm 0.03$ respectively.

This illustrates the column density of component 1† to have increase by a factor of 4.4 ± 0.7 between 1994 and 2000, while the column density of component 7a† has increased by a factor of 4.9 ± 2.0 between 1970 and 1994 and remained at a similar level in 2000. However, we must note that the strong stellar absorption creates some uncertainty in these values.

A similar comparison between the Na I data presented here with that of Hobbs (1969a), reveals no clear evidence for temporal variability. This is consistent with our interpretation that the variability is the result of changes in the structure of absorbing gas within the circumstellar environment of β Ori where the Na$^{\circ}$/Ca^{+} abundance ratio is expected to be low.

5.2.5 θ^1 Orionis A & C and θ^2 Orionis A

A comparison of the various Ca II K spectra available for θ^1 Ori A & C and θ^2 Ori A (Figures 5.9(a) to (c)) shows the overall forms of the absorption profiles to agree reasonably well, while the cores of the absorption lines are consistently shallower in the data presented by O'Dell *et al.* (1993, $R \approx 9 \times 10^4$), despite convolution with an appropriate Gaussian profile. Better agreement is seen with the absorption model of θ^1 Ori C presented by Welty *et al.* (1996, $R \approx 2.5 \times 10^5$), however differences in the continuum normalisation are likely to be present. These differences are echoed by equivalent-width measurements which show the strength of absorption to be slightly larger in the UHRF data as compared with O'Dell *et al.* (1993). The total Ca II K equivalent widths reported by O'Dell *et al.* (1993) for θ^1 Ori A & C are 105.5 ± 2 and 101 ± 2 mÅ respectively, compared to 119.2 ± 1.9

and 120.7 ± 1.2 mÅ found here. Hobbs (1978*a*) found the equivalent-width of Ca II K absorption towards θ^1 Ori C to be 120 ± 5 mÅ, in good agreement with our results, while Welty *et al.* (1996) quote 94.4 ± 0.7 mÅ and highlight the disagreement in equivalent-width measurements for this star. In the case of θ^2 Ori A, we measure a total equivalent width of 101.4 ± 0.7 mÅ, while O'Dell *et al.* (1993) quote 97.2 mÅ. While this effect may be the result of inaccurate zero- and/or continuum-level determinations in our own, or previous studies, the saturated Na I D_1 absorption present in UHRF spectra of λ & ϕ^1 Ori (discussed in § 2.2.7), suggests the uncertainty in the zero-level of the UHRF data to be small. We do note the lack of a well-determined red-wing continuum in the Ca II spectra of θ^1 Ori A & C and θ^2 Ori A, which does lead to the possibility of errors in the continuum normalisation; however, this should, if anything, act to *reduce* both the measured equivalent widths and the absorption core depths.

The Na I D_2 spectrum of θ^1 Ori C published by Hobbs (1978*a*), and used by O'Dell *et al.* (1993) in their analysis of M42, contains an absorption feature at a velocity of +37.7 km s^{-1}. O'Dell *et al.* (1993) associated this component with Ca II absorption which they observe at a velocity of +39.5 km s^{-1}. However, this Na I D_2 feature is in proximity to a telluric line previously identified by Hobbs (1978*b*) and is likely to be the result of telluric contamination. Furthermore, the very weak Na I D_2 components observed towards θ^1 Ori C & θ^2 Ori A at ≈ -16 km s^{-1} by Hobbs (1978*a*), and unexplained by O'Dell *et al.* (1993), are not observed here. The original θ^1 Ori C & θ^2 Ori A Na I D_2 spectra presented by Hobbs (1978*a*) highlight the presence of possible telluric absorption at this velocity (also identified in the telluric template presented by Hobbs (1978*b*) which we confirm as having a telluric origin, using atmospheric templates of the Na I D_2 region obtained with the MSES. Figure 5.10 shows a comparison of the Na I D_2 data presented by Hobbs (1978*a*, digitised from his paper) with Na I D_2 absorption models generated using the component parameters derived from our UHRF D_1 data in conjunction with the atomic data relevant to the D_2 transition. The sites of telluric absorption (in the Hobbs (1978*a*) data) corresponding to interstellar lines identified by O'Dell *et al.* (1993) are highlighted by the symbols '$\oplus$'.

Since much of the absorption present towards these three stars is considered to arise in clouds located in proximity to M42 (see § 3.4.1.3), a certain amount of temporal variability might be expected from such an energetic environment. However, attributing the observed differences in the line profiles to intrinsic variability in the absorption is difficult due to a

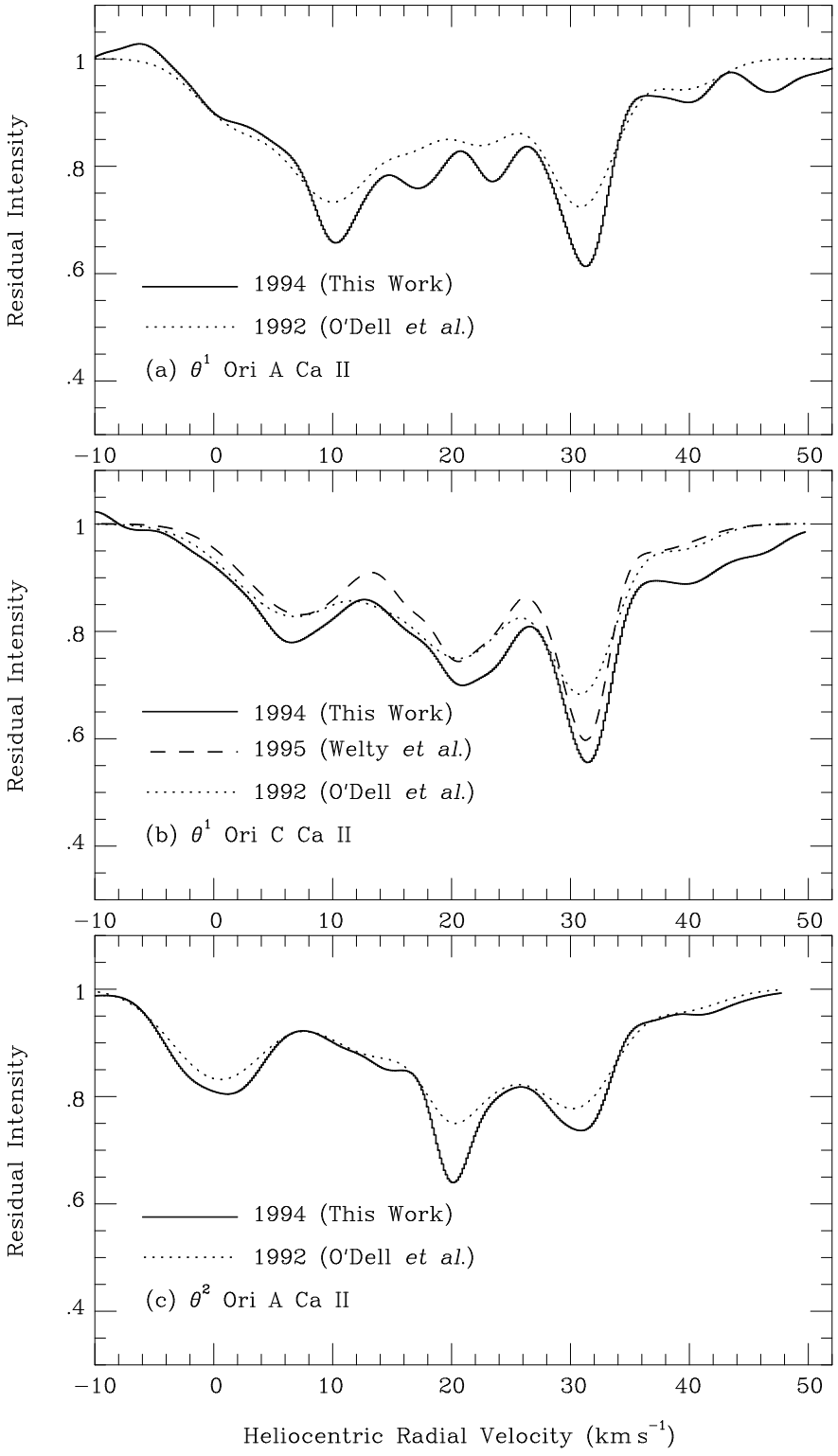

Figure 5.9: A comparison of Ca II K spectra observed by (a) the UHRF and O'Dell *et al.* (1993) towards θ^1 Ori A; (b) the UHRF, Welty *et al.* (1996) and O'Dell *et al.* (1993) towards θ^1 Ori C; and (c) the UHRF and O'Dell *et al.* (1993) towards θ^2 Ori A.

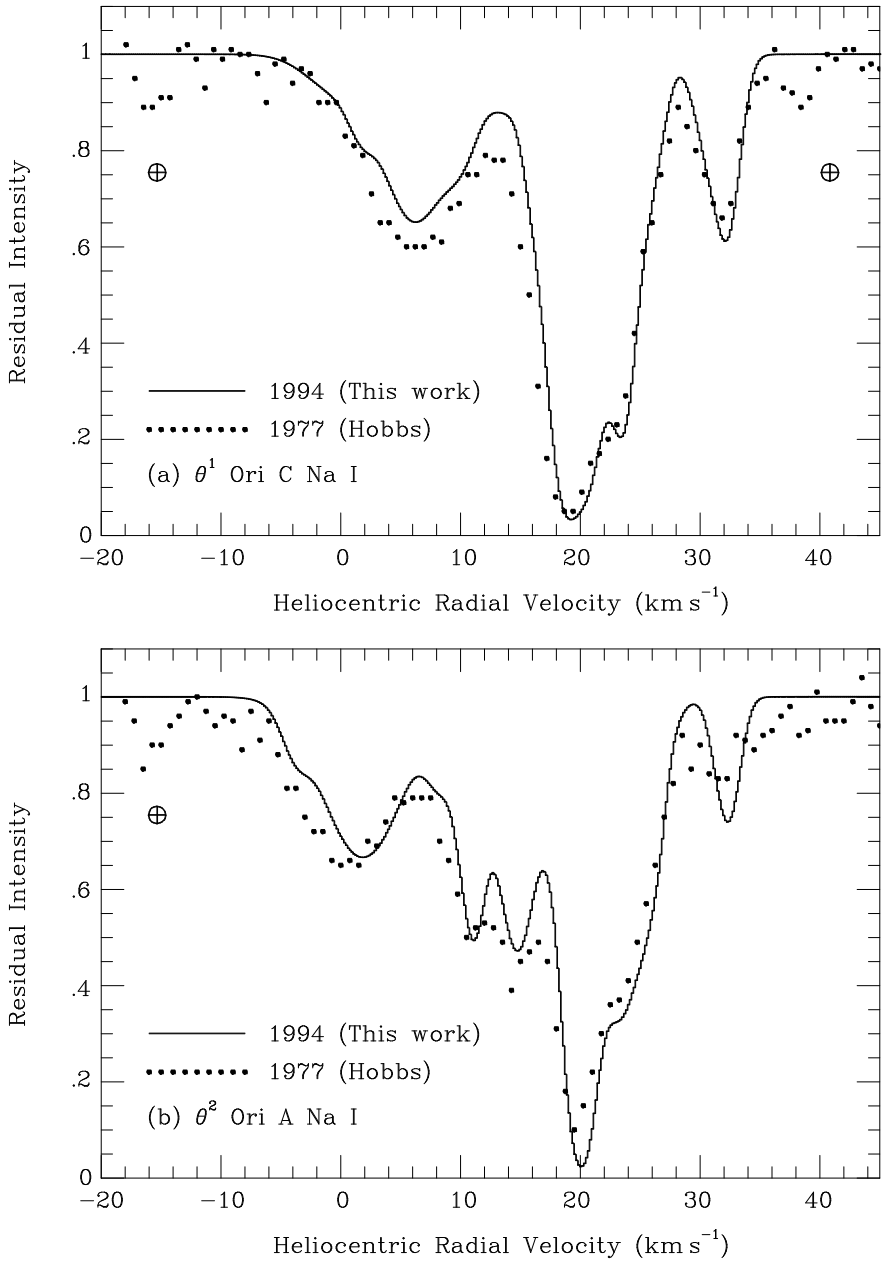

Figure 5.10: A comparison of the Na I D_2 spectra obtained by Hobbs (1978*a*) with an Na I D_2 absorption model generated from the Na I D_1 spectra obtained with the UHRF (using the component parameters derived from our UHRF D_1 data in conjunction with the atomic data relevant to the D_2 transition) for (a) θ^1 Ori C and (b) θ^2 Ori A. The sites of telluric absorption in the Hobbs (1978*a*) data are highlighted by the symbols '$\oplus$' [Note: no telluric absorption is present in the UHRF data].

lack of previous very-high-resolution data. We conclude that there is no secure evidence as yet for significant variability in these sightlines.

5.2.6 ι Orionis

Although Welty *et al.* (1994) identify several additional weak components in their Na I spectrum of ι Ori, excellent agreement is still seen with our observations (see Figure 5.11(a)). With regards to the Ca II region however, additional weak components identified by Welty *et al.* (1996) *do* produce a noticeable difference (see Figure 5.11(b)); however, we feel that these differences are unlikely to be the result of temporal variability and are easily attributable to differences in continuum normalisation.

5.2.7 σ Orionis

A comparison of Ca II *K* observations towards σ Ori (shown in Figure 5.12) appears to reveal the appearance of an absorption component, in our 1994 spectrum, at a velocity of -10.85 km s^{-1}. An examination of the original 1993 spectrum published by Welty *et al.* (1996) illustrates the presence of a very weak feature at this velocity, indicating the absorption was present, but unmodelled, by Welty *et al.* (1996). The differences in the absorption models therefore do not represent true variability in the absorption-line profiles.

5.2.8 κ Orionis

Exceptional agreement is seen between the Na I observations of κ Ori (shown in Figure 5.13) presented by Welty *et al.* (1994) and this study, apart from the presence of a weak additional component in our spectrum at a velocity of $+14.95$ km s^{-1}. However, the $+8$ to $+16$ km s^{-1} range in this spectrum does suffer from some telluric absorption. This component is most probably not variable but instead the result of some residual contamination.

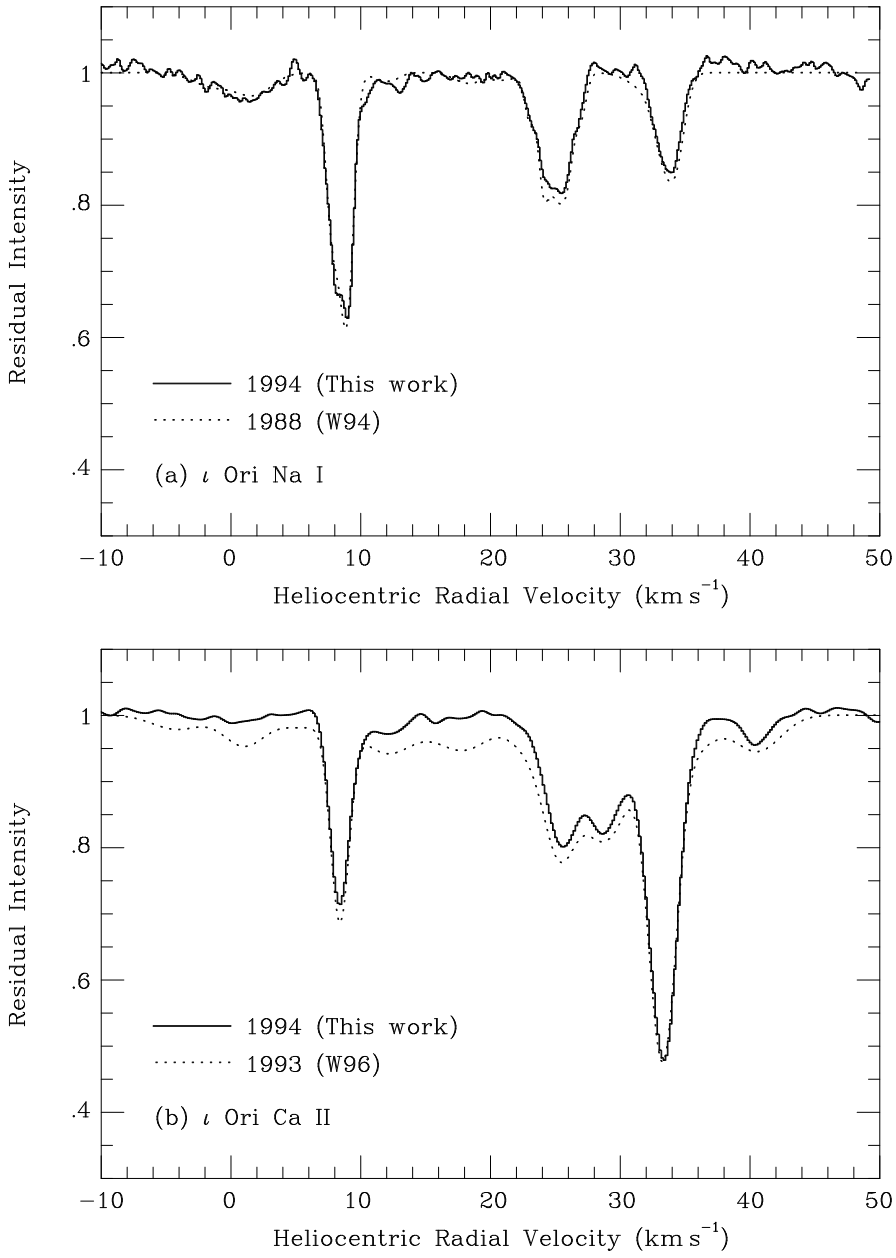

Figure 5.11: A comparison of (a) the UHRF and Welty *et al.* (1994) Na I D_1 spectra; and (b) the UHRF and Welty *et al.* (1996) Ca II K spectra, observed toward ι Ori.

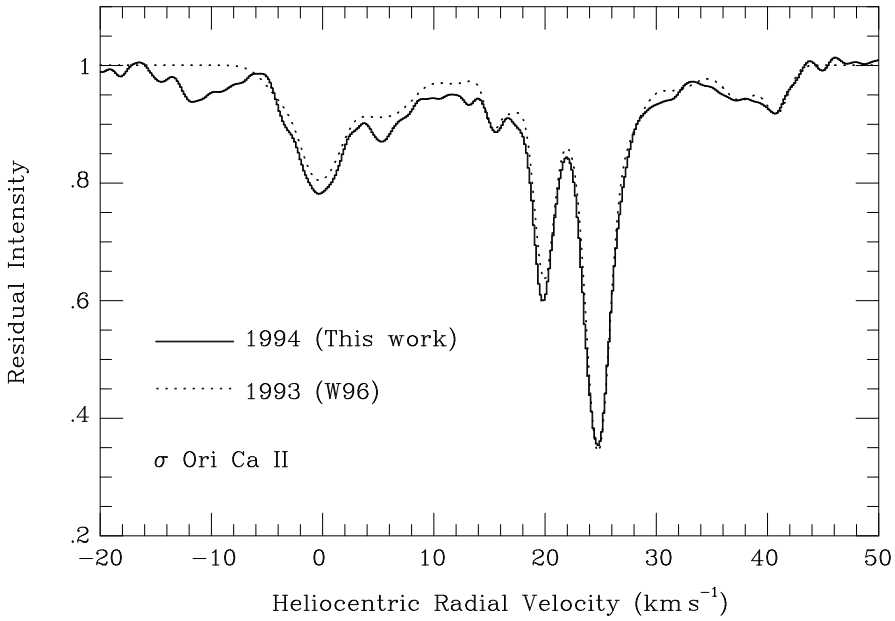

Figure 5.12: A comparison of the UHRF and Welty *et al.* (1996) Ca II K spectra observed toward σ Ori.

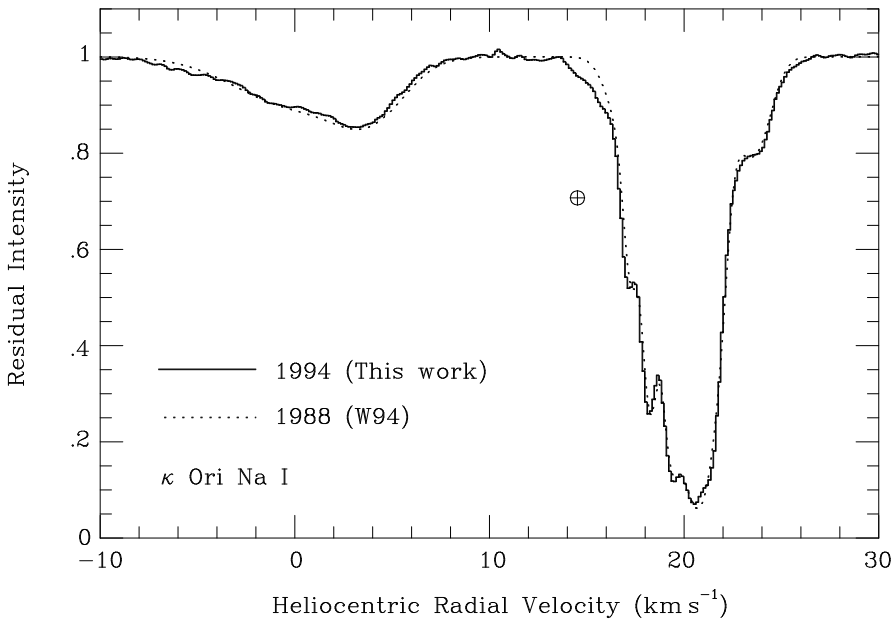

Figure 5.13: A comparison of the UHRF and Welty *et al.* (1994) Na I D_1 spectra observed toward κ Ori.

5.3 Spatial Variations in Interstellar Absorption Lines

5.3.1 Introduction

Observations of interstellar absorption lines towards extended or closely spaced targets may be used to reveal the presence of small-scale interstellar structure, since differences in absorption signify differences in the line-of-sight structure of the absorbing medium. Earlier evidence came from VLBI observations of hydrogen's 21-cm line towards extragalactic sources (Dieter *et al.*, 1976; Diamond *et al.*, 1989; Davis *et al.*, 1996; Faison *et al.*, 1998; Faison and Goss, 2001); however, optical absorption lines are being increasingly utilised. Observations of Na I towards 17 binary/common-proper-motion systems (with projected separations ranging from 480 to 29000 AU) by Watson and Meyer (1996) revealed absorption differences, and therefore structure, in every case. Conversely, observations of Ca II towards binary/common-proper-motion systems showed little evidence of small-scale structure towards binaries with separations below 2500 AU (Meyer, 1990, 1994).

The marked difference in the Na I and Ca II results arises from the different conditions which prevail in the regions where such structure is present. Both Meyer and Blades (1996) and Watson and Meyer (1996) find components with the narrower line widths to display the largest variations; Meyer and Blades (1996) also find these components to exhibit larger Na°/Ca^{+} ratios. This suggests the small-scale structure is located in the colder/denser regions, for which Na° is known to be a good tracer, whereas Ca^{+} is expected to be heavily depleted onto grain surfaces (e.g. Barlow and Silk, 1977). This is consistent with the findings of the previous section where temporal variability (and by implication small-scale structure) was detected in absorbing clouds with $T_{\rm k} < 280$ K. It is interesting to note that Lauroesch and Meyer (1999) find structure in the K I line for three out of five sightlines showing saturated Na I absorption. This indicates that the small-scale structure traced by the neutral species is present, to some extent, in clouds of all column densities.

Observations of optical absorption lines have also been made towards extended targets. Meyer and Lauroesch (1999) and Andrews *et al.* (2001) have observed Na I towards the globular clusters M15 and M92 respectively. Their observations show there to be structure on scales down to 2000 & 1600 AU in the direction of M15 & M92 respectively. These structures are expected to be due to variations in both the H I column density and Na I ionisation equilibria.

Observations of H_2CO (formaldehyde) absorption towards extragalactic continuum

sources by Marscher *et al.* (1993) and Moore and Marscher (1995) have revealed the presence of very small ($\lesssim$10 AU) high-density ($\sim 2 \times 10^6$ cm^{-3}) clumps in foreground molecular clouds. Interestingly, Moore and Marscher (1995) find the molecular species which trace the denser gas to exhibit greater spatial variations. Moore and Marscher (1995) therefore conclude that the denser gas must possess greater structure, similar to the result found for Na I (Meyer and Blades, 1996; Watson and Meyer, 1996, and now here, see § 5.3.2). Although the conditions specific to these clouds are rather different to those expected for the small-scale structure observed here, they do show that small-scale structure exists in a variety of environments.

5.3.2 δ Orionis

Here, new high-resolution observations of the D lines of Na I and the H & K lines of Ca II towards both δ Ori A and C (two components of the δ Orionis multiple stellar system discussed further in § 5.2.2.1) are used to probe the small-scale structure in this direction. These observations have been obtained with the MSES and UHRF (operating at a resolving powers of $R = 1.1 \times 10^5$ and $R = 3.8 \times 10^5$ respectively). A distance of 281 pc to these stars (the Hipparcos catalogue ESA, 1997), means their angular separation projects to a linear distance of $\approx 15,000$ AU (0.07 pc) at the stars.

These data sets will initially be modelled separately (§ 5.3.2.1 for the MSES data and § 5.3.2.2 for the UHRF data), and then a joint analysis of both will be performed in § 5.3.2.3. In each case the D lines of Na I have been modelled simultaneously with the VAPID routine in order to produce self-consistent absorption models (the same is true for the H & K lines of Ca II).

5.3.2.1 The MSES Data

We have used the MSES to observe Na I D_1 & D_2 towards both δ Ori A and C and Ca II H and K towards δ Ori A. The observations were made between 2000 February 13 and 19. Table 5.3 displays the parameters of the best-fitting absorption line profile models which are shown graphically, after convolution with the instrumental response function, in Figures 5.14 5.15 and 5.16.

The comparison of the interstellar Na I spectra of δ Ori A & C (Figure 5.17) reveals substantial differences in the line strengths of the components between the two stars.

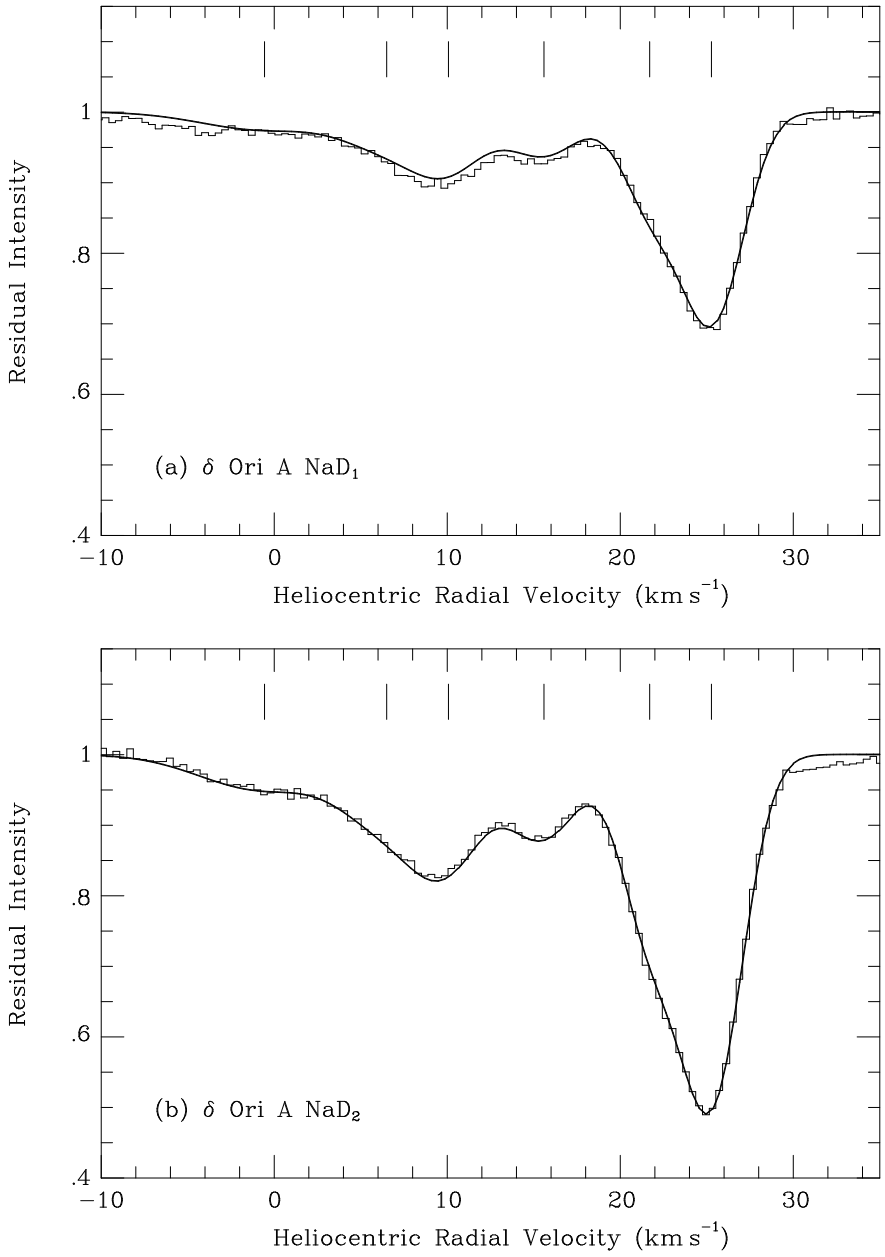

Figure 5.14: Theoretical line profiles are shown plotted over (a) Na I D_1 and (b) Na I D_2 spectra observed towards δ Ori A using the MSES. The tickmarks indicate the velocities of the individual model components listed in Table 5.3.

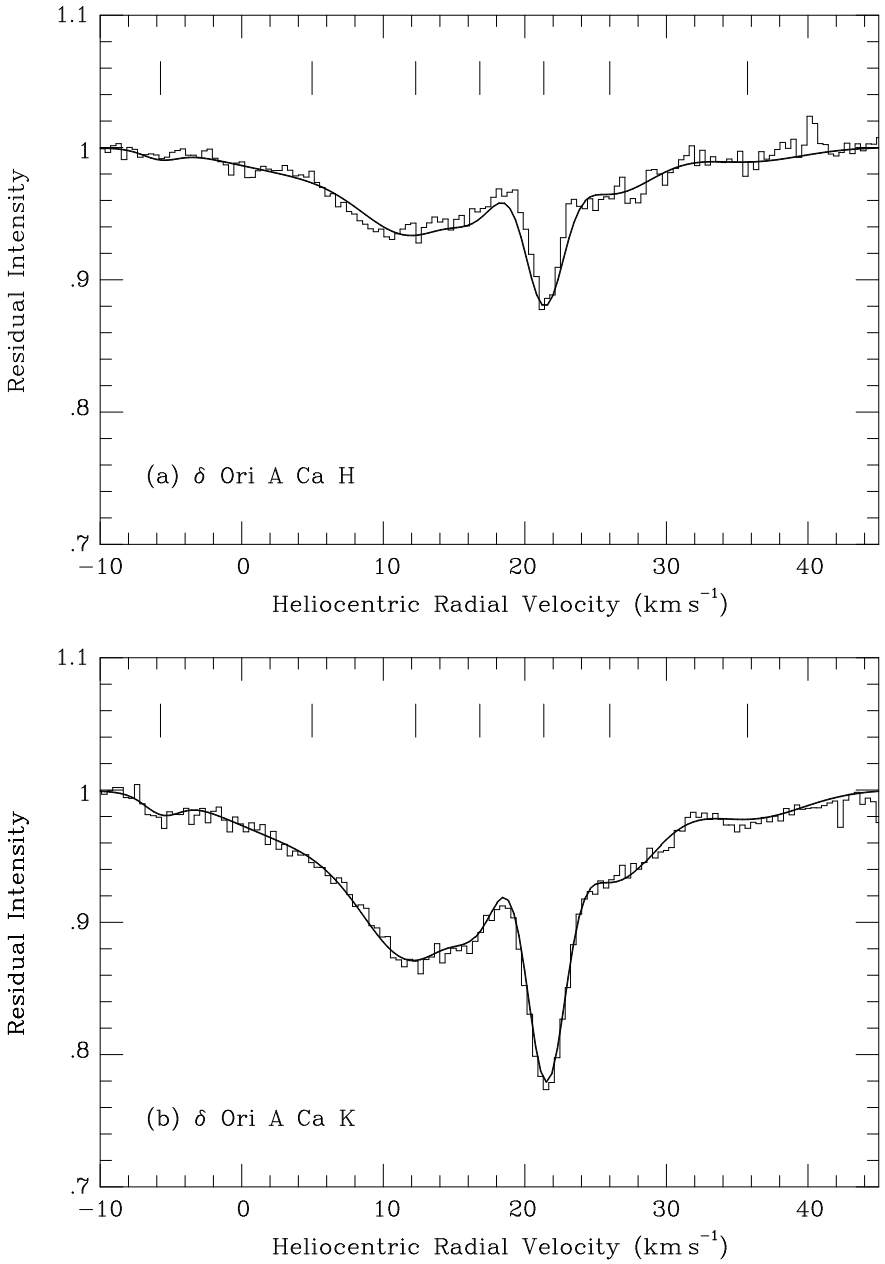

Figure 5.15: Theoretical line profiles are shown plotted over (a) Ca II H and (b) Ca II K spectra observed towards δ Ori A using the MSES. The tickmarks indicate the velocities of the individual model components listed in Table 5.3. The poor fit of the model to the +21 km s^{-1} feature in the δ Ori A Ca II H spectrum is a result of an unexplained flatfield feature; however, its excellent fit to the Ca II K absorption (which was modelled simultaneously with the Ca II H feature) indicates the model to be accurate.

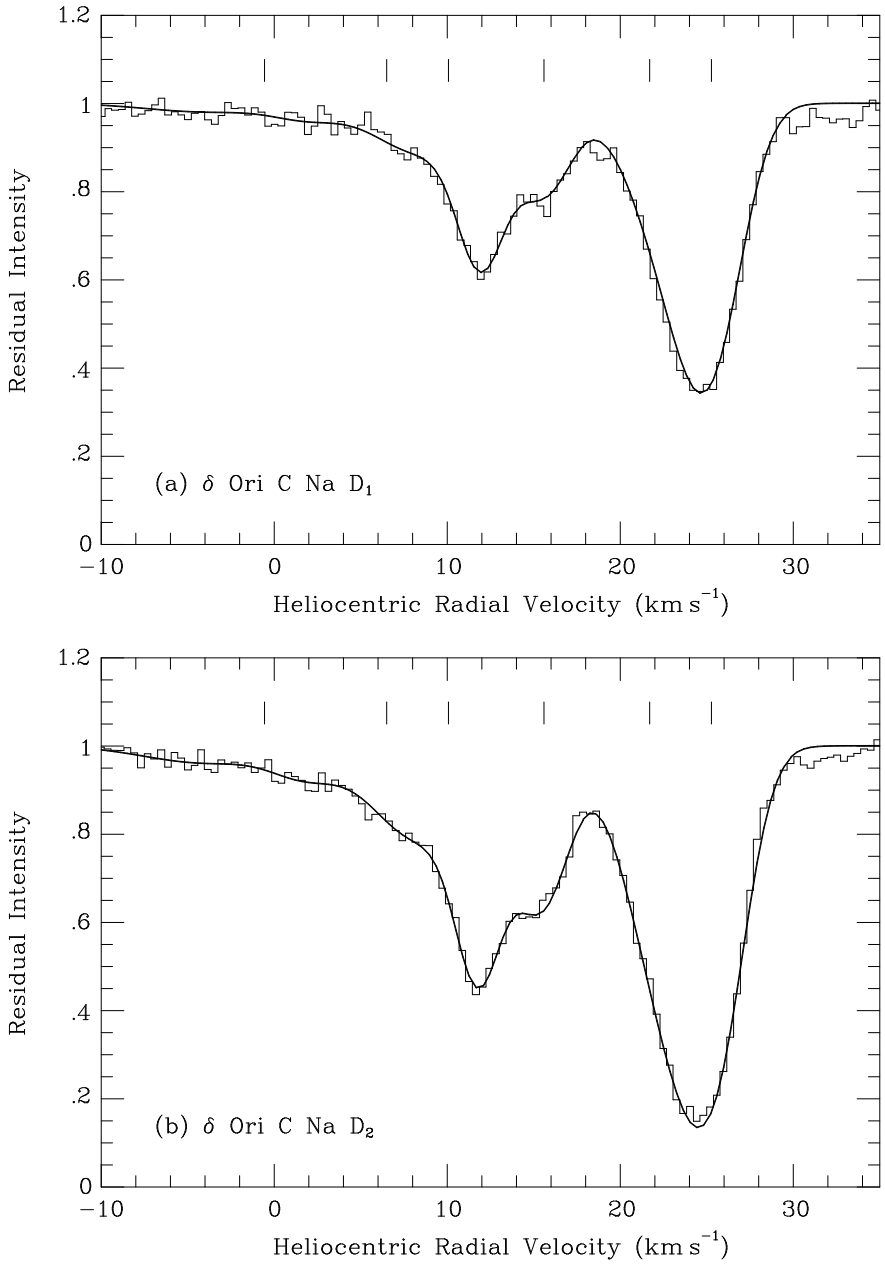

Figure 5.16: Theoretical line profiles are shown plotted over (a) Na I D_1 and (b) Na I D_2 spectra observed towards δ Ori C using the MSES. The tickmarks indicate the velocities of the individual model components listed in Table 5.3. The very weak features present at +32 km s^{-1} in the Na I D_1 and Na I D_2 spectra have not been modelled but may possibly be authentic, a higher S/N spectrum is required for their validation.

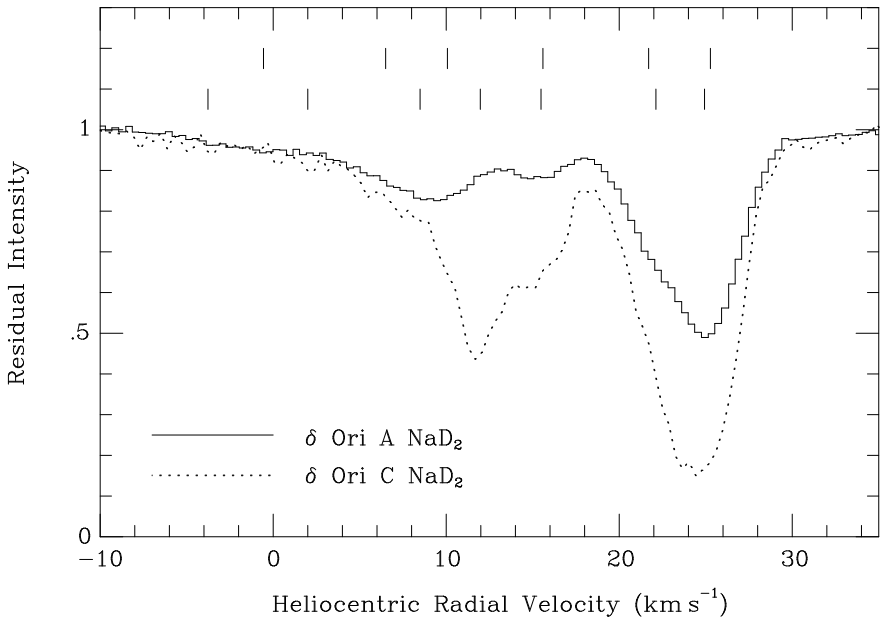

Figure 5.17: A comparison of the Na I D_2 absorption observed towards δ Ori A & C using the MSES. The plots illustrate the presence of small-scale structure in this direction. The tickmarks indicate the velocities of the individual model components listed in Table 5.3; the upper tickmarks refer to δ Ori A while the lower ones refer to δ Ori C.

Table 5.3: Velocity systems identified toward δ Ori A & C in the Ca II and Na I regions using MSES data. Signal-to-noise ratios are shown in columns 2 & 8, total equivalent widths are shown in columns 3 & 9. Column 13 contains values of $m_{\rm s}$ (defined in Equation 5.17). NB: Na I components observed towards δ Ori A & C and listed along-side the same component number (column 4), are classified as arising in the same cloud, however the same is not true for comparisons between δ Ori A Ca II and Na I component numbers.

Line	S/N	W_λ (mÅ)	Comp	$v_\odot$ (km s^{-1})	b (km s^{-1})	log N (cm^{-2})	S/N	W_λ (mÅ)	$v_\odot$ (km s^{-1})	b (km s^{-1})	log N (cm^{-2})	$m_{\rm s}$
				δ Ori A					δ Ori C			
Ca II H:	185	24 ± 1	1	-5.74 ± 0.40	0.50 ± 2.57	9.78 ± 0.25						
K:	182	44 ± 1	2	4.97 ± 6.00	7.76 ± 4.40	10.94 ± 0.47						
			3	12.29 ± 0.49	4.72 ± 1.46	11.20 ± 0.30						
			4	16.82 ± 0.20	1.64 ± 0.94	10.52 ± 0.35						
			5	21.34 ± 0.07	0.95 ± 0.17	11.07 ± 0.03						
			6	26.00 ± 0.36	4.00 ± 0.83	10.92 ± 0.08						
			7	35.73 ± 1.01	5.05 ± 1.27	10.50 ± 0.10						
Na I D_1:	192	60 ± 1	1	-0.56 ± 1.46	4.76 ± 1.19	10.68 ± 0.16	60	126 ± 2	-3.77 ± 3.01	4.73 ± 3.01	10.56 ± 0.32	0.14
D_2:	164	105 ± 1	2	6.50 ± 3.89	3.04 ± 3.25	10.79 ± 0.88	76	206 ± 3	2.00 ± 1.12	2.16 ± 2.31	10.51 ± 0.57	0.31
			3	10.07 ± 1.22	2.25 ± 1.33	10.91 ± 0.63			8.49 ± 0.52	3.28 ± 1.62	11.20 ± 0.17	0.32
			4	—	—	—			11.97 ± 0.09	0.33 ± 0.05	11.55 ± 0.04	1.00
			5	15.59 ± 0.27	2.14 ± 0.52	10.80 ± 0.08			15.48 ± 0.14	1.39 ± 0.34	11.29 ± 0.05	0.51
			6	21.70 ± 0.17	1.34 ± 0.28	11.04 ± 0.06			22.12 ± 1.75	2.08 ± 1.15	11.41 ± 0.48	0.40
			7	25.27 ± 0.09	1.68 ± 0.09	11.50 ± 0.02			24.93 ± 0.34	1.72 ± 0.20	11.96 ± 0.14	0.49

One of the components is only detected in one of the sightlines. Such a comparison also reveals the similar velocity structuring of the components, each component observed towards δ Ori A being observed towards δ Ori C with a velocity and velocity dispersion which agree within errors. None of the components are found to be significantly stronger towards δ Ori A. Interestingly, Adams (1949) also found the intensity of Ca II K absorption towards δ Ori C to also be stronger than that towards δ Ori A, consistent with what we observe in Na I.

5.3.2.2 The UHRF Data

To further investigate the small-scale structure in this sightline, higher resolution observations of both the D lines of Na I and the K line of Ca II were obtained towards both δ Ori A & C. These data were acquired on 16 and 17 August 2000 (just 6 months after the MSES data). The UHRF was operated in its lowest resolution mode, providing a resolving power of $R \approx 380,000$. Table 5.4 displays the parameters of the best-fitting absorption line profile models which are shown graphically, after convolution with the instrumental response function, in Figures 5.18 and 5.19.

The comparison of the interstellar Na I spectra of δ Ori A & C (Figure 5.20) again reveals substantial differences in the line strengths of the components between the two stars. The higher resolution of the UHRF data show the +12 km s^{-1} cloud detected in the MSES data (which is only present in the sightline towards δ Ori C), to in fact be composed of two components, each only observed towards δ Ori C.

The very weak features present at +32 km s^{-1} in the Na I D_1 and Na I D_2 spectra obtained with the MSES are again detected here. They are present at a statistically significant level and have therefore have been included in the absorption models. While no telluric absorption is present at +32 km s^{-1} in the Na I D_1 spectra, it does occur in this region of the Na I D_2 data and therefore renders the component parameters somewhat uncertain.

The observation of Ca II K towards δ Ori C reveals very strong absorption over a larger velocity range than present towards δ Ori A. The form of the line profile is characteristic of narrow interstellar lines blended with a much broader stellar line. Furthermore, the presence of a narrow absorption component near the centre of the broad profile is reminiscent of the spectra of β Pictoris-like stars such as HR10 (e.g. Welsh, Craig, Crawford and Price, 1998) where circumstellar Ca II absorption is found centred at the stellar radial

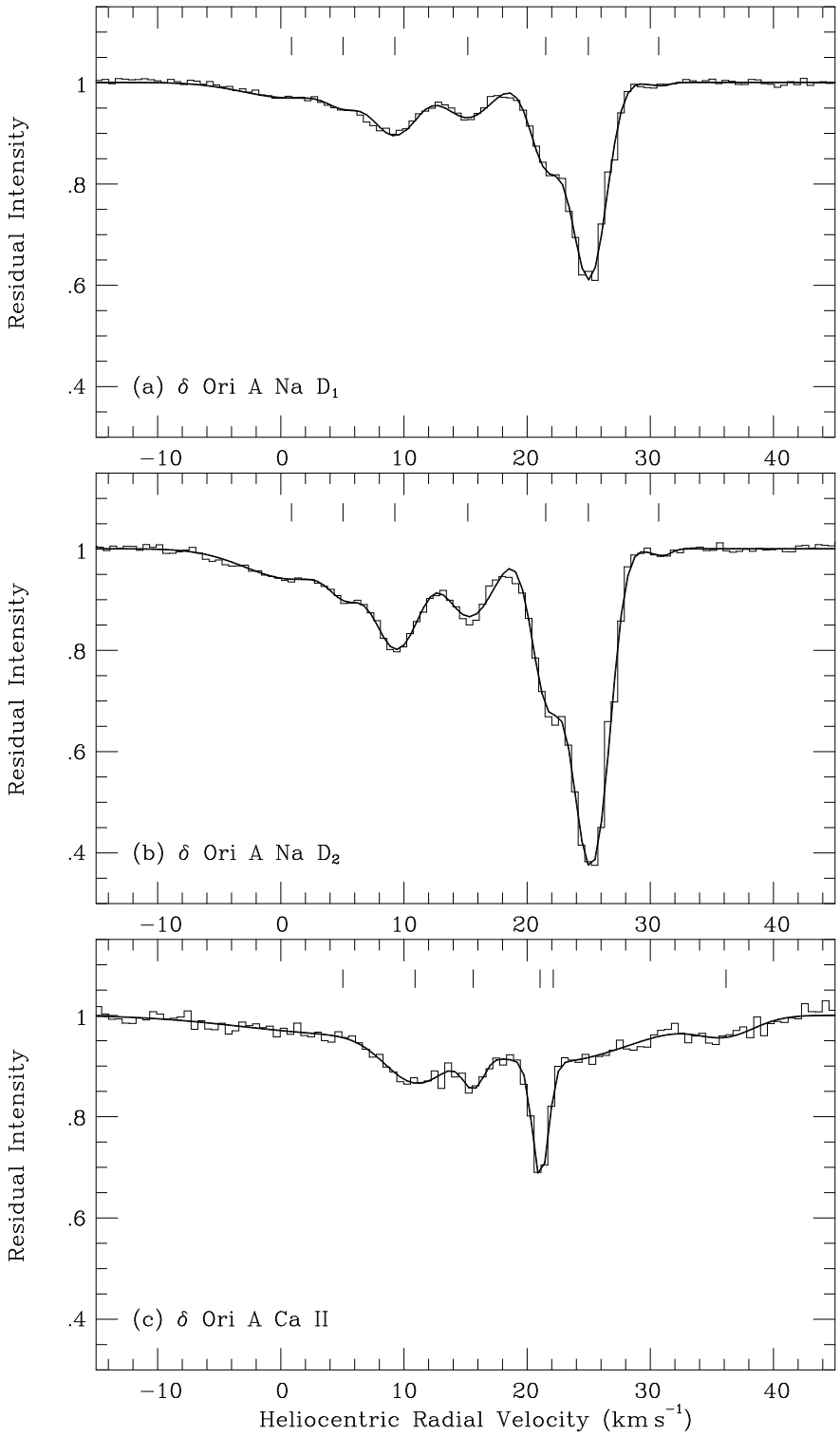

Figure 5.18: Theoretical line profiles are shown plotted over (a) Na I D_1, (b) Na I D_2, (c) Ca II K spectra observed towards δ Ori A using the UHRF. The tickmarks indicate the velocities of the individual model components listed in Table 5.4.

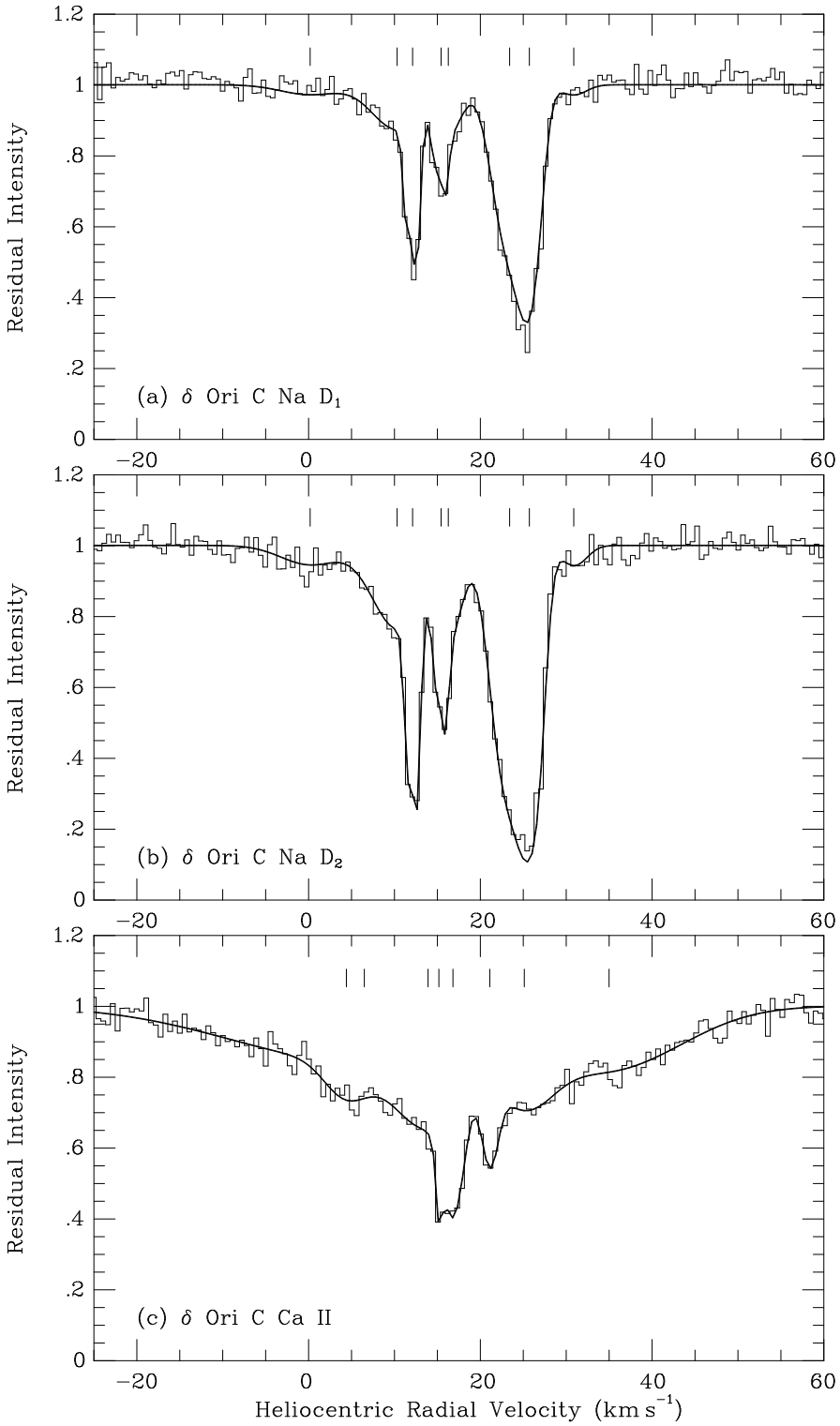

Figure 5.19: Theoretical line profiles are shown plotted over (a) Na I D_1, (b) Na I D_2, and (c) Ca II K spectra observed towards δ Ori C using the UHRF. The tickmarks indicate the velocities of the individual model components listed in Table 5.4.

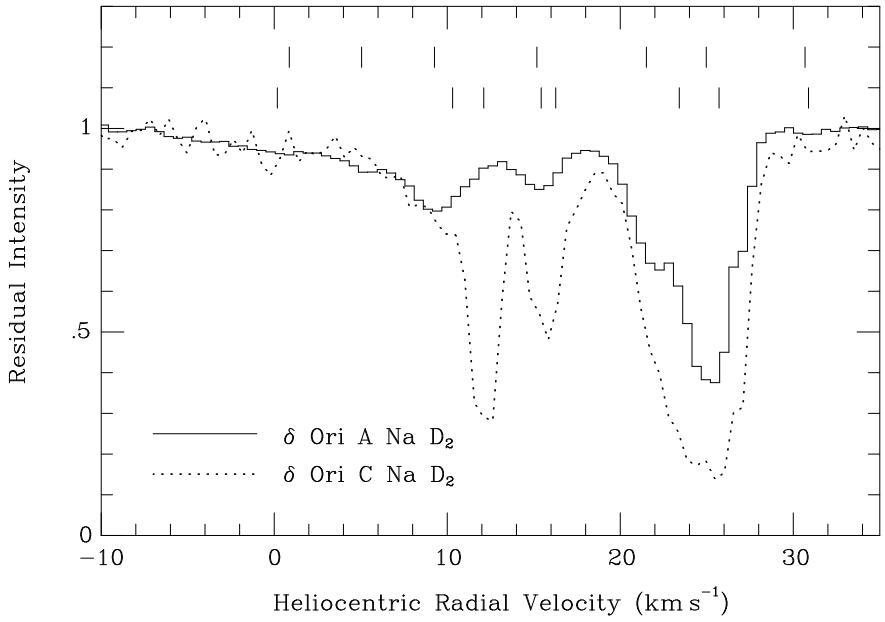

Figure 5.20: A comparison of the Na I D_2 absorption observed towards δ Ori A & C using the UHRF. The plots illustrate the presence of small-scale structure in this direction. The tickmarks indicate the velocities of the individual model components listed in Table 5.4; the upper tickmarks refer to δ Ori A while the lower ones refer to δ Ori C.

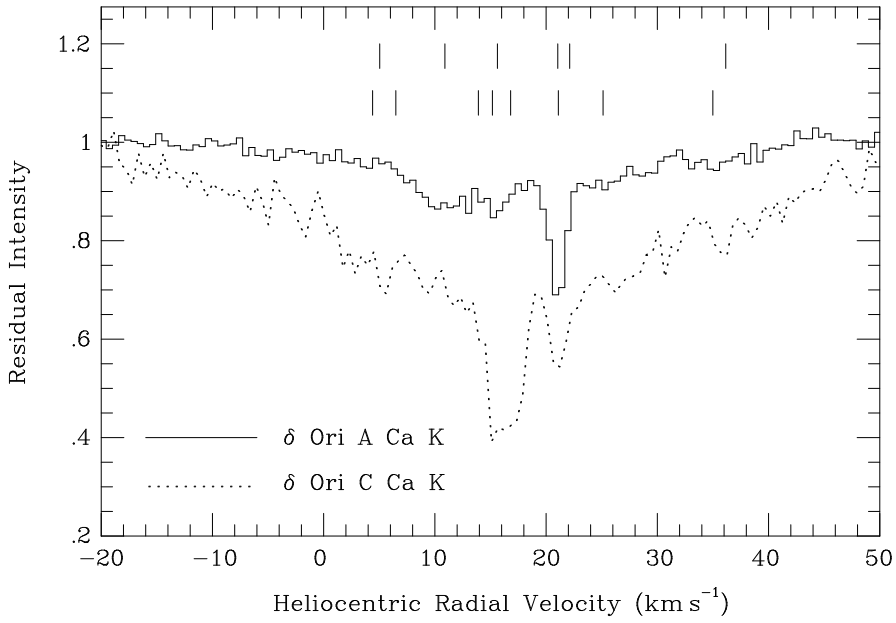

Figure 5.21: A comparison of the Ca II K absorption towards δ Ori A & C using the UHRF. The plots illustrate the presence of small-scale structure in this direction. The tickmarks indicate the velocities of the individual model components listed in Table 5.4; the upper tickmarks refer to δ Ori A while the lower ones refer to δ Ori C.

Table 5.4: Velocity systems identified toward δ Ori A & C in the Ca II and Na I regions using UHRF data. Signal-to-noise ratios are shown in columns 2 & 8, total equivalent widths are shown in columns 3 & 9. Where Na I or Ca II components observed towards δ Ori A & C and listed along-side the same component number (column 4), they are classified as arising in the same cloud; however Na I and Ca II components with the same component number do not necessarily arise in the same cloud. Column 13 contains values of $m_{\rm s}$ (defined in Equation 5.17). Values of $m_{\rm s}$ flagged with * are uncertain.

Line	S/N	W_λ (mÅ)	Comp	$v_\odot$ (km s^{-1})	b (km s^{-1})	log N (cm^{-2})	S/N	W_λ (mÅ)	$v_\odot$ (km s^{-1})	b (km s^{-1})	log N (cm^{-2})	$m_{\rm s}$
				δ Ori A					δ Ori C			
Ca II K:	93	46 ± 1	1	—	—	—	39	187 ± 3	4.40 ± 0.78	3.46 ± 1.16	11.07 ± 0.30	1.00*
			2	5.04 ± 6.74	11.78 ± 5.06	11.06 ± 0.32			6.49 ± 12.13	20.77 ± 6.94	11.98 ± 0.35	0.79*
			3	10.90 ± 0.25	3.43 ± 0.55	10.94 ± 0.13			13.91 ± 2.20	5.41 ± 2.76	11.58 ± 0.39	0.63*
			4	15.62 ± 0.15	1.06 ± 0.28	10.34 ± 0.12			15.17 ± 0.07	0.15 ± 0.44	10.87 ± 0.78	0.54*
			5	—	—	—			16.81 ± 0.14	1.52 ± 0.51	11.37 ± 0.24	1.00*
			6	21.05 ± 0.03	0.75 ± 0.05	10.84 ± 0.02			21.10 ± 0.18	1.19 ± 0.34	11.06 ± 0.22	0.25*
			7	22.12 ± 1.57	9.34 ± 1.73	11.37 ± 0.14			25.12 ± 1.09	4.47 ± 1.64	11.33 ± 0.33	0.05*
			8	36.15 ± 0.49	3.23 ± 0.80	10.49 ± 0.14			34.99 ± 3.15	11.77 ± 2.43	11.75 ± 0.28	0.90*
Na I D_1:	169	58 ± 1	1	0.87 ± 1.08	5.37 ± 1.11	10.78 ± 0.10	40	131 ± 2	0.18 ± 1.62	4.71 ± 2.25	10.69 ± 0.19	0.10
D_2:	179	108 ± 1	2	5.05 ± 0.32	1.49 ± 0.60	10.28 ± 0.25	38	198 ± 2	—	—	—	1.00*
			3	9.26 ± 0.11	2.39 ± 0.25	10.99 ± 0.04			10.31 ± 1.05	3.92 ± 1.37	11.28 ± 0.18	0.32
			4	—	—	—			12.11 ± 0.04	0.35 ± 0.05	11.39 ± 0.04	1.00
			5	—	—	—			15.43 ± 0.10	0.39 ± 0.16	10.91 ± 0.13	1.00
			6	15.18 ± 0.13	2.44 ± 0.22	10.82 ± 0.03			16.27 ± 0.79	1.97 ± 0.73	11.02 ± 0.29	0.23
			7	21.51 ± 0.06	1.39 ± 0.09	11.02 ± 0.02			23.41 ± 0.70	2.35 ± 0.47	11.76 ± 0.17	0.69
			8	24.97 ± 0.03	1.59 ± 0.04	11.51 ± 0.01			25.71 ± 0.17	1.38 ± 0.23	11.68 ± 0.20	0.19
			9	30.68 ± 0.54	0.64 ± 1.13	9.43 ± 0.25			30.88 ± 0.63	1.85 ± 1.07	10.33 ± 0.17	0.78

velocity. The locations of the possible stellar and circumstellar components are consistent with δ Ori C's measured radial velocity of $+21 \pm 5$ km s^{-1} (Wilson, 1953, although this value may be variable) while a spectral type of B2 V would be expected to produce some photospheric absorption. However, Bernacca and Perinotto (1970) have measured a projected rotational velocity of 85 km s^{-1} for this star. If accurate, such a rapid rotation would broaden the stellar line to a point were it would become the local continuum for the interstellar absorption.

The majority of the Ca II K absorption may be modelled with a single very broad component ($b = 23.95$) at a radial velocity of $+17.89$ km s^{-1} (consistent with the location of the strong narrow component at $+16$ km s^{-1}); however, a statistically significant improvement to the fit may be obtained by replacing this broad component with two narrower (but still broad) components at $+6.5$ & $+35.0$ km s^{-1}. The use of a single broad component makes little difference to the values of $v_{\odot}$ and b for the remaining circumstellar/interstellar components, but generally decreases their best fitting values of N.

Interestingly, a comparison of the Ca II K absorption detected towards δ Ori A & C (see Figure 5.21) reveals the $+21$ km s^{-1} component (shown to demonstrate temporal variability in § 5.2.2) to be visible in both sightlines. This has been discussed towards the end of § 5.2.2.2.

5.3.2.3 Joint Analysis

A joint analysis of the MSES and UHRF data may be conducted in a similar manner as that made in § 5.2.2. Since the observations were obtained within a short period of time and no differences are noticeable between them, the parameters of the variable component are not permitted to be different between the MSES and UHRF data. The differing signal-to-noise ratios of the various data-sets has been accounted for by scaling the errors on each data-point within each data-set by (1/SNR) where SNR is the signal-to-noise ratio achieved in the data.

In order to quantify the differences between the absorption present in the sightlines towards δ Ori A & C, we have made use of the parameter $m_{\rm s}$, introduced by Watson and Meyer (1996) and given by the expression,

$$m_{\rm s} = \left| \frac{N[{\rm X}]_{\rm A} - N[{\rm X}]_{\rm C}}{N[{\rm X}]_{\rm A} + N[{\rm X}]_{\rm C}} \right|, \tag{5.17}$$

where $N[{\rm X}]_{\rm A}$ and $N[{\rm X}]_{\rm C}$ represent the column densities of paired components towards

Table 5.5: Velocity systems identified toward δ Ori A & C in the Na I region through the synchronised modelling of UHRF and MSES data. Where Na I or Ca II components observed towards δ Ori A & C and listed along-side the same component number (column 2), they are classified as arising in the same cloud; however Na I and Ca IIcomponents with the same component number do not necessarily arise in the same cloud. Column 9 contains values of m_s (defined in Equation 5.17). Values of m_s flagged with * are uncertain.

Line	Comp	$v_\odot$ (km s^{-1})	b (km s^{-1})	log N (cm^{-2})	$v_\odot$ (km s^{-1})	b (km s^{-1})	log N (cm^{-2})	m_s
			δ Ori A			δ Ori C		
Ca II	1	-5.78 ± 0.38	1.16 ± 0.88	9.80 ± 0.22	—	—	—	1.00*
	2	6.00 ± 4.71	8.52 ± 3.50	11.04 ± 0.33	4.40 ± 0.78	3.46 ± 1.16	11.07 ± 0.30	0.03*
	3	—	—	—	6.49 ± 12.13	20.77 ± 6.94	11.98 ± 0.35	1.00*
	4	11.35 ± 0.54	3.79 ± 1.00	11.05 ± 0.28	13.91 ± 2.20	5.41 ± 2.76	11.58 ± 0.39	0.54*
	5	—	—	—	15.17 ± 0.07	0.15 ± 0.44	10.87 ± 0.78	1.00*
	6	16.16 ± 0.38	2.29 ± 0.47	10.75 ± 0.16	16.81 ± 0.14	1.52 ± 0.51	11.37 ± 0.24	0.61*
	7	21.03 ± 0.03	0.98 ± 0.07	11.02 ± 0.03	21.10 ± 0.18	1.19 ± 0.34	11.06 ± 0.22	0.05*
	8	25.32 ± 0.45	5.04 ± 0.84	11.01 ± 0.07	25.12 ± 1.09	4.47 ± 1.64	11.33 ± 0.33	0.35*
	9	35.90 ± 0.53	3.71 ± 0.72	10.43 ± 0.08	34.99 ± 3.15	11.77 ± 2.43	11.75 ± 0.28	0.91*
Na I	1	—	—	—	-5.80 ± 4.81	3.31 ± 4.57	10.09 ± 0.82	1.00*
	2	0.57 ± 0.71	5.41 ± 0.72	10.76 ± 0.07	0.51 ± 1.30	4.41 ± 2.68	10.59 ± 0.38	0.19
	3	5.38 ± 0.33	1.71 ± 0.51	10.38 ± 0.19	—	—	—	1.00*
	4	9.53 ± 0.12	2.43 ± 0.25	11.01 ± 0.04	10.38 ± 0.89	4.76 ± 1.30	11.38 ± 0.13	0.40
	5	—	—	—	12.00 ± 0.04	0.34 ± 0.04	11.39 ± 0.03	1.00
	6	—	—	—	15.32 ± 0.07	0.40 ± 0.13	10.94 ± 0.14	1.00
	7	15.49 ± 0.11	2.41 ± 0.18	10.83 ± 0.02	16.40 ± 0.90	1.68 ± 0.98	10.87 ± 0.43	0.05
	8	21.77 ± 0.06	1.40 ± 0.08	11.03 ± 0.02	23.37 ± 0.48	2.33 ± 0.30	11.78 ± 0.12	0.70
	9	25.25 ± 0.03	1.59 ± 0.03	11.50 ± 0.01	25.59 ± 0.12	1.35 ± 0.16	11.67 ± 0.15	0.19
	10	31.11 ± 0.35	1.35 ± 0.66	9.73 ± 0.10	31.18 ± 0.46	1.97 ± 0.78	10.29 ± 0.11	0.57

δ Ori A & C respectively. The final column of Tables 5.3 & 5.4 display the values of $m_{\rm s}$ for each component pair found in the MSES and UHRF data respectively. The final column of Table 5.5 displays the same for the joint analysis.

The possible stellar Ca II K absorption in the spectrum of δ Ori C creates uncertainty in the column densities of the interstellar components and as a result, uncertainty in the calculated values of $m_{\rm s}$. Values of $m_{\rm s}$ for the Ca II components have therefore been flagged with a * in Tables 5.4 & 5.5.

Although cloud 2 in the UHRF Na I data is apparently only present in the sightline to δ Ori A, the weak and highly blended nature of this region, coupled with the lower signal-to-noise of the δ Ori C data mean that it is quite possibly present in both sightlines. The same is true for Na I clouds 1 & 3 in the joint analysis. Values of $m_{\rm s}$ for these components have been flagged with a * in Tables 5.4 & 5.5. If we neglect flagged values of $m_{\rm s}$, its mean values are found to be 0.45 (MSES data), 0.54 (UHRF data) and 0.51 (Joint analysis). These values are in the upper range of values found by Watson and Meyer (1996) in their study of 17 sightlines, but agree with their results when plotted along with the separation of δ Ori A & C in their figure 2.

We note that, in general, those clouds producing absorption components which exhibit the largest differences between sightlines (largest $\rm m_{\it s}$) also have the smallest b-values and largest Na° column densities, an effect also reported by Meyer and Blades (1996) and Watson and Meyer (1996), and attributed to the small-scale structure occurring in colder/denser material. Moreover, with a b-value of only 0.33, cloud 4 in the MSES Na I data is the narrowest detected; it is also observed only towards δ Ori C ($m_{\rm s} = 1$). Furthermore, when considering the UHRF data, this cloud is observed to be a blend of clouds 5 & 6, each only observed towards δ Ori C and again the narrowest detected. This strengthens the argument that the observed structure is occurring in cold interstellar gas since, under the assumption of no turbulence, a strict upper limit of $\approx$ 150 K can be placed on the kinetic temperature of these clouds. This is in good agreement with the findings of Watson and Meyer (1996), where all but two components with $\rm m_{\it s} = 1$ have $b < 1.5$ km s^{-1}.

When considering the MSES data, each of the components observed towards δ Ori A possesses counterparts in the direction of δ Ori C with values of $v_{\odot}$ and b which agree within their mutual errors. This highlights the small-scale structure in this direction (when viewed at this resolution) to generally be composed of variations in column density

of clouds intersecting both sightlines rather than separate, small clouds present on single sightlines (at least on these scales).

However, since observations of δ Ori A made with a resolving power of $R \approx 10^6$ (Figure 3.3) show the line profile to be composed of many additional components, we must consider the effect of blending on the current analysis. Since each of the components detected in the MSES data is not saturated (and is therefore on the linear part of the COG), its best-fitting model column densities will be equal to the total summed column density of the components of which they are actually blends. As a result, the value of $m_{\rm s}$ measured for a cloud detected in the MSES data, will be the average of the $m_{\rm s}$ values of the separate components of which it is actually comprised (since the total column density is the same). However, it is important to note that the $R = 3.8 \times 10^5$ UHRF data reveals cloud 4 in the MSES data to be composed of two blended components. Furthermore, the UHRF ($R = 3.8 \times 10^5$) observations show some of the clouds detected towards both δ Ori A & C in the MSES observations to possess values of $v_{\odot}$ and b which do not reside within their mutual error bounds, and therefore may be the result of separate absorbing clouds. This being the case, the values of $m_{\rm s}$ will represent lower limits.

Thus, if higher resolution observations in general reveal a larger number of components only present in single sightlines, a greater mean value of $m_{\rm s}$ will be obtained. As a result, the observations of 17 sightlines made by Watson and Meyer (1996), which used a resolving power of $R \approx 2 \times 10^5$, may underestimate the small-scale structure actually present.

Those components which we only detect towards δ Ori C, are characterised by similar parameters to that of the time-variable absorption reported towards δ Ori A (attributed to filamentary material in the H I shell around the Orion-Eridanus superbubble; see § 5.2.2). Their velocity, although some 10 km s^{-1} lower than the δ Ori A time-variable component, still fall within the range of velocities expected for material contained within the same expanding H I shell and lying in this sightline (cf. the maps presented in fig. 8 of Brown *et al.*, 1995).

By applying the empirical relationship between N(Na I) and N(H I) (Ferlet *et al.*, 1985, see Equation 5.3) to Na I clouds 5 & 6 in the joint analysis (see Table 5.5) and assuming $n_{\rm H} = 10$ cm^{-3}, we find the clouds to have radial extents of 1.6 & 0.6 pc respectively. Alternatively, by assuming their radial extent not to exceed the separation of the stars (0.07 pc), we find $n_{\rm H} > 220$ and > 80 cm^{-3} respectively. Similar results are obtained for small-scale structure observed in Na I by Watson and Meyer (1996) who, using the

latter assumption, find densities of $n_{\rm H} \geq 10^3$ cm^{-3} in some cases. However, we note that the relationship between N(Na I) and N(H I) is not well defined at the lower Na° column densities observed here (Welty *et al.*, 1994). In a study of small-scale structure toward the globular cluster M15, Meyer and Lauroesch (1999) find H I column densities inferred from Na I data to be 10 times higher than estimates from 21-cm observations, suggesting an enhanced Na° column density that does not necessarily trace an increased H I column. Similar findings were made by Bates *et al.* (1995).

The conditions prevailing within the sheets and filaments which are proposed to give rise to the small-scale structure (Heiles, 1997) would lead to an enhanced recombination rate, causing the less highly ionised species (such as Na°) to become further enhanced. The differences in the strengths of the various Na I absorption components towards δ Ori A & C may well result from a similar cause. Indeed, although observations of Na I towards the binary μ Cru by Meyer and Blades (1996) identified significant structure, subsequent observations of Na I, C I, Mg I, Cr II and Zn II made by Lauroesch *et al.* (1998) were able to show that only the neutral species exhibit these *spatial* variations strongly. This is best interpreted as being due to a change of ionisation state, rather than total column density, and indicates that the line-of-sight to μ^1 Cru passes through a denser, colder core (with a higher recombination rate) within a larger cloud which is seen towards both μ^1 and μ^2 Cru.

The spatial scales studied with observations of binary systems are much larger than those probed by temporal variability (see § 5.2). When these scales are coupled with a likely enhancement in the Na° abundance it becomes more easy to reconcile these observations with gas densities pertaining to diffuse clouds. However, Lauroesch *et al.* (2000), who detect significant differences in the Na I profiles between the binary stars HD 32039/40, also identify differences in S II. Since S II is a dominant ionisation stage, these differences must, to some extent, trace the total column density of the clouds rather than just environmental differences (such as temperature, electron density and the radiation field) and therefore ionisation balance.

5.3.3 Other Sightlines

5.3.3.1 λ Ori Association

Although we detect significant differences between the spectra of stars located at the centre of the λ Ori association (specifically λ Ori, ϕ^1 Ori, HD 36894, HD 36895 and HD 36881), their separations project to linear scales (typically $\lesssim$1 pc) which are much larger than those studied in Chapter 5. Furthermore, the majority of these differences are likely to be due to the stars residing at different distances. Sightlines to those stars located further away will therefore intersect a greater number of clouds, giving the appearance of small-scale structure. These observations cannot therefore be used in the same way as observations of multiple stellar systems which are known to possess the same distances.

5.3.3.2 M42 Region

Since the distances to θ^1 Ori A and C (and to some extent θ^2 Ori A) are very similar, the differences in absorption occurring in these sightlines will represent small-scale structure. The projected separation of θ^1 Ori A and C corresponds to small-scale structures of $<$ 6000 AU, while that for θ^1 Ori A and θ^2 Ori A corresponds to $<$ 67000 AU. However, the lack of absorption in the sightline towards the nearby star ι Ori, suggests that the structure is mainly present in proximity to the M42 region (see § 3.4.1). The differences will therefore largely represent small-scale structure in the Orion Nebula, rather than the diffuse ISM.

5.4 Conclusions

5.4.1 Temporal Variations

Observations of δ Ori A made with the UHRF in its highest resolution mode ($R \approx 900,000$) have revealed the presence of a cool ($T_k \leq 280$ K) variable absorption component at a heliocentric velocity of +21.3 km s^{-1}. The component is detected in Na I D_1, where clear hyperfine splitting is seen, and Ca II K. Comparison of our data with existing spectra suggest the component to have consistently increased in strength from 1966 to 1994, and subsequently reduced in intensity by 2000.

In principle, the variable absorption could occur in either the circumstellar environment, or in the foreground ISM. However, the fact that the component has remained stable in velocity for many years, argues against an origin in the immediate vicinity of this complicated multiple stellar system. This conclusion is further supported by the very narrow line widths ($b = 0.45 \pm 0.01$ km s^{-1} for Na I), which imply low kinetic temperatures ($T_{\rm k} < 280$ K) and turbulent velocities ($v_{\rm t} < 0.35$ km s^{-1}).

Temporal variability over such a short period implies the absorbing cloud has a small tangential extent. By assuming an upper limit of 50 km s^{-1} for the transient cloud's tangential velocity, the linear size of the cloud can be limited to < 300 AU (with detectable structure over scales of < 6.6 AU). If the variations are due to displacements in the line of sight (caused by the proper motion of δ Ori) the linear size of the cloud must then be < 15 AU, with detectable structure over scales of < 0.3 AU. Such small distances suggest the cloud to be filamentary in nature, otherwise, very high gas densities are required, inconsistent with the cloud's measured Na$^\circ$/Ca$^+$ ratio (≈ 1 in 1994). Furthermore, observations made in 2000 indicate that the Na$^\circ$/Ca$^+$ ratio underwent a substantial reduction between 1994 and 2000, interpreted as being due to a reduced recombination rate as the line-of-sight probes closer to the edge of the dense filamentary structure. We suggest an origin within filamentary material associated with the expanding H I shell surrounding the Orion-Eridanus superbubble.

Observations of ζ Ori similarly show the presence of a cool ($T_{\rm k} < 268$ K; $v_{\rm t} < 0.31$ km s^{-1}), temporally variable absorption component at a velocity of -1 km s^{-1}. Although this velocity is somewhat removed from that of δ Ori A's variable component, the H I observations of Brown *et al.* (1995) show that the Orion-Eridanus shell may indeed have material at this velocity in the direction of ζ Ori.

Assuming a plausible upper limit of 50 km s^{-1} for the cloud's tangential velocity, it is possible to deduce that the cloud possesses structure over scales of < 70 AU. Alternatively, if the proper motion of ζ Ori is responsible for a displacement of the line-of-sight, the cloud must possess structure over scales of < 7 AU. Since further observations of ζ Ori are not available, it is not possible to estimate the likely size of the absorbing cloud.

Similar attempts to identify temporal variability in interstellar absorption lines made by Welty *et al.* (1994) and Welty *et al.* (1996), found no evidence for temporal variability; however, the success of our investigation is primarily due to the availability of the observations made by Welty *et al.* (1994) and Welty *et al.* (1996). In hindsight, subtle variations can also be seen between the observations by Welty *et al.* (1994) and by Hobbs (1969*a*), and between those of Welty *et al.* (1996) and Marschall and Hobbs (1972). In previous studies where temporal variability has been detected, the observed changes are generally considered to be the result of a displacement in the line-of-sight due solely to the proper motion of the target. We have shown that motion of the absorbing cloud is important and is likely to make a more significant contribution to the displacement of the line-of-sight, relative to the cloud, and therefore must be considered.

These observations therefore add to the growing body of evidence for small-scale ($\lesssim$100 AU) structure within the diffuse ISM. However, the observations strongly imply that the absorbing medium must be highly non-spherical, and support the conclusion of Heiles (1997) that it is most likely filamentary in structure. The fact that the line-of-sight towards both δ Ori A and ζ Ori intercept the expanding H I shell surrounding the Orion-Eridanus superbubble, makes this an especially plausible interpretation.

Temporal variability is also detected in the Ca II line profile of β Ori, but is however considered to occur in the star's circumstellar environment. Variability is detected in two components with velocities of -32 & $+9$ km s^{-1} (our clouds 1† & 7a† respectively). The clouds are characterised by high temperatures (1210 & 4130 K for clouds 1† & 7a† respectively) and the Na°/Ca^{+} ratios are low (< 0.04 & $\lesssim 0.66$ for clouds 1† & 7a† respectively), consistent with a circumstellar environment.

With regards to the remaining sightlines, no conclusive evidence for line profile variability has been detected. In the case of θ^1 Ori A & C and θ^2 Ori A, differences are detected but are however considered to be a result of errors in continuum normalisation rather than true variability in the line-of-sight absorption.

5.4.2 Spatial Variations

We present high-resolution ($R \approx 110,000$ & 380,000) observations of the D lines of Na I and the H & K lines of Ca II, clearly demonstrating variations in the strengths of interstellar absorption lines between two stars in the well known multiple system δ Orionis. The two stars, δ Ori A & C, are separated by 52 arcsec which corresponds to a projected separation of 15000 AU (0.07 pc). These differences are therefore indicative of small-scale spatial structure in the interstellar medium in this direction over distances of less than $\approx$ 15000 AU.

The magnitude of the column-density differences vary between components. It is notable that components with the largest Na I column densities and lowest velocity dispersions are, in general, found to be subject to the greatest differences; in fact the narrowest components detected are only observed in the sightline to δ Ori C. This effect has also been reported by Meyer and Blades (1996).

Our observations have shown additional structure to be detectable in the higher-resolution data. As a result, we are able to show that previous investigations of small-scale interstellar structure (which are generally made with lower-resolutions), are likely to have underestimated the extent to which small-scale structure is present in the ISM.

Although the line-of-sight variations detected here may trace differences in the spatial extent and/or density of the absorbing clouds, they may also reflect changes in the ionisation equilibria due to changes in the prevailing physical conditions (e.g. temperature, electron density and local radiation field). In any case, these observations add weight to the view that small-scale structure is ubiquitous in the ISM (e.g. Heiles, 1997, and references therein).

CHAPTER 6

Analysis of Temperature and Turbulence[1]

Where an interstellar cloud has been observed in two co-spatial species (primarily Na I and K I) an analysis of the broadening measured for each species may be used to derive strict limits on the kinetic temperature and turbulent velocity prevailing within the cloud. Following the analysis of twelve clouds, it is found that turbulent velocities are almost certainly subsonic.

6.1 Introduction

As has been described in detail in § 1.2.1, interstellar line broadening is dominantly the result of two effects, namely Doppler broadening due to (a) the kinetic temperature of the absorbers, $T_{\rm k}$, and (b) the line-of-sight rms turbulent velocity within the cloud, $v_{\rm t}$. If the velocity spectrum of the turbulence is Gaussian, then the b-value resulting from these two broadening mechanisms is described by Equation 1.13,

$$b = \sqrt{\frac{2kT_{\rm k}}{m} \; + \; 2v_{\rm t}^2}.$$

Thus by observing two species which are considered to exist co-spatially, and which have an adequate mass differential, e.g. Na & K, it becomes possible to solve Equation 1.13 simultaneously for both $T_{\rm k}$ and $v_{\rm t}$ (see Dunkin and Crawford, 1999).

Since these calculations depend critically on the component structures obtained from our models, this type of analysis is best suited to isolated velocity components, where confusion with nearby blended absorption is at a minimum. Furthermore, for the intrinsically

[1] The majority of the work presented in this chapter has been previously published in Price *et al.* (2001*a*)

weak K I line to be detectable, the Na I line must be strong, but not saturated. In order for these results to be meaningful, the intrinsic widths of the lines must be determined, something best suited to very-high-resolution/high signal-to-noise data.

The Ultra-High-Resolution Facility (hereinafter UHRF) is capable of resolving intrinsic line widths for components with b-values as low as 0.2 km s^{-1} (which in the case of Na, corresponds to a cloud with $T_{\rm k} = 50$ K, and $v_{\rm t} = 0.05$ km s^{-1}). Furthermore, the ability of the UHRF to distinctly resolve the hfs of narrow (and not strongly blended) Na I D_1 components places rigorous limits on the range of permitted b-values. Many examples of resolved hfs components are visible in the UHRF spectra, a notable example being the 2.90 km s^{-1} component observed towards ϵ Ori, which has a derived b-value of 0.35 km s^{-1} (discussed in § 6.2.2).

The derived value of $T_{\rm k}$ can subsequently be used to determine the isothermal sound speed, $C_{\rm s}$ in a cloud, using the relation

$$C_{\rm s} = \sqrt{\frac{kT_{\rm k}}{\mu}}, \tag{6.1}$$

where μ is the mean mass per particle, the derivation of which is detailed below.

6.1.1 Derivation of μ

The calculation of μ requires assumptions to be made regarding the composition and state of the gas concerned. Although hydrogen is by far the most abundant species, the effect of helium will be important. A value of μ representing an atomic hydrogen gas containing 10% helium by number is frequently assumed (e.g. Spitzer, 1978, pg. 216–7). The calculation of μ can be made in the following way.

$$\mu = \frac{n_{\rm H}\ m_{\rm H} + n_{\rm He}\ m_{\rm He}}{n_{\rm H} + n_{\rm He}} \tag{6.2}$$

substituting 0.1 $n_{\rm H}$ for $n_{\rm He}$, and 4 $m_{\rm H}$ for $m_{\rm He}$ we find,

$$\mu = \frac{n_{\rm H}\ m_{\rm H} + (0.1\ n_{\rm H})(4\ m_{\rm H})}{n_{\rm H} + 0.1\ n_{\rm H}} \tag{6.3}$$

$$\mu = \frac{1.4\ m_{\rm H}}{1.1} \tag{6.4}$$

$$\mu = 1.27\ m_{\rm H} \tag{6.5}$$

A more important issue however, is the adopted fractional abundance of molecular species. The fraction of hydrogen locked up in the molecular form will be the most

Table 6.1: Values of kinetic temperature ($T_{\rm k}$), turbulent velocity ($v_{\rm t}$), three-dimensional turbulent velocity ($\equiv \sqrt{3}v_{\rm t}$) and isothermal sound speed ($C_{\rm s}$; relating to atomic H with 10% He by number) for clouds simultaneously observed in two co-extensive species. Columns 1, 2 & 3 show the sightline studied and its total column densities of H I and H_2. Column 4 displays the species used in the analysis, while columns 5 and 6 display the component number and the heliocentric radial velocity (taken from the Na I counterpart, as listed in Tables 3.11, 3.13 & 3.14). Columns 7 to 10 display exact solutions, where available, while columns 11 to 14 display all values allowed within the 1σ error limits quoted in Tables 3.11, 3.13 & 3.14. In the cases where no solutions within the 1σ error bounds are available, 2σ error limits are used and the results are listed in parenthesis in columns 11 to 14.

1	2	3	4	5	6	7	8	9	10	11	12	13	14
Star	log $[N]_{tot}$		Method	Cloud	$v_\odot$	$T_{\rm k}$	$v_{\rm t}$	$\sqrt{3}v_{\rm t}$	$C_{\rm s}$	$\Delta T_{\rm k}$	$\Delta v_{\rm t}$	$\Delta\sqrt{3}v_{\rm t}$	$\Delta C_{\rm s}$
	[H]	[H_2]				(K)	(km s^{-1})	(km s^{-1})	(km s^{-1})	(K)	(km s^{-1})	(km s^{-1})	(km s^{-1})
ϵ Ori	20.45	16.57	Na I/Ca II	2	2.90	86	0.17	0.30	0.75	22 – 148	0.11 – 0.22	0.18 – 0.39	0.38 – 0.98
			Na I/K I	5	10.94	355	0.26	0.46	1.52	0 – 584	0.00 – 0.43	0.00 – 0.75	0.00 – 1.96
			Na I/K I	11	24.77	77	0.37	0.65	0.71	0 – 404	0.18 – 0.42	0.32 – 0.73	0.00 – 1.63
ζ Ori	20.41	15.73	Na I/K I	2e†	-1.07	—	—	—	—	0 – 293	0.00 – 0.33	0.00 – 0.56	0.00 – 1.38
			Na I/K I	8a	22.97	—	—	—	—	(0 – 92)	(0.18 – 0.25)	(0.31 – 0.44)	(0.00 – 0.78)
			Na I/K I	8b	23.19	—	—	—	—	(0 – 1023)	(0.00 – 0.61)	(0.00 – 1.05)	(0.00 – 2.59)
			Na I/K I	11a	26.20	—	—	—	—	0 – 101	0.00 – 0.19	0.00 – 0.33	0.00 – 0.81
			Na I/K I	11b	26.41	—	—	—	—	508 – 841	0.00 – 0.30	0.00 – 0.52	1.82 – 2.35
κ Ori	20.52	15.68	Na I/K I	6	17.76	—	—	—	—	(0 – 332)	(0.00 – 0.32)	(0.00 – 0.55)	(0.00 – 1.47)
			Na I/K I	7	18.86	—	—	—	—	0 – 280	0.00 – 0.32	0.00 – 0.55	0.00 – 1.35
			Na I/K I	8	20.25	356	0.34	0.59	1.53	0 – 757	0.00 – 0.52	0.00 – 0.91	0.00 – 2.23
			Na I/K I	9	21.05	—	—	—	—	0 – 244	0.00 – 0.30	0.00 – 0.51	0.00 – 1.26

important consideration, due to the abundance of atomic hydrogen. Positive detections of molecular hydrogen have been made towards ϵ, ζ and κ Ori at velocities corresponding to each K I component (see figure 3, figure 7 and table 1 of Jenkins *et al.*, 2000; Jenkins and Peimbert, 1997; Spitzer and Morton, 1976, respectively). The presence of molecular hydrogen in these clouds will of course increase the mean mass per particle, therefore reducing the prevailing isothermal sound speed.

To account for the possible presence of molecular hydrogen in these clouds Equation 6.2 may be adapted to calculated an enhanced value of μ.

$$\mu = \frac{n_{\rm H}\ m_{\rm H} + n_{\rm H_2}\ m_{\rm H_2} + n_{\rm He}\ m_{\rm He}}{n_{\rm H} + n_{\rm H_2} + n_{\rm He}} \tag{6.6}$$

If we assume 50% of the hydrogen atoms to be locked up in molecular hydrogen, i.e. $n_{\rm H} = 2\ n_{\rm H_2}$, we find,

$$\mu = \frac{(n_{\rm H}/2)\ m_{\rm H} + (n_{\rm H}/4)(2\ m_{\rm H}) + n_{\rm He}\ m_{\rm He}}{(n_{\rm H}/2) + (n_{\rm H}/4) + n_{\rm He}} \tag{6.7}$$

if we again substitute $0.1\ n_{\rm H}$ for $n_{\rm He}$, and $4\ m_{\rm H}$ for $m_{\rm He}$ we find,

$$\mu = \frac{(n_{\rm H}/2)\ m_{\rm H} + (n_{\rm H}/4)(2\ m_{\rm H}) + 0.1\ n_{\rm H}\ (4m_{\rm H})}{(n_{\rm H}/2) + (n_{\rm H}/4) + 0.1\ n_{\rm H}} \tag{6.8}$$

$$\mu = \frac{1.4\ n_{\rm H}\ m_{\rm H}}{(17/20)\ n_{\rm H}} \tag{6.9}$$

$$\mu = 1.65\ m_{\rm H} \tag{6.10}$$

In the situation where all of the hydrogen is present in the molecular form, μ takes the value $2.33\ m_{\rm H}$. However, the column densities of molecular hydrogen are seen to be small with respect to those of hydrogen. Total H I and H_2 column densities are shown in Table 6.1, taken from Savage *et al.* (1977). These values signify that in each case, less than 0.03% of the H is locked up in H_2 over the entire sightline. In reality, molecular hydrogen is likely to be preferentially found in the same (colder/denser) regions where the Na I and K I absorption is thought to arise, but the fraction of hydrogen in the molecular form is still expected to be small. Even if 50% of the hydrogen atoms in these regions were to be in the molecular form, the change in μ described above only results in a $\approx 14\%$ decrease in $C_{\rm s}$.

Where the best fitting b-values of corresponding Na I and K I components provide a solution to Equation 1.13, "exact solutions" are said to be obtained (see columns 7–10 of

Table 6.1). Furthermore, 1σ error limits quoted in Tables 3.3, 3.11, 3.13 and 3.14 may also been adopted for each b-value, providing a range of allowed solutions to Equation 1.13 (see columns 11–14 of Table 6.1).

6.2 The Sightlines

Observations of both Na I and K I have been made for the sightlines towards β, ϵ, ζ, and κ Orionis, which are discussed individually below.

6.2.1 β Orionis

Absorption from K I has not been positively identified towards β Ori (refer to Figure 3.2). This is consistent with the relatively weak strength of Na I towards this star. Although our sample of Na I, K I pairs is far too small for a meaningful statistical analysis, a comparison of Na° and K° column densities shows a typical ratio Na°/K° ≈ 60, leading to an expected K° column density towards β Ori of only $\log N \approx 9.00$ from the strongest Na I component, which is below our detection threshold.

6.2.2 ϵ Orionis

Observations of K I towards ϵ Ori reveal the presence of two main absorption components (refer to Figure 3.10). Although the higher-velocity component exhibits slight asymmetry, it can be accurately modelled with a single absorbing cloud.

Exact solutions are achievable for both clouds and show both $v_{\rm t}$ and $\sqrt{3}v_{\rm t}$ to be subsonic. Only in the extreme case where the majority of hydrogen is present in the molecular form does the sound speed of ϵ Ori's $+24.77$ km s^{-1} component permit supersonic, three-dimensional turbulent motions. Over the full 1σ error range, supersonic turbulence is only permitted when $T_{\rm k}$ resides near its lower limit.

A very narrow Na I absorption component with one of the clearest examples of hfs is present at a velocity of $+2.90 \pm 0.01$ km s^{-1}. Although too weak to be accurately modelled, a possible signature of K I absorption is present at a similar velocity ($\approx +2.7$ km s^{-1}), with an equivalent width of ≤ 0.5 mÅ. Furthermore, a comparison of the Na I and Ca II spectra of ϵ Ori illustrates a narrow Ca II absorption component at a velocity of $+2.88 \pm 0.01$ km s^{-1}. This system is a clear example of both Na I and Ca II absorption from a cool cloud occurring at (within the errors) the same velocity. By assuming the case of

purely thermal ($v_t = 0$) or purely turbulent ($T_k = 0$) broadening, it is possible to place strict upper limits on both the T_k and v_t prevailing in the regions where the Na I and Ca II absorption is occurring, without having to assume the species are co-spatial. In the case of Na°, $T_k \leq 169$ K and $v_t \leq 0.25$ km s^{-1}, while for Ca^+, $T_k \leq 231$ K and $v_t \leq 0.22$ km s^{-1}.

It is generally observed that line broadening in Ca II is greater than that seen in Na I (interpreted to be due to Ca^+ preferentially occupying the warmer outer regions of a cloud; e.g. Barlow *et al.*, 1995). However, in this case it is Na I which is seen to exhibit the largest broadening. The fact that the lighter Na atom is subjected to greater broadening may signify that the species exist co-spatially. This being the case it is possible to solve Equation 1.13 in the same way as has been done for Na I and K I (see first entry of Table 6.1). Both the line-of-sight and three dimensional turbulent velocities are well below the corresponding sound speeds for either a purely atomic or a purely molecular gas, indicating the turbulence to be subsonic in all cases. We find that three dimensional supersonic turbulent motions are only permitted in an atomic gas when T_k is *at* its lower limit. It is interesting to note that, while this cloud is cold, it has a Na°/Ca^+ ratio of 1.78, illustrating that not all the Ca has been depleted. Since Ca is rapidly depleted onto grain surfaces (Barlow *et al.*, 1995), the recent removal of Ca atoms from grains would be implied, consistent with Na and Ca being co-extensive.

6.2.3 ζ Orionis

Between velocities of +20 & +30 km s^{-1}, the interstellar Na I spectrum of ζ Ori is dominated by two features (refer to Figure 3.12). Modelling of these two features requires five components for a satisfactory fit. Examination of this star's K I interstellar spectrum echoes the presence of the two major Na I features, but further investigation reveals the components to be asymmetric, such that four of the five Na I components have corresponding K I components. The highly blended nature of this region leads, in general, to larger errors for the weak K I components. An additional weak K I component is also present at -1.31 km s^{-1}, corresponding to the temporally variable Na I component at -1.07 km s^{-1}(see § 5.2.3).

None of the clouds permit exact solutions for T_k and v_t, while clouds 8(a) and 8(b) do not allow any physical solutions within their respective 1σ error ranges. In this case, 2σ error ranges can be applied, resulting in an allowed range for T_k and v_t for both clouds. These results are listed in parenthesis in Table 6.1. In the case of cloud 11(b), the line-

of-sight and three dimensional turbulence is subsonic, even in a molecular gas. For the remaining clouds, supersonic turbulence is only allowed when $T_{\rm k}$ is near its lower limit.

6.2.4 κ Orionis

Observations of K I towards κ Ori reveal the presence of two absorption features, near +18 and +20 km s^{-1}. Although each region may be accurately fitted with a single component, the +20 km s^{-1} feature coincides with three strong Na I components and so has been modelled with three corresponding K I components.

Only cloud 8 permits exact solutions for $T_{\rm k}$ and $v_{\rm t}$, while cloud 6 has no physical solutions within its 1σ error range. If 2σ errors are applied to cloud 6, an allowed range for $T_{\rm k}$ and $v_{\rm t}$ may be calculated. These results are listed in parenthesis in Table 6.1. Supersonic turbulence is again only permitted when $T_{\rm k}$ is near its lower limit.

6.3 Discussion

A comparison of $v_{\rm t}$ and $\sqrt{3}v_{\rm t}$ with $C_{\rm s}$ from the available exact solutions to Equation 1.13 (Table 6.1, columns 7–10) demonstrates the turbulent motions to be subsonic in all cases. If a molecular gas is assumed, only ϵ Ori's cloud 11 permits supersonic three dimensional turbulent motions, if 50% or more of the H nuclei are in the form of H_2.

Similarly, where exact solutions are not available, a comparison of the range of turbulent velocities and sound speeds permitted within the adopted b-value error ranges (shown in Table 6.1, columns 11–14) indicates that the turbulent motions are generally subsonic, unless $T_{\rm k}$ is near its lower limit.

However, this is subject to a selection effect. In the two extreme cases where either $T_{\rm k}$ or $v_{\rm t}$ is zero, we find that the allowed b-values of the two observed species range from being equal ($\frac{b_K}{b_{Na}} = 1.0$) to differing by a factor equal to the square root of their mass ratio respectively ($\frac{b_K}{b_{Na}} = 0.7679$). Outside this range no physical solutions are permitted. Since the errors associated with the b-values of K I are in general much larger than those of their Na I counterparts (weaker components; lower S/N), solutions for $T_{\rm k}$ and $v_{\rm t}$ are available for each b-value allowed within the 1σ error range of several Na I components (clouds 2e† & 11a towards ζ Ori and clouds 7, 8 (although an exact solution is available for this cloud) & 9 towards κ Ori). This illustrates that the line broadening in *both* species should be determined to a level of accuracy such that solutions for $T_{\rm k}$ and $v_{\rm t}$ are not obtainable over

the entire range of permitted b-values of either of the species. If this is not achieved, the range of permitted values of $T_{\rm k}$ and $v_{\rm t}$ is not restricted any further than that which may be obtained from the observation of a single species.

When the turbulent velocity exceeds the isothermal sound speed, turbulent velocities become supersonic. In the limit, where $C_{\rm s} = v_{\rm t}$, it is possible to substitute Equation 6.1 for $v_{\rm t}$ in Equation 1.13 thus deriving the following expression for b,

$$b = \sqrt{\frac{2kT_{\rm k}}{m} + \frac{2kT_{\rm k}}{\mu}} \tag{6.11}$$

Values of m relating to both sodium and potassium may be substituted into Equation 6.11,

$$\frac{b_K^2}{b_{Na}^2} = \frac{\frac{2kT_{\rm k}}{39U} + \frac{2kT_{\rm k}}{\mu}}{\frac{2kT_{\rm k}}{23U} + \frac{2kT_{\rm k}}{\mu}} \tag{6.12}$$

where U is the atomic mass unit. Rearranging, we find

$$\frac{b_K^2}{b_{Na}^2} = \frac{23(\mu + 39U)}{39(\mu + 23U)} \tag{6.13}$$

$$\frac{b_K}{b_{Na}} = 0.9784 \tag{6.14}$$

Therefore, for $0.7679 < \frac{b_K}{b_{Na}} < 0.9784$ solutions will be subsonic, while for those solutions where $0.9784 < \frac{b_K}{b_{Na}} < 1.0$, supersonic turbulence results. This illustrates that where solutions for $T_{\rm k}$ and $v_{\rm t}$ are available for each b-value within the Na I error range, 91% of the possible solutions describe subsonic turbulence in a purely atomic gas. When considering the perhaps more realistic case of three dimensional turbulence ($\equiv \sqrt{3}\times v_{\rm t}$), we find,

$$\frac{b_K}{b_{Na}} = 0.9620 \tag{6.15}$$

and the value falls to 87%, again for a purely atomic gas. If hydrogen is partially molecular, the applicable value of μ will of course result in a lower sound speed, therefore altering the limit at which turbulent motions become supersonic. In the extreme case where *all* of the hydrogen is present in the molecular form (highly unlikely for the clouds observed here), we find $\frac{b_K}{b_{Na}} = 0.9703$ and $\frac{b_K}{b_{Na}} = 0.9508$ for line-of-sight and three dimensional turbulence respectively. Thus the percentage of solutions for Equation 1.13 resulting in subsonic turbulence becomes 87% and 79%, again for line-of-sight and three dimensional turbulent motions respectively.

Therefore, in the cases where solutions to Equation 1.13 are available over the entire error range of b (for a given species), the range of permitted solutions will inherently show turbulence to remain subsonic unless $T_{\rm k}$ resides near its lower limit.

Although this is the case for four of the clouds analysed here, results from each of the remaining eight clouds (three of which allow exact solutions), show turbulent motions to be subsonic. For this reason we are confident that turbulent motions are indeed likely to be subsonic.

6.4 Conclusions

We have observed interstellar absorption components from both of the group 1 metals Na I and K I (which are expected to be co-spatial) in a total of 11 clouds, in the sightlines to three stars. Furthermore, observations of Na I and Ca II (which are not normally expected to be co-spatial), have highlighted a cloud in the direction of ϵ Ori, in which the lighter Na atoms are observed to experience greater broadening than the heavier Ca atoms. This is not normally observed for interstellar gas, and is interpreted as the species existing co-spatially.

By solving Equation 1.13 simultaneously for each of these clouds, it has been possible to place strict limits on the kinetic temperature, $T_{\rm k}$, and line-of-sight rms turbulent velocity, $v_{\rm t}$, prevailing in each of the twelve clouds.

Four of the clouds permit solutions for the best-fitting b-values in each species and our results show both the line-of-sight and three dimensional turbulence ($\equiv \sqrt{3}v_{\rm t}$) to be subsonic. Of the remaining eight clouds, for which exact solutions are not obtainable, five have solutions within the 1σ error range of b and three have solutions within the 2σ error range of b. For those clouds which don't permit exact solutions, the allowed range of results show the turbulent motions to be subsonic unless $T_{\rm k}$ is near its lower limit.

We have also shown that the b-values in both species must be determined to a level of accuracy such that solutions for $T_{\rm k}$ and $v_{\rm t}$ may not be obtained for each value of b within the permitted range of either of the species. If this is not achieved the range of permitted values of $T_{\rm k}$ and $v_{\rm t}$ is not restricted any further than that which may be obtained from the observation of a single species. As a result the allowed range of solutions for $T_{\rm k}$ and $v_{\rm t}$ will inherently show turbulent motions to be subsonic unless $T_{\rm k}$ resides near its lower limit. This condition has not been met for four of the clouds analysed here.

Be that as it may, results from each of the remaining eight clouds (three of which allow exact solutions), show turbulent motions to be subsonic. We are therefore confident that turbulent motions are almost certainly subsonic.

Chapter 7

Conclusions

The resolving power of these data exceeds all known previous observations for many of the targets. As a result, these observations enable many of the blended lines seen in this complex sightline to be resolved for the first time. Our ultra-high-resolution data have thus allowed a much more accurate perspective to be obtained of the absorbing medium in this direction, and highlight the necessity for ultra-high-resolution/high signal-to-noise observations when studying the diffuse interstellar medium (ISM).

Following the absorption line modelling of these data, they are used to investigate the velocity structure of the Orion region, and the intervening ISM. Excellent agreement between the independently modelled Na I, Ca II and K I absorption components means that many of the individual interstellar clouds are likely to have been identified. Observations of closely spaced targets in the M42 region and λ Ori association have been used to identify absorption systems, where absorption from individual interstellar clouds may be seen in more than one sightline. This allows the likely line-of-sight velocity structure of the ISM to be discerned. In the case of the λ Ori association, the detection of strong Ca II absorption at a velocity of $\approx +7$ km s^{-1} demonstrates the rings of infrared (Zhang *et al.*, 1989) and CO (Lang *et al.*, 2000; Maddalena and Morris, 1987) emission around the λ Ori association to actually be part of an expanding shell.

Na$^{\circ}$/Ca^{+} ratios have been obtained for each individual cloud, providing an indication of their prevailing physical conditions. Plotting Na$^{\circ}$/Ca^{+} against radial velocity (see Figure 3.14) illustrates the Routly Spitzer effect (whereby clouds with larger Na$^{\circ}$/Ca^{+} abundance ratios are preferentially found at lower absolute velocities Routly and Spitzer,

1952) and highlights the presence of distinct groups, which are utilised in the analysis of the ISM in this direction. Furthermore, we detect a small shift in the mean velocity of absorption with large Na°/Ca^{+} ratios over the region. This is consistent with this absorption arising in the neutral gas marking the boundary of the Orion-Eridanus superbubble which shows a similar trend in H I observations made by Brown *et al.* (1995, cf. their fig 8).

Where a cloud has been observed in two species expected to exist co-spatially (generally sodium and potassium), the line broadening produced in each species has been used to determine the kinetic temperature and line-of-sight rms turbulent velocity. We demonstrate that these calculations will preferentially show $v_{\rm t}$ to be sub-sonic unless $T_{\rm k}$ is near its lower limit if the line widths have not been determined to a sufficient degree of accuracy; nonetheless, we find that turbulent motions are almost certainly subsonic.

The comparison of our observations with those presented in earlier studies has allowed us to identify striking line-profile variations in the spectra of three stars, the most notable being δ Ori A. Multiple observations of δ Ori A have highlighted the presence of a variable interstellar absorption component at a velocity of $+21.3$ km s^{-1} which we detected in Na I, where clear hyperfine splitting is seen, and Ca II. The radial velocity of the component is consistent with an origin within filamentary material associated with the expanding H I shell surrounding the Orion-Eridanus superbubble.

Comparison of our data with existing spectra suggest the component to have consistently increased in strength from 1966 to 1994, and subsequently reduced in intensity by 2000. Temporal variability over such a short period implies the absorbing cloud to have a small tangential extent. By assuming an upper limit of 40 km s^{-1} for the transient cloud's tangential velocity (equal to the expansion velocity of the Orion-Eridanus shell), the linear size of the cloud can be limited to < 250 AU (with detectable structure over scales of < 5.3 AU). However, if the variations are due to displacements in the line of sight (caused by the proper motion of δ Ori) the linear size of the cloud must then be < 15 AU, with detectable structure over scales of < 0.3 AU. Such small distances suggest the cloud to be filamentary in nature, otherwise, very high gas densities are required, inconsistent with the clouds measured Na°/Ca^{+} ratio (≈ 1 in 1994). Furthermore, observations made in 2000 indicate that the Na°/Ca^{+} ratio underwent a substantial reduction between 1994 and 2000, interpreted as being due to a reduced recombination rate as the line-of-sight probes closer to the edge of the dense filamentary structure.

We also present observations which clearly demonstrate variations in the strengths of interstellar absorption lines between two stars in the well known multiple system δ Orionis. The two stars, δ Ori A & C, are separated by 52 arcsec which corresponds to a projected separation of 15000 AU (0.07 pc). These detections therefore highlight structure in the interstellar gas over scales $<$ 15000 AU. The magnitude of the column-density differences varies between components, and it is notable that the narrower/stronger components are observed to exhibit the greatest differences (indeed, the narrowest components detected are only present towards δ Ori C), implying the small-scale structure to preferentially be found in cool gas.

Although these line-of-sight variations, detected in Na I, may trace differences in the spatial extent and/or density of the absorbing clouds, they may also reflect changes in the ionisation equilibria due to changes in the prevailing physical conditions (e.g. temperature, electron density and local radiation field).

It is notable that while significant differences exist in the strength of the interstellar absorption components identified towards δ Ori A and C, only one, that at +21.3 km s^{-1}, exhibits temporal variability over the period considered here. This component has a radial velocity consistent with it arising in a swept-up shell at the periphery of the Orion-Eridanus superbubble, where high tangential velocities ($\approx$ 40 km s^{-1}) might be expected. This would also be consistent with the low measured Na$^{\circ}$/Ca^{+} ratio of this component ($\lesssim$1). Thus, while most of the (apparently non-variable) differences between these two neighbouring sightlines can be attributed to the seemingly ubiquitous small-scale structure in the cold neutral medium (Heiles, 1997), it seems likely that the *variable* component towards δ Ori A has an origin specifically related to the Orion-Eridanus shell.

These observations therefore add to the growing body of evidence for ubiquitous small-scale ($\sim$ 100 AU) structure within the diffuse ISM (e.g. Heiles, 1997, and references therein). However, the observations strongly imply that the absorbing medium must be highly non-spherical, and support the conclusion of Heiles (1997) that it is most likely filamentary in structure. The fact that the line-of-sight intercepts the expanding H I shell surrounding the Orion-Eridanus superbubble, makes this an especially plausible interpretation.

Filamentary material associated with expanding shells will, in general, be especially conducive to the detection of temporal variability. Shell material will be preferentially detected when the line-of-sight is tangential to the shell since the column density of the

gas will be much larger; at the same time, the motion of the material is likely to be perpendicular to the line-of-sight (since it will be moving in a radial direction with respect to the shell). It is therefore possible to detect large changes in column density over short time-scales.

Future Work

Of the work presented in this thesis, the further study of small-scale interstellar structure deserves particular consideration. To this end, a successful proposal to observe κ Vel with the UHRF has been made by Dr. Ian Crawford (awarded three nights 1–3 March 2002 inclusive; semester 02A). The proposal, entitled "Characterisation of the Variable Interstellar Absorption Component Towards κ Velorum", intends to re-observe Na I, Ca II and K I, in addition to making new observations of Ca I and CH. Observations of both Ca I & Ca II will allow, through an analysis of the Ca ionisation balance, an estimation of the value of $n_{\rm e}$, in turn allowing an estimation of $n_{\rm H}$. Using the chemical models presented by Nguyen *et al.* (2001), Nguyen (submitted) has shown that under the conditions proposed to prevail within small-scale interstellar structure (Heiles, 1997), detectable quantities of CH should be present. Thus, the observation of CH will provide further constraints on these conditions and may be compared with those found from the Ca I & Ca II observations. In fact, Pan *et al.* (2001) have recently found structure in CN, CH and CH^+ towards the multiple systems HD 206267 & HD 217035, suggesting the structure is present in gas with spatial densities of $n \lesssim 10^3$ cm^{-3}.

Further investigation of the δ Ori sightline should include ultra-high-resolution ($R \approx 10^6$) observations of Na I towards δ Ori C. The justification for this observation, which may be conducted through the UHRF service programme, would be two-fold. Firstly, it would demonstrate whether the small-scale structure in this direction is composed of variations in the column density of clouds present towards both δ Ori A & C, or is the result of many smaller clouds present in single sightlines. Secondly, our observations have shown a temporally variable interstellar Na I component in the spectrum of δ Ori A to possess corresponding Ca II absorption in the spectra of both δ Ori A & C; detection of a corresponding Na I component in the spectrum of δ Ori C would establish the cloud as being filamentary in nature (since the variability detected towards δ Ori A has been shown to imply an upper limit of 300 AU for the size of the cloud, while the separation of δ Ori A & C is 15,000 AU); else the Na I transient represents a small "core" within a much larger cloud.

Further observations of Na I towards δ Ori A would establish whether the transient absorption represented the passage of a single cloud/filament (specifically related to Orion-Eridanus shell material) or is in fact a part of a larger cloud composed of aligned sheets of

cold, dense gas within warmer less-dense material (of the type proposed by Heiles, 1997, to explain small-scale interstellar structure). If the latter case is true, observations should show an oscillating variation in the Na° column density.

Although additional observation of the neighbouring sightline to δ Ori B would provide further constraints on the small-scale structure in this direction, this star is far too faint (V = 14) to allow observation with the UHRF.

Furthermore, there are many sightlines to other binary systems which have been shown to possess small-scale structure. Re-observing these with the UHRF will show if the amount of structure present has in fact been underestimated, as is concluded in Chapter 5.

Acknowledgements

Foremost, I would like to thank Ian Crawford for the support which he has provided throughout the course of my Ph.D., his tireless enthusiasm for the subject has provided me with continual motivation. I would also like to thank Ian for the valuable time he has spent reading through my work, and for taking the time to apply for post-doctoral funding so that I might continue my research. I would also like to recognise the supervision which Ian provided for my fourth year project - without which I probably wouldn't have done a Ph.D.

I wish to thank the various people in the department who have helped me with a wide range of topics; Ian Howarth for developing the VAPID routine, and taking the pain out of line-profile modelling! Mike Barlow for proof reading my papers and Chapter 1 of this thesis; Pete Storey for help with atomic absorption cross-sections, and all other members of the department who have been so willing to help.

I would like to thank PPARC for the award of a Research Studentship and providing funding for the numerous field-trips necessary for my work. I wish to thank both PATT and the Mount Stromlo Observatory for the award of telescope time on the AAT and Mount Stromlo 74-inch telescope respectively, and the staff of both observatories for their help in setting up the instruments. I thank Raylee Stathakis and Stuart Ryder of the AAO for their help with UHRF service and user observation of δ Ori. This research has made use of the SIMBAD database operated at CDS, Strasbourg, France.

A special thank you goes to Tammay Nguyen for the support and encouragement she has given me, both during my Ph.D. and before. Tammay has helped me in ways far too numerous to list, without her I would have undoubtedly been lost.

I would like to thank my parents, to whom this thesis is dedicated, for both the moral

and financial support which they have been so willing to provide. Without their help, this thesis would not have been possible.

I would like to thank Chris Evans, Stuart Colley and Phil O'Neill for the solutions they have provided to a wide range of problems; John Deacon for house-training my laptop; Yiannis Tsamis and Richard Townsend for thesis template files; Angela Speck for introducing me to the wonders of LaTeX and Barbara Ercolano for some much needed help with my dreadful FORTRAN programming skills.

Finally I wish to thank all of my friends who were able to take my mind off work when that was what was required (and sometimes when it wasn't).

Frontispiece

A representative colour image of the inner Orion Nebula composed of 81 near-infrared exposures taken with ESO's Very Large Telescope (VLT) using the Infrared Spectrometer And Array Camera (ISAAC). Credit goes to Mark McCaughrean of the Astrophysikalisches Institut Potsdam. The bright stars at the centre of the image are the Trapezium (from the top, clockwise; θ^1 Ori B, A, C & D). The two bright stars at the bottom left of the image are θ^2 Ori A (right) and θ^2 Ori B (left). The blue emission stretching diagonally across the bottom left of the image (between the Trapezium and θ^2 Ori A & B is the Orion Bar. North is up and East is to the left.

List of Publications

The following papers have been based on the work presented in this thesis:

Price R. J., Crawford I. A., Barlow M. J., 2000, MNRAS, **312**, L43

Price R. J., Crawford I. A., Howarth I. D., 2001, MNRAS, **321**, 553

Price R. J., Crawford I. A., Barlow M. J., Howarth I. D. 2001, MNRAS, **328**, 555

Howarth I. D., Price, R. J., Crawford, I. A. and Hawkins, I., 2002, MNRAS, (accepted)

Bibliography

Adams, W. S., 1943, *ApJ*, **97**, 105

Adams, W. S., 1944, *PASP*, **56**, 119

Adams, W. S., 1949, *ApJ*, **109**, 354

Aldrovandi, S. M. V. and Pequignot, D., 1974, *Revista Brasileira de Fisica*, **4**, 491

Allen, C. W., 1973, *Astrophysical Quantities* (The Athlone Press, London)

Andrews, S. M., Meyer, D. M. and Lauroesch, J. T., 2001, *ApJ*, **552**, 73

Baade, W. and Minkowski, R., 1937, *ApJ*, **86**, 119

Balick, B., Gammon, R. H. and Hjellming, R. M., 1974, *PASP*, **86**, 616

Bally, J., Langer, W. D., Wilson, R. W., Stark, A. A. and Pound, M. W., 1990, in *Fragmentation of Molecular Clouds and Star Formation*, volume 147 of *IAU Symposium*, p. 11

Barlow, M. J., 1978, *MNRAS*, **183**, 417

Barlow, M. J. and Cohen, M., 1977, *ApJ*, **213**, 737

Barlow, M. J., Crawford, I. A., Diego, F., Dryburgh, M., Fish, A. C., Howarth, I. D., Spyromilio, J. and Walker, D. D., 1995, *MNRAS*, **272**, 333

Barlow, M. J. and Silk, J., 1977, *ApJ*, **211**, 83

Barnard, E. E., 1895, *Popular Astronomy*, **2**, 151

Bates, B., Shaw, C. R., Kemp, S. N., Keenan, F. P. and Davis, R. D., 1995, *ApJ*, **444**, 672

Beals, C. S., 1936, *MNRAS*, **96**, 661

Bergoffen, M. J. and Van Buren, D., 1988, *AJ*, **95**, 130

Bernacca, P. L. and Perinotto, M., 1970, *Contr. Oss. Astrof. Padova in Asiago*, **239**, 1

Bevington, P. R., 1969, *Data Reduction and Error Analysis for the Physical Sciences* (McGraw-Hill, New York)

Blaauw, A., 1964, in *The O Associations in the Solar Neighborhood*, volume 2 of *Annual Review of Astronomy and Astrophysics*, p. 213

Black, J. H. and van Dishoeck, E. F., 1988, *ApJ*, **331**, 986

Blades, J. C., Sahu, M. S., He, L., Crawford, I. A., Barlow, M. J. and Diego, F., 1997, *ApJ*, **478**, 648

Boss, B., 1937, *General Catalogue of 33342 Stars for the Epoch 1950* (Carnegie Institute Publishing, Washington D.C.)

Bowers, R. and Deeming, T., 1984*a*, *Astrophysics I: Stars* (Jones and Bartlett Publishers, Boston, MA)

Bowers, R. and Deeming, T., 1984*b*, *Astrophysics II: Interstellar Matter and Galaxies* (Jones and Bartlett Publishers, Boston, MA)

Brown, A. G. A., Hartmann, D. and Burton, W. B., 1995, *A & A*, **300**, 903

Cha, A. N. and Sembach, K. R., 2000, *ApJS*, **126**, 399

Chromey, F. R., Elmegreen, B. G. and Elmegreen, D. M., 1989, *AJ*, **98**, 2203

Cleary, M. N., 1977, *Ph.D. Thesis* (Australian National University)

Cowie, L. L. and Songaila, A., 1986, in *High-Resolution Optical and Ultraviolet Absorption-Line Studies of Interstellar Gas*, volume 24 of *Annual Review of Astronomy and Astrophysics*, p. 499

Cowie, L. L., Songaila, A. and York, D. G., 1979, *ApJ*, **230**, 469

Cowie, L. L. and York, D. G., 1978, *ApJ*, **223**, 876

Cox, D. P. and Smith, B. W., 1974, *ApJ*, **189**, 105

Crawford, I. A., 1990, *The Observatory*, **110**, 145

Crawford, I. A., 1992, *MNRAS*, **259**, 47

Crawford, I. A., 1995, *MNRAS*, **277**, 458

Crawford, I. A., Barlow, M. J. and Blades, J. C., 1989, *ApJ*, **336**, 212

Crawford, I. A., Howarth, I. D., Ryder, S. D. and Stathakis, R. A., 2000, *MNRAS*, **319**, 1

Crawford, I. A., Rees, I. A. and Diego, F., 1987, *The Observatory*, **107**, 147

Crinklaw, G., Federman, S. R. and Joseph, C. L., 1994, *ApJ*, **424**, 748

Danks, A. C. and Sembach, K. R., 1995, *AJ*, **109**, 2627

Danks, A. C., Walborn, N. R., Vieira, G., Landsman, W. B., Gales, J. and García, B., 2000, *ApJ*, **547**, 155

Davis, R. J., Diamond, P. J. and Goss, W. M., 1996, *MNRAS*, **283**, 1105

Deshpande, A. A., 2000, *MNRAS*, **317**, 199

Deutschman, W. A., Davis, R. J. and Schild, R. E., 1976, *ApJS*, **30**, 97

Diamond, P., Goss, W. M., Romney, J. D., Booth, R. S., Kalberla, P. M. W. and Mebold, U., 1989, *ApJ*, **347**, 302

Dickey, J. M. and Lockman, F. J., 1990, *Annual Review of Astronomy and Astrophysics*, **28**, 215

Diego, F., 1993, *Applied Optics*, **32**, 6284

Diego, F., Fish, A. C., Barlow, M. J., Crawford, I. A., Spyromilio, J., Dryburgh, M., Brooks, D., Howarth, I. D. and Walker, D. D., 1995, *MNRAS*, **272**, 323

Dieter, N. H., Welch, W. J. and Romney, J. D., 1976, *ApJ*, **206**, 113

Duley, W. W. and Williams, D. A., 1984, *Interstellar Chemistry* (Academic Press, London)

Dunkin, S. K. and Crawford, I., 1999, *MNRAS*, **302**, 197

Dyson, J. E. and Williams, D. A., 1997, *The Physics of the Interstellar Medium* (Institute of Physics Publishing, Bristol and Philadelphia)

Elmegreen, B. G., 1997, *ApJ*, **477**, 196

ESA, 1997, *The Hipparcos and Tycho Catalogues* (ESA SP-1200)

Evans, D. S., 1967, in *The Revision of the General Catalogue of Radial Velocities*, volume 30 of *IAU Symposium*, p. 57

Faison, M. D. and Goss, W. M., 2001, *AJ*, **121**, 2706

Faison, M. D., Goss, W. M., Diamond, P. J. and Taylor, G. B., 1998, *AJ*, **116**, 2916

Federman, S. R., 1982, *ApJ*, **257**, 125

Ferlet, R., Vidal-Madjar, A. and Gry, C., 1985, *ApJ*, **298**, 838

Field, G. B., Goldsmith, D. W. and Habing, H. J., 1969, *ApJ*, **155**, 149

Frail, D. A., Weisberg, J. M., Cordes, J. M. and Mathers, C., 1994, *ApJ*, **436**, 144

Franco, J., Tenorio-Tagle, G., Bodenheimer, P., Rozyczka, M. and Mirabel, I. F., 1988, *ApJ*, **333**, 826

Frisch, P. C., Sembach, K. and York, D. G., 1990, *ApJ*, **364**, 540

Gahm, G. F., 1994, *Baltic Astronomy*, **3**, 85

Galkina, T. S., 1976, *Krymskaia Astrofizicheskaia Observatoriia, Izvestiia*, **54**, 128

Genzel, R. and Stutzki, J., 1989, in *The Orion Molecular Cloud and Star Forming Region*, volume 27 of *Annual Review of Astronomy and Astrophysics*, p. 41

Goudis, C., 1982, *The Orion Complex: A Case Study of Interstellar Matter* (Dordrecht, Reidel)

Guthrie, B. N. G., 1986, *MNRAS*, **220**, 559

Gwinn, C. R., 2001, *ApJ*, **561**, 815

Hartmann, J., 1904, *ApJ*, **19**, 268

Harvey, A. S., Stickland, D. J., Howarth, I. D. and Zuiderwijk, E. J., 1987, *The Observatory*, **107**, 205

Heger, M. L., 1919, *Lick Obs. Bull.*, **10**, 59

Heiles, C., 1997, *ApJ*, **481**, 193

Heiles, C., 1999, in *New Perspectives on the Interstellar Medium*, volume 168 of *ASP Conference Series*, p. 211

Heintz, W. D., 1980, *ApJ*, **44**, 111

Hobbs, L. M., 1969*a*, *ApJ*, **157**, 135

Hobbs, L. M., 1969*b*, *ApJ*, **157**, 165

Hobbs, L. M., 1969*c*, *ApJ*, **158**, 461

Hobbs, L. M., 1971, *ApJ*, **166**, 333

Hobbs, L. M., 1973, *ApJ*, **181**, 79

Hobbs, L. M., 1974, *ApJ*, **191**, 381

Hobbs, L. M., 1978*a*, *ApJS*, **38**, 129

Hobbs, L. M., 1978*b*, *ApJ*, **222**, 491

Hobbs, L. M., 1984, *ApJS*, **56**, 315

Hobbs, L. M., Ferlet, R., Welty, D. E. and Wallerstein, G., 1991, *ApJ*, **378**, 586

Hobbs, L. M., Wallerstein, G. and Hu, E. M., 1982, *ApJ*, **252**, 17

Hobbs, L. M. and Welty, D. E., 1991, *ApJ*, **368**, 426

Hoffleit, D. and Jaschek, C., 1982, *The Bright Star Catalogue, Fourth edition* (New Haven: Yale University Observatory (4th edition))

Howarth, I. D., Murray, J., Mills, D. and Berry, D. S., 1998, *Starlink User Note*, **No. 50.21**

Howarth, I. D., Price, R. J., Crawford, I. A. and Hawkins, I., 2002, *MNRAS*, submitted

Howarth, I. D. and Prinja, R. K., 1989, *ApJS*, **69**, 527

Isobe, S., 1973, in *Interstellar Dust and Related Topics*, volume 52 of *IAU Symposium*, p. 433

Israelian, G., Chentsov, E. and Musaev, F., 1997, *MNRAS*, **290**, 521

Jenkins, E. B., 1978, *ApJ*, **220**, 107

Jenkins, E. B. and Meloy, D. A., 1974, *ApJ*, **193**, 121

Jenkins, E. B. and Peimbert, A., 1997, *ApJ*, **477**, 265

Jenkins, E. B., Woźniak, P. R., Sofia, U. J., Sonneborn, G. and Tripp, T. M., 2000, *ApJ*, **538**, 275

Jura, M., 1976, *ApJ*, **206**, 691

Kitchin, C. R., 1998, *Astrophysical Techniques* (Institute of Physics Publishing, Bristol)

Koch, R. H. and Hrivnak, B. J., 1981, *ApJ*, **248**, 249

Kulkarni, S. R. and Heiles, C., 1987, in *Interstellar Processes (eds. D. J. Hollenbach and H. A. Thronson, Jr.)*, Reidel, Dordrecht, proceedings of the symposium on interstellar processes, held in Grand Teton National Park, July 1986, p. 87

Lambert, D. L. and Danks, A. C., 1986, *ApJ*, **303**, 401

Lang, W. J., Masheder, M. R. W., Dame, T. M. and Thaddeus, P., 2000, *A & A*, **357**, 1001

Lasker, B. M., 1966, *ApJ*, **143**, 700

Lauroesch, J. T. and Meyer, D. M., 1999, *ApJ*, **519**, 181

Lauroesch, J. T., Meyer, D. M. and Blades, J. C., 2000, *ApJ*, **543**, 43

Lauroesch, J. T., Meyer, D. M., Watson, J. K. and Blades, J. C., 1998, *ApJ*, **507**, 89

Longair, M. S., 1994, *High Energy Astrophysics; Volume 2: Stars, the Galaxy and the interstellar medium* (Cambridge University Press)

Lynas-Gray, A. E., 1993, *Computer Physics Comm.*, **75**, 135

Maddalena, R. J. and Morris, M., 1987, *ApJ*, **323**, 179

Maddalena, R. J., Morris, M., Moscowitz, J. and Thaddeus, P., 1986, *ApJ*, **303**, 375

Marschall, L. A. and Hobbs, L. M., 1972, *ApJ*, **173**, 43

Marscher, A. P., Moore, E. M. and Bania, T. M., 1993, *ApJ*, **419**, 101

Mathews, W. G., 1965, *ApJ*, **142**, 1120

McAlister, H. A. and Hendry, E. M., 1982, *ApJS*, **49**, 267

McKee, C. F. and Ostriker, J. P., 1977, *ApJ*, **218**, 148

McNutt, D. P. and Mack, J. E., 1963, *J. geophys. Res.*, **68**, 3419

Meaburn, J., 1976, *Detection and Spectrometry of Faint Light* (D. Reidel Publishing Company, Dordrecht)

Meyer, D. M., 1990, *ApJ*, **364**, 5

Meyer, D. M., 1994, in *The First Symposium on the Infrared Cirrus and Diffuse Interstellar Clouds*, volume 58 of *ASP Conference Series*, p. 3

Meyer, D. M. and Blades, J. C., 1996, *ApJ*, **464**, 179

Meyer, D. M. and Lauroesch, J. T., 1999, *ApJ*, **520**, 103

Münch, G. and Taylor, K., 1974, *ApJ*, **192**, 93

Milman, A. S., Knapp, G. R., Kerr, F. J. and Knapp, S. L., 1975, *AJ*, **80**, 93

Moore, E. M. and Marscher, A. P., 1995, *ApJ*, **452**, 671

Morton, D. C., 1991, *ApJS*, **77**, 119

Murdin, P. and Penston, M. V., 1977, *MNRAS*, **181**, 657

Nguyen, T. K., submitted, *Ph.D. Thesis* (University College London)

Nguyen, T. K., Hartquist, T. W. and Williams, D. A., 2001, *A & A*, **366**, 662

O'Dell, C. R., Valk, J. H., Wen, Z. and Meyer, D. M., 1993, *ApJ*, **403**, 678

O'Dell, C. R. and Wen, Z., 1992, *ApJ*, **387**, 229

O'Dell, C. R., York, D. G. and Henize, K. G., 1967, *AJ*, **72**, 820

Osterbrock, D. E., 1989, *Astrophysics of Gaseous Nebulae and Active Galactic Nuclei* (University Science Books, Mill Valley, California)

Oudmaijer, R. D., Drew, J. E., Barlow, M. J., Crawford, I. A. and Proga, D., 1997, *MNRAS*, **291**, 110

Pan, K., Federman, S. R. and Welty, D. E., 2001, *ApJ*, **558**, 105

Peimbert, M., 1982, in *Symposium on the Orion Nebula - To Honor Henry Draper*, volume 395 of *Annals of the New York Academy of Sciences*, p. 24

Phillips, A., Pettini, M. and Gondhalekar, P., 1984, *MNRAS*, **206**, 337

Pickering, W. H., 1890, *Siderial Messenger*, **9**, 2

Pottasch, S. R., 1972, *A & A*, **20**, 245

Press, W. H., Teukolsky, S. A., Vetterling, W. T. and Flannery, B. P., 1992, *Numerical Recipes in* FORTRAN, *2nd edition* (Cambridge University Press)

Price, R. J., Crawford, I. A. and Barlow, M. J., 2000, *MNRAS*, **312**, 43

Price, R. J., Crawford, I. A., Barlow, M. J. and Howarth, I. D., 2001*a*, *MNRAS*, **328**, 555

Price, R. J., Crawford, I. A. and Howarth, I. D., 2001*b*, *MNRAS*, **321**, 553

Reynolds, R. J. and Ogden, P. M., 1979, *ApJ*, **229**, 942

Rogerson, J. B., Spitzer, L., Drake, J. F., Dressler, K., Jenkins, E. B. and et al., 1973, *ApJ*, **181**, 97

Routly, P. M. and Spitzer, J. L., 1952, *ApJ*, **115**, 227

Savage, B. D., Bohlin, R. C., Drake, J. F. and Budich, W., 1977, *ApJ*, **216**, 291

Sharpless, S., 1959, *ApJS*, **4**, 257

Shortridge, K., Meyerdierks, H., Currie, M., Clayton, M., Lockley, J., Charles, A., Davenhall, C., Taylor, M., Ash, T., Wilkins, T., Axon, D., Palmer, J. and Holloway, A., 1999, *Starlink User Note*, **No. 86.17**

Shull, J. M. and Van Steenberg, M. E., 1982, *ApJS*, **48**, 95

Singh, M., 1982, *A & SS*, **87**, 269

Solomon, P. M., Rivolo, A. R., Barrett, J. and Yahil, A., 1987, *ApJ*, **319**, 730

Spitzer, J. L., 1968, *Diffuse Matter in Space* (John Wiley, New York)

Spitzer, J. L., 1978, *Physical Processes in the Interstellar Medium* (John Wiley, New York)

Spitzer, J. L. and Morton, W. A., 1976, *ApJ*, **204**, 731

Tenorio-Tagle, G., 1979, *A & A*, **71**, 59

Trumpler, R. J., 1931, *PASP*, **43**, 255

Vallerga, J. V., Vedder, P. W., Craig, N. and Welsh, B. Y., 1993, *ApJ*, **411**, 729

van der Werf, P. P. and Goss, W. M., 1989, *A & A*, **224**, 209

van Dishoeck, E. F., 1988, *Rate Coefficients in Astrochemistry* (Kluwer Academic Publishers, Dordrecht)

Wade, C. M. A., 1957, *AJ*, **62**, 148

Wade, C. M. A., 1958, *Rev. Mod. Phys.*, **30**, 946

Wallace, P. T. and Clayton, C. A., 1996, *Starlink User Note*, **No. 78.8**

Warren, W. H. and Hesser, J. E., 1978, *ApJS*, **36**, 497

Watson, J. K. and Meyer, D. M., 1996, *ApJ*, **473**, 127

Welsh, B. Y., Craig, N., Crawford, I. A. and Price, R. J., 1998, *A & A*, **338**, 674

Welsh, B. Y., Vedder, P. W. and Vallerga, J. V., 1990, *ApJ*, **358**, 473

Welty, D. E. and Fitzpatrick, E. L., 2001, *ApJ*, **551**, 175

Welty, D. E. and Hobbs, L. M., 2001, *ApJS*, **133**, 345

Welty, D. E., Hobbs, L. M. and Kulkarni, V. P., 1994, *ApJ*, **436**, 152

Welty, D. E., Hobbs, L. M., Lauroesch, J. T., Morton, D. C., Spitzer, L. and York, D. G., 1999, *ApJS*, **124**, 465

Welty, D. E., Morton, D. C. and Hobbs, L. M., 1996, *ApJS*, **106**, 533

Wen, Z., 1993, *Ph.D. Thesis* (Rice University)

Wilson, R. E., 1953, *General Catalogue of Stellar Radial Velocities* (Carnegie Institute Publishing, Washington DC)

Wilson, R. E., 1963, *General Catalogue of Stellar Radial Velocities* (Carnegie Institute Publishing, Washington DC)

York, D. G., 1974, *ApJ*, **193**, 127

Zhang, C. Y. and Green, D. A., 1991, *AJ*, **101**, 1006

Zhang, C. Y., Laureijs, R. J., Chlewicki, G., Clark, F. O. and Wesselius, P. R., 1989, *A & A*, **218**, 231

Zuckerman, B., 1973, *ApJ*, **183**, 863